SKB

Deformation zone stability and co-seismic secondary fracture displacements at Forsmark

Billy Fälth

SVENSK KÄRNBRÄNSLEHANTERING

Deformation zone stability and co-seismic secondary fracture displacements at Forsmark

Billy Fälth, Clay Technology AB

Abstract

The work presented in this report had two main objectives:

- To make estimates of the long-term stability of the steeply dipping deformation zones ZFMNW0017, ZFMNW1200, ZFMWNW0123, ZFMWNW0809A, ZFMENE0060A and ZFMENE0062A at the site in Forsmark where SKB is planning to build a spent nuclear fuel repository. The focus was on the stability under forebulge stress conditions at the beginning of a glacial cycle. However, the potential impact of the heat generation within the repository was also addressed.

- To make estimates of the co-seismic secondary fracture displacements that potentially could be generated at about 500 m depth at the Forsmark repository site if an earthquake rupture would occur on a nearby deformation zone under either present-day, forebulge or endglacial conditions. The intention was to generate estimates of secondary fracture displacements that are based on less pessimistic assumptions than those applied in earlier similar studies for Forsmark. The sensitivity of the estimated fracture displacements to variations in several input parameters was examined.

The stress fields used in the stability calculations as well as in the calculations of secondary displacements were the sum of a background stress field and glacially induced stresses. Three background stress fields were considered. In the Base case stress field, reverse stress conditions were assumed above 2 km depth while strike-slip conditions prevailed below 2 km. At depths down to about 1 km, the stress field was in general accordance with the "most likely" stress model reported for the Forsmark site. At larger depths, the stress anisotropy, and hence the potential for zone instability, predicted by the Base case model was significantly higher than that of the Forsmark site stress model. For the other two background stress fields, the minor horizontal principal stress σ_h was reduced at depths above 2 km such that, at 500 m depth, the reduction was 11 % and 43 % of σ_h respectively. In the 11 % reduction model, the σ_H-to-σ_h ratio at 500 m depth was 2, in agreement with the maximum ratio reported for Forsmark. In the 43 % reduction model, $\sigma_h = \sigma_v$ above 2 km depth, giving a strike-slip stress regime.

The glacially induced stresses were obtained from a Glacial Isostatic Adjustment simulation based on the University of Main ice-sheet model (UMISM) reconstruction of the Weichselian glaciation (Näslund 2006, Lund et al. 2009). The stresses were picked when the potential for zone instability is at its maximum in the forebulge and endglacial cases, respectively.

The stability of the steep zones was evaluated in terms of Coulomb Failure Stress (*CFS*), which was calculated analytically. Based on the calculations, the following could be concluded regarding the stability under forebulge conditions:

- Given the Base case background stress field, no zone becomes unstable for any assumption of the stress trend or for any of the zone orientations considered here.

- The sensitivity of the stability to the variations in zone strike and dip is modest. At the depth with the lowest stability, *CFS* varies by about 1 MPa, at most, for variations in zone strike and dip within the reported uncertainty ranges.

- Assuming 11 % σ_h reduction, the ZFMNW0017, ZFMNW1200, ZFMWNW0123 and ZFMWNW0809A obtain modest instability close to the ground surface (*CFS* reaching 2 to 3 MPa). With 43 % σ_h reduction, all zones except ZFMENE0060A and ZFMENE0062A obtain considerable *CFS* values that reach between 5 and 10 MPa at the surface.

- ZFMENE0060A and ZFMENE0062A have considerable stability margins at all depths and for all assumptions made here.

Given that the Base case or the 11 % σ_h reduction background stress fields are assumed, the stability changes induced by the heating will have too low magnitudes for any of the steep zones to become unstable.

For the 11 % and 43 % σ_h reduction cases where unstable conditions were found, numerical what-if forebulge earthquake rupture simulations were performed to evaluate the potential for extensive earthquake ruptures and for co-seismic secondary fracture displacements in the projected repository volume. Secondary displacements were simulated on 150 m diameter target fractures. The following could be observed:

- For the background stress field with 11 % σ_h reduction, which is regarded to be the most relevant one out of those considered in the simulations, the rupture was effectively restricted to the rupture initiation region where a forced rupture was imposed. This indicates that the conditions for having an extensive rupture with implications for the repository safety are not fulfilled.

- Applying the hypothetical background stress field with 43 % σ_h reduction gave a considerable increase of the simulated earthquake magnitudes and rupture areas. Ruptures that propagate along the entire deformation zone surface traces were obtained.

- The secondary fracture shear displacements were very modest in all cases. In the 11 % σ_h reduction case, no fracture moved more than 0.1 mm. Applying the 43 % reduction model gave a maximum displacement of about 4 mm.

Numerical what-if earthquake rupture simulations were performed assuming present-day as well as endglacial stress conditions, and secondary fracture displacements were calculated for 17 generic and site-specific target fracture sets. Fractures located at distances in the range 0 to 1 400 m from the ZFMA2 deformation zone were considered. In all simulated cases, the rupture was initiated on ZFMA2. The impact of variations in the following input parameters was examined:

- Hypocentre location.

- Fault dynamic friction coefficient (moment magnitude).

- Background (present-day) stress field orientation.

- Background σ_h stress magnitude.

- Rock mass Young's modulus in repository volume.

- Coupling between stress transients and pore pressure.

- Target fracture friction coefficient.

- Model discretisation.

In total 51 simulations were performed. When considering the simulated earthquake sources the following observations could be made:

- When assuming Base case fault properties the present-day synthetic earthquake generated a moment magnitude of M_w 4.6 while the endglacial model generated a moment magnitude of M_w 5.0. This corresponds to an increase in seismic moment by a factor of about four.

- The seismic moment generated in the endglacial model was about 1/8 of the seismic moment generated in the endglacial model by Fälth et al. (2016). Hence, the present simulation can be regarded to represent a considerably less pessimistic case than that simulated by Fälth et al. Yet, the moment magnitudes and fault average displacements simulated in both the present-day and endglacial models here, appear to be on par with those generated by earthquakes that nucleate at considerably larger depths where the stress levels and the expected earthquake stress drops are higher. Hence, the synthetic earthquakes simulated here should represent realistic-pessimistic cases.

When considering the simulated secondary displacements on target fractures at distances longer than 100 m from the ZFMA2 slip plane, the following could be observed:

- For the gently dipping low-stability target fracture set considered in the present-day model, the largest displacement became some 5 mm when assuming Base case fault properties. For the same fracture set, the maximum displacement in the endglacial case was about 8 mm.

- The largest displacement generated in the endglacial case was 9 mm (Base case assumptions). This was obtained on a gently dipping generic low-stability fracture set. For the same conditions, no displacement generated on the site-specific fracture sets exceeded 1 mm.

- A general observation is that the largest displacements tend to be generated on gently dipping low-stability fractures. This is in accordance with results in previous studies (Fälth et al. 2016, Fälth et al. 2010)

- The fracture shear velocity tends to be proportional to the shear displacement. The highest shear velocity observed here reached about 200 mm/s.

The simulations of secondary displacements at distances shorter than 100 m from the ZFMA2 slip plane indicate that the displacement induced on a fracture in mechanical contact with the slip plane and/or the damage zone can be highly sensitive to the properties of the damage zone. In the present models, the displacements on some fractures in mechanical contact with the slip plane and/or the damage zone increased several times when the damage zone was included in the model. However, the impact of this on fractures outside the damage zone was modest and of no practical importance. No simulated displacement on fractures in contact with the damage zone and/or the slip plane of ZFMA2 exceeded 30 mm.

Out of the model input parameter variations that were made here, the variation in target fracture friction coefficient appears to have the largest potential to influence the results. For a generic fracture set dipping 55°, a reduction in friction coefficient led to a considerable increase in co-seismic displacements. The largest displacement reached about 9 mm, i.e., on par with the largest displacement obtained on the gently dipping sets.

It could be concluded that the sensitivity in the results to the other parameter variations made here was modest. The change in the secondary displacements in response to these parameter variations amounted to a few mm, at most. The largest secondary displacement simulated here on fractures at distances ≥ 100 m from the ZFMA2 slip plane amounted to about 12 mm. This result was obtained in a simulation where the rock mass Young's modulus had been reduced 30 % around selected fractures. Furthermore, it is also indicated by the results that including the effect of pore pressure transients in the simulation tends to give slightly reduced secondary displacements as compared to a simulation without pressure variations. Hence, the Base case assumption with no pore pressure coupling should promote pessimistic results.

Sammanfattning

Arbetet som presenteras i denna rapport hade två huvudsyften:

- Att göra en bedömning av långtidsstabiliteten hos de brantstående deformationszonerna ZFMNW0017, ZFMNW1200, ZFMWNW0123, ZFMWNW0809A, ZFMENE0060A och ZFMENE0062A på platsen i Forsmark där SKB planerar att bygga ett förvar för använt kärnbränsle. Fokus var på stabiliteten vid de spänningsförhållanden som råder i inledningen av en glaciationscykel ("forebulge"). Potentiell inverkan av värmeutvecklingen i förvaret undersöktes emellertid också.

- Att göra en uppskattning av de seismiskt inducerade sekundärsprickrörelser som potentiellt kan genereras på cirka 500 m djup i Forsmarkförvaret om en jordskalvsrörelse inträffar längs en närliggande deformationszon under dagens förhållande, under de förhållanden som råder vid "forebulge" eller vid slutet av en glaciation (ändglaciala förhållanden). Intentionen var att göra uppskattningar av sekundärrörelser som är baserade på mindre pessimistiska antaganden än de som applicerades i tidigare liknande studier för Forsmark. Känsligheten hos de beräknade sprickrörelserna för variationer hos ett flertal indataparametrar undersöktes.

De spänningsfält som användes både i stabilitetsberäkningarna och i beräkningarna av sekundärrörelser var summan av ett bakgrundsspänningsfält och glacialt inducerade spänningar. Tre bakgrundsspänningsfält beaktades. Som grundantagande applicerades ett reverst spänningsfält på djup mindre än 2 km medan ett lateralt spänningsfält rådde under 2 km. På djup ner till cirka 1 km var spänningsfältet i generell överensstämmelse med den "mest sannolika" spänningsmodellen som rapporterats för Forsmark. På större djup var spänningsanisotropin, och således potentialen för zoninstabilitet, signifikant högre än den som ges av spänningsmodellen för Forsmark. I de andra två bakgrundspänningsfälten reducerades den minsta horisontella huvudspänningen σ_h på djup över 2 km på så sätt att reduktionen på 500 m djup uppgick till 11 % respektive 43 %. I 11 %-modellen uppgick σ_H-σ_h-kvoten till 2 på 500 m djup, i överensstämmelse med den högsta kvoten rapporterad för Forsmark. I 43 %-fallet var $\sigma_h = \sigma_v$ över 2 km djup, vilket ger ett lateralt spänningsfält.

De glacialt inducerade spänningarna erhölls från en Glacial Isostatic Adjustment simulering baserad på UMISM-rekonstruktionen av Weichselglaciationen (Näslund 2006, Lund et al. 2009). Spänningar valdes vid de tidpunkter då potentialen för zoninstabilitet är som störst för de förhållanden som råder i inledningen ("forebulge ") respektive i slutet av en glaciation.

Stabiliteten hos de branta zonerna utvärderades med hjälp av stabilitetsmåttet Coulomb Failure Stress (*CFS*), vilket beräknades analytiskt. Baserat på beräkningarna kunde följande slutsatser dras angående stabiliteten vid "forebulge"-förhållanden:

- Givet att grundantagandet om bakgrundsspänningsfältet appliceras blir ingen zon instabil för någon av de spänningsorienteringar eller zonorienteringar som beaktas här.

- Känsligheten hos stabiliteten för variationer i zonernas strykning och stupning är modest. På det djup med den lägsta stabiliteten varierar *CFS* som mest cirka 1 MPa, givet variationer i strykning och stupning inom de rapporterade osäkerhetsintervallen.

- Med antagande om 11 % σ_h-reduktion erhålls modest instabilitet nära markytan (*CFS* når 2 till 3 MPa) på ZFMNW0017, ZFMNW1200, ZFMWNW0123 och ZFMWNW0809A. Antas 43 % σ_h-reduktion får alla zoner utom ZFMENE0060A och ZFMENE0062A avsevärda *CFS*-värden, vilka uppgår till mellan 5 och 10 MPa vid ytan.

- ZFMENE0060A och ZFMENE0062A har avsevärda stabilitetsmarginaler på alla djup och för alla antaganden som görs här

Givet att bakgrundsspänningsfältet följer grundantagandet eller antagandet om 11 % σ_h-reduktion kommer stabilitetsförändringarna inducerade av uppvärmningen att ha för låga magnituder för att medföra instabilitet på någon av de branta zonerna.

För de beräkningsfall med 11 % och 43 % σ_h-reduktion där instabilitet erhölls, genomfördes numeriska "forebulge"-simuleringar av jordskalv i syfte att utvärdera potentialen för omfattande förkastnings-uppsprickning och seismiskt inducerade sekundärsprickrörelser i den planerade förvarsvolymen. Sekundära rörelser simulerades på målsprickor med 150 m diameter. Följande kunde observeras:

- För bakgrundsspänningsfältet med 11 % σ_h-reduktion, vilket anses vara det mest relevanta av de spänningsfält som beaktades i simuleringarna, var uppsprickningen effektivt sett begränsad till det initieringsområde på zonen där uppsprickningen forcerades. Detta indikerar att förutsättningar för en omfattande förkastningsuppsprickning med potentiella konsekvenser för förvarets säkerhet inte existerar.

- Genom att applicera det hypotetiska fallet med 43 % σ_h-reduktion erhölls en avsevärd ökning av de simulerade jordskalvsmagnituderna och av de uppspruckna förkastningsareorna. Uppsprickning längs zonernas hela ytspår erhölls.

- Sekundärsprickrörelserna var mycket måttliga i alla simulerade fall. I fallet med 11 % σ_h-reduktion blev ingen sprickrörelse större än 0.1 mm. Fallet med 43 % σ_h-reduktion gav en största rörelse på cirka 4 mm.

Numeriska jordskalvssimuleringar genomfördes för dagens spänningsfält (bakgrundsspänningsfält) samt för ändglaciala spänningsförhållanden, och sekundärsprickrörelser beräknades för 17 generiska och platsspecifika målsprickset. Sprickor på 0 till 1 400 m avstånd från ZFMA2-zonen beaktades. I alla beräkningsfall, initierades förkastningsuppsprickningen på ZFMA2. Inverkan av variationer i följande indataparametrar undersöktes:

- Hypocenter.
- Dynamisk friktionskoefficient hos förkastningen (momentmagnitud).
- Orienteringen hos bakgrundsspänningsfältet.
- Bakgrundsspänningsfältets σ_h-magnitud.
- Elasticitetsmodulen hos bergmassan i förvarsvolymen.
- Koppling mellan spänningstransienter och portryck.
- Målsprickornas friktionskoefficient.
- Modelldiskretisering.

Totalt 51 simuleringar genomfördes. Följande kunde observeras gällande de simulerade jordskalvskällorna:

- För grundantaganden om förkastningsegenskaper genererade ett skalv vid dagens spännings-förhållanden en momentmagnitud på M_w 4.6 medan den ändglaciala modellen genererade moment-magnituden M_w 5.0. Detta motsvarar cirka fyra gångers ökning av det seismiska momentet.

- Det seismiska moment som genererades i den ändglaciala modellen är cirka 1/8 av det seismiska moment som genererades i den ändglaciala modellen i Fälth et al. (2016). Simuleringen här kan följaktligen anses representera ett avsevärt mindre pessimistiskt fall än det som simulerades av Fälth et al. (2016). De momentmagnituder och förkastningsmedelrörelser som simulerades för såväl dagens spänningsfält som för ändglaciala spänningsförhållanden förefaller likväl vara lik-värdiga med de som genereras vid jordskalv som initieras på avsevärt större djup där spänningar och förväntade spänningstapp är högre. De syntetiska jordskalven som simuleras här bör således representera realistiska-pessimistiska fall.

Följande kunde observeras för sekundärsprickrörelser simulerade på avstånd längre än 100 m från ZFMA2:

- För det svagt sluttande sprickset med låg stabilitet som beaktades i simuleringen med dagens spänningar blev den största rörelsen omkring 5 mm, givet grundantaganden om förkastnings-egenskaper. För samma sprickset blev den maximala rörelsen cirka 8 mm i det ändglaciala fallet.

- Den största rörelsen som genererades i det ändglaciala fallet var 9 mm (för grundantaganden). Detta erhölls för ett svagt sluttande generiskt set med låg stabilitet. För samma antaganden erhölls ingen rörelse större än 1 mm på de platsspecifika seten.

- En generell observation är att de största rörelserna tenderar att genereras på svagt sluttande sprickor med låg stabilitet. Detta är i överensstämmelse med resultat från tidigare studier (Fälth et al. 2010, Fälth et al. 2016).

- Skjuvhastigheten tenderar att vara proportionell mot skjuvrörelsen. Den högsta skjuvhastigheten som observerades här uppgick till cirka 200 mm/s.

Simuleringarna av sekundärskjuvrörelser på avstånd mindre än 100 m från ZFMA2-skjuvplanet indikerar att rörelsen, som induceras på en spricka i mekanisk kontakt med skjuvplanet och/eller den uppspruckna zonen, kan ha en hög känslighet för egenskaperna hos den uppspruckna zonen. I modellerna ökade rörelsen flerfaldigt på några sprickor i kontakt med skjuvplanet och/eller den uppspruckna zonen när den uppspruckna zonen inkluderades i modellen. Inverkan av detta på sprickor utanför zonen var emellertid modest och utan praktisk betydelse. Ingen simulerad rörelse på sprickor i kontakt med den uppspruckna zonen och/eller ZFMA2-skjuvplanet översteg 30 mm.

Utav de indataparametervariationer som gjordes här, framstår det som att en variation i målsprickornas friktionskoefficient har den största potentialen att påverka resultaten. För ett generiskt sprickset med dip 55° ledde en reduktion av friktionskoefficienten till en betydande ökning av de seismiskt inducerade sprickrörelserna. Den största sprickrörelsen uppgick till ungefär 9 mm, i paritet med den största rörelsen som erhölls för de svagt sluttande sprickseten.

För de övriga parametervariationerna som gjordes, kunde det konstateras att känsligheten i resultaten är modest. Förändringar i sekundärrörelser relaterade till dessa parametervariationer uppgick till några mm, som mest. Den största sekundärsprickrörelsen som simulerades här på sprickor på avstånd ≥ 100 m från ZFMA2-skjuvplanet uppgick till cirka 12 mm. Detta resultat erhölls i en simulering där bergmassans elasticitetsmodul hade reducerats 30 % runt utvalda sprickor. Vidare indikerar resultaten att om effekten av portryckstransienter inkluderas i simuleringen så tenderar detta att ge något reducerade sekundärsprickrörelser i jämförelse med en simulering utan portrycksvariationer. Grundantagandet utan portrycksvariationer bör således bidra till att ge större simulerade sprickrörelser.

Contents

1 Background and introduction

1.1 Background

The concept for final disposal of high-level spent nuclear fuel developed by the Swedish Nuclear Fuel and Waste Management Co (SKB) is the KBS-3 system, in which the spent fuel will be encapsulated in canisters consisting of a cast iron insert surrounded by a copper shell (Figure 1-1a). The canisters will be emplaced in vertical deposition holes in crystalline rock at a depth of approximately 500 m and surrounded by a bentonite clay buffer for isolation and protection (SKB 2011). Based on data from an extensive site investigation campaign (SKB 2008), SKB has chosen Forsmark located in south-eastern Sweden as their candidate site for the Spent Fuel Repository.

SKB must show that the long-term repository safety complies with the regulations set up by the authorities. Since the fuel will be hazardous for very long times, the time perspective of the safety assessment is hundreds of thousands of years (SKB 2011). Hence, the assessment must consider the potential effects of low-probability intraplate earthquakes occurring at shallow depths under present-day stress conditions, as well as earthquakes induced by the effects of future glaciations. The long-term safety assessment is focused on the effects on the repository after closure, when all equipment used during construction and operation is removed and the openings are backfilled.

Shaking alone is not considered to have the potential to jeopardize the integrity of the buffer-canisters system, which is confined by the bedrock (SKB 2010a, 2011). The only risk to the repository associated with seismicity is that of canister damage caused by seismically induced fracture shear displacements across canister positions (Fälth et al. 2010); Figure 1-1b). If the shear displacement is large, the shear velocity not too low and the intersection geometry is unfortunate, the deformation could cause damage to the canister and leakage of radionuclides. According to the canister damage criterion presently applied by SKB, a canister intersected by a fracture that is sheared more than 50 mm at seismic velocity (~ 1 m/s) is counted as damaged (SKB 2011).
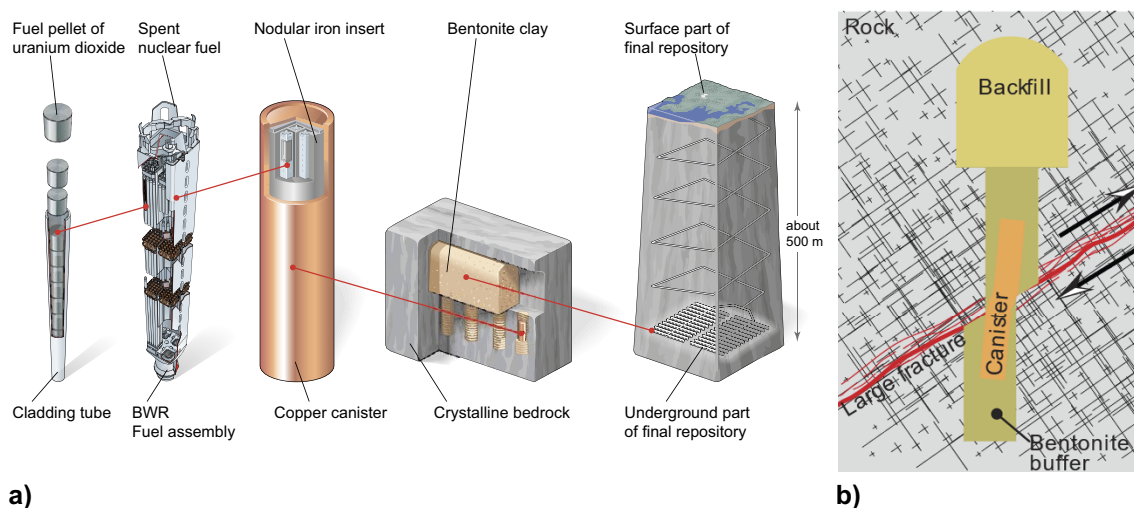

Figure 1-1. *a) Schematic of the KBS-3 system for geological final disposal of high-level spent nuclear fuel. b) Schematic of canister shearing due to slip on a large fracture. Redrawn from Fälth et al. (2010).*

To minimize the seismic hazard, canisters will not be placed within deformation zones that are considered large enough to host major earthquakes (Case #1 in Figure 1-2). Deformation zones that have the potential to generate canister-damaging displacements are judged to be safely detected and avoided during construction of the repository (Hökmark et al. 2019). However, there is still a concern that the combined dynamic and static stress effects generated by an earthquake rupture and the associated fault displacement may induce large secondary shear displacements on fractures at some distance from the rupturing fault plane (Case #3 in Figure 1-2). According to the repository layout rules currently adopted by SKB, canisters will not be deposited within a 100 m respect distance from the boundary of a deformation zone with a trace length exceeding 3 km. Still, there is, at least theoretically, a chance that a canister which is located close to an earthquake zone could be intersected by a large fracture that is mechanically connected to the slip plane of the zone (Case #2 in Figure 1-2). Compared to Case #3, Case #2 could potentially lead to larger secondary displacements.

As input to the post-closure safety assessment of the repository, estimates of seismically induced secondary fracture displacements at repository depth are needed. Due to the lack of observations, the estimates are made by means of numerical simulations. To generate background material to the safety assessment SR-Site, Fälth et al. (2010) performed simulations of secondary fracture displacements using generic model geometries and generic stress models. Later on, based on site investigation data, Fälth et al. (2016) made simulations of secondary displacements specifically for the Forsmark site. A compilation of simulation results produced after SR-Site as well as an evaluation of their validity was made by Hökmark et al. (2019). In their compilation, they included the simulation results by Fälth et al. (2016) as well as results from studies performed within the Finnish nuclear waste management programme (Fälth and Hökmark 2012, 2015, Fälth et al. 2019).

Hökmark et al. (2019) identified a number of issues to be addressed in future work to reduce the conservativeness in the modelling input assumptions and to strengthen the confidence in the modelling results. The work presented in this report is intended to address several of the issues identified by Hökmark et al. (2019). Two of the issues concern the stability of the steep deformation zones at Forsmark, in particular, the stability during the initial phase of a glacial cycle. For a major earthquake to be possible, the conditions must be such that the stability is low over a significant area of a deformation zone. The stability depends on the zone orientation, its properties and the local crustal stress field. As will be shown below, given the stress model reported for Forsmark, the steep deformation zones at Forsmark have significant stability margins. Hence, there may be a potential to reassess the need for respect distances to these zones.
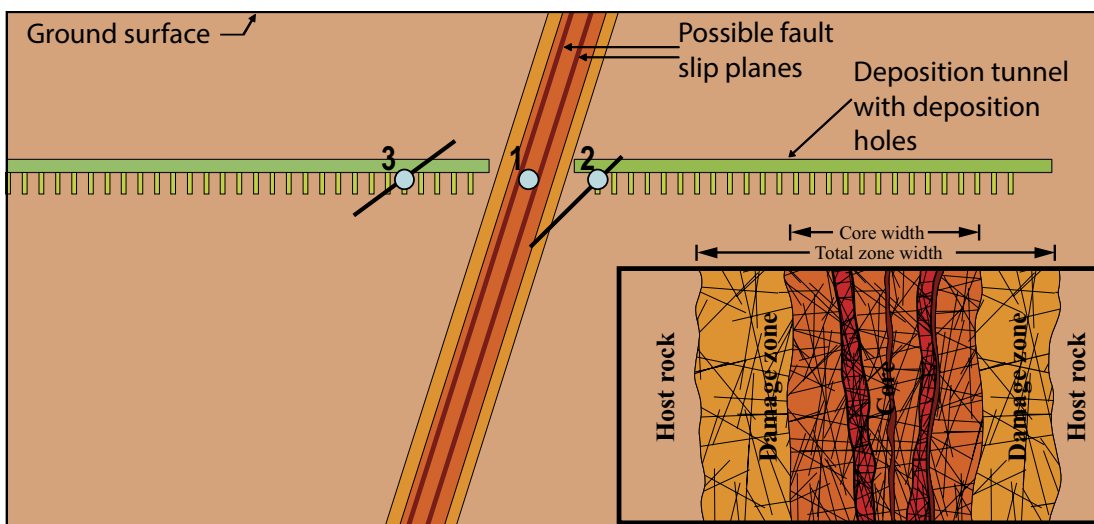

Figure 1-2. *Shear displacement across a deposition hole can potentially occur because the deposition hole is intersected by 1) a slipping earthquake fault, 2) a fracture that is mechanically connected to a slipping earthquake fault, 3) a fracture that is remotely reactivated by a slipping earthquake fault. The inset shows deformation zone components. Redrawn from Fälth et al. (2010).*

Some of the other issues identified by Hökmark et al. (2019) concern simulated secondary displacements. The simulations presented here aim at generating a set of results for the Forsmark site that are based on less pessimistic assumptions than those applied by Fälth et al. (2016). The sensitivity of the results to variations in the input assumptions is also examined. In addition, results from simulations of secondary displacements on fractures in contact with the rupturing fault zone (Case #2 in Figure 1-2) are presented.

To give further background to the work presented in this report, the following subsections provide a brief description of the Forsmark site (1.2) and of the present-day seismicity in Sweden (1.3). There is also a subsection that describes the current understanding about how faults may become unstable due to glacial loads (1.4). The final subsection in this chapter gives an overview of the results generated in the previous studies made on the issues that are addressed here (Fälth et al. 2016, Fälth et al. 2015, Hökmark et al. 2019).

1.2 The Forsmark repository site

The Forsmark site is located about 120 km north of Stockholm. The bedrock at Forsmark is dominated by Precambrian igneous rocks. The repository rock volume is situated within the north-western part of a tectonic lens, the Forsmark lens, which formed between 1.87 and 1.85 billion years ago during the Svecokarelian orogeny (Stephens et al. 2007). The bedrock within the lens is relatively homogeneous and dominated by medium-grained granite. Borehole data support the conceptual model that the lens is a major geological structure that can be traced from the ground surface down to at least 1 km depth (Stephens et al. 2007).

The resulting site model is based on geological mapping of boreholes and drill cores and geophysical measurements of rock mechanical and thermal properties (SKB 2008). A map view according to the geological model (Stephens et al. 2007) of the dominating deformation zones at the site is shown in Figure 1-3a. Only zones with trace lengths > 3 km are considered to have the potential to generate earthquakes large enough to jeopardize the integrity of the repository (Fälth et al. 2010). The outlines of the seven deformation zones with trace lengths > 3 km in the nearest vicinity of the planned repository is shown in Figure 1-3b. Out of these zones, only ZFMA2 is gently dipping, while the other zones all are close to vertical. The plots in Figure 1-3 show that ZFMA2 is terminated against the larger ZFMNW0017 zone. The repository is planned to be in the footwall of ZFMA2, between ZFMNW1200 and ZFMWNW0809A (Figure 1-3a). It can be noted in Figure 1-3a that the respect distance rule has implications for the extensions of the repository areas.

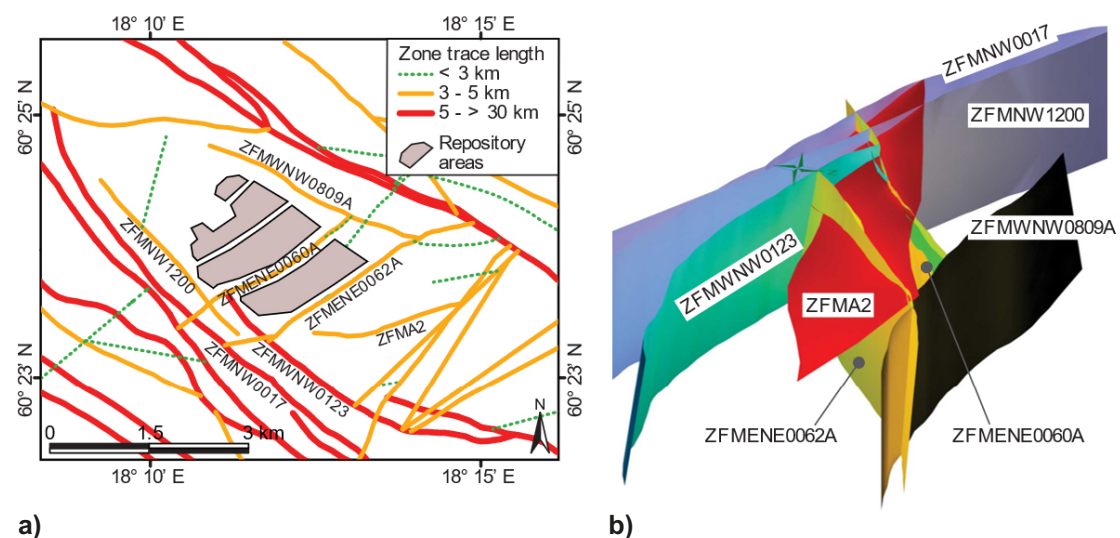**a)**   **b)**

Figure 1-3. *a) Deformation zone map at the projected repository depth 470 m in Forsmark, and b) 3D view of the zones surrounding the repository volume (from Fälth et al. 2016). Among the seven zones with lengths > 3 km close to the repository, only one (ZFMA2) is gently dipping.*

1.3   Present-day seismicity in Sweden

Sweden is presently a low seismicity area, far from plate boundaries, with most of the earthquakes located in the south-western portion of the country, along the coast of the Gulf of Bothnia and in Norrbotten (Bödvarsson et al. 2006, Lund et al. 2017, Slunga 1991). About one to two seismic events are recorded every day by the Swedish National Seismic Network (SNSN), but the majority of these are small and at such depths that they pose no serious threat to constructions (Bödvarsson et al. 2006, Lund et al. 2021). Here are some examples of significant events. The foci of the Skövde 1986 magnitude 4.5 earthquake and its aftershocks were located at 20–35 km depth (Arvidsson et al. 1992) and the 2008 Skåne County magnitude 4.3 earthquake had a focal depth of about 10 km. Two other events are the 2014 Sveg magnitude 4.1 event at 12 km depth (Lund et al. 2014) and the 2016 Bottenviken magnitude 4.1 event with an estimated focal depth somewhere in the range 18–22 km (Lund et al. 2016).

1.4   Glacially induced faulting

A glacial cycle, with kilometres of ice covering the Earth's surface for long periods of time, has a significant impact on the stress field in the upper crust. The weight of the ice is causing the crust beneath the ice cover to bend down into the viscous mantle (Lund et al. 2009). The down-bending is accompanied by an uplift of the crust in front of the ice margin, a state called "forebulge". The defor-mation of the crust induces stress changes to the prevailing background stress field that influence the stability of deformation zones (Fälth 2018, Hökmark et al. 2019, Lund et al. 2009). The magnitude and orientations of the glacially induced stress changes depend on the glacial evolution (thickness of the ice, its spatial extent and temporal evolution), as well as on the elastic and rheological properties of the crust and mantle (Hökmark and Fälth 2014, Lund et al. 2009). The glacial stress changes mean that deformation zones, which are stable and seismically quiet under present-day stress conditions, could potentially be reactivated and host earthquakes. The present-day stability on a deformation zone as well as the amount of glacially induced stability reduction, and hence the potential for reactivation, depend on the orientation of the zone, the orientation and magnitude of the background (present-day) stresses as well as on the orientation and magnitude of the glacially induced stress changes (Hökmark and Fälth 2014). Given the evidence for endglacial faulting in northern Fennoscandia (Lagerbäck and Sundh, 2008) and stability estimates based on results from Glacial Isostatic Adjustment (GIA) simulations (Figure 2-4), there are two stages during a glacial cycle that are considered to be potentially critical for fault stability (cf Figure 1-4); (i) the beginning of the glaciation when an ice cap approaches the actual site (the forebulge) and (ii) the end of glaciation when the stabilising ice cover melts away.

The uplift that is generated by the approaching ice during the forebulge reduces the horizontal stresses in the upper crust and gives reduced stability of steeply dipping fault zones (Figure 1-4b). This could potentially lead to earthquake triggering on such zones (Steffen and Steffen, 2021). Evidence of fore-bulge seismic activity within the Baltic shield in connection with preceding glacial cycles are scarce. To the author's knowledge, there is one location where evidence for seismic activity in front of the ice margin of an advancing ice has been found. Pisarska-Jamroży et al. (2018) interpreted deformations in sediment layers at the Rügen Island to have been induced by seismic activity in front of the margin of the advancing Weichselian ice some 20 000 years ago. However, according to Pisarska-Jamroży et al. (2018), the seismicity was not induced in the forebulge but by crustal down-warping in front of the ice.

The reason for the limited number of observations of seismic events in front of the ice margin may be that such events generated small displacements which were mainly of strike-slip type, and hence did not leave any clearly visible fault scarps. Even if fault scarps were generated, these may have been eroded by the progressing ice. Yet, another explanation may simply be that no such events have occurred.

The results from a study of fault stability evolution during the latest Weichselian glaciation in Olkiluoto, Finland (Hökmark and Fälth 2014) indicated that the time scale for fault stability loss during the forebulge was about one order of magnitude longer than the time scale for fault stability loss during the end of the glaciation. This can be attributed to the high viscosity of the mantle. This means that the time scale for the crustal down-bending beneath the ice and for the corresponding development of the forebulge was long compared to the time scale for the melting of the stabilising ice cap at the end of the

glaciation. Hökmark and Fälth (2014) suggested that the low stress change rates during the forebulge could have favoured aseismic fault movements at the expense of seismic events. They also noted that, during the forebulge, the shear stresses that potentially could have generated strike-slip movements on steep zones, were significantly lower than the shear stresses available for reverse faulting on gently dipping faults at the end of the glaciation.

Based on the observations made by Hökmark and Fälth (2014) of the relatively low strain rates and shear stresses during the forebulge, one could argue that these are general features that will characterize also the forebulge that will develop in the beginning of a future glaciation. However, considering uncertainties in the prevailing background stresses and in the stress changes that could be induced by future glacial loads, there is, at least theoretically, a non-zero probability that the stress alterations induced by a future approaching ice cap can lead to the initiation of an earthquake on steeply dipping fault zones.
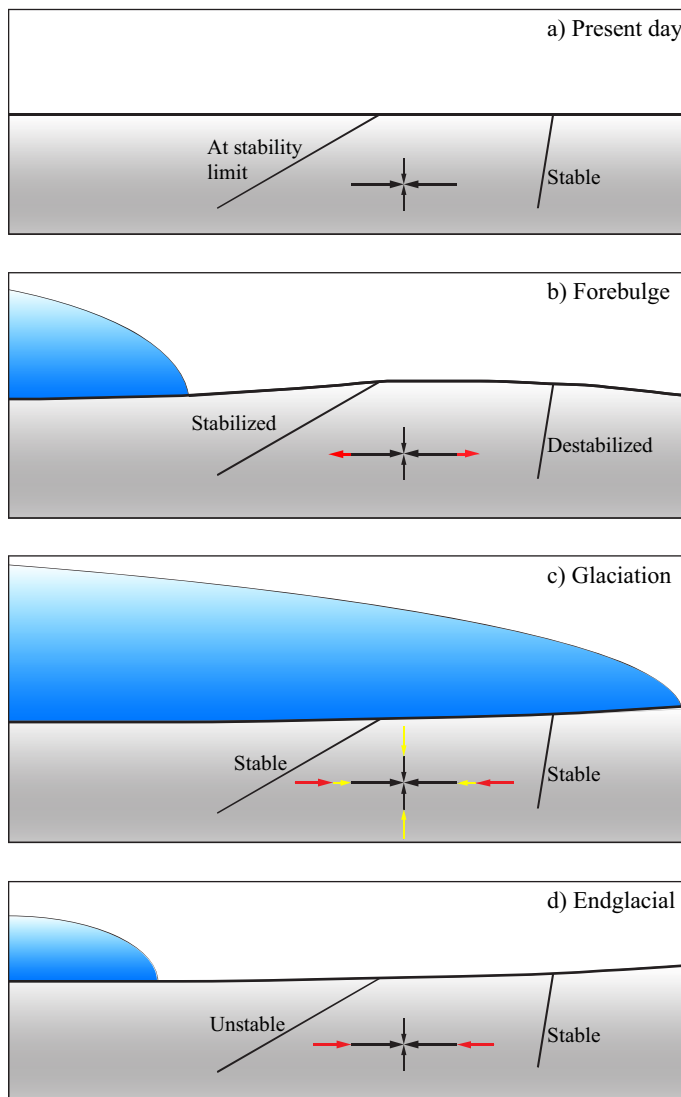
Figure 1-4. *Schematic of stress evolution in the upper crust during a glacial cycle. a) Present-day reverse stress field. b) Stress field during forebulge at the beginning of glaciation. Reduction of horizontal stress (red) and reduced stability of steep fractures and deformation zones c) Stress field under the stabilizing ice cover with the vertical stress increased by the weight of the ice and horizontal stress increased due to the direct elastic response to the vertical load (yellow), tectonic strain accumulation and crustal flexure (red). d) Stress field in region below and outside the margin of the retreating ice. Stresses induced by tectonic strain accumulation and crustal flexure remain (red), giving increased stress anisotropy and possibly reactivation of gently dipping fractures and deformation zones. Note: The arrows are not to scale.*

While the potential for reactivation of steeply dipping deformation zones during the forebulge appears to be uncertain, the stress situation at the end of a glaciation is particularly considered to increase the risk of earthquake triggering. This time period is characterised by increased stress anisotropy in the crust due to the melting of the stabilising ice cap in combination with remaining horizontal excess stresses (Figure 1-4d). The excess stresses have been induced during glaciation by the down-bending of the crust beneath the ice (Lund et al. 2009). There may also be additional horizontal stress excess due to tectonic stresses that have been accumulated beneath the stabilizing ice cover. Increased horizontal stresses destabilise gently dipping fault zones and promote reverse-type faulting (Hökmark and Fälth 2014). This type of fault movement is in accordance with the endglacial faulting that took place in Fennoscandia at the end of the latest Weichselian glaciation. Even though the most prominent traces of endglacial faulting in Fennoscandia are found in the northern parts of the region (Lagerbäck and Sundh 2008, Munier et al. 2020), it cannot be excluded that significant events will take place further south in connection with future glacial cycles.

1.5 Previous studies

To give further background to the work presented in this report, this section summarises previous estimates of deformation zone stability and secondary fracture displacements at Forsmark.

1.5.1 Deformation zone stability

According to the most likely stress model developed for the Forsmark site (Martin 2007) there is a reverse faulting stress field prevailing at Forsmark down to at least 1 km depth. Under such stress conditions, steeply dipping deformation zones tend to have high stability due to high compression and the relatively low stress anisotropy in the horizontal plane. On the other hand, gently dipping zones tend to be less stable.

As discussed in Section 1.4, the forebulge means that the high-stability steeply dipping zones will lose stability. The opposite holds in the endglacial phase when excess in horizontal stresses in combination with the loss of the stabilising vertical ice load leads to destabilisation of gently dipping structures.

Hökmark et al. (2019) estimated the stability of the seven local Forsmark deformation zones depicted in Figure 1-3 for three stress stages: present-day, forebulge and the endglacial phase. They did this using the Coulomb Failure Stress (*CFS*) as stability measure. *CFS* is calculated as (Harris 1998)

$$CFS = \tau - \mu(\sigma_n - P) - c. \tag{1-1}$$

Here, τ and σ_n are the shear- and normal stresses acting on a hypothetical fault or fracture plane while P is pore pressure, c is cohesion and μ is the coefficient of friction. Hence, *CFS* is the difference between the shear load and the shear resistance of the fault or fracture and is thus a measure of the potential for slip. A positive *CFS* value means unstable conditions.

In their *CFS* calculation Hökmark et al. (2019) assumed $\mu = 0.65$, $c = 0$ and the pore pressure P to be hydrostatic for present-day and forebulge conditions. For endglacial conditions, excess pore pressures of 1, 2 and 3 MPa, respectively, were schematically assumed for the three different depths (0.5, 1.5 and 3 km) that were considered, in order to account, at least approximately, for potential effects of pore pressures remaining behind the retreating ice margin (Lönnqvist and Hökmark 2013). Furthermore, they applied a reverse background stress field in general accordance with the Forsmark stress model of Martin (2007) down to about 1 km depth. At depths larger than about 2 km, the stress field was assumed to be of strike-slip type, in agreement with observations (Lund and Zoback 1999, Slunga 1991). The glacially induced stresses were obtained from a GIA simulation based on the UMISM reconstruction of the Weichselian glaciation (Lund et al. 2009).

Figure 1-5 shows the *CFS* values calculated by Hökmark et al. (2019) at 0.5, 1.5 and 3 km depth, respectively, for the seven local Forsmark zones (Figure 1-3b). The following can be observed:

- ZFMA2 is the only gently dipping zone and is also the zone with the lowest stability at shallow depths under present-day conditions. It is also the only zone that will be further destabilised under endglacial conditions due to the excess of horizontal stresses. The other zones, which have dip angles between 80 and 90 degrees, all have *CFS* values below about -8 MPa at all three depths under present-day conditions. They also become further stabilized in the endglacial stage due to the increase of horizontal stresses.

- Under forebulge conditions the opposite trend holds. Then, there is a reduction of horizontal stresses in the upper crust and corresponding reduction of compression on steep deformation zones. This is reflected in the *CFS* results in Figure 1-5. Due to the reduced compression, the steeply dipping zones become destabilized at all depths, but the *CFS* values stay below −5 MPa everywhere. ZFMA2 on the other hand gains some stability.
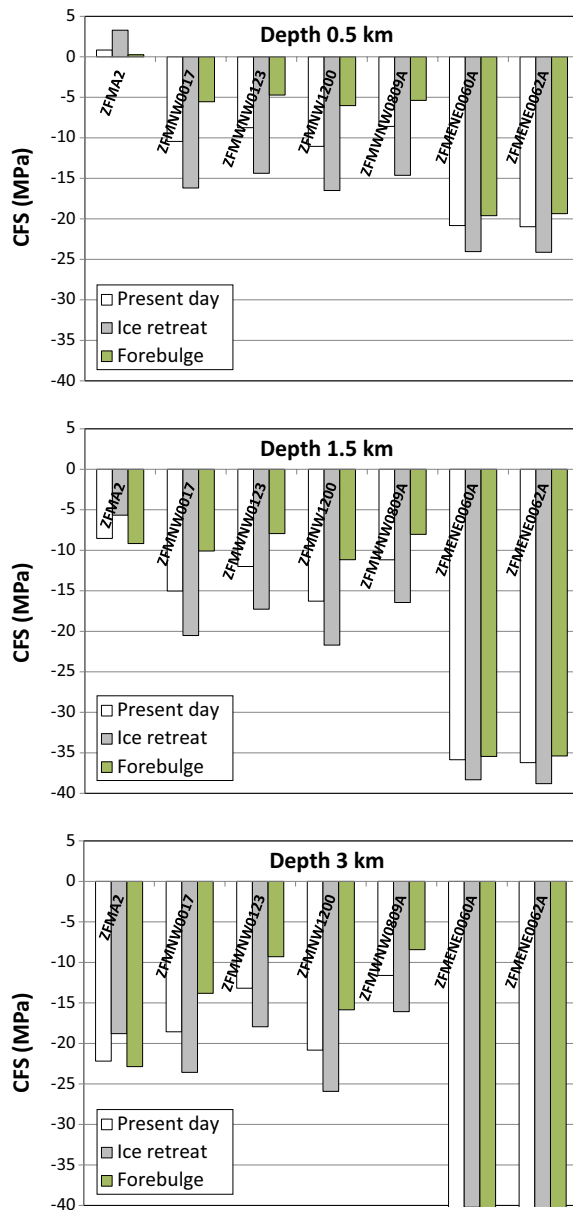

Figure 1-5. Stability in terms of Coulomb Failure Stress (CFS) at three depths on the seven local Forsmark deformation zones with trace lengths > 3 km (Hökmark et al. 2019). Values < 0 mean stable conditions, cf Equation (1-1).

To summarise, the results indicate that the low-stability ZFMA2 zone is the only one of the local Forsmark zones that potentially could have been reactivated during the latest glaciation. The steep zones, on the other hand, all had significant stability margins during all stages of the glacial cycle.

The results presented here are based on a reconstruction of the latest Weichselian glaciation, but can potentially be concluded to hold also for future glacial cycles. It may be possible to show that a local deformation zone, for reasonably pessimistic assumptions about properties and loads, will be stable enough that a large earthquake on that zone can be excluded as a realistic possibility. If earthquakes with potential implications for the repository safety can be excluded, this could have implications for the design of the repository as well as for the safety assessment.

To explore the possibility that the steep deformation zones at Forsmark will remain stable for all potential future load scenarios, the sensitivity to the input assumptions should be examined. As noted in Section 1.4, both orientation and magnitudes of the background stress field have importance for the stability of the steeply dipping deformation zones. According to the rock mechanics site data report (Glamheden et al. 2007) there is a $\pm 15°$ uncertainty in the reported trend of the major horizontal principal stress at Forsmark. There are also uncertainties in the given stress magnitudes. For instance, the ratio between the given minor and major horizontal principal stress magnitudes (σ_H/σ_h) is about 1.8 at the depth of the repository. However, according to Glamheden et al. (2007) the ratio is expected to be in the range 1.4–2. A higher ratio means a larger stress anisotropy and a higher potential for instability.

As with the orientation of the stresses, the orientation of a deformation zone is important for the relation between the shear- and normal load acting on it, and thus for its stability. According to the site model for Forsmark (Stephens and Simeonov 2015) the uncertainty in strike and dip of the local steep deformation zones is in the range 5–10°.

Further, the thermal load from the deposited fuel will give rise to thermal stress additions in the repository host rock. This can alter the stability of faults and fractures within and around the repository. At repository depth, the increased horizontal compression will stabilize steeply dipping faults. At some distance above and below the repository, however, the associated reduction of the horizontal stresses may instead lead to reduced stability of steep faults (Hökmark et al. 2010). In contrast to glacial stress additions, which influence the stress field in the upper crust on a scale corresponding to the size of the ice cap, the thermal stresses will influence the rock volume on a relatively small scale. Even so, the magnitude of the thermal stress additions will only reach a few MPa (Hökmark et al. 2010). Hence, the probability that steeply dipping faults at Forsmark become unstable over significant areas due to the thermal loading should be low. However, this should be shown.

1.5.2   Secondary fracture displacements

To generate background material to be used as input to the previous safety assessment for the repository for spent nuclear fuel, SR-Site, Fälth et al. (2010) simulated co-seismic secondary fracture displacements. In their simulations they used models with generic geometries and applied generic stress fields. In two following studies, simulations of secondary fracture displacements based on Forsmark data were carried out (Fälth et al. 2016, Fälth et al. 2015). The modelling assumptions applied in these two latter studies were similar and the results were similar. However, the study by Fälth et al. (2016) was more extensive. As background to the work presented in this report, the results from that study are described and discussed in this section.

Fälth et al. (2016) performed simulations of co-seismic secondary fracture displacements in Forsmark for endglacial conditions. They applied an initial stress field that is the sum of a background stress field and glacially induced stress additions. At shallow depths, the background stress field was in general agreement with the present-day reverse-type stress field prevailing at the Forsmark site. At depths below 2 km, the stress field was assumed to be of strike-slip type. The glacially induced stress additions were obtained from GIA simulations (Lund et al. 2009) of the Weichselian glacial cycle. The stress additions were picked at the time instance when the stabilising ice cap has just disappeared from the site. At this instance, the stress anisotropy and corresponding potential for fault reactivation is at the highest.

Fälth et al. (2016) concluded that the gently dipping ZFMA2 zone has the lowest stability under present-day conditions out of the seven zones in the nearest vicinity of the repository volume (cf Figure 1-3 and Figure 1-5). They also observed that it is also the only zone that will be further destabilised under endglacial conditions. Hence, they simulated an endglacial earthquake rupture that was initiated on ZFMA2. However, they also included the steep ZFMNW0017 zone in the model since they considered it potentially important for the response of ZFMA2 (Figure 1-6). Considering 22 fracture orientations, both site specific and generic (Figure 1-6c), they calculated secondary displacements on so-called target fractures located at different distances (in the range 200–1 000 m) from ZFMA2. The target fractures were located both in the hanging wall and in the footwall of ZFMA2, as shown in Figure 1-6. Considering several different rupture scenarios, they examined the potential impact on the secondary displacements of the hypocentre location, the strength of the adjoining ZFMNW0017 zone, the amount of fault pre-stress (initial stress) as well as of the residual strength of the rupturing ZFMA2 zone.

As a basic assumption, Fälth et al. (2016) applied infinite fault zone shear strength during application of the initial stresses, i.e., no aseismic pre-slip was allowed. This led to a high stress drop $\Delta\tau$ and associated large zone displacements during rupture. Stress drop $\Delta\tau$ is the difference between the initial fault shear stress τ_1 and the final fault shear stress τ_2, i.e., $\Delta\tau = \tau_1 - \tau_2$. Contours of stress drop generated in the Fälth et al. (2016) Base case simulation and in a case with reduced initial fault stress are shown in Figure 1-7. As seen in that figure, the simulated stress drop is on the order of several megapascals on the ZFMA2 zone, which is shallow and extends only to 1–1.5 km depth. This amount of stress drop is in general comparable with intraplate events (Scholz 2002) where the rupture occurs at much larger depths (several kilometres).
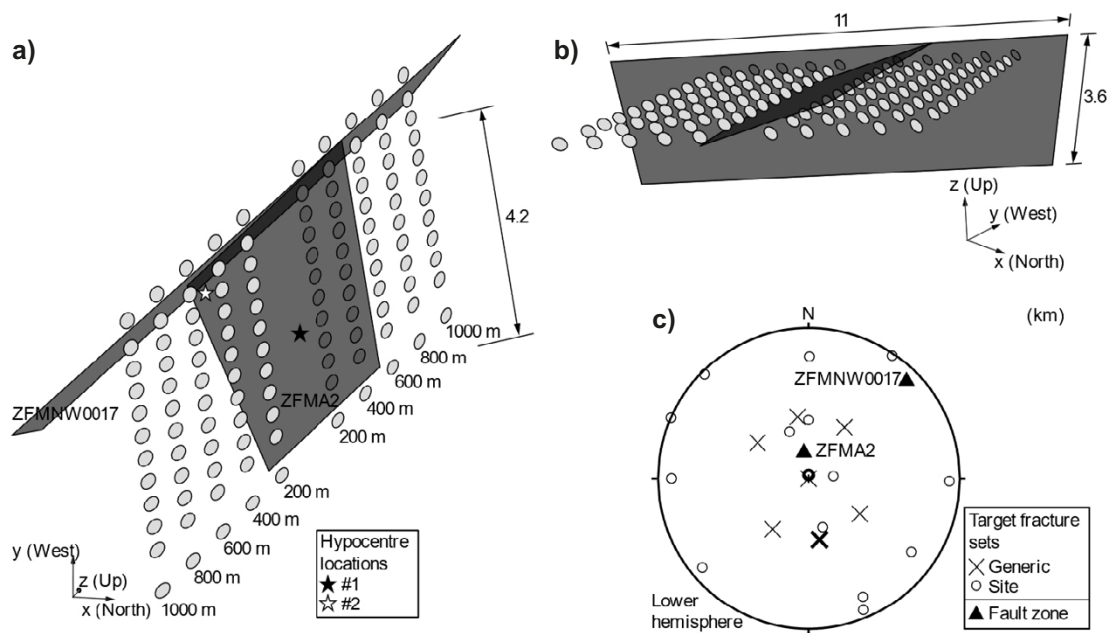

Figure 1-6. *Outline of the model used in the previous Forsmark study. a) View from above of the ZFMA2 and ZFMNW0017 zones as well as of the target fractures. The two alternative hypocentres are indicated. b) Same as a) but viewed from northwest. c) Orientations of the target fractures and the zones. Redrawn from Fälth et al. (2016).*
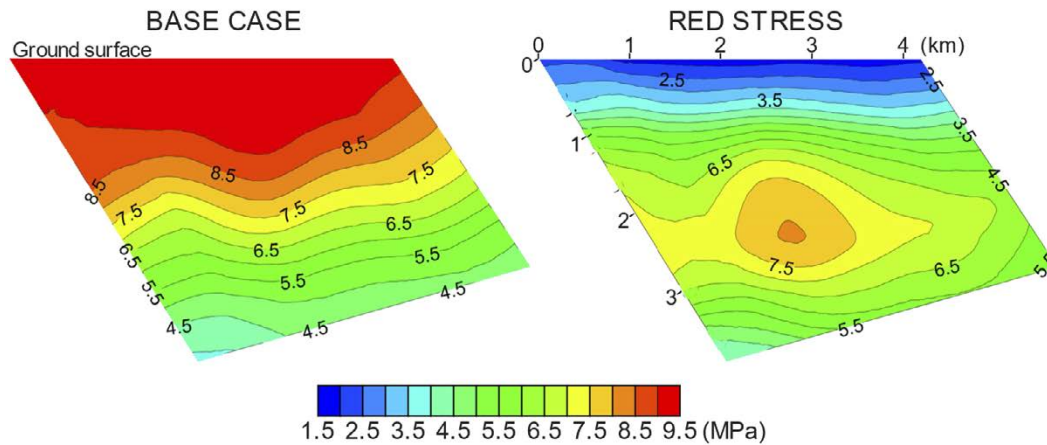
Figure 1-7. *Contours of simulated stress drop on ZFMA2. Left: Case where no aseismic fault slip was allowed prior to rupture initiation, giving high initial stress and high stress drop. Right: Case with reduced initial fault stress. Redrawn from Fälth et al. (2016).*

The assumption of infinite strength on ZFMA2 and the high stress drops that were generated during rupture, led to considerable fault slip and moment magnitudes in the synthetic earthquakes simulated by Fälth et al. (2016). This is illustrated in Figure 1-8, where the moment magnitudes-rupture area relations of the synthetic earthquakes are plotted along with the corresponding data for crustal earthquakes (Wells and Coppersmith 1994). The synthetic events plot in the upper end of the data range. When doing this comparison, one should keep in mind that the events in the Wells and Coppersmith (1994) database occurred under present-day conditions while the synthetic earthquakes were intended to simulate endglacial events, for which the magnitude-to-area relation is uncertain. The traces of endglacial faulting found in northern Fennoscandia indicate very considerable fault movements (Lagerbäck and Sundh, 2008). The exact mechanisms that triggered these movements and that gave these large fault offsets are not known. However, the potential for large reverse fault movements should possibly be higher under endglacial conditions, due to increased horizontal stresses, as indicated in Figure 1-5 (Steffen and Steffen 2021). So, in that respect, it may be relevant to expect the magnitude-to-area ratio to be, in general, higher for endglacial events than for events occurring under present-day conditions. How much higher this ratio would be is not clear, though.

As noted above, there is another possibly more important parameter hidden in the data presented in Figure 1-8. The synthetic earthquakes are simulated on a very shallow zone, which extends to 1–1.5 km depth, while the real events in the Wells and Coppersmith (1994) database occur on much larger depths. At larger depths the stresses are higher, and since the stress drop is, in general, related to the stress level (Scholz 2002), earthquakes occurring at larger depths should have the potential to generate higher stress drops and correspondingly larger displacements on a given rupture area. Figure 1-9 shows average slip versus focal depth for events from the Wells and Coppersmith catalogue. The average slip values u_{avg} of the catalogue events were calculated from (Hanks and Kanamori 1979, Kanamori and Anderson 1975)

$$u_{avg} = \frac{M_0}{RA \cdot G} \text{ m}$$

with

$$M_0 = 10^{1.5(M_w+6.07)} \text{ Nm}$$

(1-2)

where the values of rupture area RA and moment magnitude M_w were according to Figure 1-8, and M_0 denotes the seismic moment. The shear modulus G was assumed to be 30 GPa. The focal depths were obtained through a literature search and the references are given in Table 1-1. The catalogue events show a significant scatter in slip for given focal depths. This can probably be attributed partly to uncertainties in the determination of moment magnitudes and rupture areas, but there may also be a real scatter depending on ambiguities in the underlaying physics.
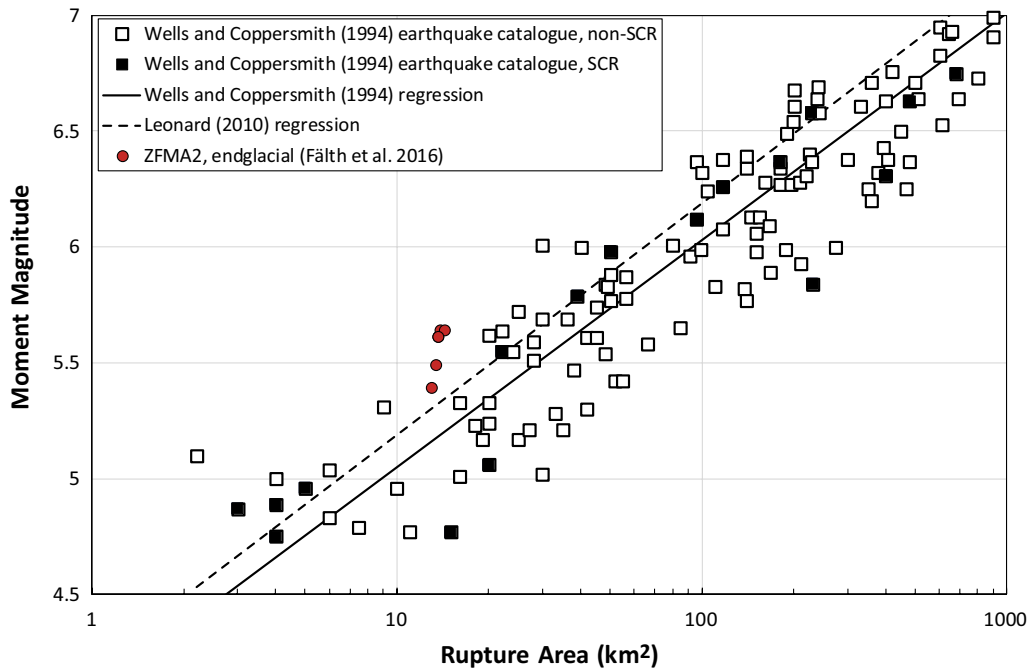
Figure 1-8. *Moment magnitude versus rupture area for crustal earthquakes plotted along with corresponding database regressions and the simulation results of the endglacial earthquakes on the ZFMA2 zone in Forsmark from Fälth et al. (2016). "SCR" means "Stable Continental Region".*

For comparison, the data from the synthetic earthquakes on ZFMA2 are plotted in Figure 1-9. These events have focal depths of about 500 m and 1 000 m and the depth extent of the zone is a little more than 1 000 m, as noted above. Given the Wells and Coppersmith (1994) catalogue events, one would possibly expect such a shallow earthquake to generate an average displacement that is of the order of 0.05 m. Then, considering the effect of endglacial stress additions, a corresponding endglacial event could possibly be expected to generate displacements in the range 0.05–0.1 m. However, as seen in Figure 1-9 these earthquakes generate average displacements that are several times larger than that. This indicates that the displacements generated in these simulated ZFMA2 events are strongly exaggerated, and that they can be considered outlier events.

Table 1-1. Focal depth references in Figure 1-9.

Ref no.	EQ no. in W&C 1994*	Reference	Ref no.	EQ no. in W&C 1994*	Reference
1	180	(Westaway et al. 1989)	20	149	(Frankel, 1984)
2	214	(Hauksson et al. 1988)	21	212	(Wei & Chung, 1993)
3	197	(USGS, 2020)	22	110	(Hartzell & Brune, 1979)
4	97	(Ellsworth et al. 1973)	23	224	(Ma & Kanamori, 1991)
5	77	(Thatcher & Hamilton, 1973)	24	211	(Langer & Bollinger, 1991)
6	242	(Walter, 1993)	25	173	(Nabelek & Suarez, 1989)
7	198	(Zhou et al. 1993)	26	195	(Wesson and Nicholson 1986)
8	236	(Dreger & Helmberger, 1991)	27	93	(Johnson & McEvilly, 1974)
9	231	(Hauksson & Jones, 1991)	28	176	(Moreno & Camelbeeck, 2013)
10	165	(Choy et al. 1983)	29	142	(Hasegawa & Wetmiller, 1980)
11	136	(Peppin et al. 1989)	30	166	(Frankel, 1984)
12	234	(Horton et al. 1997)	31	94	(Johnson & McEvilly, 1974)
13	184	(Spence et al. 1996)	32	126	(USGS, 2020)
14	88	(Ellsworth, 1975)	33	226	(USGS, 2020)
15	133	(Haessler et al. 1980)	34	138	(USGS, 2020)
16	59	(Evans & McEvilly, 1982)	35	207	(USGS, 2020)
17	150	(Courjault-Radé et al. 2009)	36	213	(USGS, 2020)
18	237	(Hardebeck, 2010)	37	235	(USGS, 2020)
19	155	(Mauk et al. 1982)			

* Earthquake number in the earthquake catalogue of Wells & Coppersmith (1994).
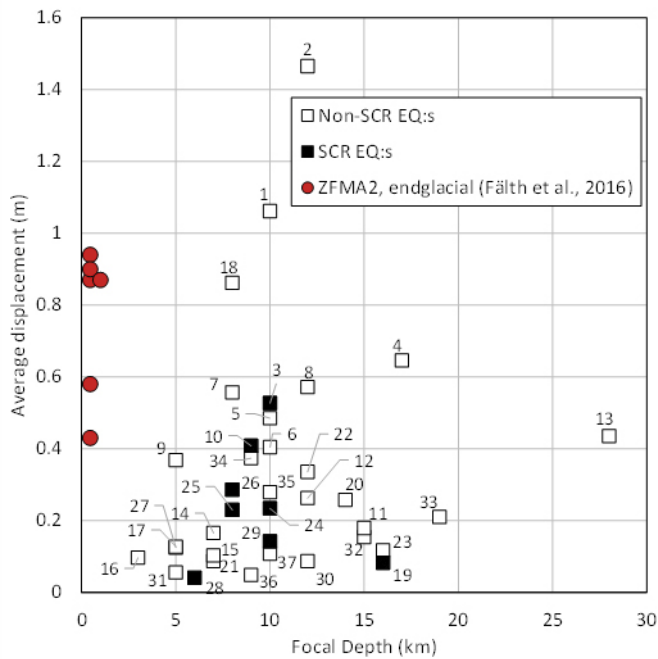
Figure 1-9. *Average fault slip versus focal depth for crustal earthquakes from the Wells and Coppersmith (1994) catalogue plotted along with corresponding results from simulations of endglacial earthquakes on ZFMA2 in Forsmark. The catalogue events are from the data set presented in Figure 1-8, but limited to a rupture area of 40 km². "SCR" means "Stable Continental Region". The data labels refer to the references in Table 1-1 supporting the given focal depths.*

The largest simulated secondary fracture displacement in the Fälth et al. (2016) simulations amounted to about 60 mm (on 300 m diameter fractures) and was generated in the hanging wall of ZFMA2, close to the edge of the zone and hence outside the planned repository volume (cf Figure 1-3). The largest displacement found in the footwall was slightly below 40 mm, and was generated in a simulation case where the hypocentre was located at the lower position (#2 in Figure 1-6a). In general, the displacements were modest. On average, about 80 % of the fractures in the footwall of ZFMA2 moved less than 10 mm in the simulation case with the hypocentre located at the lower position. In the other simulation cases the displacements were generally smaller.

The model for rupture propagation that was adopted as a Base case assumption by Fälth et al. (2016) uses a controlled and constant rupture propagation speed and infinite shear strength ahead of the rupture front. In their study, Fälth et al. did not report any results showing the co-seismic evolution of fault stress. However, in another study, Fälth and Hökmark (2015) adopted a similar model for rupture propagation and could conclude that the assumption of infinite fault strength ahead of the rupture front gave large stress peaks at the front. They also observed that this led to stronger secondary effects and larger co-seismic secondary fracture displacements as compared to a case where the fault strength was limited.

The considerable stress drops and fault displacements generated by the synthetic earthquake sources simulated by Fälth et al. (2016, 2015), along with the adopted rupture protocol, which tends to generate strong stress peaks, suggest that the simulated co-seismic secondary fracture displacements can be regarded to be overestimates rather than underestimates.

1.6 Objectives and scope

The work presented in this report had two main objectives:

- To make estimates of the long-term stability of the six steeply dipping deformation zones at Forsmark, ZFMNW0017, ZFMNW1200, ZFMWNW0123, ZFMWNW0809A, ZFMENE0060A and ZFMENE0062A. Focus was lain on forebulge conditions, when the stability of steep zones tends to be lowest, cf Section 1.4 and Section 1.5.1. In addition, the impact on the zone stability of the heat generated by the decaying spent fuel was examined.

- To make estimates of co-seismic secondary fracture displacements that potentially can be generated within the projected repository volume at the Forsmark site. The intention was to generate estimates of secondary fracture displacements that are based on less pessimistic assumptions than those applied by e.g. Fälth et al. (2016). The sensitivity of the results to model input parameter variations was also examined. Several of the model cases and the variations in model input tested here address items that were identified by Hökmark et al. (2019) to be important for further examination.

The stress fields used in this work were the sum of a background stress field and glacial stress additions from a GIA simulation (Lund et al. 2009) based on the University of Main ice sheet model (UMISM) reconstruction of the Weichselian glaciation (Näslund 2006). Differences in the glacial evolution (temporal evolution, thickness, and extent of the ice cap) may lead to differences in the induced stress changes and in the corresponding impact on zone stability. It is unclear if the spatial extents and temporal evolutions of future glaciations will differ significantly from those of the latest Weichselian glaciation. However, as of yet, no stress data based on alternative glacial scenarios other than the UMISM reconstruction is available for the Forsmark site.

Using analytic calculations, the stability of the steeply dipping deformation zones under forebulge conditions is evaluated in terms of *CFS*. The sensitivity of *CFS* to the stress magnitudes and the orientation of the background stress field is examined. Variations in zone strike and dip within the ranges given by Forsmark site data are also considered. For those cases where instability is indicated, what-if dynamic earthquake rupture simulations are performed to study the fault response and to obtain estimates of the potential for secondary fracture shear displacements within the projected repository volume.

Using the same numerical model geometry as that used in the simulations of forebulge earthquake ruptures, simulations of what-if earthquake ruptures occurring under present-day and endglacial conditions are performed. In all these simulations it is assumed that the earthquake rupture is initiated on the ZFMA2 zone. As concluded earlier (Fälth et al. 2016, Hökmark et al. 2019), this is the local Forsmark deformation zone (cf Figure 1-3, Figure 1-5), which, due to its shallow position and gently dipping geometry, has the lowest stability under present-day stress conditions. It is also the only local zone that will be further destabilised under endglacial conditions. Based on this observation, earthquake ruptures initiated under present-day conditions as well as under endglacial conditions are simulated. The focus is on ruptures occurring under endglacial conditions when the ZFMA2 stability is estimated to be lowest.

Based on the observations made in Section 1.5.2, it is judged that there is room for less pessimistic and less exaggerated model assumptions to be applied in the present models compared to those applied by Fälth et al. (2016, 2015). Based on comparisons of model output with corresponding data reported for crustal earthquakes, model input parameter values are set such that the simulated earthquake ruptures can be expected to generate realistic-pessimistic secondary stress effects.

As in the Fälth et al. (2016) study, several target fracture orientations are considered. The models include generic orientations as well as orientations that are based on site data.

The shortest fault-to-fracture distance (fault plane to target fracture centre) considered in the previous Forsmark studies (Fälth et al. 2016, Fälth et al. 2015, Fälth et al. 2010) was 200 m. In the present work, a specifically designed model geometry is built where target fractures close to and in contact with the ZFMA2 slip plane are included. In this model the fault-to-fracture distances are in the range 0 to 150 m.

To obtain a better foundation for setting bounds to the uncertainties in the results, and to increase the confidence in the conclusions, the impact on the results of variations in several model input assumptions is examined. These are discussed below:

- Considering the shallow position of ZFMA2 and its gently dipping geometry, modest alterations in the background horizontal stress trend are not judged to give any significant difference in its response and in the associated secondary displacements. The stability of the adjacent steeply dipping zones may be more sensitive to the stress trend, but this is not expected to have any dramatic implications for the results either. However, given the uncertainty in the present-day stress trend at Forsmark (Glamheden et al. 2007, Martin 2007), the potential importance of this is demonstrated here. In addition, the potential impact of a reduced minor horizontal stress magnitude is examined since it may give a lower stability of steep zones and fractures.

- In the calculations by Fälth et al. (2016), it was assumed that the pore pressure in all discontinuities is constant. It is known, however, that stress alterations in rocks can induce pore pressure perturbations that depend on the magnitude of the stress change, the load rate and the permeability of the rock mass (Scholz 2002, Simpson 2001). Hence, the stress waves generated during fault rupture may result in pore pressure transients in the rock mass surrounding an earthquake source fault. Since pore fluid pressure influences the stability of faults and fractures, pressure transients may have implications for the potential of co-seismic fracture displacements. Here, the impact on the secondary displacements of considering stress-induced pore pressure transients is examined.

- For a given shear stress change on a fracture, the resulting shear displacement scales inversely with the shear modulus of the surrounding rock mass (Eshelby 1957). Hence, a spatial variation of the rock mass deformation modulus may mean that the potential for larger secondary fracture displacements is higher at some positions. To examine how strong this effect may be, a case with a schematically modelled spatial variation in the rock mass deformation modulus is analysed.

- The hypocentre location has importance for how the earthquake rupture propagates as well as for the magnitude and mode of the stress waves that are generated. This has implications for the amount of secondary displacements that may be induced (Fälth et al. 2016). Here, two hypocentre locations are tested.

- The shear resistance of the host rock fractures has importance for how easily they can be reactivated by a stress transient induced by, e.g., a nearby earthquake source. Here, in addition to the Base case assumption of the target fracture friction coefficient, two alternative values are tested.

- The numerical discretisation has importance for how stresses and strains are calculated. In dynamic simulations it has an impact on how stress waves are propagated in the model volume (Fälth et al. 2019, Kuhlemeyer and Lysmer 1973). The impact on the results of refining the model discretisation is examined.

1.7   This report

The remaining part of this report is divided into seven chapters according to the following:

- Chapter 2 describes the input data that is used in the analyses made here.

- The calculations made for estimating the stability of the steep deformation zones are presented in Chapter 3.

- In Chapter 4 the numerical modelling approach is described.

- The results from the forebulge earthquake rupture simulations are presented in Chapter 5.

- The results from the present-day and endglacial earthquake rupture simulations are presented in Chapter 6.

- Chapter 7 contains a discussion of the relevance and validity of the simulations.

- In Chapter 8 the results are summarised and the conclusions are presented.

2　Input data

2.1　Deformation zone geometries

The geometries of the deformation zones are set according to the deformation zone model of Forsmark (Stephens and Simeonov 2015). In reality, deformation zones are not perfectly planar but may show spatial variations in both dip and strike (cf Figure 1-3b). In addition, there will inevitably be uncertainties in the determination of the orientation of a deformation zone. In the analytic zone stability calculations carried out here, the average values of zone strike and dip given by the Forsmark site deformation zone model are adopted as a basic assumption (Table 2-1). However, the uncertainty ranges given by the site model are also considered. The values used in the earthquake rupture simulations are the average values.

Table 2-1. Deformation zone data (Stephens and Simeonov 2015).

Zone	Strike θ (°)	Dip δ (°)	Trace length (m)
ZFMA2	80 ± 15	24 ± 10	4 000
ZFMNW0017	135 ± 5	85 ± 10	7 900
ZFMWNW0123	117 ± 5	82 ± 10	5 100
ZFMNW1200	138 ± 5	85 ± 10	3 300
ZFMWNW0809A	116 ± 5	90 ± 10	3 300
ZFMENE0060A	239 ± 5	85 ± 10	3 100
ZFMENE0062A	58 ± 5	85 ± 10	3 400

2.2　Stress field

The stress field controls the normal- and shear loads on discontinuities. Hence, it is of great importance both for the stability of deformation zones and fractures, and for the amount of slip that could be generated on such structures in the case they become unstable. Here, two types of stress fields are used as input to the zone stability calculations and to the numerical earthquake rupture simulations: (i) a background (present-day) stress field and (ii) glacially induced stress additions obtained from a GIA simulation. The stress models are presented in the following two subsections.

2.2.1　Background (present-day) stress field

The stress model developed for the Forsmark repository site (Glamheden et al. 2007, Martin 2007) can be regarded to be valid down to some 1 000 m depth. According to the model there is a reverse faulting stress regime at Forsmark. The notion of a reverse stress regime at shallow depths is in agreement with conclusions made by Stephansson et al. (1991) regarding stresses in the Fennoscandian shield. At larger depths, the uncertainties regarding both stress regime and stress magnitudes are larger. However, there are observations that give some indications. Measurements made in the Siljan region (Lund and Zoback 1999) as well as earthquake source mechanisms analysed by Slunga (1991) indicate that a strike-slip stress regime dominates at depth in the Baltic Shield. Furthermore, the results of Lund and Zoback (1999) agree with the notion that the crust is in frictional equilibrium on optimally oriented faults (Zoback and Townend 2001).

As a Base case assumption, the background stress field applied here (Equation (2-1)) agrees with the "most likely" Forsmark site stress model down to 500 m depth. To obtain strike-slip stress conditions at larger depths (cf the discussion above), the minor horizontal principal stress σ_h is modelled using a bi-linear depth dependence below 500 m depth. It is modelled such that it is equal to the vertical stress σ_v at 2 km depth. At depths below 2 km, the σ_h-depth relation is set such that strike-slip stress condi-

tions are obtained ($\sigma_h < \sigma_v$). The choice of 2 km depth for stress regime transition is schematic but is based on the notions made above of reverse stress conditions down to at least 1 km depth in Forsmark and strike-slip stress conditions at larger depths. The magnitudes of the principal components of the Base case stress field are defined by

$$\sigma_H = \begin{cases} 19 - 8z & -0.15 \leq z \leq 0 \\ 9.1 - 74z & -0.4 \leq z \leq -0.15 \\ 29.5 - 23z & -0.5 \leq z \leq -0.4 \\ 23.5 - 35z & z \leq -0.5 \end{cases}$$

$$\sigma_h = \begin{cases} 11 - 6z & -0.15 \leq z \leq 0 \\ 6.8 - 34z & -0.4 \leq z \leq -0.15 \\ 9.2 - 28z & -0.5 \leq z \leq -0.4 \\ 13.3 - 19.9z & 2 \leq z \leq -0.5 \\ 21 - 16z & z \leq -2 \end{cases} \qquad (2\text{-}1)$$

$$\sigma_v = -26.5z$$

where σ_H, σ_h and σ_v are the major horizontal, the minor horizontal and the vertical stress components, respectively, in MPa and z is depth in kilometres (negative downwards). Figure 2-1 shows the background stress field (full lines). Comparing the horizontal stress anisotropy at 1 km depth of the Forsmark stress field (dashed lines) with the anisotropy of the Base case stress field used here, it appears that the stress field here overestimates the stress anisotropy (Figure 2-1). If the Forsmark stress field is extrapolated to 4 km kilometres depth (dotted lines) the horizontal anisotropy would practically disappear, making all steeply dipping local deformation zones extremely stable. For the stress field applied here, the anisotropy instead increases with depth. The stress anisotropy of the stress field defined by Equation (2-1) corresponds to frictional equilibrium on optimally oriented fault planes (Jaeger and Cook 1979) with a friction coefficient of $\mu = 0.41$ at 2 km depth, $\mu = 0.55$ at 5 km depth and $\mu = 0.61$ at 7.5 km depth. The assumption of a stress anisotropy corresponding to a friction coefficient in the range 0.5 to 0.6 at 4–6 km depth is in agreement with the observations made in the Siljan region by Lund and Zoback (1999).
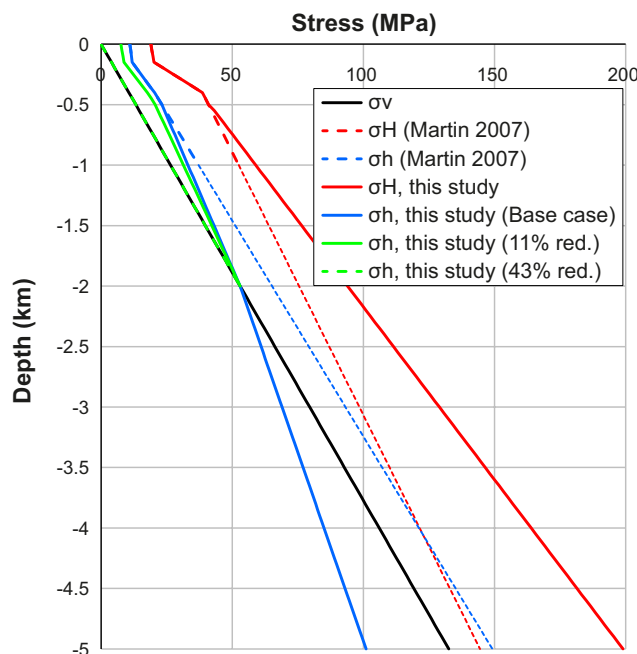

Figure 2-1. *Forsmark background (present-day) stress field as given by Martin (2007) and Glamheden et al. (2007) along with the stress fields used in this study. The green lines show the two alternative σ_h models above 2 km depth. The thin dotted lines show stresses at depths larger than 1000 m as given by an extrapolation of the Martin (2007) model.*

As Base case assumption the major horizontal stress trend is assumed to be N145°E, in accordance with the Forsmark site stress model (Glamheden et al. 2007, Martin 2007) and other data from south-central Sweden (Lund and Zoback 1999, Slunga 1991) indicating that the direction of the maximum horizontal stress is in agreement with push from the Mid-Atlantic Ridge, i.e., in the range N120°E – N150°E. To account for uncertainty in the orientation of the proposed Forsmark stress field (Glamheden et al. 2007, Martin 2007), a 20° uncertainty in the σ_H stress trend is considered. When evaluating stabilities of the steep deformation zones, two additional trends, N125°E and N165°E, are considered in addition to the base case assumption of N145°E.

For endglacial conditions, when an earthquake rupture is assumed to initiate on ZFMA2, the stability of that zone as well as of the adjoining ZFMNW0017 zone (cf Section 1.5.2) is considered most important. Assuming endglacial conditions and N165°E background σ_H stress trend means a marginal (3 %) CFS increase (reduced stability) on ZFMA2 relative to the case with N145°E stress trend while CFS is reduced 1 % on ZFMNW0017. For stress trend N125°E, CFS on ZFMA2 is reduced about 8 % and increased some 14 % on ZFMNW0017. Given the larger alterations of deformation zone CFS obtained in the case with N125°E, this alternative background stress field is considered for the endglacial rupture scenario.

Furthermore, according to the proposed Forsmark stress field (Glamheden et al. 2007, Martin 2007), the horizontal stress ratio σ_H/σ_h is in the range 1.4 to 2 at repository depth. For the stress field adopted here (Equation (2-1)), this ratio is about 1.8 at 500 m depth. To account for uncertainty in the stress magnitudes, a case is tested where σ_h is schematically reduced at depths above 2 km such that $\sigma_H/\sigma_h \approx 2$ at 500 m depth, i.e. in the upper end of the stress ratio range proposed by Glamheden et al. (2007). This means an 11 % σ_h reduction at 500 m depth. The ratio $\sigma_H/\sigma_h \approx 2$ could also be achieved by increasing σ_H, but that would give a slightly higher stability of steep zones than the case with reduced σ_h. At the other depths above 2 km σ_h is reduced proportionally, such that the reduction is largest at the surface (31 %) and zero at 2 km depth.

In addition, a case is included where the minor horizontal stress is set equal to the vertical stress (i.e. $\sigma_h = \sigma_v$) at all depths above 2 km. This means 43 % σ_h reduction at 500 m depth (Figure 2-1). It should be noted, however, that this latter case can be regarded to be a hypothetical case. The considerable stress anisotropy associated with this stress field assumption is illustrated by the CFS results shown in Figure 2-2. The CFS calculation indicates that steep zones at Forsmark would be in a state of failure under present-day conditions, assuming the 43 % σ_h reduction case.

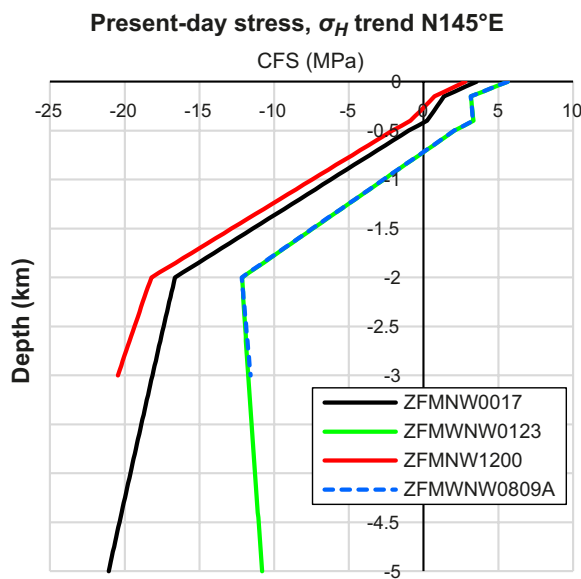**Present-day stress, σ_H trend N145°E**

Figure 2-2. CFS versus depth under present-day stress conditions on four of the steep Forsmark zones assuming 43 % σ_h reduction and friction coefficient 0.7.

2.2.2 Glacially induced stresses

Figure 2-3 shows the glacial stress evolution assumed for the Forsmark site. These glacial stresses were obtained by Lund et al. (2009) from a GIA analysis performed using the UMISM reconstruction (Näslund 2006) of the Weichselian glaciation as input. As seen in the figure, the forebulge state is characterized by a reduction in horizontal stress. This gives reduced compression and corresponding loss of stability on steeply dipping structures (cf Section 1.4). To maximise the potential for faulting, the glacial stresses that are added to the background stresses are picked at the stages when the instability is at its maximum. For the steeply dipping zones this means the forebulge stage (39 kyrs in Figure 2-3 and Figure 2-4) and for ZFMA2 the endglacial stage (58 kyrs in Figure 2-3 and Figure 2-4).
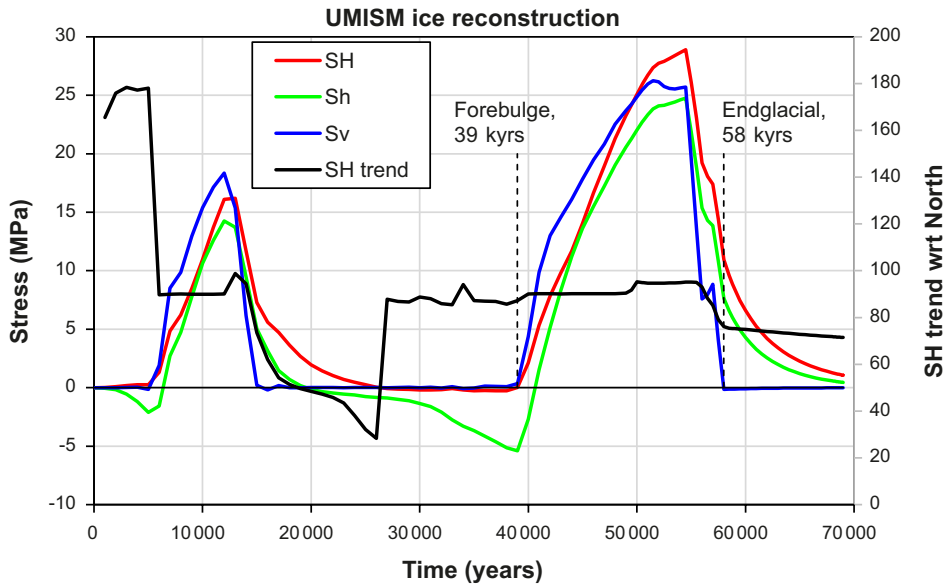

Figure 2-3. *Principal components and orientation of glacially induced stresses at 500 m depth in Forsmark as calculated by Lund et al. (2009). The results are based on the UMISM reconstruction (Näslund 2006) of the Weichselian glaciation.*
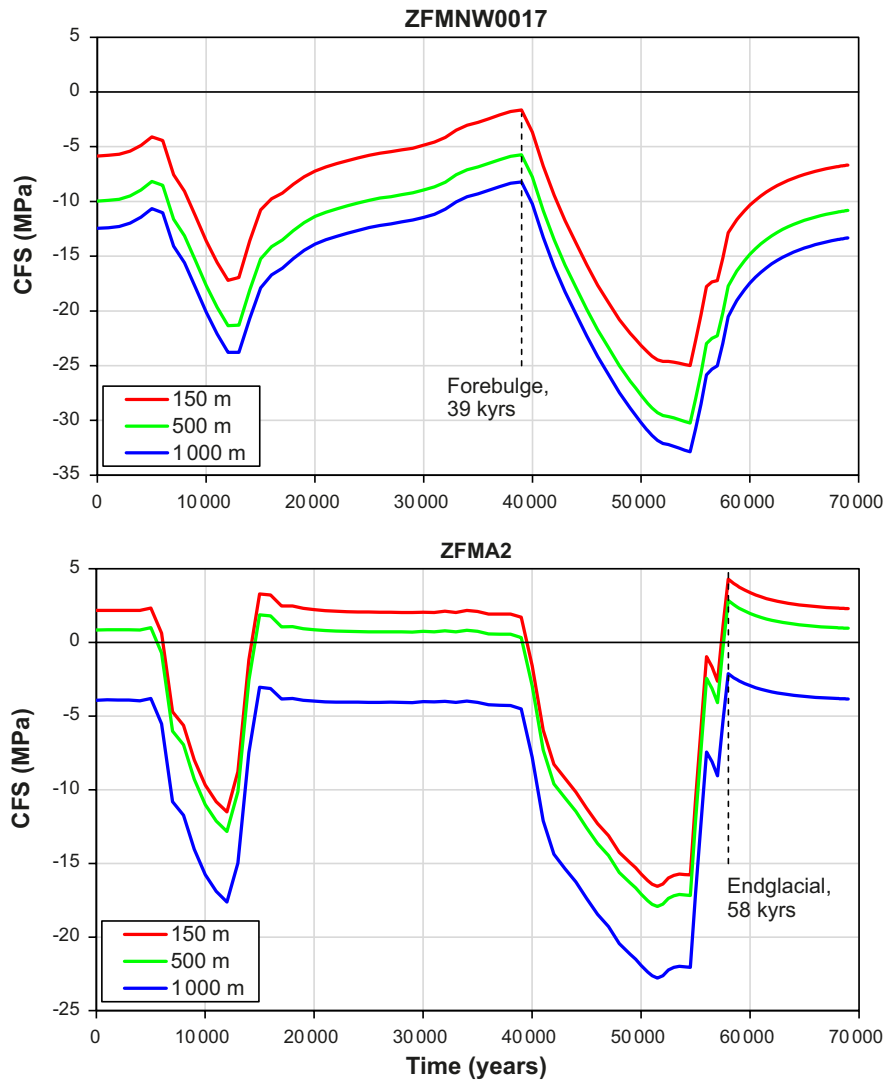
Figure 2-4. *Temporal evolution of CFS (Equation (1-1)) (assuming μ = 0.7) at three depths on the steeply dipping ZFMNW0017 (upper) and on the gently dipping ZFMA2 (lower) when applying the Base case background stress field (Equation (2-1)) and adding the glacial stresses in Figure 2-3.*

3 Stability of the steeply dipping zones

3.1 Forebulge stress conditions

The stability of the six steep Forsmark deformation zones (Table 2-1) is evaluated in terms of *CFS* (Equation (1-1)). *CFS* is calculated at different depths under forebulge stress conditions for different zone orientations (strikes and dips), different background stress field orientations and different magnitudes of the background σ_h stress component at shallow depths. The two longest zones (ZFMNW0017 and ZFMWNW0123) are assumed to reach 5 km depth while the maximum depth extension for the other zones is assumed to be 3 km. The basic assumption is to set the friction coefficient of the zones to $\mu = 0.7$, in accord with site data (Glamheden et al. 2007). The porewater pressure is assumed to be hydrostatic. The following parameter variations are made:

- Three values of the σ_H trend of the background stress field are tested: N125°E, N145°E and N165°E.

- Three levels of the background σ_h magnitude above 2 km depth are tested: Base case level (Equation (2-1)), the Base case level reduced by 11 % and 43 %, respectively, at 500 m depth (see discussion in Section 2.2.1).

- The strikes of the zones are varied according to the uncertainty ranges given in Table 2-1.

- The dip angles of the zones are varied according to the uncertainty ranges given in Table 2-1. Note that for all zones, the upper end of the range means a dip angle > 90°. Here, the maximum dip is set to 90°.

- A lower value $\mu = 0.6$ of the friction coefficient is tested.

In Figure 3-1 it is shown how *CFS* varies with depth for the six zones assuming their average values of strike and dip (Table 2-1). The diagrams show results for the three σ_H stress trends tested here. For the σ_H stress trend that yields the lowest stability (different trends for different zones), the cases with the background σ_h magnitude reduced 11 % and 43 %, respectively, at 500 m depth are also considered. This "critical" stress trend is also adopted when the lower friction coefficient $\mu = 0.6$ is considered.

The sensitivity to variations in deformation zone strike and dip is illustrated by contour plots in Figure 3-2 for ZFMNW0017. The corresponding results for all six zones are presented in Appendix A. These plots were generated assuming the Base case σ_h stress magnitude (Equation (2-1)). Each column shows results for one σ_H trend. In the upper row, *CFS* values for different strikes are presented (keeping the dip angle at the nominal value) while *CFS* variations with respect to dip are shown in the bottom row (keeping the strike at the nominal value).
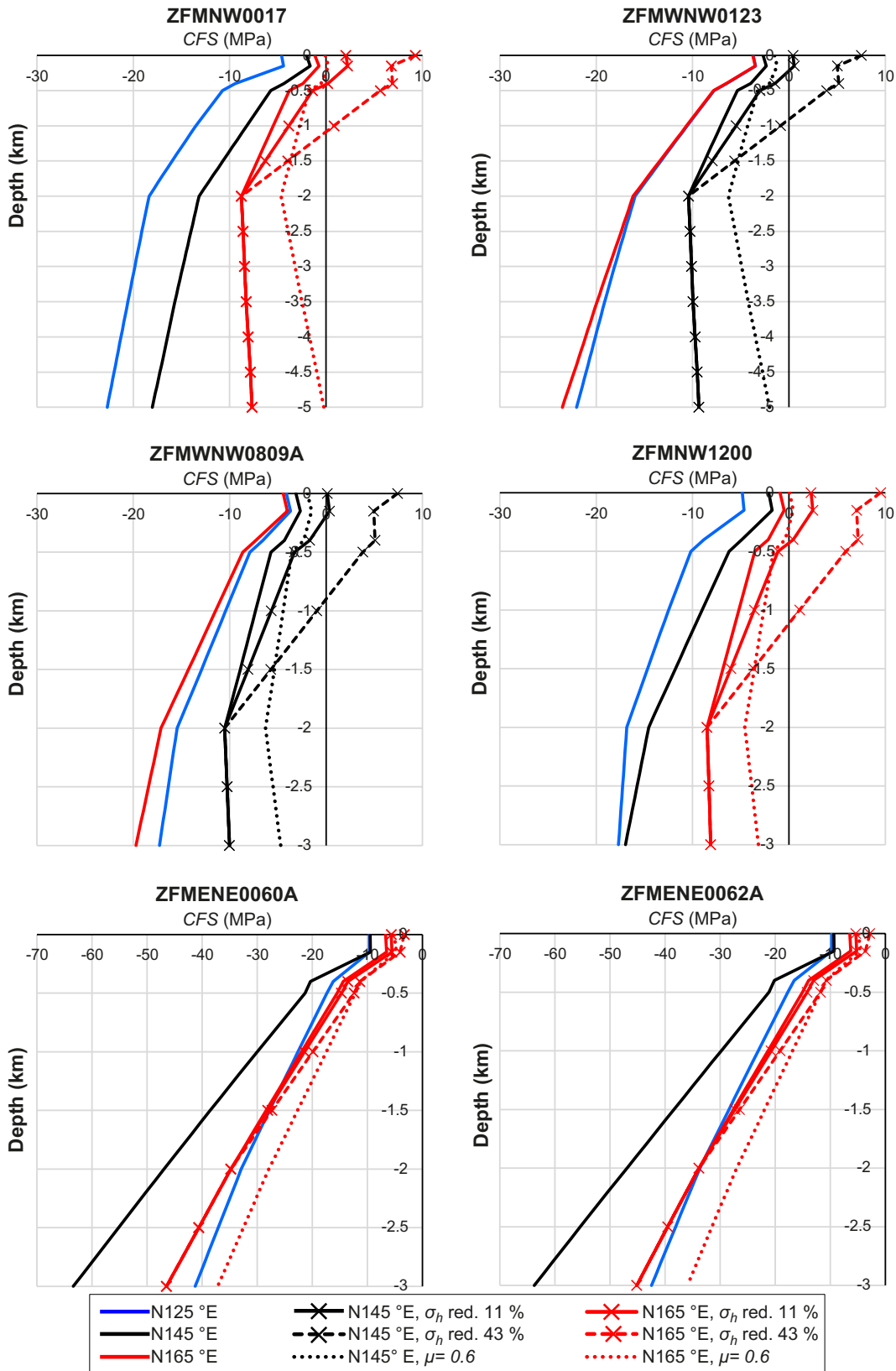
Figure 3-1. *CFS versus depth for the six steep deformation zones. Three background σ_H trends, three background σ_h magnitudes and one alternative friction coefficient are considered.*

The following can be observed in Figure 3-1 and Figure 3-2:

- Assuming Base case background stress conditions (i.e. no σ_h reduction) all zones are stable at all depths and for all values of strike and dip. Given their average orientations, all zones have stability margins exceeding 5 MPa (i.e. $CFS < -5$ MPa) over more than 85 % of their depth extensions. The smallest stability margin is obtained on ZFMNW0017, ZFMNW1200, ZFMENE0060A and ZFMENE0062A for the N165°E stress trend and on ZFMWNW0123 and ZFMWNW809A when assuming the N145°E trend (Figure 3-1, Figure 3-2, Appendix A).

- Reducing σ_h gives a stability reduction due to the increased σ_H-σ_h difference and the associated increase in stress anisotropy in the horizontal plane (Figure 3-1). With 11 % σ_h reduction, positive CFS values are obtained down to about 0.5 km depth on ZFMNW0017 and ZFMNW1200. On ZFMWNW0123 and ZFMWNW0809A minor instability is obtained close to the surface. With 43 % σ_h reduction, all zones except ZFMENE0060A and ZFMENE0062A obtain positive CFS values that reach almost 10 MPa at the surface on some zones.

- Setting $\mu = 0.6$ gives minor instability close to the surface on ZFMNW0017 and ZFMNW1200.

- The contour plots in Figure 3-2 show that, for the σ_H trend that yields the lowest stability on ZFMNW0017 (i.e. N165°E), the sensitivity to the variations in strike and dip is modest. At the depths with the lowest stability, CFS varies less than 1 MPa for strike and dip angles deviating from the nominal values (right column). The modest sensitivity to variations in zone orientation at the locations with the lowest stability is a general feature that can be observed for all zones (see Appendix A) (see also e.g. Figures 6-3 and 6-4 in Hökmark and Fälth (2014), which illustrate how CFS may vary with fault orientation).

- ZFMENE0060A and ZFMENE0062A have considerable stability margins. The CFS values are below 2 MPa at all depths and for all assumptions made here (Figure 3-1, Appendix A).

To summarize, it can be concluded that σ_h must be reduced significantly for the shear load to exceed the shear strength on any of the steep zones. The 43 % σ_h reduction case yields considerable instability at the ground surface while the instability in the 11 % σ_h reduction case is more modest. The question is then, given that these types of stress fields would develop and result in an initiation of slip movement, could the movement result in a runaway rupture that propagates over significant zone areas? Could such an event have any impact on the repository volume in terms of significant secondary fracture shear displacements? This is examined using dynamic earthquake rupture model simulations. The description of these models is given in Chapter 4 and the simulation results are presented in Chapter 5.
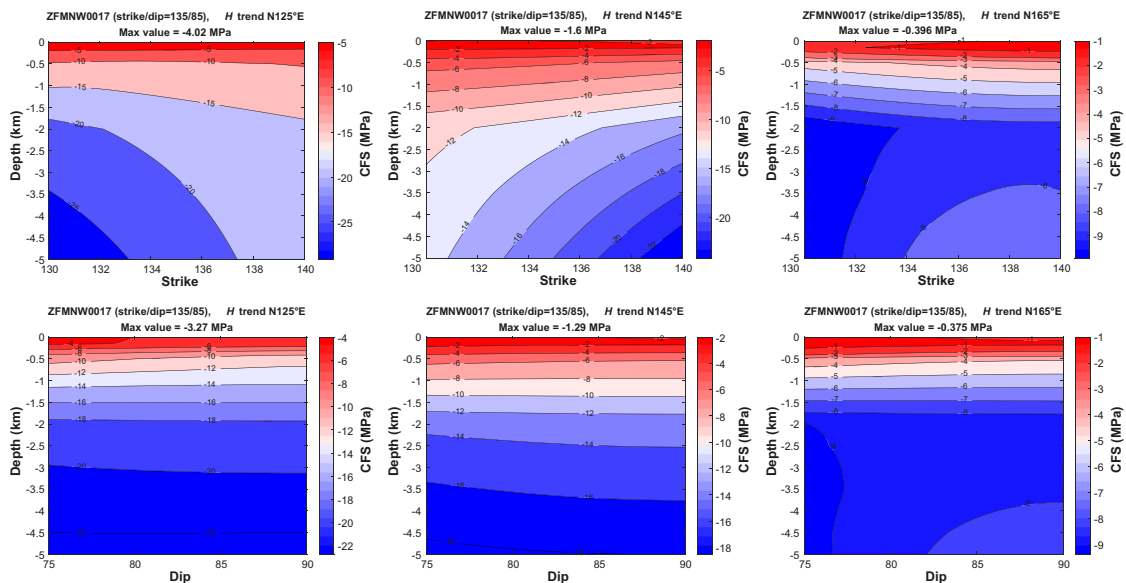

Figure 3-2. *CFS on ZFMNW0017 for different assumptions of the background σ_H trend, deformation zone dip and deformation zone strike. The corresponding results for all six zones are presented in Appendix A.*

3.2 Thermal stress conditions

In addition to the forebulge stability of the steep Forsmark zones which was assessed in the previous section, the impact of the heat generation in the repository on the stability of these zones is also examined. The results of this are presented in this section.

The impact of the heat generation is here assumed to be separated from the impact of the glacial load. Hence, it is assumed that the time scale for the thermal pulse is short enough that the temperature in the repository rock volume will have time to return to the undisturbed background level prior to next glaciation. Thermal calculations (Hökmark et al. 2010) show that the remaining excess temperature in the vicinity of the repository will be some 2–3 °C about 10 000 years after repository closure.

The stability of the steeply dipping zones will primarily depend on the horizontal stresses. Thermo-mechanical calculations show that the thermal load will give horizontal stress changes in the vicinity of the repository (see Figure 6-16 in Hökmark et al. 2010). The effect will be strongest at the repository horizon at around 500 m depth. At that depth, the heating will give rise to increased horizontal stresses. This will be accompanied by horizontal stress reductions above and below the repository depth.

A reduction of the stability will take place if the horizontal stresses σ_H and σ_h are reduced and/or the σ_H-σ_h difference becomes larger. Hence, a stability reduction would not take place at repository depth in response to the heating, but potentially above or below the repository horizon. As indicated in the previous section, the horizontal compression and the associated stability tends to be lowest close to the ground surface. Thus, the impact of the heating should be most critical there.

Using an analytic thermo-mechanical solution, Hökmark et al. (2010) calculated thermally induced stress additions around a generic square-shaped repository (Figure 3-3a). In their calculation, Hökmark et al. (2010) assumed the mean values of thermal, thermo-mechanical and mechanical properties reported for rock domain RFM029 and fracture domain FFM01 at Forsmark. The canister and tunnel spacings were set to 6 m and 40 m, respectively. The calculation results in Figure 3-3b indicate that the stress component perpendicular to the repository edge (σ_{xx}) will be reduced by about 1 MPa, at most, close to the ground surface some 100 m outside the repository footprint. Given the stress orientation at Forsmark and the orientations of the local steep zones, this would correspond approximately to the possible reduction of σ_h in Forsmark as well as the possible loss of compression on the ZFMNW0017, ZFMWNW0123, ZFMNW1200 and ZFMWNW0809A zones. The stress reduction in the direction parallel with the repository edge (Figure 3-3c) is larger, some 4 MPa at the same position. This reduction would take place approximately in the σ_H direction in Forsmark. Hence, the average horizontal stress would be reduced by (1 + 4)/2 = 2.5 MPa at the surface, which should promote instability. However, the σ_H-σ_h difference is reduced by some 3 MPa, and this should instead promote stability. At the repository horizon, the stress will be increased by at least 3 MPa in both directions some 100 m outside the repository footprint.

To examine the possible impact on zone stability of the heating, the following thermally induced stress alterations are schematically and pessimistically applied here. The stability reductions following these stress changes should represent an upper bound of the possible impact of the heating outside the repository areas where the steep deformation zones are located:

- At 500 m depth, the major and minor horizontal stresses σ_H and σ_h are both increased by 3 MPa.

- At all other depths, the major and minor horizontal stresses σ_H and σ_h are both reduced by 2.5 MPa.

Hence, at all depths except the repository depth, the same average stress reduction (2.5 MPa) is applied as that estimated from the Hökmark et al. (2010) results, but no reduction of the σ_H-σ_h difference is made. This gives a pessimistic estimate of the stability.

The zone stability is evaluated by applying both the Base case present-day stress field and the stress field with σ_h reduced 11 % at repository depth (see Section 2.2.1). In accordance with the assumptions made in Section 3.1, the zones are assumed to have a friction coefficient of 0.7 (Glamheden et al. 2007).
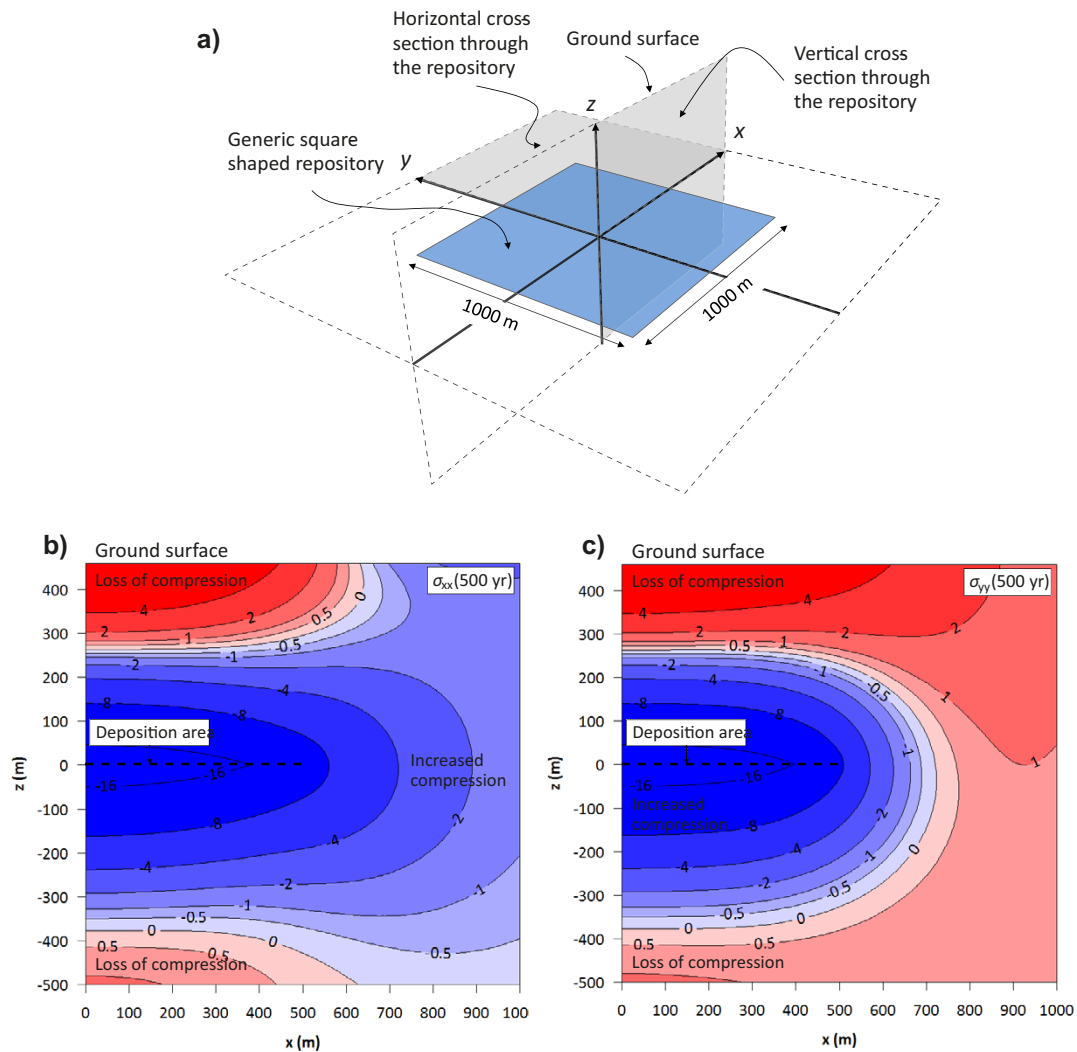
Figure 3-3. *a) Schematic view of the generic square-shaped repository layout and locations of plotting planes. Due to symmetry, the results are only shown in the grey-shaded area. b) Thermally induced horizontal stress additions perpendicular to the repository edge (σxx) in a vertical cross-section passing through the centre of the repository and c) thermally induced horizontal stress additions parallel with the repository edge (σyy). The contours are in MPa and the stresses are calculated after 500 years of heating (Figure 6-1 and Figure 6-2 in Hökmark et al. (2010).*

The effects at four depths of the thermally induced stress changes are illustrated by the Mohr-circle diagrams in Figure 3-4. In the diagrams, stresses in the σ_H-σ_h plane are considered. Hence, the results are formally valid for vertical deformation zones, but are judged to be relevant also for the zones considered here, which all have dips larger than 80°. The solid line circles represent the present-day stress states while the dashed line circles represent the stress states altered by the heating. The upper diagram shows results assuming the Base case stress field while the 11 % σ_h reduction stress field is applied when generating the results presented in the lower diagram.

The results in Figure 3-4 indicate that for both stress field assumptions there is a considerable stability margin (low *CFS* values) for all steep zone orientations at all depths under present-day stress conditions in Forsmark, even though the 11 % σ_h reduction stress field gives lower stability margins. The heating means that the stability margins are reduced (increased *CFS*) above and below the repository horizon while the stability is increased at repository depth. The stability is maintained at all depths. The lowest stability margin, about 0.5 MPa, is obtained close to the ground surface on optimally oriented zones when applying the 11 % σ_h reduction stress field. This would be approximately the case for ZFMWNW0123 and ZFMWNW0809A when assuming σ_H trend N145°E. If the stress trend instead is assumed to be N165°E, ZFMNW0017 and ZFMNW1200 would be close to optimally oriented.

It should be noted that the influence from the heating is local and focused to the volume near the repository. This contrasts with the impact of glacial loads, which affect the stress field in the crust on a much larger scale. Hence, the potential changes in stability indicated in Figure 3-4 will take place only on the parts of the deformation zones that are close to the repository areas. At longer distances, the effects of the heating will be significantly smaller.

Based on the results it can be concluded that the stability changes induced by the heating will have too low magnitudes for any of the steep zones to become unstable.
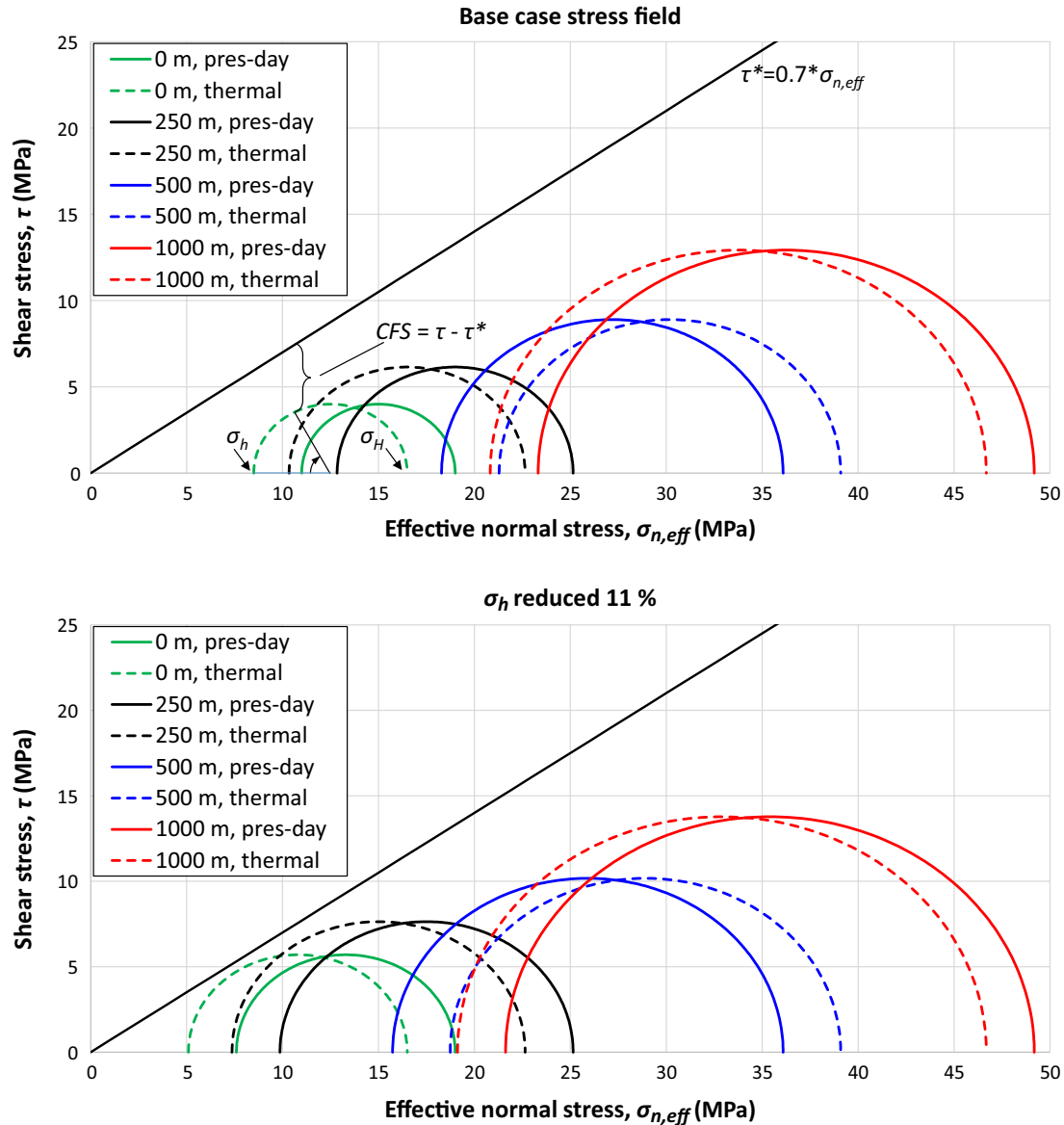

Figure 3-4. *Mohr circle diagrams showing stresses in the $\sigma_H - \sigma_h$ plane at different depths. The solid line circles show the present-day stress state while the dashed line circles show the stress state after addition of thermally induced stresses. Upper: Base case stress field. Lower: The 11 % σ_h reduction case (see Section 2.2.1). The optimal zone orientation giving the lowest stability (highest CFS) is indicated in the upper diagram for 0 m depth after heating.*

4 Numerical modelling approach

4.1 Numerical tool

The numerical simulations are performed using 3DEC, version 7 (Itasca 2020), a simulation tool that is based on the distinct element method (Cundall 1971). 3DEC simulates the response of discontinuous media subjected to static or dynamic loads using an explicit time-stepping solution scheme. Joint planes can be kept active to model an assemblage of blocks or glued together to simulate a continuum. Blocks may behave either as rigid or deformable material. Deformable blocks are discretised using finite-difference elements. Forces and relative motions along deformable block boundaries are controlled by so-called subcontacts. Because 3DEC is capable of handling large numbers of arbitrarily oriented discontinuities, it is well suited for the simulation of displacements on arbitrarily oriented faults and fractures.

4.2 Model geometry

The same model geometry is used for simulating forebulge, present-day and endglacial earthquake ruptures. The model comprises a box of continuum where the upper boundary represents the ground surface. The model's outer dimensions are shown in Figure 4-1. Centrally located in the model, joint planes representing the seven local Forsmark deformation zones are included (Figure 4-1 and Figure 4-2, cf Figure 1-3). The values of zone strike and dip adopted in the 3DEC model are the average values given by the Forsmark deformation zone model (Stephens and Simeonov 2015). The zone joint planes have trace lengths and orientations according to Table 2-1. The ZFMNW0017 and ZFMWNW0123 zones are assumed to reach 5 km depth while the shorter ZFMNW1200, ZFMWNW0809A, ZFMENE0060A and ZFMENE0062A are assumed to reach 3 km depth. ZFMA2 reaches its maximum depth of 1.4 km at the intersection with ZFMNW0017.

The target fractures are located within the planned repository areas in the footwall of ZFMA2 (see Figure 4-3, cf Figure 1-3). There are 76 circular fractures with radius 75 m and with their centres at 470 m depth. Each fracture consists of 16 circle sector-shaped joint planes (Figure 4-3, right). The fracture radius used here is half of the radius used in the models analysed by e.g. Fälth et al. (2016). A smaller fracture size is used here since it means that a larger number of fractures can be included in the same model volume. This gives a better coverage of fracture positions. Yet smaller fractures would allow for even more fractures in the model. However, this would mean that a finer discretisation should be needed to obtain the same resolution of the fracture surfaces.

For quasi-static conditions, fracture displacements scale with fracture size (Eshelby 1957). This appears to hold also for co-seismic fracture displacements (Fälth et al. 2010). Hence, the results generated here can be rescaled to be valid for other fracture sizes, given that the new fracture size does not mean that the loading of the fracture differs significantly from the loading of the original fracture.

The distances between each fracture centre and the nearest point on each deformation zone plane are given in Appendix B. Co-seismic secondary fracture displacements are calculated for several fracture orientations. To examine many combinations of fracture position and fracture orientation, the same fracture orientation is set at all 76 fracture positions in each model run.

The model is discretised using finite difference elements. In the inner volume containing the deformation zones (Figure 4-4a), the element edge length is 40–50 m. According to the criterion by Kuhlemeyer and Lysmer (1973) for proper wave transmission, the longest edge length should not be longer than 1/10–1/8 of the shortest wavelength in the spectrum (see also Fälth et al. 2015). Adopting the 1/10-criterion and the S-wave velocity in Table 4-2, edge lengths in the range 40–50 m correspond to proper transmission of waves with frequencies in the range 6–8 Hz. The model volume containing the target fractures (Figure 4-4b) is discretised with an edge length of about 12 m, corresponding to $N = 12$ edge lengths per fracture diameter (Figure 4-3, right). This allows for transmission of 27 Hz waves. The model contains approximately 9 million finite difference zones.

The repository is planned to be located inside fracture domains FFM01 and FFM06 at Forsmark (Olofsson et al. 2007). Hence, the fracture sets of these fracture domains as given by the Forsmark Discrete Fracture Network (DFN) model (Fox et al. 2007) are used as reference when setting target fracture orientations. According to the Forsmark DFN model, the repository volume contains mainly sub horizontal and steeply dipping fractures. To obtain a better case coverage, particularly for fracture orientations that potentially give low fracture stability, several generic fracture sets are added (Figure 4-5). There are some fracture sets that have similar orientations and hence can be expected to obtain similar mechanical response. To reduce the computational work, some of these "overlapping" sets were omitted here. The dip angle of the gently dipping generic fracture sets is chosen to give minimum fracture stability (maximum *CFS*), given an endglacial stress field (Figure 4-6). As indicated by the *CFS* contours in Figure 4-6, most of the target fracture sets have considerable stability margins under endglacial conditions. The fracture sets considered in the forebulge earthquake simulations are shown in Figure 4-7. Since the most severe secondary effects are expected in the endglacial phase, that is the focus here. This is the rationale for including more fracture sets in those simulations. A summary of all the target fracture sets considered here is given in Table 4-1.

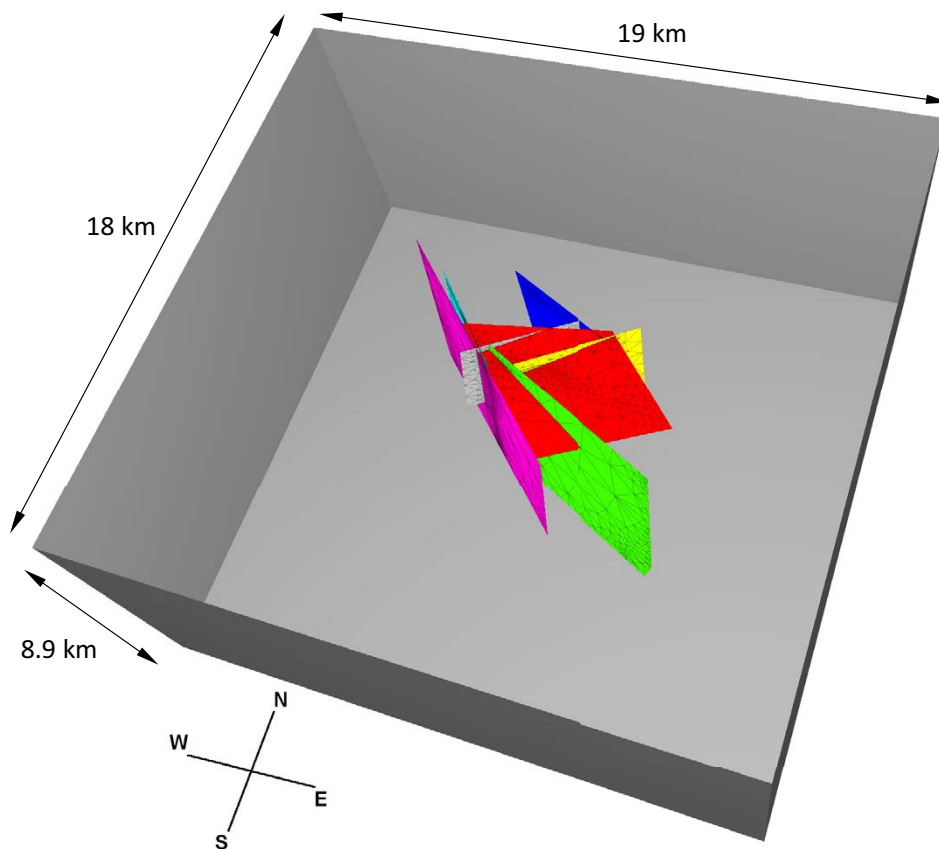All joint planes representing deformation zones and target fractures are planar.

Figure 4-1. *Model outlines. The model comprises a box with deformation zone planes and target fracture planes located in the centre.*
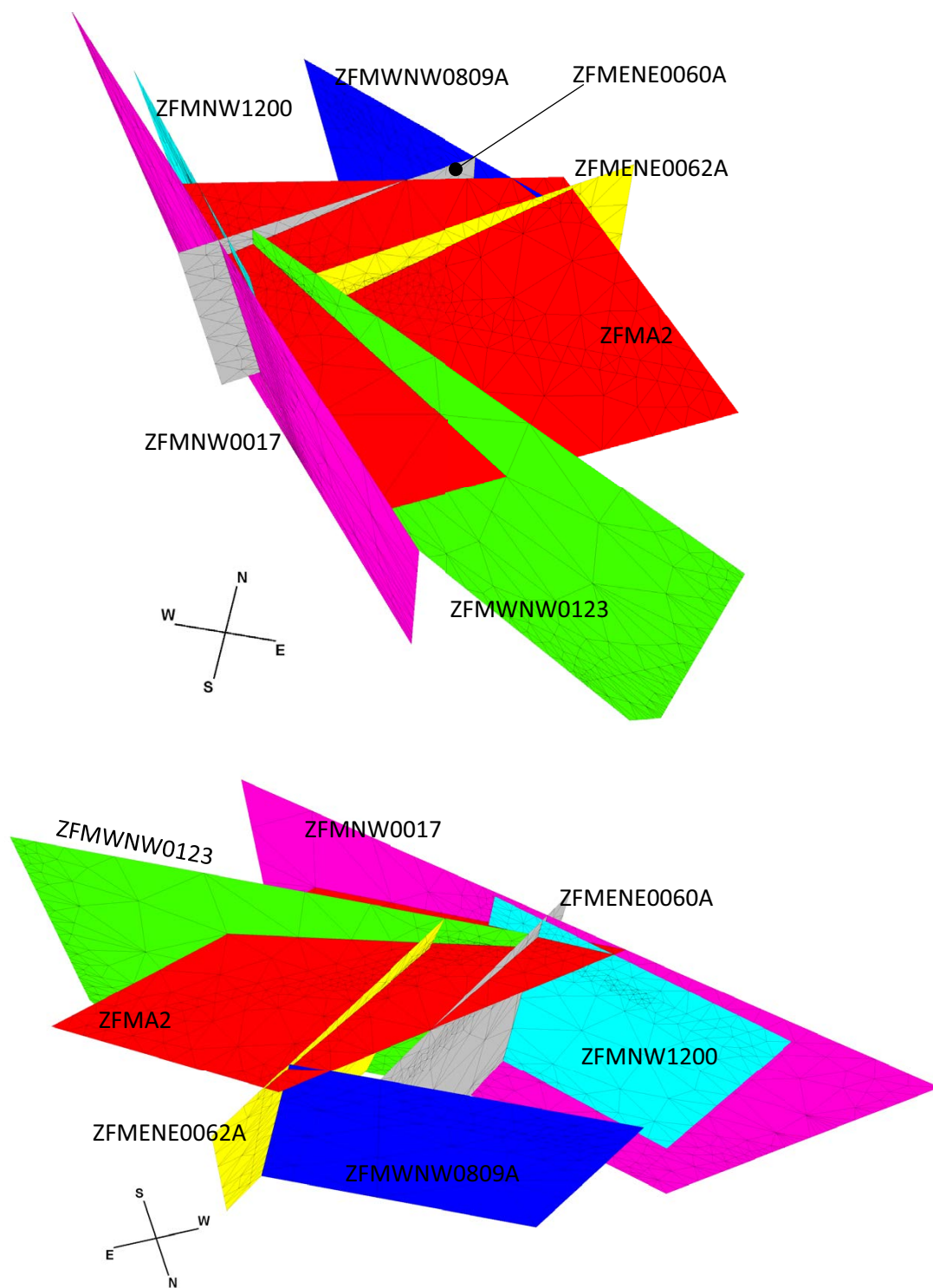
Figure 4-2. *The deformation zone system. Upper: View from southeast. Lower: View from northeast.*
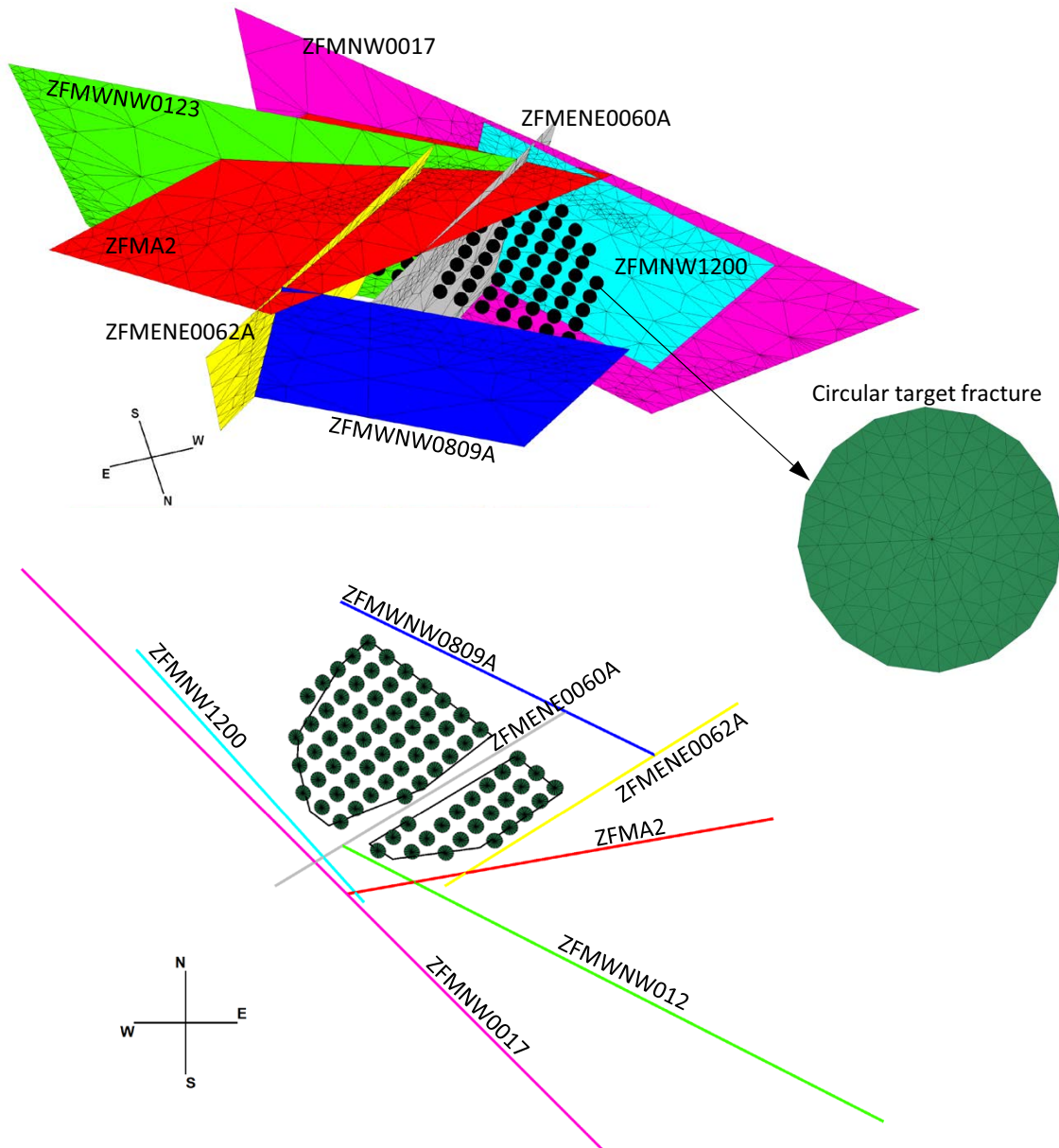
Figure 4-3. *The deformation zone system and target fractures. Upper: 3D-view from northeast. Lower: Horizontal section at the repository horizon (470 m depth) showing the locations of the seven zone planes. The circles show the locations of the target fractures while the black lines indicate the outlines of the planned repository areas (cf Figure 1-3). The right inset shows a close-up of a target fracture consisting of 16 circle sector-shaped joint planes.*
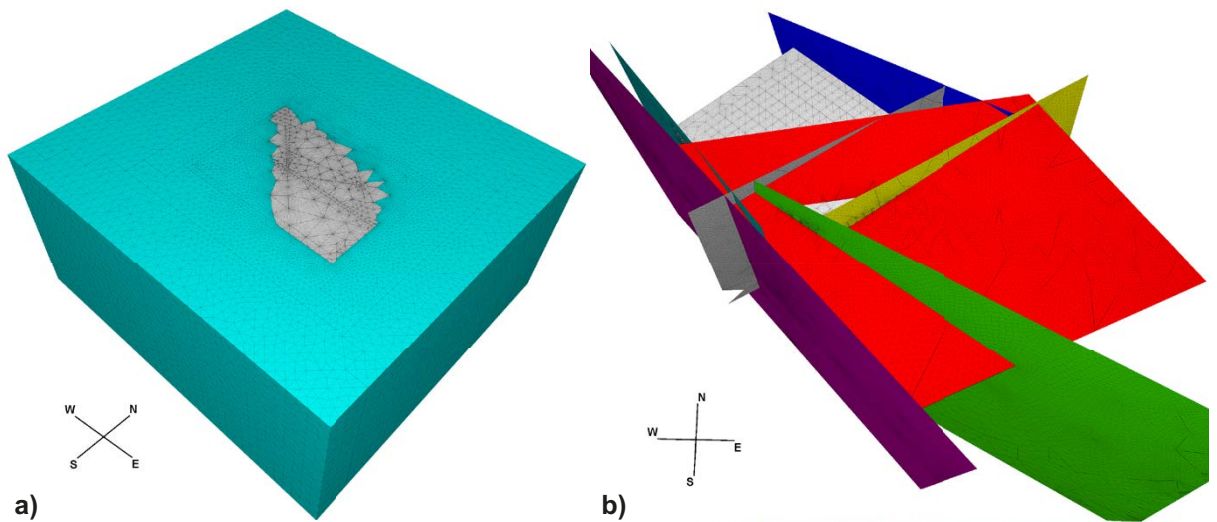
Figure 4-4. *a) Model block overview. The inner volume containing the deformation zones and target fractures is shown in grey while the outer volume is shown in turquoise. b) Close-up of the repository volume (grey) surrounded by the deformation zone planes*
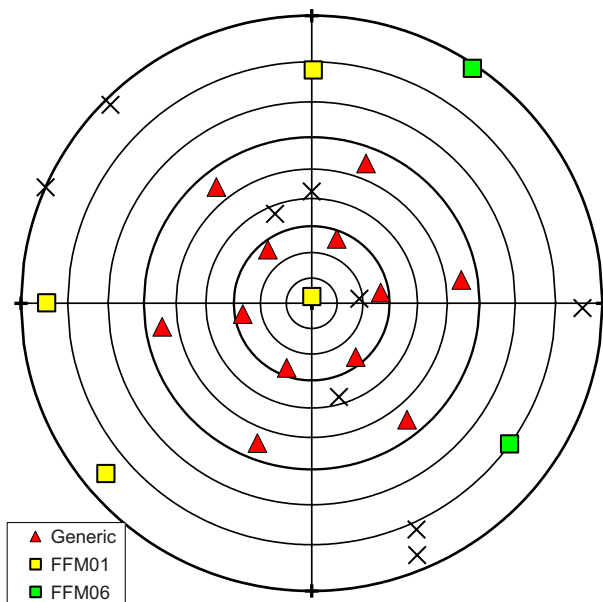

Figure 4-5. *Target fracture orientations. The square-shaped symbols indicate Forsmark-specific fractures sets while the triangles indicate generic sets. The black crosses represent Forsmark sets that are omitted here.*
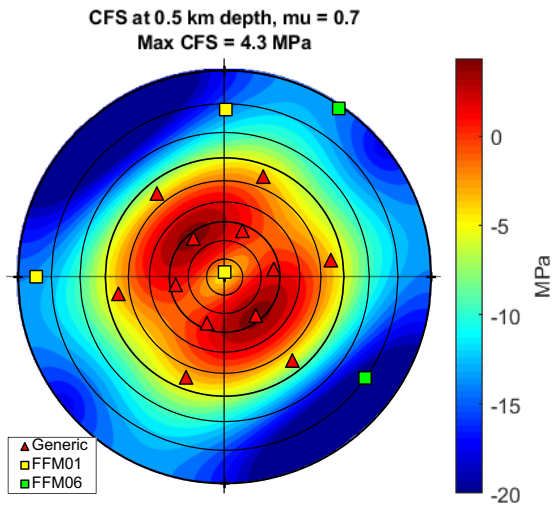
Figure 4-6. *Target fracture orientations considered in the present-day and endglacial simulation plotted along with contours of CFS (Equation (1-1)) on differently oriented planes. The CFS values were calculated assuming N145°E background σ_H trend, endglacial stress conditions at 500 m depth, 1 MPa excess pore pressure and μ = 0.7.*

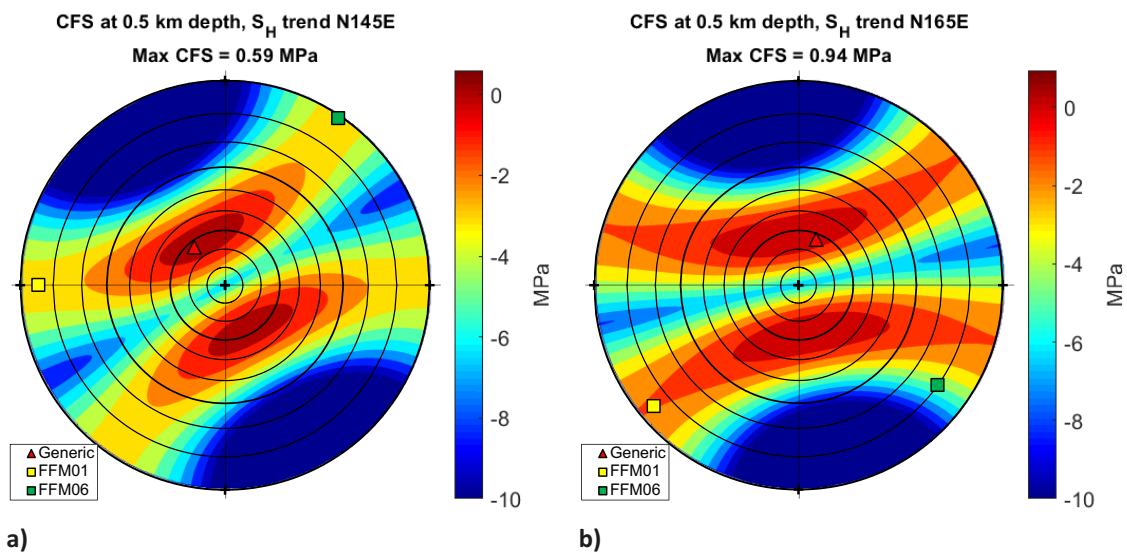a)   b)

Figure 4-7. *Target fracture orientations considered in the forebulge simulations plotted along with contours of CFS (Equation (1-1)) on differently oriented planes at 500 m depth under forebulge conditions. The CFS values are calculated for the 11 % σ_h reduction case and assuming μ = 0.7. a) The trend of background σ_H assumed to be N145°E. The target fracture sets considered in the cases with ruptures on ZFMWNW0123 and ZFMWNW0809A. b) The trend of background σ_H assumed to be N165°E. The target fracture sets considered in the cases with ruptures on ZFMNW0017 and ZFMNW1200.*

Table 4-1. Target fracture sets.

Fracture set	Orientation	
	Dip δ (°)	Dip direction θ (°)
Forsmark sets		
FFM01 EW†	78	180
FFM01 NS	85	90
FFM01 SH	3	181
FFM01 NW	85	50
FFM06 NE	80	306
FFM06 NW†	89	214
Generic sets		
GEN 27/21	27	21
GEN 27/81	27	81
GEN 27/141	27	141
GEN 27/201	27	201
GEN 27/261	27	261
GEN 27/321	27	321
GEN 55/21	55	21
GEN 55/81†	55	81
GEN 55/141	55	141
GEN 55/201	55	201
GEN 55/261†	55	261
GEN 55/321	55	321

† To avoid badly shaped blocks and ill-conditioned finite difference zones, the following adjustments were made:

– In set FFM01 EW, the dip of fracture #71 (cf Appendix B) was set to 77°.

– In set FFM06 NW, the dip/dip direction was set to 85/210°

– In set GEN 55/81, the dip of fracture #70 (cf Appendix B) was set to 56.5°.

– In set GEN 55/261, the dip of fracture #71 (cf Appendix B) was set to 54°.

4.3 Material properties

The rock mass is assumed to be homogeneous, isotropic and continuous. In the majority of the models linear elasticity is assumed with the elastic parameter values (Table 4-2) in agreement with Forsmark site data (Glamheden et al. 2007). In some of the models where short fault-target fracture distances are considered, a damage zone surrounding the fault slip plane is represented by a Mohr-Coulomb material with a reduced deformation modulus. The reduction is in agreement with Forsmark data (Glamheden et al. 2007). The strength parameter values are also representative for values reported for Forsmark. The higher value of friction coefficient (0.78) is the same as that assumed for the deformation zone slip planes during dynamic rupture (see Table 4-2 and the discussion below).

All zones as well as the target fractures are assumed to respond to loads according to an idealized elasto-plastic material model with constant stiffnesses in both the normal and shear directions, with failure according to a Coulomb criterion (Itasca 2020) (Figure 4-8). For the target fractures, the coefficient of friction (Table 4-2) is set according to Forsmark data (Glamheden et al. 2007). The same value is assigned to the deformation zones during the quasi-static calculation step (see Section 4.4).

Table 4-2. Material property parameter values.

Component	Parameter	Value	Comment
Rock mass	Young's modulus, E (GPa)	70	
	Poisson's ratio, v (-)	0.24	
	Density, ρ (kg/m³)	2700	
	P wave velocity, V_p (km/s)	5.5	
	S wave velocity, V_s (km/s)	3.2	
Damage zone[†]	Young's modulus, E (GPa)	50	
	Poisson's ratio, v (-)	0.24	
	Density, ρ (kg/m³)	2700	
	Friction coefficient	0.7 or 0.78	
	Cohesion (MPa)	0.5	
	Tensile strength (MPa)	0	
Target fractures	Friction coefficient, $\mu = \tan(35°)$	0.7	Also alternative values 0.6; 0.8 (Chapter 6)
	Cohesion, c (MPa)	0	
	Normal stiffness, k_n (GPa/m)	10	
	Shear stiffness, k_s (GPa/m)	10	
Deformation zone slip planes	Static friction coefficient, μ_s	0.7	During quasi-static step
		0.78	During dynamic step
	Dynamic friction coefficient, μ_d	0.46[††]	
	Reference slip velocity, v* (m/s)	0.24[††]	
	Cohesion c (MPa)	0.5	
	Normal stiffness, k_n (GPa/m)	10	
	Shear stiffness, k_s (GPa/m)	10	

[†] Damage zone is included only in models considering short fault-fracture distances (Section 6.1).

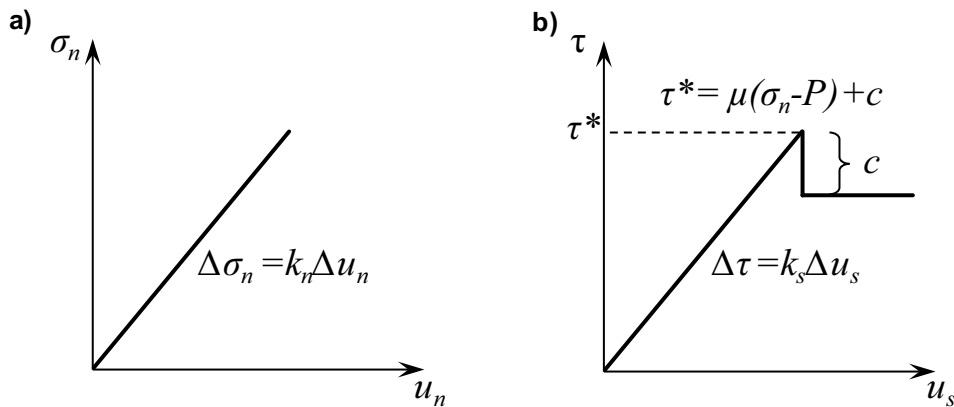[††] Values based on a simulation of a present-day earthquake rupture on ZFMA2 (see Section 6.4.1)

Figure 4-8. *Idealized elasto-plastic joint material model. a) The normal stress σ_n is a function of the constant normal stiffness k_n and the normal displacement u_n. (b) The shear stress τ is a function of the constant shear stiffness k_s and the shear displacement u_s. The shear strength τ^* is governed by a Coulomb criterion where μ, P and c are friction coefficient, pore pressure and cohesion, respectively (Itasca 2020).*

For the earthquake rupture simulation, it is assumed that the fault friction coefficient μ is a function of the slip velocity v, i.e., $\mu = \mu(v)$. The friction coefficient is modelled according to the velocity-weakening law proposed by Beeler et al. (2008) (Figure 4-9),

$$\mu(v) = \mu_d + \frac{\mu_s - \mu_d}{1 + \frac{v}{v^*}\left[1 - e^{-(v/v^*)^2}\right]}. \tag{4-1}$$

Here, μ_s, μ_d and v^* are the static friction coefficient, the dynamic friction coefficient and the reference velocity, respectively. The static friction coefficient μ_s determines the peak strength of the fault, i.e., at which stress level slip is initiated. Hence, it has importance for how easily slip is initiated and for the rupture propagation. A higher value of μ_s tends to slow down propagation but may also mean that stronger stress peaks are generated at the rupture front. This could give stronger simulated secondary stress effects (Fälth and Hökmark 2015). Parts of the fault plane may be at the stability limit at the time of rupture initiation. Thus, to obtain a well-defined and stable earthquake rupture process, μ_s is set to 0.78, which is higher than the friction coefficient set during the preceding quasi-static calculation step (see Section 4.4, Table 4-2).

The dynamic friction coefficient μ_d determines the fault strength at high slip velocities. Hence, it determines the amount of strength degradation and the corresponding stress drop $\Delta\tau$ that is generated by the synthetic earthquake. Stress drop is a fundamental parameter that controls fault slip (Eshelby 1957) as well as dynamic earthquake source parameters, such as fault slip velocity and rupture velocity. All these source parameters scale with stress drop (Scholz 2002). Thus, a higher stress drop tends to give a stronger earthquake source with higher rupture velocity, higher fault slip velocity and larger fault slip. The value of μ_d is determined by comparison of results from a simulation of a present-day earthquake on ZFMA2 with earthquake catalogue data, see Section 6.4.1.

The third parameter v^* is a reference slip velocity that determines how quickly the fault friction coefficient degrades from μ_s to μ_d as the slip velocity increases. This parameter also has importance for the amount of stress drop $\Delta\tau$ that is generated by the simulated earthquake. Here, v^* is set to a value that appears to give a stable rupture initiation process as well as continued stable propagation. For convenience, this parameter is kept constant when the value of μ_d is calibrated (see Section 6.4.1). The values of μ_s, μ_d, and v^* are presented in Table 4-2.

The velocity-weakening law in Equation (4-1) is intended to model the effect of degradation of surface contacts as well as the effect of frictional heating as the fault slips. In contrast to constitutive laws that depend on slip, e.g. the slip-weakening law proposed by Ida (1972), the law in Equation (4-1) models fault re-strengthening as the slip velocity is reduced again after a slip episode. Since no slip dependence is modelled, the strength is fully recovered as the velocity goes back to zero. Hence, this model response may be considered less realistic compared to the response of rate-and-state laws (Ruina 1983), which include dependence on both slip and slip rate. However, the velocity-weakening law in Equation (4-1) is easier to implement and is considered relevant for the purpose of this study. According to the test simulation results reported in Appendix C, a simulation where the velocity-weakening model is applied tends to generate stronger secondary effects than a corresponding simulation where the slip-weakening model is applied.

To initiate the rupture, the approach described by Bizzarri (2010) is adopted. Starting at the pre-defined hypocentre a radially expanding rupture is enforced to propagate at a constant rupture speed v_{force} within a circular nucleation region Σ_{nucl}. In general, the size of the nucleation region can be arbitrarily chosen. However, it must be large enough that the strain energy at the enforced rupture front has time to grow to a level at which the spontaneous rupture can be maintained. Here, the nucleation region radius is set to 750 m. The forced rupture speed v_{force} can also, in general, be arbitrarily chosen. Based on testing, it is here set to 50 % of the shear wave velocity V_s of the surrounding medium (cf Table 4-2). This value was found to provide a reasonably smooth transition from forced to spontaneous rupture propagation.

The friction coefficient of the fault is determined according to

$$\mu = \begin{cases} \mu_{nucl} = \min\{\mu^{VW}, \mu^{TW}\} & \forall (x,y,z) \in \Sigma_{nucl}, \\ \mu^{VW} & \forall (x,y,z) \notin \Sigma_{nucl}, \end{cases} \tag{4-2}$$

where μ^{VW} (velocity-weakening) is determined by Equation (4-1) and μ^{TW} (time-weakening) is given by

$$\mu^{TW} = \begin{cases} \mu_s - (\mu_s - \mu_d)\dfrac{(t - t_{force})}{t_0} & t - t_{force} < t_0. \\ \mu_d & t - t_{force} \geq t_0 \end{cases} \tag{4-3}$$

Here, t_{force} is the time of rupture initiation and t_0 is the time over which the strength is ramped down from μ_s to μ_d, here set at 0.15 s. At some time during the initiation process, the ruptured area is large enough that the rupture starts to propagate spontaneously, governed by the velocity-weakening law (Equation (4-1)). Note that since the velocity-weakening law (Equation (4-1)) is assigned to all deformation zone planes, the rupture may, depending on the local stress conditions, jump from one plane to another.

Since slip velocities are used as input to the velocity-weakening function (Equation (4-1)), some notes on the slip velocity calculation are given here. The calculated velocity depends on the time interval over which it is averaged (the reciprocal of the sampling frequency). A shorter interval tends to give higher velocities and a noisier solution. Slip velocity is available as an output parameter from 3DEC and is calculated during every timestep, which here is on the order of $5 \times 10^{-5} - 10^{-4}$ s. Here, in addition to being an input to the velocity-weakening law, the fault slip velocity is used to assess the relevance of the simulation. To obtain slip velocities that are evaluated over a time interval that is judged relevant for the problem and to obtain a numerically stable solution, the sampling interval used in the velocity calculation is longer than the model timestep. During simulation, the slip velocity is calculated as a moving temporal average of the 3DEC output velocities using a time interval of 0.05 s. The peak value of the temporal average at each fault location is stored. For illustrative purposes, the peak slip velocity values presented in the contour plots in this report are determined from the stored peak values as a moving spatial average over a circular area with 80 m radius.
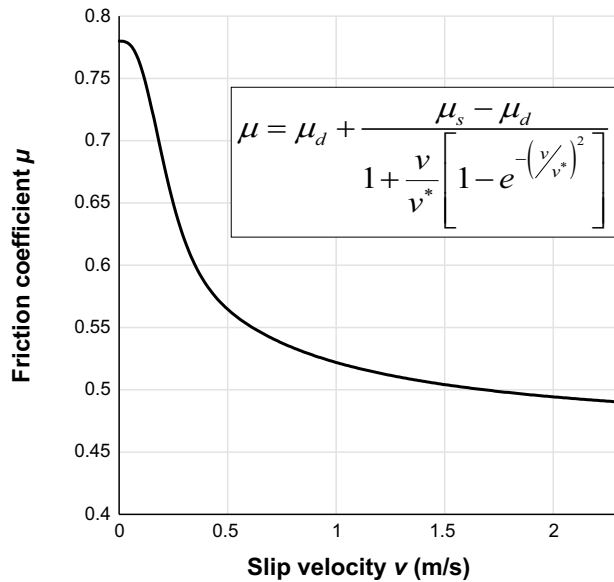

Figure 4-9. *Velocity-weakening law (Beeler et al. 2008) (Equation (4-1)) with $\mu_s = 0.78$, $\mu_d = 0.46$ and $v^* = 0.24$ m/s.*

4.4 Calculation sequence

The calculation sequence comprises two steps.

The first step, the quasi-static calculation step, means that material properties are assigned according to Table 4-2, the initial stresses are applied, and the model is run quasi-statically until static equilibrium is achieved. Recall that three initial stress fields are considered (see Section 2.2): Present-day, Forebulge and Endglacial. During this calculation step the unstable parts of the deformation zones and the target fractures will slip aseismically until all stress excess is relaxed. When simulating forebulge and endglacial conditions, this quasi-static slip can be regarded as a gradual adjustment of the bedrock in response to the change in stress conditions induced by the glacial load (cf Figure 2-3 and Figure 2-4). The final state of the quasi-static calculation step is the point of departure for the following dynamic step.

The quasi-static modelling step is followed by the dynamic step when the earthquake rupture is initiated as described in Section 4.3. The locations of the initiation points are described in Chapter 5 and 6. The parts of the deformation zones that slipped quasi-statically during the preceding quasi-static calculation step are at the stability limit at the time of rupture initiation. This means that these parts are very sensitive to small disturbances and will very easily start to slip as soon as the code is switched to dynamic simulation mode. To suppress this and to obtain a more distinct rupture propagation, the static friction coefficient is set to $\mu_s = 0.78$ during the dynamic calculation step (Table 4-2).

Note that all displacements generated during the quasi-static calculation step are reset prior to dynamic rupture initiation. Hence, the displacements presented for the dynamic calculation step are co-seismic only.

5 Forebulge earthquake scenarios

In this chapter, the results from the forebulge earthquake scenarios are presented. In all cases it is schematically assumed that the rupture is initiated at 500 m depth, i.e., the centre of the circular initiation region (cf Section 4.3) is located at this depth. The initiation points in the different cases are indicated in Figure 5-1. These locations were chosen to be at some distance from the repository. Results from several studies (Andrews 2005, Fälth 2018, Johri et al. 2014, Xu et al. 2012) show that the secondary effects induced around the rupture front tend to be stronger at longer rupture propagation distances.
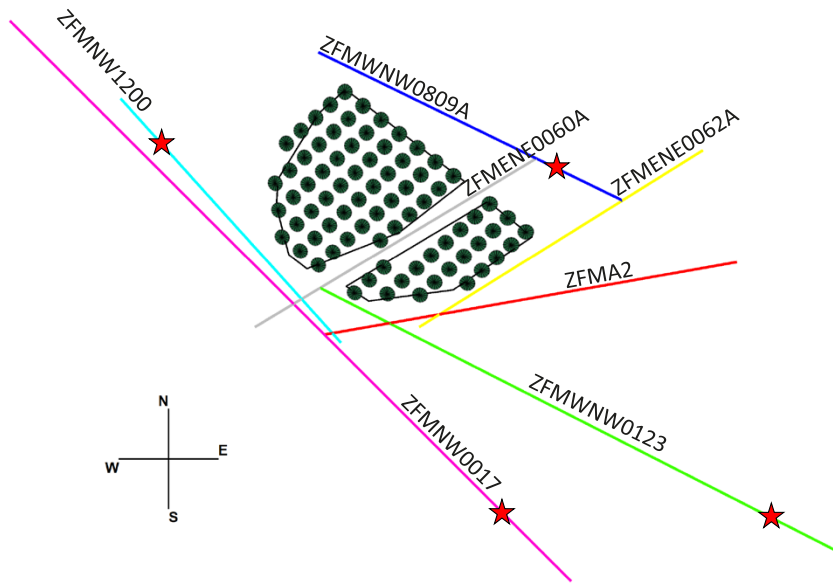

Figure 5-1. *Horizontal section at the repository horizon (470 m depth) showing the locations of the seven zone planes. The circles show the locations of the target fractures while the black lines indicate the outlines of the planned repository areas (cf Figure 1-3). The rupture initiation points are indicated by red stars. See Appendix B for an overview of the target fracture locations and their distances from each zone plane.*

5.1 Simulated cases

Initiation of earthquake ruptures are simulated on the four deformation zones for which the *CFS* calculations in Section 3.1 predict unstable conditions. For each zone, the two cases of background σ_h reduction are considered, and for each of these cases three target fracture orientations are considered (Figure 4-7). This gives 24 model simulations which are summarised in Table 5-1. In all cases, hydrostatic pore pressure is assumed. Note that no actual porewater transport calculations are performed in any of the simulations here.

Table 5-1. Model summary.

Model name	Deformation zone	Background stress		Target fracture dip/dip dir.
		σ_h red. (%)	σ_H trend (°)	
ZFMNW0017_FFM01NW_Shred11	ZFMNW0017	11	165	85/50
ZFMNW0017_FFM01NW_Shred43	ZFMNW0017	43	165	85/50
ZFMNW0017_FFM06NE_Shred11	ZFMNW0017	11	165	80/306
ZFMNW0017_FFM06NE_Shred43	ZFMNW0017	43	165	80/306
ZFMNW0017_Gen27-201_Shred11	ZFMNW0017	11	165	27/201
ZFMNW0017_Gen27-201_Shred43	ZFMNW0017	43	165	27/201
ZFMNW1200_FFM01NW_Shred11	ZFMNW1200	11	165	85/50
ZFMNW1200_FFM01NW_Shred43	ZFMNW1200	43	165	85/50
ZFMNW1200_FFM06NE_Shred11	ZFMNW1200	11	165	80/306
ZFMNW1200_FFM06NE_Shred43	ZFMNW1200	43	165	80/306
ZFMNW1200_Gen27-201_Shred11	ZFMNW1200	11	165	27/201
ZFMNW1200_Gen27-201_Shred43	ZFMNW1200	43	165	27/201
ZFMWNW0123_FFM01NS_Shred11	ZFMWNW0123	11	145	85/90
ZFMWNW0123_FFM01NS_Shred43	ZFMWNW0123	43	145	85/90
ZFMWNW0123_FFM06NW_Shred11	ZFMWNW0123	11	145	85/210
ZFMWNW0123_FFM06NW_Shred43	ZFMWNW0123	43	145	85/210
ZFMWNW0123_Gen27-141_Shred11	ZFMWNW0123	11	145	27/141
ZFMWNW0123_Gen27-141_Shred43	ZFMWNW0123	43	145	27/141
ZFMWNW0809A_FFM01NS_Shred11	ZFMWNW0809A	11	145	85/90
ZFMWNW0809A _FFM01NS_Shred43	ZFMWNW0809A	43	145	85/90
ZFMWNW0809A _FFM06NW_Shred11	ZFMWNW0809A	11	145	85/210
ZFMWNW0809A _FFM06NW_Shred43	ZFMWNW0809A	43	145	85/210
ZFMWNW0809A _Gen27-141_Shred11	ZFMWNW0809A	11	145	27/141
ZFMWNW0809A _Gen27-141_Shred43	ZFMWNW0809A	43	145	27/141

5.2 Results

The result presentation is divided into two parts. The first part concerns the model response during the quasi-static modelling step while results from the dynamic modelling step are presented in the second part.

5.2.1 Quasi-static calculation step

As described in Section 4.4, the quasi-static modelling step means that the model is allowed to adjust to the applied stress field. Here, this means that the upper parts of the zones, which initially are in a state of failure (cf Figure 3-1), will slip. The extent and amount of slip depends on the stress field. As indicated by the *CFS* plots in Figure 3-1 the case with larger σ_h reduction will give more extensive slip. This is what can be seen in the simulation results shown in Figure 5-2 and Figure 5-3. It can also be noted how the σ_H trend impacts on the stability of the different zones. For instance, ZFMNW0123 and ZFMWNW0809A generate larger displacements in the case with σ_H trend N145°E (cf Figure 5-2 and Figure 5-3), as predicted by the *CFS* results in Figure 3-1.

Note also that the gently dipping ZFMA2 generates slip. Even though it is stabilised by the forebulge stress additions, it is in a state of failure close to the ground surface, given the stress field applied here (cf Figure 1-5).

The stress field also affects the target fracture stability. Figure 5-4 shows shear displacements on the target fractures in the ZFMNW0017_FFM01NW_Shred11 (upper) and ZFMNW0017_FFM01NW_ Shred43 (lower) models. The plots illustrate the considerable impact that the σ_h reduction has on steep fractures. In the case with 11 % σ_h reduction, only elastic and insignificant displacements are generated while the fractures become unstable and slip in the case with 43 % σ_h reduction. Given that 11 % σ_h reduction is assumed, none of the steep target fracture sets tested in the forebulge models here become unstable and slip during the quasi-static calculation step. The two gently dipping sets are relatively insensitive to the amount of σ_h reduction. For both cases of σ_h reduction, they generate 3–4 mm shear displacement, at most, during this calculation step.
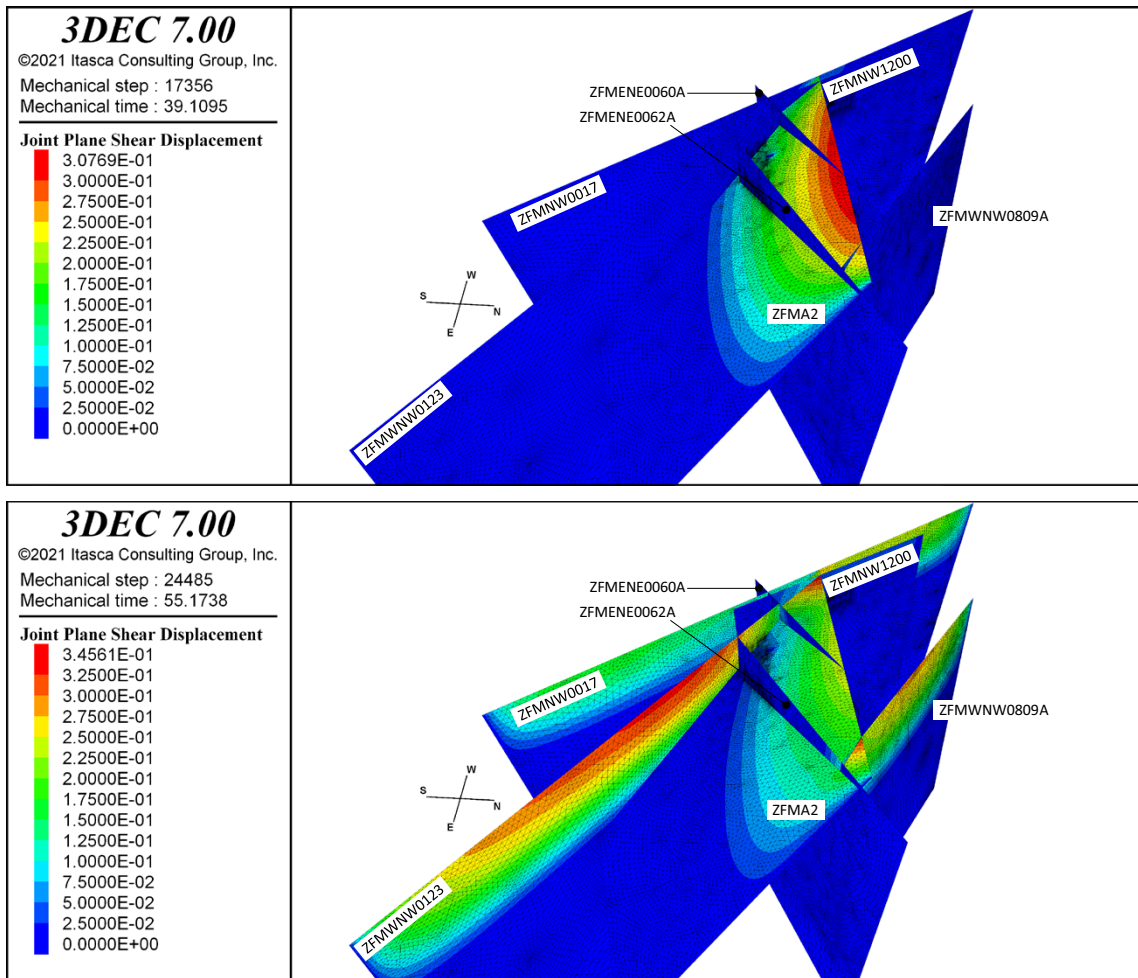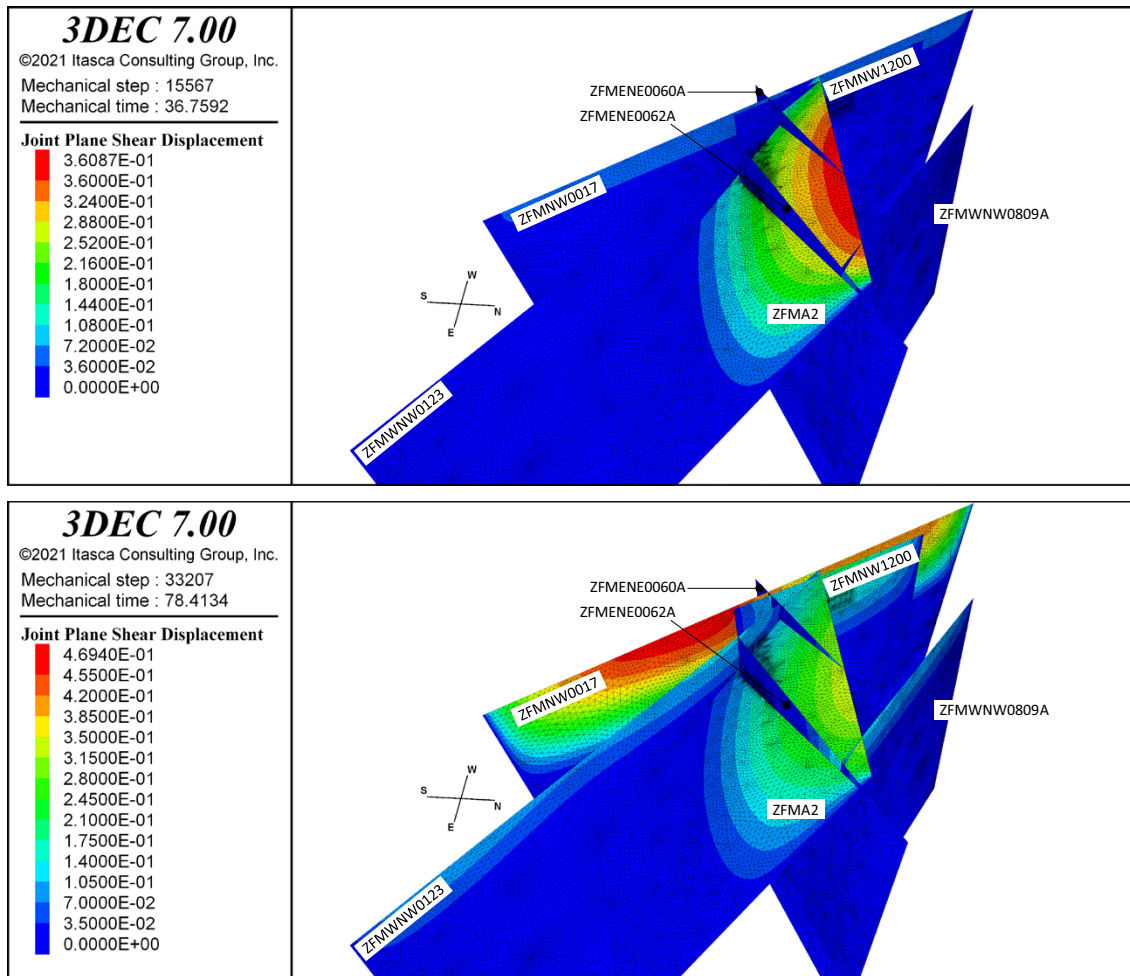

Figure 5-2. *Fault zone shear displacements (m) generated during the quasi-static modelling step in the case with background σ_H trend N145°E. Upper: Background σ_h reduction 11 %. Lower: Background σ_h reduction 43 %.*

Figure 5-3. *Fault zone shear displacements (m) generated during the quasi-static modelling step in the case with background σ_H trend N165°E. Upper: Background σ_h reduction 11 %. Lower: Background σ_h reduction 43 %.*
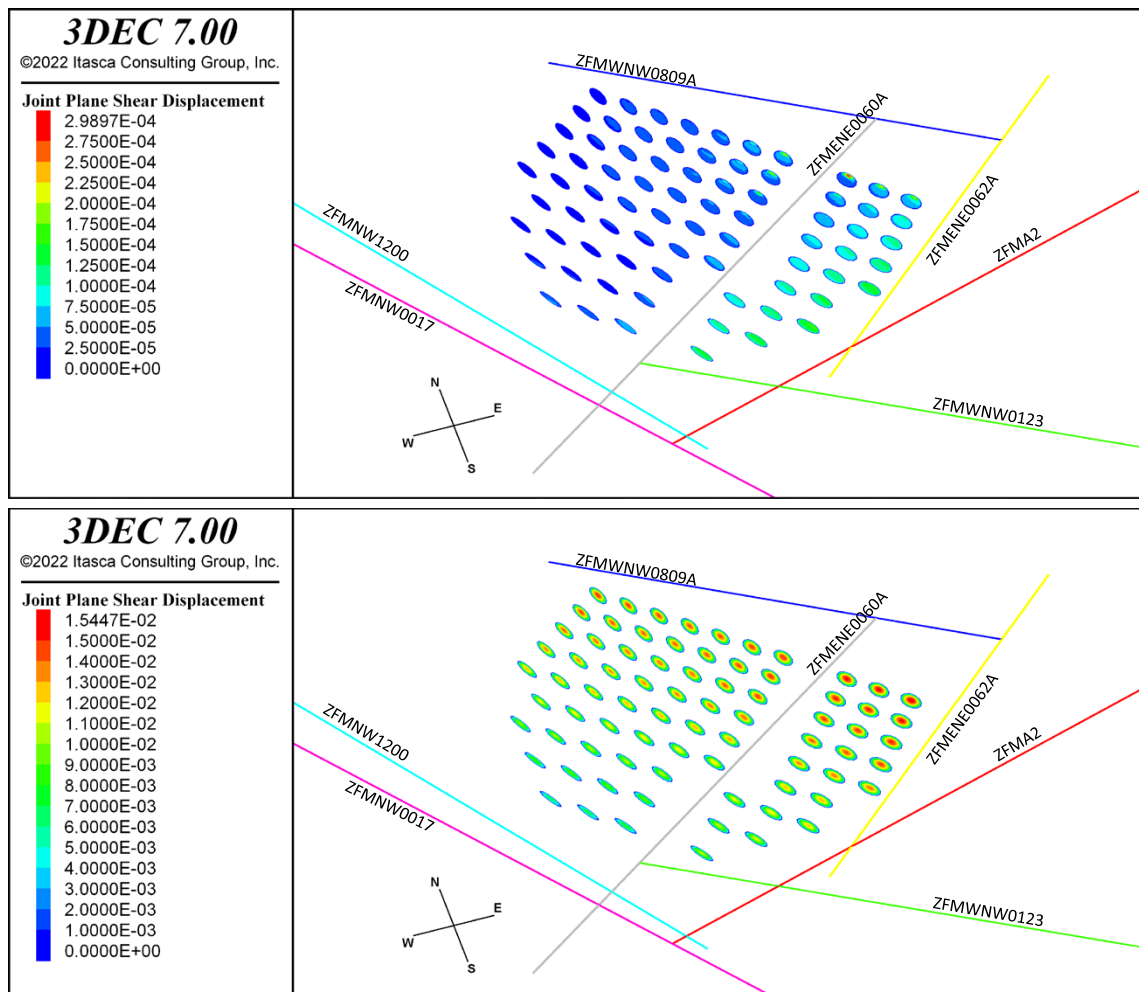
Figure 5-4. Target fracture shear displacements (m) generated during the quasi-static modelling step. Upper: ZFMNW0017_FFM01NW_Shred11 model (background σ_h reduction 11 %). Lower: ZFMNW0017_ FFM01NW_Shred43 model (background σ_h reduction 43 %).

5.2.2 Dynamic calculation step

Recall that all displacements generated during the previous quasi-static calculation step are reset prior to rupture initiation. Hence, the displacements presented here are co-seismic only.

The low stability close to the ground surface is reflected in the model's response to the simulated rupture initiation. An example of the model response is found in Figure 5-5 to Figure 5-7. The figures show normalised rupture velocity (V_r/V_s), peak slip velocity and fault slip in the case with 43 % σ_h reduction and rupture initiation on ZFMNW0017. In this case ZFMNW0017 ruptures along its entire length. Note, however, that the rupture is restricted to the upper part of the zone where unstable conditions were predicted by the analytic *CFS* calculations in Chapter 3. The rupture propagation velocity is in the range $0.8\,V_s - 0.9\,V_s$, which is typically observed in real earthquakes (Scholz 2002). The highest slip velocities are in the order of 1 m/s, which also is in accord with observations (Olsen et al. 1997, Wald and Heaton 1994, Wald et al. 1996). Slip and slip velocities tend to be higher at longer distances from the hypocentre. This can be attributed to the progressive increase in stress effects around the rupture front. These effects tend to be stronger as the rupture front progresses and the ruptured area expands. This has been observed also in other earthquake rupture simulations (Bizzarri 2011, Fälth and Hökmark 2015). It can also be noted that the low stability leads to rupture initiation also on ZFMNW1200, which has an orientation very similar to that of ZFMNW0017 (cf Table 2-1).

The following earthquake source parameters are presented in Table 5-2 (cf Equation (1-2)): stress drop $\Delta\tau$, seismic moment M_0, moment magnitude M_w, average fault displacement u_{avg} and rupture area RA. Note that the earthquake source parameters are independent of what target fracture set is considered. Hence, source parameters from only eight models (out of 24) are presented in Table 5-2 (cf Table 5-1). The earthquake shown in Figure 5-5 to Figure 5-7 has a moment magnitude of M_w 4.9 and a rupture area of 17 km^2 (Table 5-2). It is recalled here that the case with 43 % σ_h reduction is a hypothetical bounding case where a strike-slip background stress field is modelled at all depths. This means that a considerable instability is estimated on the steep zones close to the ground surface.

A significantly different model response is obtained when the 11 % σ_h reduction is applied. This is indicated in Figure 5-8. The fault slip becomes much more limited and is restricted to an area that is a little larger than the circular rupture nucleation region (cf Section 4.3). The stability of the ZFMNW0017 zone is too high to admit further propagation of the rupture. The seismic moment generated in this simulation is about 1/17 of the moment generated in the 43 % σ_h reduction case and the rupture area is reduced by a factor of 7 (Table 5-2). This strong impact of the assumed stress field is observed for all the forebulge earthquakes simulated here, as seen in Table 5-2 as well as in the plots in Appendix D where rupture velocities, slip velocities and fault slip are shown for all rupture scenarios.
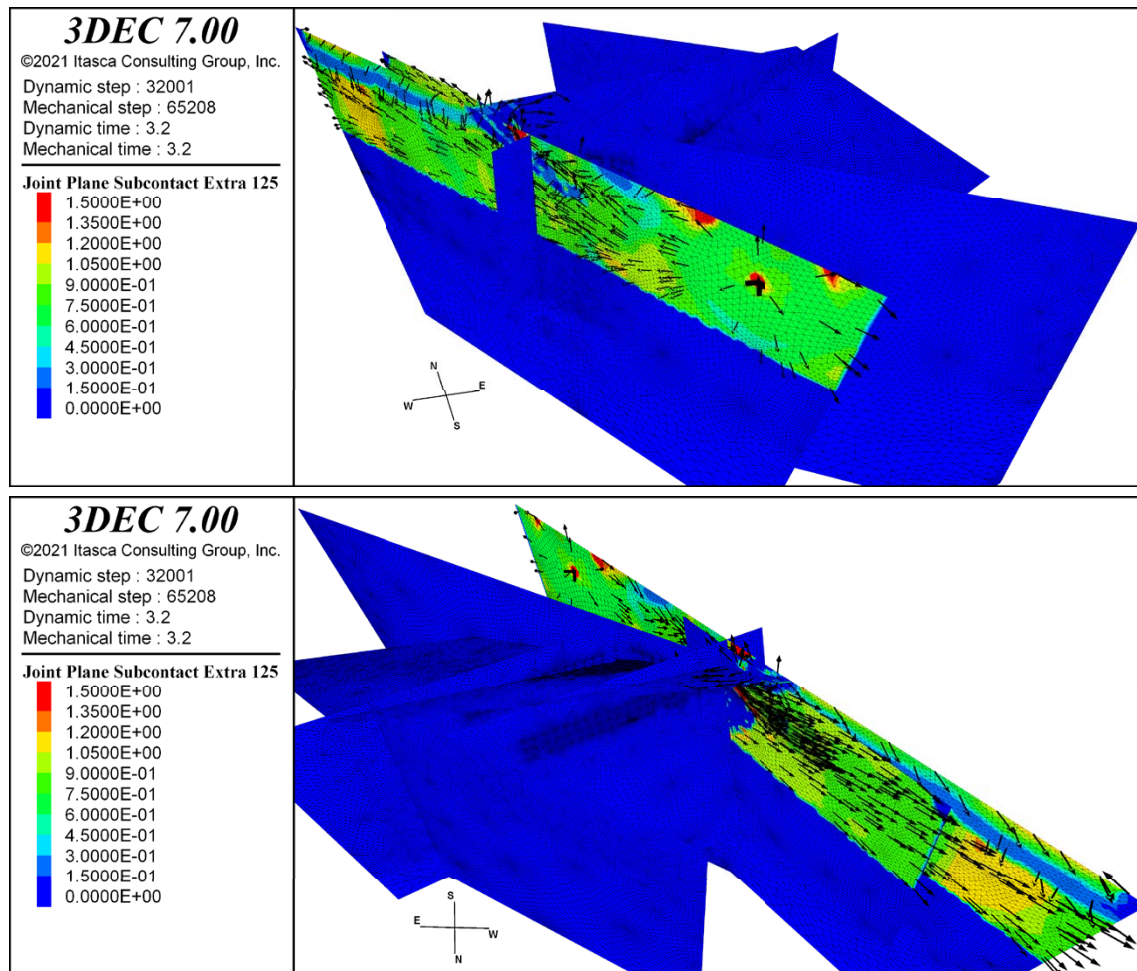

Figure 5-5. *Two views showing V_r/V_s along with rupture direction vectors in the case with 43 % σ_h reduction and rupture initiation on ZFMNW0017. Note that even ZFMNW1200 ruptures in this case. The black cross indicates the hypocentre. Corresponding plots for all rupture scenarios are presented in Appendix D.*

For the 11 % σ_h reduction stress model, which can be regarded the most relevant one out of the two stress models applied in the rupture simulations, the largest simulated earthquake has a moment magnitude of M_w 4.0 and an average slip of 0.02 m (Table 5-2).

Table 5-2. Source parameters.

| Model name	$\Delta\tau_{avg}$ (MPa)	M_0 (Nm)	M_w	u_{avg} (m)	RA (km²)
ZFMNW0017_FFM01NW_Shred11	0.63	1.4×10^{15}	4.0	0.020	2.5
ZFMNW0017_FFM01NW_Shred43	1.1	2.4×10^{16}	4.9	0.051	17
ZFMNW1200_FFM01NW_Shred11	0.67	1.5×10^{15}	4.0	0.019	2.8
ZFMNW1200_FFM01NW_Shred43	0.93	1.4×10^{16}	4.7	0.045	11
ZFMWNW0123_FFM01NS_Shred11	0.28	6.4×10^{14}	3.8	0.012	1.9
ZFMWNW0123_FFM01NS_Shred43	0.54	1.4×10^{16}	4.7	0.029	16
ZFMWNW0809A_FFM01NS_Shred11	0.44	4.6×10^{14}	3.7	0.010	1.6
ZFMWNW0809A_FFM01NS_Shred43	0.74	4.7×10^{15}	4.4	0.024	7.1
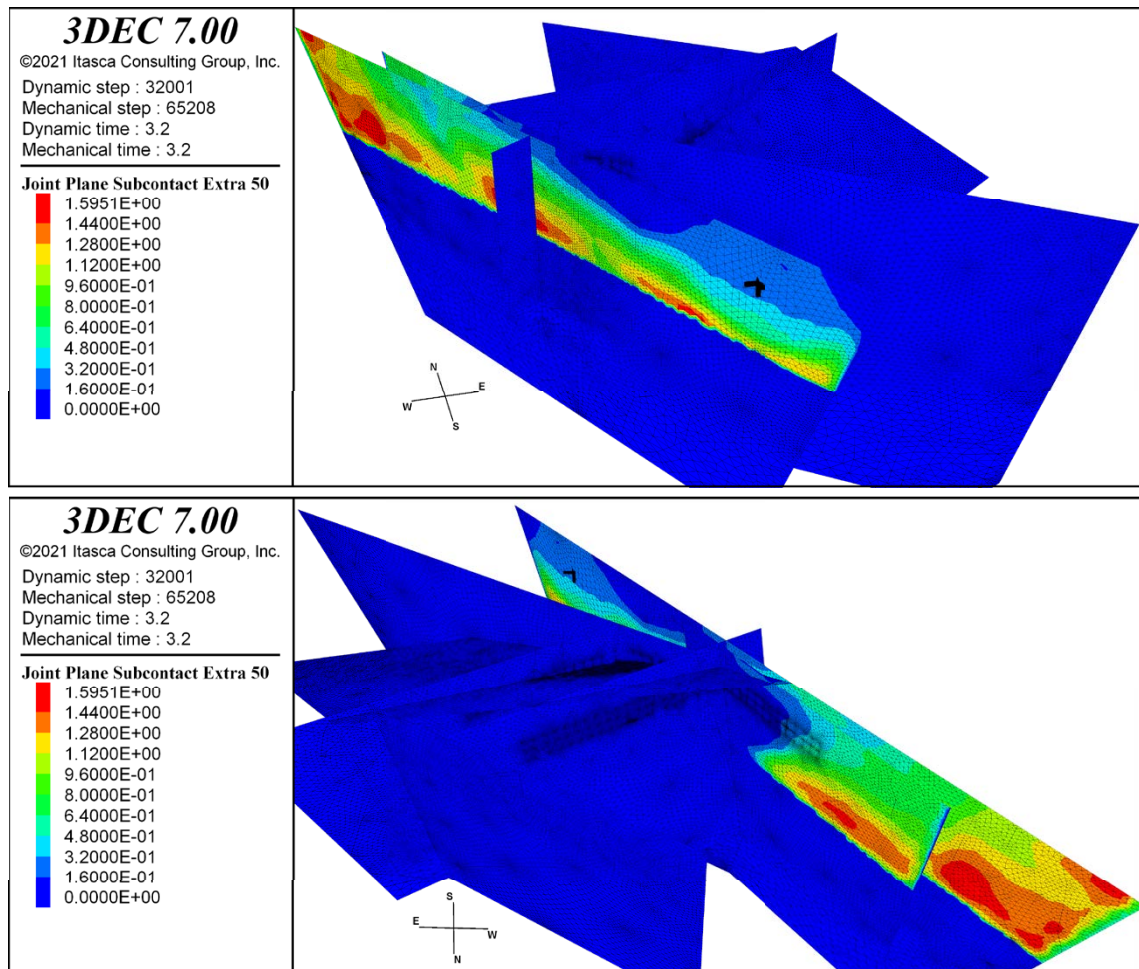
Figure 5-6. *Two views showing peak slip velocity (m/s) in the case with 43 % σ_h reduction and rupture initiation on ZFMNW0017. Note that even ZFMNW1200 ruptures in this case. The black cross indicates the hypocentre. For illustrative purposes, the plotted values are determined from the stored peaks values using a moving spatial averaging over a circular area with 80 m radius. Corresponding plots for all rupture scenarios are presented in Appendix D.*
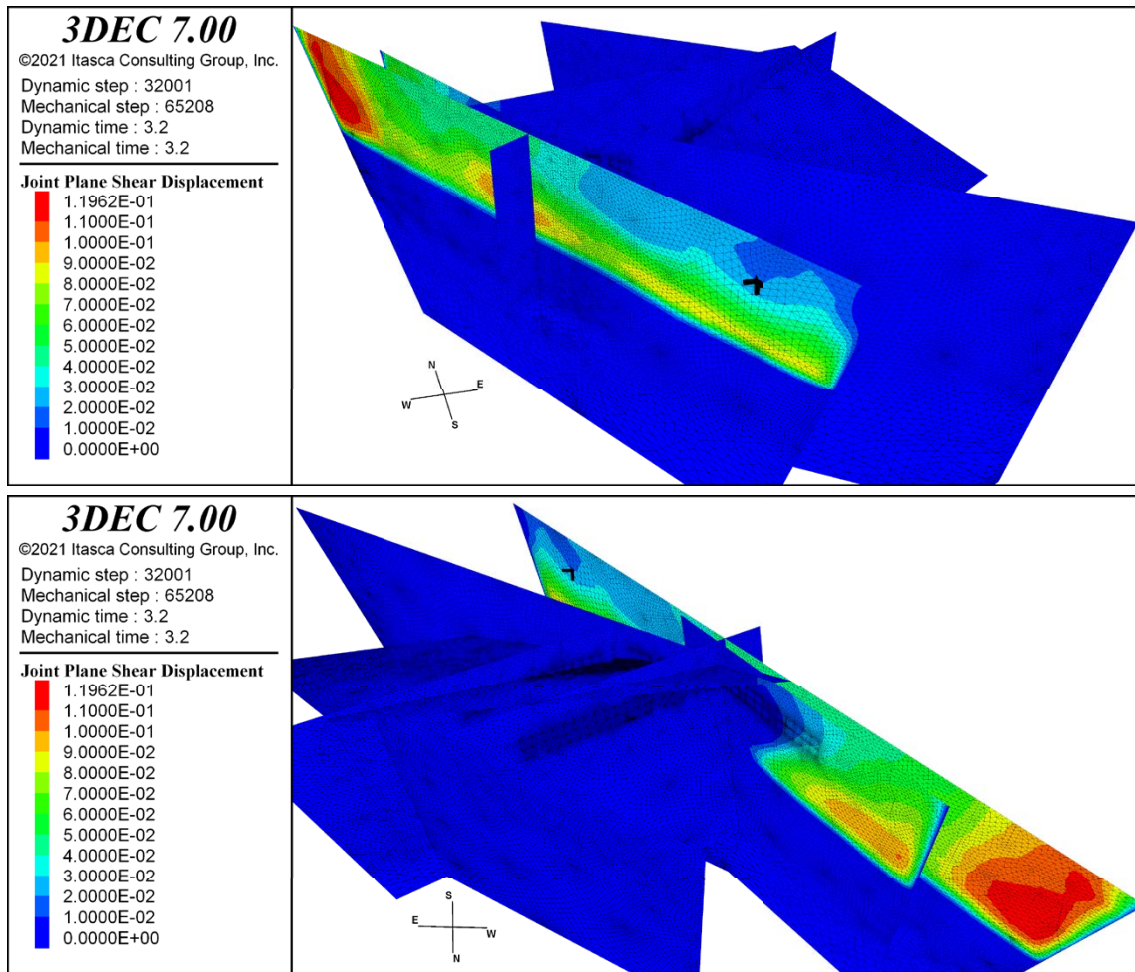
Figure 5-7. Two views showing fault slip (m) in the case with 43 % σ_h reduction and rupture initiation on ZFMNW0017. Note that even ZFMNW1200 ruptures in this case. The black cross indicates the hypocentre. Corresponding plots for all rupture scenarios are presented in Appendix D.
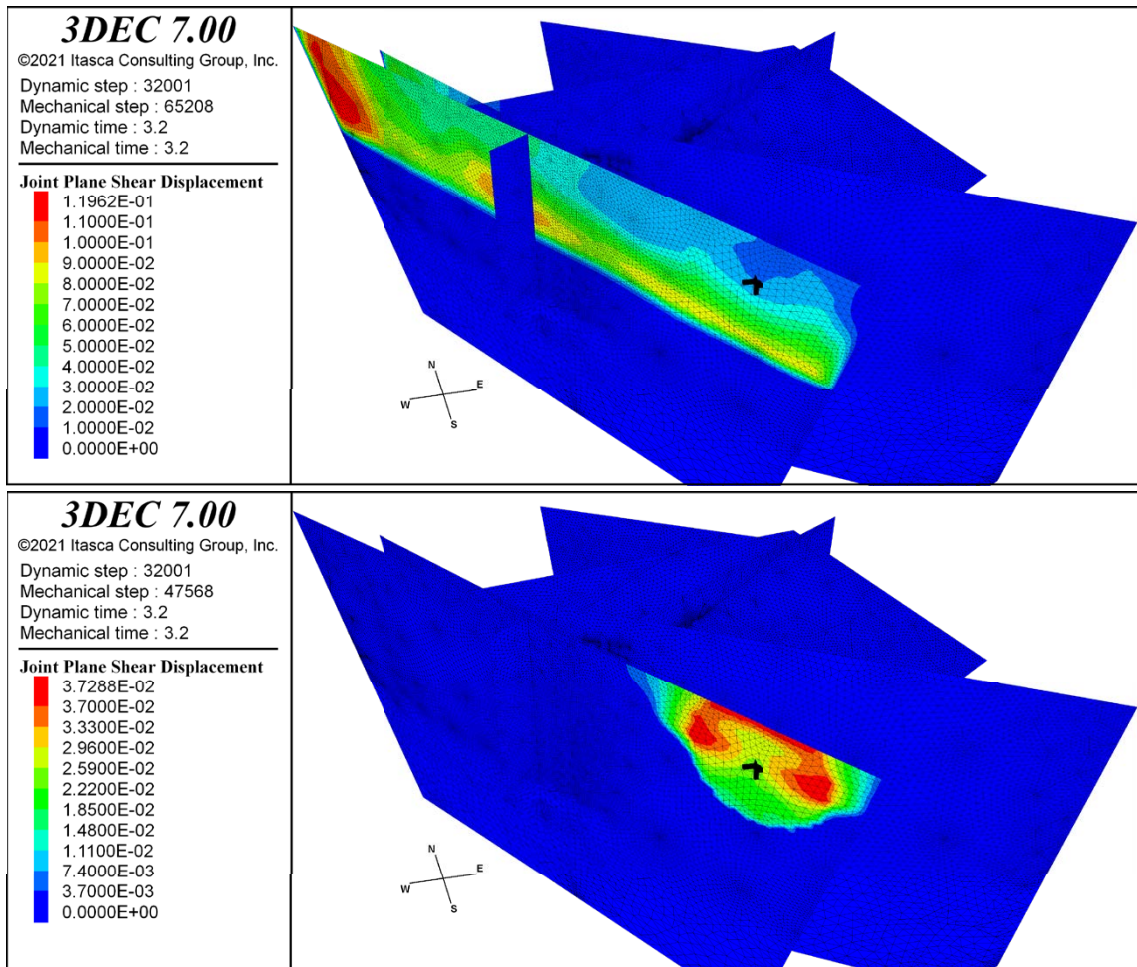
Figure 5-8. *Fault slip (m) in the case with rupture initiation on ZFMNW0017. Upper: 43 % σ_h reduction case. Lower: 11 % σ_h reduction case. The black cross indicates the hypocentre.*

The temporal evolution of the target fracture shear displacements is monitored at the target fracture centres and the peak displacement values are stored. In Figure 5-9, the peak displacements in all model simulations are plotted versus distance from target fracture centre to the nearest location on the deformation zone plane where the earthquake rupture is initiated. The following can be observed:

- In the case with 11 % background σ_h reduction, the simulated earthquakes become small, as shown above, and only insignificant target fracture displacements are generated. No displacement exceeds 0.1 mm.

- In the case with 43 % background σ_h reduction, the secondary displacements become larger. However, the displacements are in general small. No displacement exceeds 4 mm. There is a general trend that the displacements become larger at shorter distances, even though there are exceptions. Smaller displacements at shorter distances can be attributed to stress relaxation and fracture stabilisation associated with the fault displacement that takes place during the preceding quasi-static calculation step (see Section 5.2.1).
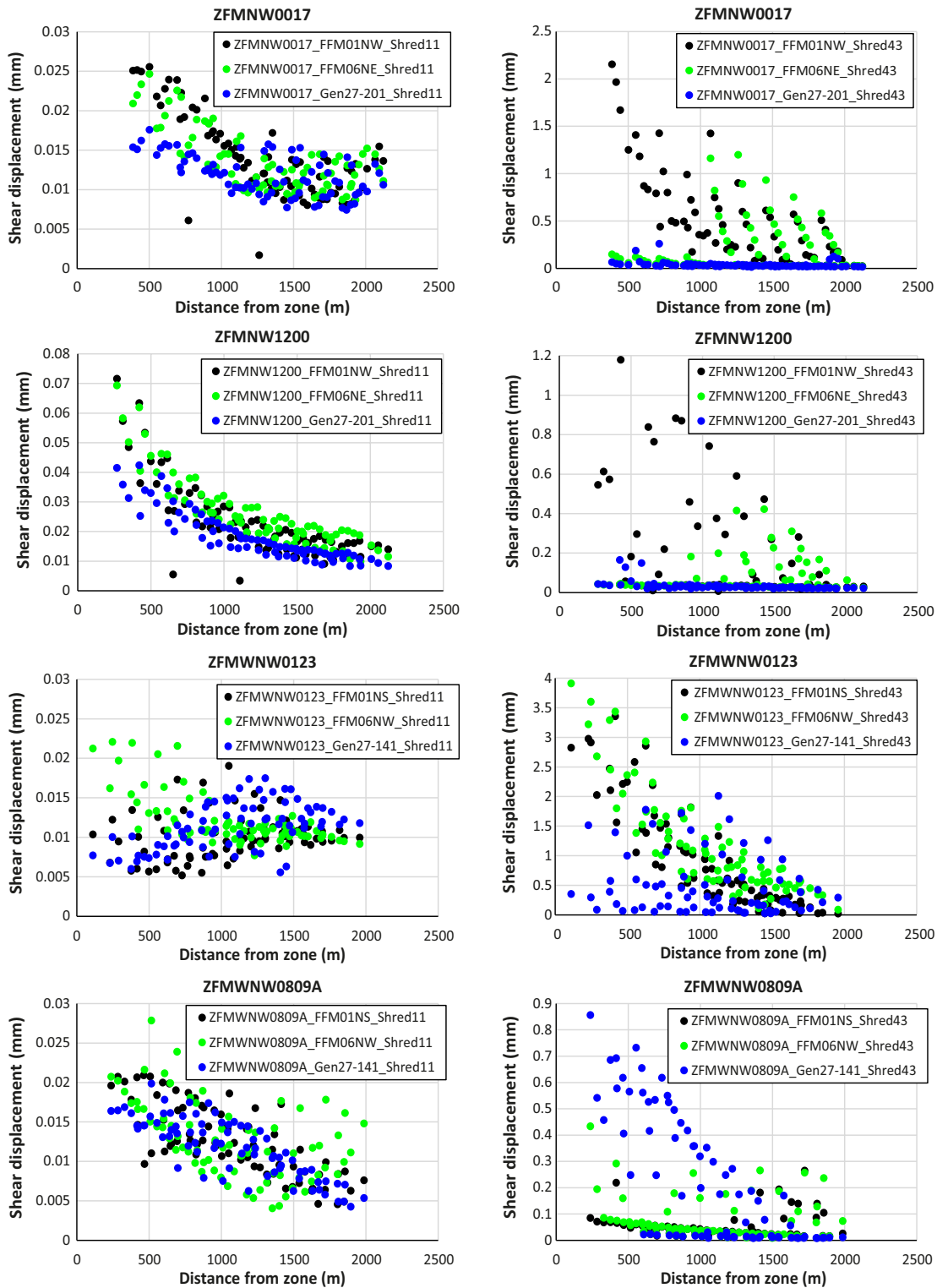
Figure 5-9. *Co-seismic target fracture peak shear displacements versus distance from the deformation zone plane where the earthquake rupture is initiated. The distances are measured from the centres of the target fractures to the closest point on the zone plane (see Appendix B for an overview of the target fracture locations). Left column: Case with 11 % background σ_h reduction. Right: Case with 43 % background σ_h reduction.*

6 Present-day and endglacial earthquake scenarios

The present-day and endglacial earthquake scenarios are presented in this chapter. In all cases it is assumed that the rupture is initiated on ZFMA2, which is the Forsmark zone that has the lowest stability under present-day and endglacial stress conditions. The earthquake rupture is initiated at a pre-defined hypocentre (HC1 or HC2 in Figure 6-1), i.e., the centre of the circular rupture nucleation region (cf Section 4.3) is located at this position. As a Base case assumption, the location named HC1 is used. To examine the sensitivity to the location of the rupture initiation, HC2 is adopted in some cases. Both hypocentres are located at 900 m depth. The hypocentre locations were set to be at some distance from the repository. Results from several studies (Andrews 2005, Fälth 2018, Fälth and Hökmark 2015, Johri et al. 2014, Xu et al. 2012) show that the secondary effects induced around the rupture front tend to be stronger at longer rupture propagation distances.

The following two subsections describe the model geometry used when simulating secondary displacements at short distances and how porewater pressure is applied in the models.
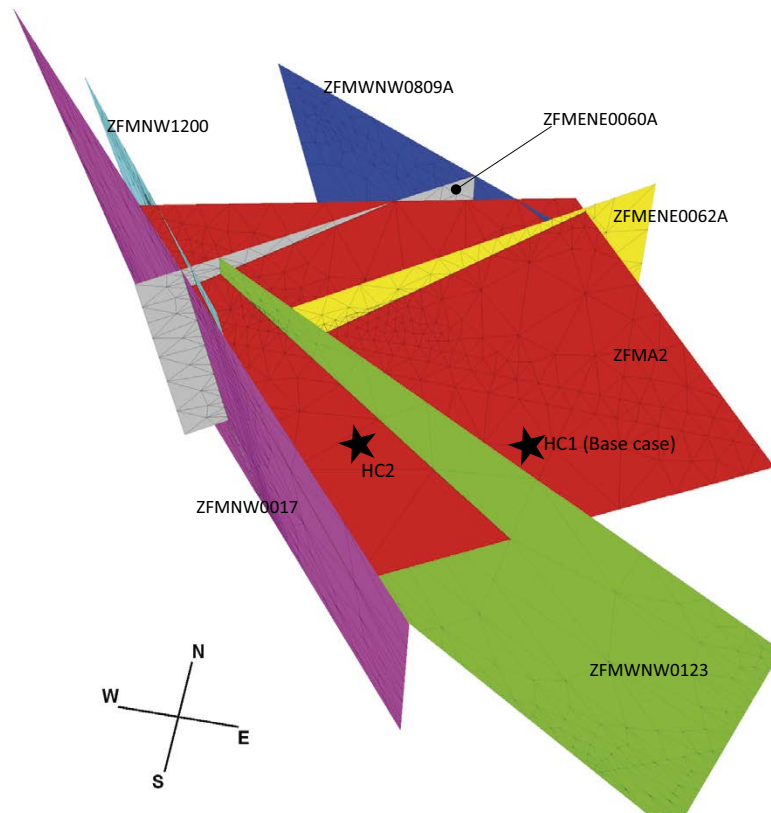

Figure 6-1. *Locations of the two hypocentres HC1 and HC2 on ZFMA2.*

6.1   Target fractures at short distances

The shortest distance between the centres of the target fractures shown in Figure 4-3 and the ZFMA2 plane is 90 m (see Appendix B). To examine how large fracture displacements that potentially could be induced on fractures at even shorter distances and on fractures intersecting the slipping ZFMA2 plane, a specifically designed model geometry is set up. Figure 6-2 shows the locations and orientations of the target fractures included in the model. Fractures from 14 sets (see Table 4-1) are included at 4 perpendicular distances (0 m, 50 m, 100 m and 150 m) from the ZFMA2 plane. All fractures have radius 75 m. To obtain results that systematically indicate the dependence on distance, the fractures within each row have the same orientation. As seen in Figure 6-2, the rows are at different lateral positions along ZFMA2. Hence, the different fracture sets will be subjected to different co-seismic loads. However, it is judged that this geometry is relevant for the purpose of the model since it makes it possible to examine how secondary displacements for a given fracture set vary with distance from the fault slip plane.

To reduce the complexity of the model geometry, voids are made in ZFMWNW0123 and in ZFMENE0062A to avoid intersections with the target fractures (Figure 6-2). From the Base case simulation results, it turns out that these zones generate only minor displacements. Thus, these voids have modest importance for the model response. The difference in seismic moment between the Base case model and the model with target fractures at short distances (no damage zone) amounts to about 5 % (Table 6-2). This difference can also be attributed to the intersections between target fractures and the ZFMA2 plane.

As can be seen in Figure 6-2, the fractures within each row overlap for some orientations. Thus, for each modelling case the simulation is run twice. In each run, only the fractures in every other row (e.g., at 0 m and 100 m) are active while the fractures at the other two distances are inactivated by assignment of high strength properties (Figure 6-3).

To test the potential impact of the actual thickness of the ZFMA2 zone, a Mohr-Coulomb material model (Itasca 2020) is assigned to the continuum within a 50 m wide region along the ZFMA2 joint plane in some cases. According to the geological model of Forsmark (Stephens and Simeonov 2015), the average thickness of the ZFMA2 zone is 34 m, but varies within a span between 20 m and 50 m. So, the value assumed here represents an upper bound of the ZFMA2 damage zone thickness. Two friction coefficients of the damage zone material are tested: 0.78 and 0.7. The lower value is in agreement with Forsmark data (Glamheden et al. 2007). The higher value is equal to the strength assumed for the deformation zone planes (see Section 4.3). The model cases are summarised in Table 6-1.

To avoid badly shaped blocks and ill-conditioned finite difference zones, the following adjustments are made in the target fracture orientations (cf Table 4-1):

- Facture set GEN 27/81:   Dip direction set to 80°.
- Facture set GEN 27/261:   Dip direction set to 260°.
- Facture set GEN 55/81:   Dip direction set to 80°.
- Facture set GEN 55/261:   Dip direction set to 260°.
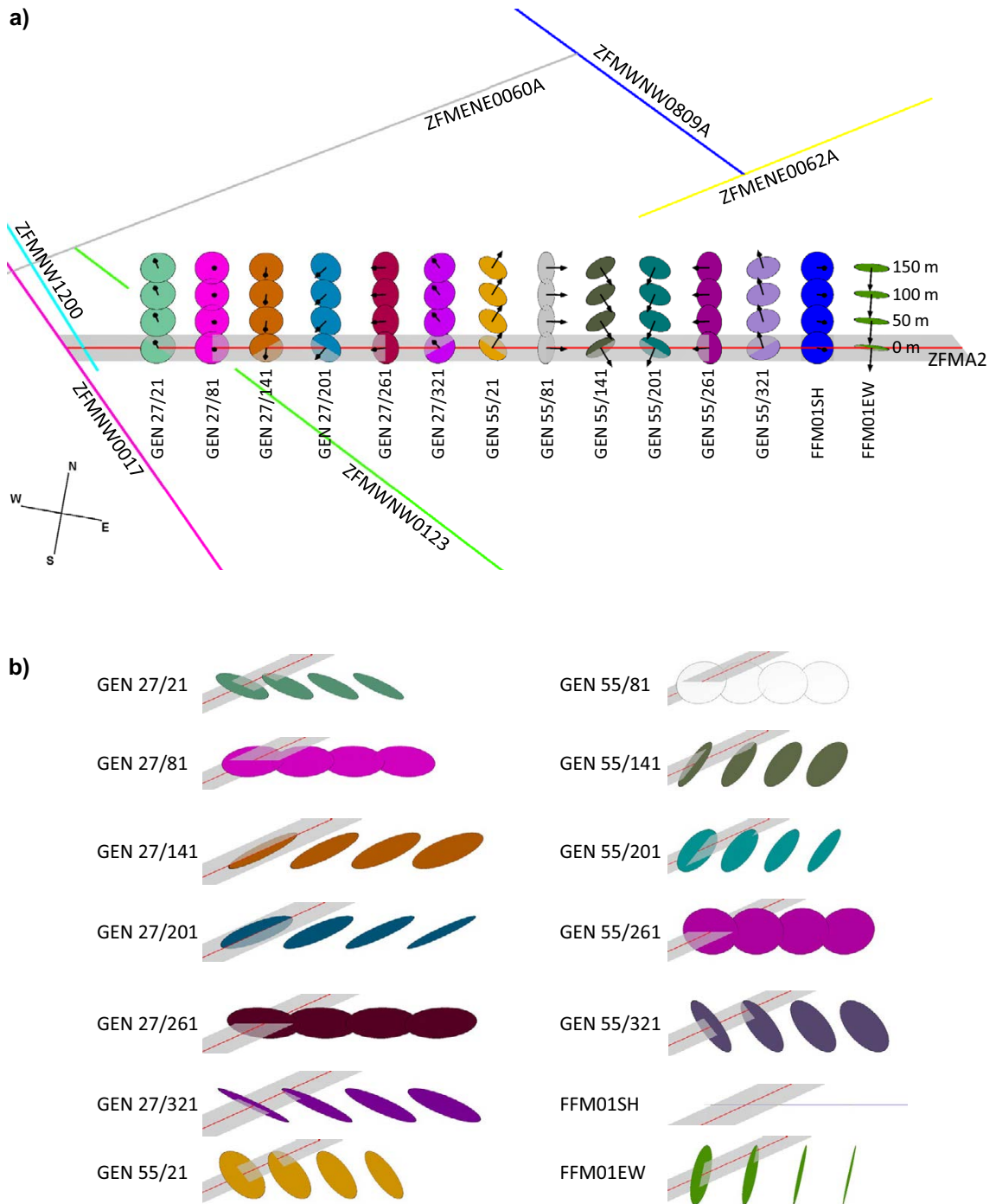- Facture set FFM01SH: Dip set to 0°.

Figure 6-2. *The locations and orientations of the target fractures included at short distances from the ZFMA2 slip plane, here shown in red. The shaded region indicates the extent of the 50 m wide damage zone in the case it was included. a) Map view at 470 m depth. The arrows indicate the normal directions of the fracture planes. b) Vertical sections perpendicular to the strike of ZFMA2 showing each fracture set.*
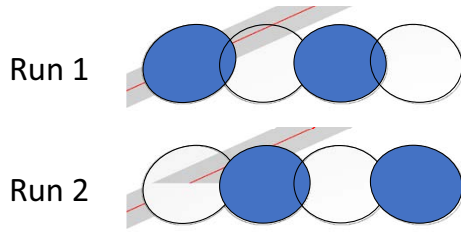
Figure 6-3. *For every modelling case two runs are performed. In each run, every second target fracture is deactivated by assignment of high strength properties. This is illustrated here for the GEN 55/81 target fracture set (cf Figure 6-2).*

6.2 Porewater pressure

For present-day conditions, hydrostatic porewater pressure is assumed. However, during glaciation increased pore pressures will develop in the bedrock beneath the ice sheet and may remain after ice retreat. The residual pore overpressure is an uncertain quantity that will depend on, for instance, the duration of the ice cover, the average subglacial meltwater pressure, and on the bedrock's hydraulic properties (Lönnqvist and Hökmark 2013). Around the margin of the retreating ice, the residual excess pore pressure at 500 m depth might be of the order of 1 MPa (Chan et al. 2005, Hökmark et al. 2010). Here, when assuming endglacial conditions, the effect of a glacially induced excess pore pressure P_e is applied in all discontinuities in addition to the effect of the hydrostatic pore pressure. The excess pore pressure P_e is set according to

$$P_e = \begin{cases} -\dfrac{1}{0.15}z & -0.15 \leq z < 0 \\ 1 & z < -0.15 \end{cases} \text{ MPa,} \tag{6-1}$$

where z is depth in kilometres, i.e., the excess pore pressure is set to be zero at the ground surface and then to increase linearly with depth down to 150 m. At larger depths it is set constant at 1 MPa. Hence, it is assumed that some excess pressure has time to be drained close to the surface prior to rupture initiation. In the previous Forsmark simulation by Fälth et al. (2016), it was schematically assumed that the excess pressure is 1 MPa also at the surface. Here, this assumption was considered extreme and overly pessimistic. In addition, such an assumption means that the effective normal stress on the gently dipping ZFMA2 zone would be zero close to the surface. This would give zero shear resistance and lead to numerical difficulties and long model running times.

The basic assumption is that the porewater pressure is constant, i.e., no coupling between stress altera-tions in the rock mass and the porewater pressure is considered. However, it is known that the pore pressure may be influenced by stress changes in the rock (Rice and Cleary 1976). The potential impact of this on the co-seismic target fracture displacements is examined here for some modelling cases by modelling temporal variations $P(t)$ in the porewater pressure according to

$$P(t) = P_0 + \Delta P = P_0 + \frac{1}{3}B[\sigma_{kk}(t) - \sigma_{kk}(t = 0)] \tag{6-2}$$

where P_0 is the initial pore pressure (including excess pressure P_e), B is Skempton's coefficient and σ_{kk} is the trace of the stress tensor in the rock mass. Thus, the change in pore pressure is assumed to be proportional to the change in average stress, $\sigma_{kk}/3$ (Rice and Cleary 1976). This means that the hydraulic coupling ($B \neq 0$) works to maintain stability at locations subjected to average stress reduc-tions and promotes instability at locations where the stress increases.

Skempton's coefficient B is the change of pore pressure per unit change of average stress under undrained conditions. For co-seismic loads, which are the focus in this study, the time scale of the stress change is short compared to the time scale of pore water diffusion. Thus, it is relevant to assume undrained conditions. Skempton's coefficient takes values in the range [0, 1] and is poorly constrained (Simpson 2001). The value depends on the mechanical properties of the bedrock (Rice and Cleary 1976) as well as on the stress conditions (Mesri et al. 1976). In their laboratory experiments Mesri et al. (1976) obtained values near one at low confining stresses, but values in the range 0.33–0.69 for a stress of about 10 MPa. Other studies show values in the range 0.5–0.85 (Makhnenko and Labuz

2016, Simpson 2001). Here, to test the potential impact of porewater coupling, Skempton's coefficient is set to $B = 0.5$ in some simulation cases. The simulation of porewater transients is restricted to the target fractures. Also note that no actual porewater transport calculations are performed in any of the simulations here.

6.3 Simulated cases

Two main earthquake rupture scenarios are considered:

- A rupture occurring under present-day stress conditions.

- A rupture occurring under endglacial stress conditions.

All model cases are summarised in Table 6-1. There are three present-day models with different assumptions regarding the fault dynamic friction coefficient μ_d. Based on the results from these models, $\mu_d = 0.46$ is applied as a Base case assumption (cf Table 4-2) in the endglacial rupture scenario, which is the focus here. This value of μ_d is also used in the forebulge rupture simulations presented in Chapter 5.

To examine how sensitive the results may be to variations in target fracture orientation (cf Table 4-1) and to other input parameters, several endglacial model cases are considered. The following input parameters are varied:

- Hypocentre location. The hypocentre location has importance for how the earthquake rupture propagates as well as for the magnitude and mode of the stress waves that are generated. This has implications for the amount of secondary displacements that may be induced (Fälth et al. 2016, Fälth et al. 2019). In three models with different target fracture orientations, the rupture initiation is set at an alternative hypocentre location, HC2 (Figure 6-1).

- Primary fault dynamic friction coefficient μ_d. A lower dynamic friction coefficient means higher stress drop on the fault during earthquake rupture and hence a stronger seismic source. Three alternative values of μ_d are tested.

- Background (present-day) σ_H stress trend. The orientation of the stress field influences the stability of the target fractures and of the primary fault. It also affects the evolution of fault rupture and fault slip. In three models with different target fracture orientations the background σ_H stress trend is set to N125°E. This means a 20° difference relative to the Base case assumption N145°E.

- Background (present-day) σ_h stress magnitude. The background σ_h is reduced such that it becomes equal to σ_v at depths above 2 km (see Section 2.2.1). Hence, a strike-slip background stress field is applied in this depth range.

- Young's modulus around target fractures. The potential impact of spatial variations in the rock mass stiffness is examined by reducing Young's modulus in volumes surrounding chosen target fractures (Figure 6-4). To get a clear response, the volumes are set to surround fractures on which the strongest secondary stress effects are expected (cf Figure 6-17). The volumes extend between 588 m and 353 m depth. According to Forsmark site data (Glamheden et al. 2007) the uncertainty in the deformation modulus of the rock mass amounts to a few percent. Here, to obtain a clear and measurable model response, Young's modulus is reduced by 30 % within the indicated volumes.

- Skempton's coefficient B. As discussed in Section 6.2 porewater transients may have an impact on fracture stability. The basic assumption is to omit effects of porewater coupling ($B = 0$). To test how the porewater coupling may change the results, Skempton's coefficient is set to $B = 0.5$ in two models.

- Target fracture friction coefficient. Two alternative values (0.6 and 0.8) of the target fracture friction coefficient are tested. This is done for two generic fracture sets and for two site-specific sets.

- Finite difference element edge length (discretisation). Two cases are tested where the average finite element length is set to 80 % and 60 %, respectively, of the average Base case edge length.
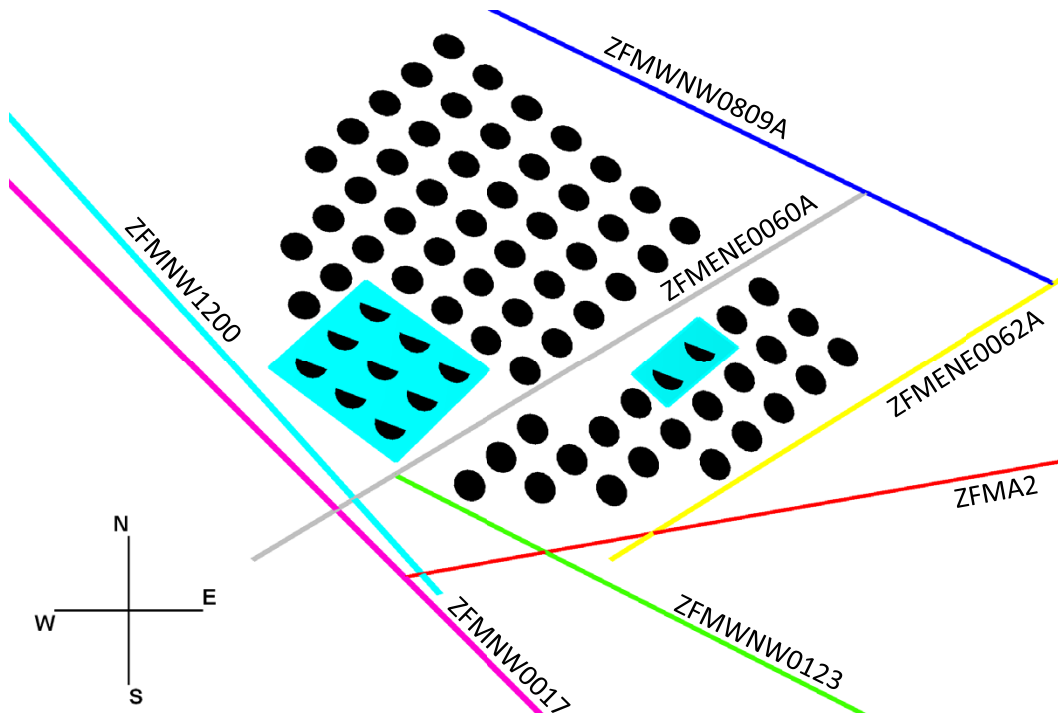
Figure 6-4. *Map view at 470 m depth showing in turquoise the volumes where Young's modulus is reduced in the Gen27-21_SH145_UM-EG_LowY model.*

Table 6-1. Model summary.

Model name	Target fracture set	σ_H trend	Comment
Present-day			
Gen27-321_SH145_PD_mud044	GEN 27/321	145	$\mu_d = 0.44$
Gen27-321_ SH145_PD_mud045	GEN 27/321	145	$\mu_d = 0.45$
Gen27-321_ SH145_PD_mud046	GEN 27/321	145	$\mu_d = 0.46$
Endglacial[†]			
Gen27-21_SH145_UM-EG	GEN 27/21	145	
Gen27-21_SH145_UM-EG_f	GEN 27/21	145	80 % Fin. diff. el. edge length
Gen27-21_SH145_UM-EG_f2	GEN 27/21	145	60 % Fin. diff. el. edge length
Gen27-21_SH145_UM-EG_B05	GEN 27/21	145	Skempton $B = 0.5$
Gen27-21_SH145_UM-EG_LowY	GEN 27/21	145	Reduced Young's modulus
Gen27-21_SH145_UM-EG_HC2	GEN 27/21	145	Hypocentre 2
Gen27-21_SH145_UM-EG_mud043	GEN 27/21	145	$\mu_d = 0.43$
Gen27-21_SH145_UM-EG_mud044	GEN 27/21	145	$\mu_d = 0.44$
Gen27-21_SH145_UM-EG_mud045	GEN 27/21	145	$\mu_d = 0.45$
Gen27-21_SH125_UM-EG	GEN 27/21	125	Background σ_H trend 125°
Gen27-81_SH145_UM-EG	GEN 27/81	145	
Gen27-141_SH145_UM-EG	GEN 27/141	145	
Gen27-141_SH145_UM-EG_HC2	GEN 27/141	145	Hypocentre 2
Gen27-141_SH125_UM-EG	GEN 27/141	125	Background σ_H trend 125°
Gen27-201_SH145_UM-EG	GEN 27/201	145	
Gen27-261_SH145_UM-EG	GEN 27/261	145	
Gen27-261_SH145_UM-EG_HC2	GEN 27/261	145	Hypocentre 2
Gen27-261_SH145_UM-EG_targmu06	GEN 27/261	145	Target fracture $\mu = 0.6$
Gen27-261_SH145_UM-EG_targmu08	GEN 27/261	145	Target fracture $\mu = 0.8$
Gen27-261_SH125_UM-EG	GEN 27/261	125	Background σ_H trend 125°
Gen27-321_SH145_UM-EG	GEN 27/321	145	
Gen55-21_SH145_UM-EG	GEN 55/21	145	
Gen55-81_SH145_UM-EG	GEN 55/81	145	
Gen55-141_ SH145_UM-EG	GEN 55/141	145	
Gen55-141_SH145_UM-EG_B05	GEN 55/141	145	Skempton $B = 0.5$
Gen55-141_SH145_UM-EG_targmu06	GEN 55/141	145	Target fracture $\mu = 0.6$
Gen55-141_SH145_UM-EG_targmu08	GEN 55/141	145	Target fracture $\mu = 0.8$
Gen55-201_SH145_UM-EG	GEN 55/201	145	
Gen55-201_SH145_UM-EG_Shred43	GEN 55/201	145	Background σ_h red. 43 %
Gen55-261_SH145_UM-EG	GEN 55/261	145	
Gen55-321_SH145_UM-EG	GEN 55/321	145	
FFM01SH_SH145_UM-EG	FFM01 SH	145	
FFM01EW_SH145_UM-EG	FFM01 EW	145	
FFM01NS_SH145_UM-EG	FFM01 NS	145	
FFM01NS_SH145_UM-EG_targmu06	FFM01 NS	145	Target fracture $\mu = 0.6$
FFM01NS_SH145_UM-EG_targmu08	FFM01 NS	145	Target fracture $\mu = 0.8$
FFM01NS_SH145_UM-EG_Shred43	FFM01 NS	145	Background σ_h red. 43 %
FFM06NW_SH145_UM-EG	FFM06 NW	145	
FFM06NW_SH145_UM-EG_Shred43	FFM06 NW	145	Background σ_h red. 43 %
FFM06NE_SH145_UM-EG	FFM06 NE	145	
FFM06NE_SH145_UM-EG_targmu06	FFM06 NE	145	Target fracture $\mu = 0.6$
FFM06NE_SH145_UM-EG_targmu08	FFM06 NE	145	Target fracture $\mu = 0.8$
Endglacial, short distances (see Figure 6-2, Figure 6-3)			
RUN1_SH145_UM_EG	Several	145	No damage zone
RUN2_SH145_UM_EG	Several	145	No damage zone
RUN1_SH145_UM_EG_mu07	Several	145	Damage zone, $\mu = 0.7$
RUN2_SH145_UM_EG_mu07	Several	145	Damage zone, $\mu = 0.7$
RUN1_SH145_UM_EG_mu078	Several	145	Damage zone, $\mu = 0.78$
RUN2_SH145_UM_EG_mu078	Several	145	Damage zone, $\mu = 0.78$

[†] The Base case assumption of zone property is adopted, i.e., $\mu_d = 0.46$, unless indicated otherwise in the comments above.

6.4 Results

The section is divided into two main parts. Section 6.4.1 contains results showing the response of the primary fault, i.e., the earthquake sources for the simulated cases. In Section 6.4.2, the secondary stress effects and the response of the target fractures are presented.

6.4.1 Fault response

In the following two subsections the fault response during the two calculation steps is presented. The response during the dynamic earthquake rupture is of main interest. However, the quasi-static response is also presented here because it helps the understanding of the co-seismic target fracture results.

Quasi-static calculation step

As noted earlier, given the reverse-faulting background stress regime prevailing at shallow depths in Forsmark, and given the properties assumed here, gently dipping deformation zones and fractures will be close to failure or even in a state of failure. The instability will be further increased under endglacial conditions (cf e.g. Figure 2-4). Hence, during the quasi-static calculation step, when the deformation zone joint planes and the target fracture joint planes are assigned properties according to Table 4-2, some of them will generate slip. The slip will be in accordance with the location and orientation of respective joint plane. Gently dipping planes that dip along the major principal stress σ_H will slip most while steeply dipping planes, which are clamped by the high horizontal stresses, will have much higher stability margins and hence will generate little or no slip.

Shear displacements on the deformation zones generated under present-day and endglacial stress conditions are shown in Figure 6-5 and Figure 6-6, respectively. ZFMA2 is the only zone that is unstable. Hence, this is basically the only zone that generates slip. However, minor shear displacements may take place close to the ground surface on ZFMNW0017 along its intersection with ZFMA2. Due to the increased horizontal stresses in the endglacial model, the maximum slip becomes more than twice that generated in the present-day model. The considerable slip generated on ZFMA2 during this calculation step has a significant impact on the stability of the target fractures, as shown below.
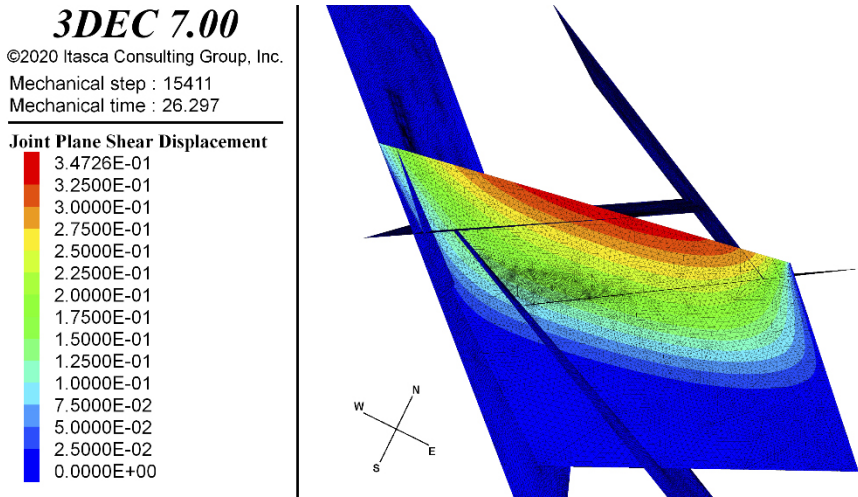

Figure 6-5. *Deformation zone shear displacement (m) generated during the quasi-static calculation step in the Gen27-321_ SH145_PD_mud045 model (present-day stresses).*
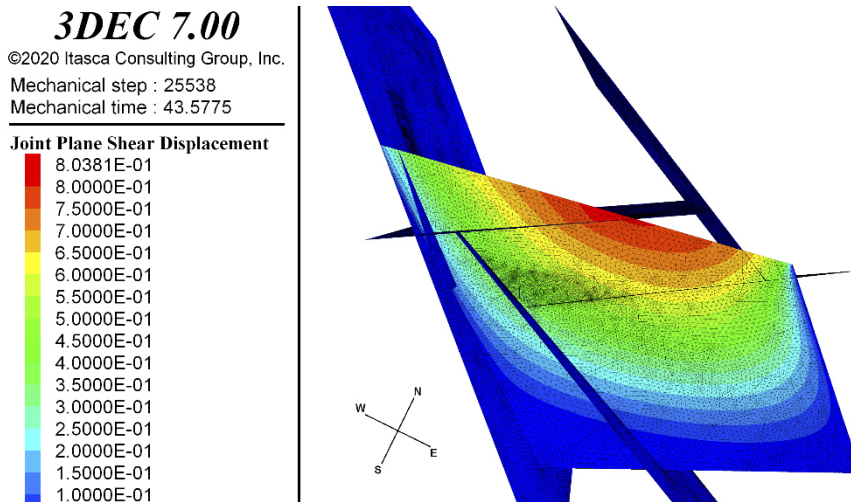
***Figure 6-6.** Deformation zone shear displacement (m) generated during the quasi-static calculation step in the Gen27-321_SH145_UM-EG model (endglacial stresses).*

Dynamic calculation step

In the following two subsections the results from the present-day and endglacial earthquake rupture simulations are presented and discussed. Recall that all displacements generated during the previous quasi-static calculation step are reset prior to rupture initiation. Hence, the displacements presented here are co-seismic only.

Present-day conditions

A summary of the source parameters for all simulated cases is given in Table 6-2. A comparison of the responses of the three present-day models shows that, for the present-day scenario the resulting average stress drop $\Delta\tau_{avg}$ and moment magnitude M_w is sensitive to the dynamic friction coefficient μ_d. Increasing μ_d from 0.44 to 0.46 gives a reduction in average stress drop of about 40 % while the moment magnitude is reduced by 0.2 units. As seen in Table 6-2 this corresponds approximately to a 50 % reduction in seismic moment M_0 (cf Equation (1-2)). What can also be noticed in Table 6-2 is that both average slip u_{avg} and rupture area RA increase when μ_d is reduced. The rupture area increases partly because the rupture propagates deeper down along ZFMA2 and partly because of the intersection with the other zones (Figure 6-7). Slip is generated close to the surface on the adjoining zones, particularly on ZFMNW0017 along the intersection with ZFMA2. When μ_d is reduced, the ruptured area on the adjoining zones is increased. The slip generated on ZFMNW0017 also explains why the slip on ZFMA2 tends to be largest in the northwest corner.

The sensitivity to μ_d warrants some commenting. In the velocity-weakening constitutive model applied here for simulating fault rupture, the friction coefficient is a function of slip velocity (Figure 4-9). The constitutive parameter μ_d determines the lowest possible friction coefficient that can be obtained at high slip velocities. How much the fault friction is actually reduced during the dynamic rupture process, and thus how much slip that is generated, depends not only on the values of the input parameters to the velocity-weakening model, but also on a complex interplay between the stress conditions, fault geometry and hypocentre location. Apparently, the conditions in the present-day case simulated here yield a high sensitivity to μ_d. In the next section, where the results from the endglacial scenario are presented, a more elaborated discussion of the dynamic source parameters is given.
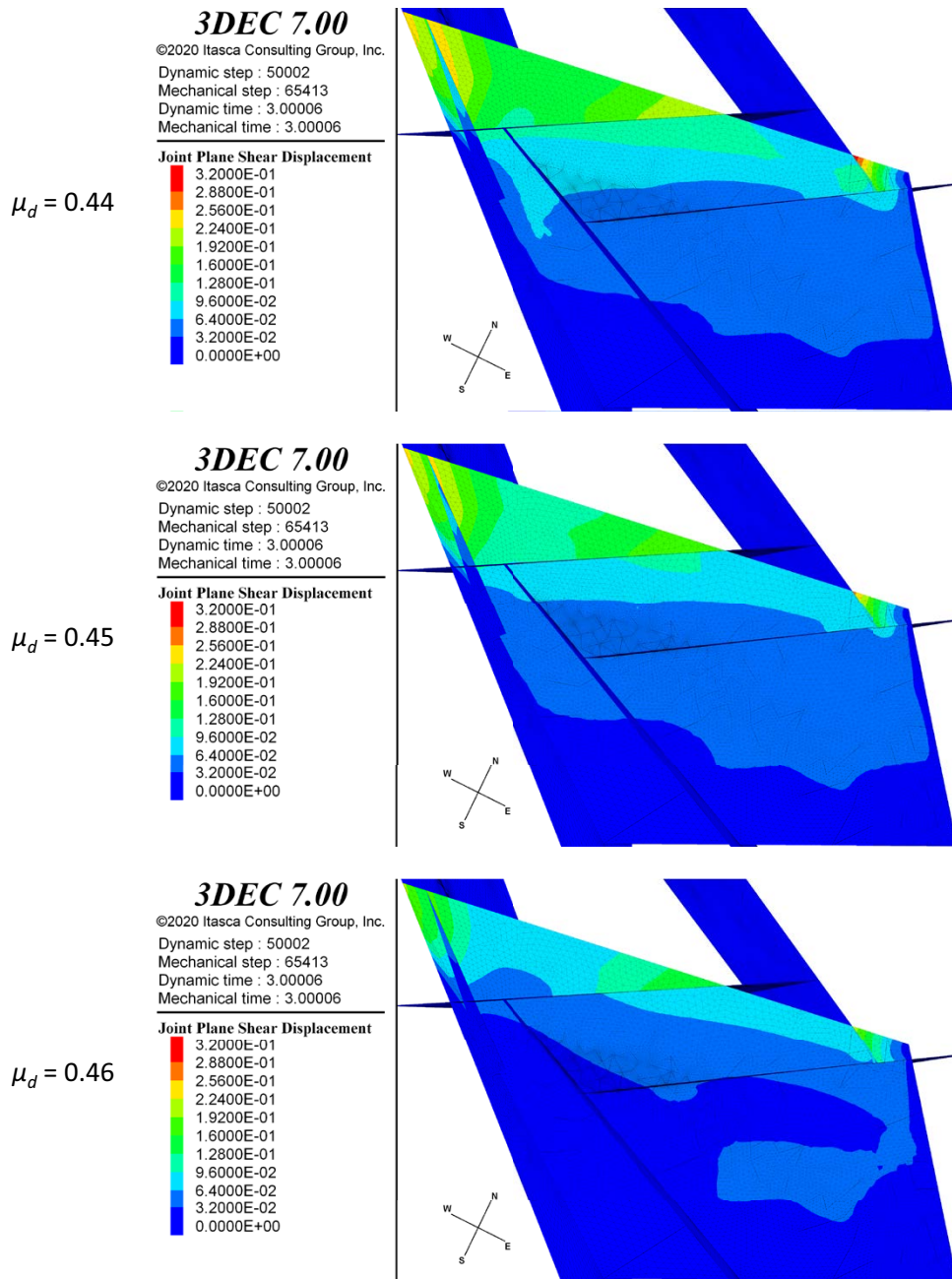
$\mu_d = 0.44$

$\mu_d = 0.45$

$\mu_d = 0.46$

Figure 6-7. *Contours of shear displacement (m) generated under present-day stress conditions. Results for the three cases of μ$_d$ are shown (model Gen27-321_SH145_PD_mud046, Gen27-321_SH145_PD_mud045 and Gen27-321_SH145_PD_mud044, cf Table 6-2).*

The moment magnitude-rupture area relations of the three synthetic present-day earthquakes are plotted in Figure 6-8 along with corresponding data obtained from the Wells and Coppersmith (1994) database. According to the diagram it appears that, for given rupture areas, the moment magnitudes of the simulated earthquakes are low compared to those of the real earthquakes. However, as noted in Section 1.5.2, all the database earthquakes occur at much larger depths than the synthetic earthquakes. Hence, due to the higher stress levels at larger depths, higher stress drops and larger displacements are generated for a given rupture area (Scholz 2002). Figure 6-9a shows how moment magnitude is related to focal depth for the synthetic earthquakes and for the data base earthquakes. Figure 6-9b shows average displacement versus focal depth for the same data set. The diagrams in Figure 6-9 show that the moment magnitudes and the average displacements generated in all three synthetic present-day earthquakes are on par with those generated by real earthquakes with much larger focal depths. This becomes particularly clear when comparing with the data for SCR events, which should be relevant

for Swedish conditions (cf Section 1.3). In addition, according to the Wells and Coppersmith (1994) catalogue data, it appears very unlikely that an earthquake rupture would be initiated at all above 1 km depth.

It appears that all three synthetic present-day earthquakes should represent very unlikely scenarios. Given the shallow depth and the corresponding low stress drops and small displacements that can be expected (Figure 6-9), $\mu_d = 0.46$ is adopted as a Base case assumption for all simulations presented in this report (cf Section 4.3).
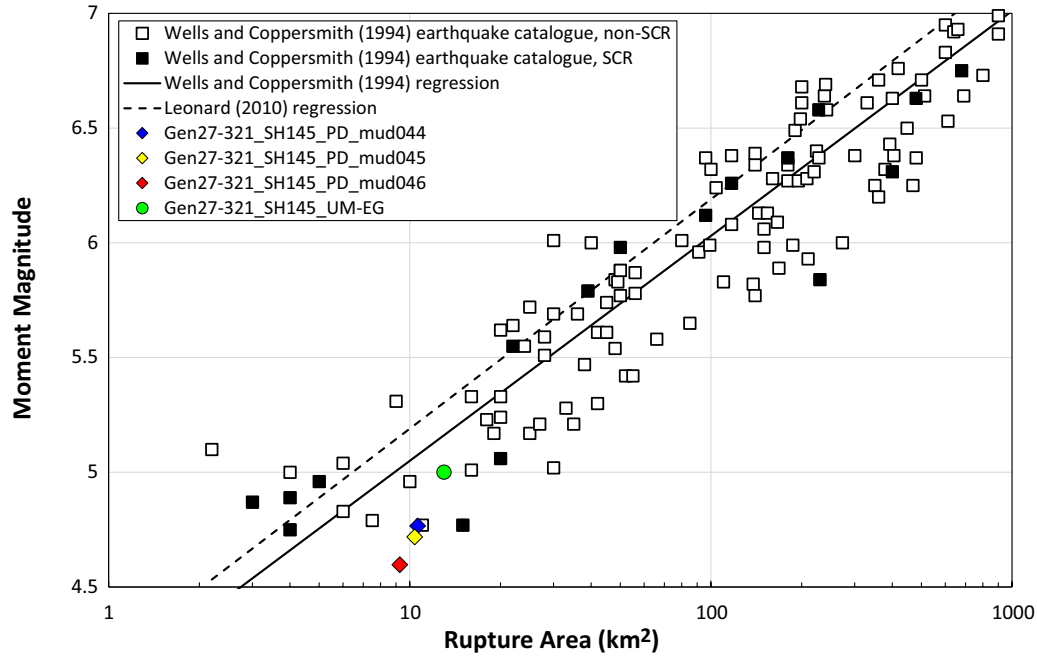
Figure 6-8. *Moment magnitude M_w versus rupture area RA for simulations of the three present-day earthquakes and one endglacial earthquake plotted along with corresponding data for earthquakes in the Wells and Coppersmith (1994) catalogue. "SCR" means Stable Continental Region.*
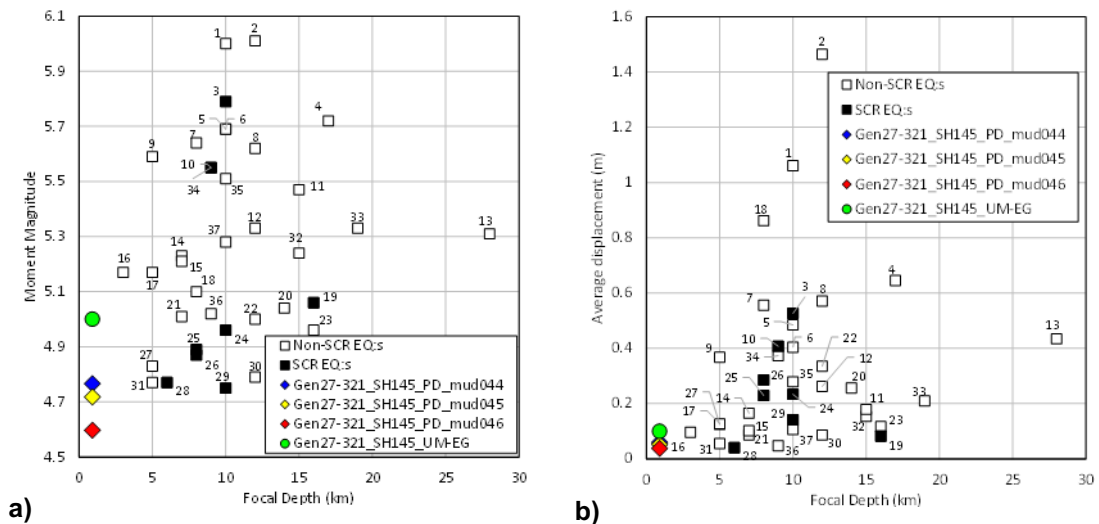
Figure 6-9. *a) Moment magnitude Mw versus focal depth for simulations of the three present-day earthquakes and one endglacial earthquake plotted along with corresponding data for earthquakes in the Wells and Coppersmith (1994) catalogue. b) Average displacement versus focal depth for the simulated earthquakes and the catalogue events. "SCR" means Stable Continental Region. The catalogue data set is limited to earthquakes with rupture areas up to 40 km². The data labels refer to the references in Table 1-1 supporting the given focal depths. The average displacements were calculated as described in Section 1.5.2.*

Table 6-2. Source parameters.

Model name	M_w	M_0 (-10^{16} Nm)	$\Delta\tau_{avg}$ (MPa)	u_{avg} (m)	RA (km²)
Present-day					
Gen27-321_SH145_PD_mud044	4.8	1.8	0.52	0.060	11
Gen27-321_SH145_PD_mud045	4.7	1.5	0.44	0.052	10
Gen27-321_SH145_PD_mud046	4.6	1.0	0.30	0.038	9
Endglacial					
Gen27-21_SH145_UM-EG	5.0	3.9	1.3	0.10	13
Gen27-21_SH145_UM-EG_f	5.0	3.9	1.2	0.10	14
Gen27-21_SH145_UM-EG_f2	5.0	4.0	1.2	0.11	14
Gen27-21_SH145_UM-EG_B05	5.0	3.9	1.3	0.10	13
Gen27-21_SH145_UM-EG_LowY	5.0	3.9	1.3	0.10	13
Gen27-21_SH145_UM-EG_HC2	5.0	4.4	1.6	0.12	13
Gen27-21_SH145_UM-EG_mud043	5.1	5.8	1.5	0.15	14
Gen27-21_SH145_UM-EG_mud044	5.1	4.9	1.4	0.13	14
Gen27-21_SH145_UM-EG_mud045	5.0	4.4	1.3	0.11	14
Gen27-21_SH125_UM-EG	4.9	2.9	0.90	0.084	12
Gen27-81_SH145_UM-EG	5.0	3.9	1.2	0.10	14
Gen27-141_SH145_UM-EG	5.0	3.8	1.2	0.10	13
Gen27-141_SH145_UM-EG_HC2	5.0	4.4	1.2	0.10	13
Gen27-141_SH125_UM-EG	4.9	2.8	0.88	0.083	12
Gen27-201_SH145_UM-EG	5.0	3.9	1.2	0.10	13
Gen27-261_SH145_UM-EG	5.0	3.8	1.2	0.10	13
Gen27-261_SH145_UM-EG_HC2	5.0	4.4	1.6	0.12	13
Gen27-261_SH145_UM-EG_targmu06	5.0	3.8	1.2	0.10	13
Gen27-261_SH145_UM-EG_targmu08	5.0	3.8	1.2	0.10	13
Gen27-261_SH125_UM-EG	4.9	2.9	0.90	0.083	12
Gen27-321_SH145_UM-EG	5.0	3.8	1.2	0.10	13
Gen55-21_SH145_UM-EG	5.0	3.9	1.2	0.10	13
Gen55-81_SH145_UM-EG	5.0	3.9	1.2	0.10	13
Gen55-141_SH145_UM-EG	5.0	3.9	1.2	0.10	13
Gen55-141_SH145_UM-EG_B05	5.0	3.9	1.2	0.10	13
Gen55-141_SH145_UM-EG_targmu06	5.0	3.9	1.2	0.10	13
Gen55-141_SH145_UM-EG_targmu08	5.0	3.9	1.2	0.10	13
Gen55-201_SH145_UM-EG	5.0	3.9	1.2	0.10	13
Gen55-201_SH145_UM-EG_Shred43	5.0	3.5	1.1	0.090	14
Gen55-261_SH145_UM-EG	5.0	3.9	1.3	0.10	13
Gen55-321_SH145_UM-EG	5.0	3.9	1.2	0.10	13
FFM01SH_SH145_UM-EG	5.0	3.8	1.2	0.10	14
FFM01EW_SH145_UM-EG	5.0	3.9	1.2	0.10	13
FFM01NS_SH145_UM-EG	5.0	3.9	1.2	0.10	13
FFM01NS_SH145_UM-EG_targmu06	5.0	3.9	1.2	0.10	13
FFM01NS_SH145_UM-EG_targmu08	5.0	3.9	1.2	0.10	13
FFM01NS_SH145_UM-EG_Shred43	5.0	3.5	1.1	0.090	14
FFM06NW_SH145_UM-EG	5.0	3.9	1.2	0.10	14
FFM06NW_SH145_UM-EG_Shred43	5.0	3.6	1.1	0.091	14
FFM06NE_SH145_UM-EG	5.0	3.8	1.2	0.10	13
FFM06NE_SH145_UM-EG_targmu06	5.0	3.8	1.2	0.10	13
FFM06NE_SH145_UM-EG_targmu08	5.0	3.8	1.2	0.10	13
Endglacial, short distances (see Figure 6-2, Figure 6-3)					
RUN1_SH145_UM_EG	5.0	4.1	1.2	0.11	13
RUN2_SH145_UM_EG	5.0	4.1	1.2	0.11	13
RUN1_SH145_UM_EG_mu07	5.0	4.5	1.3	0.12	13
RUN2_SH145_UM_EG_mu07	5.0	4.5	1.3	0.12	13
RUN1_SH145_UM_EG_mu078	5.0	4.7	1.3	0.12	13
RUN2_SH145_UM_EG_mu078	5.0	4.7	1.3	0.12	13

SKB TR-22-13

Endglacial conditions

When comparing the source parameters of the present-day and endglacial models (Table 6-2, Figure 6-8, Figure 6-9) it becomes clear that there is a significant difference in model response. This is what can be expected from the considerable horizontal stress additions in the endglacial case. Applying the same fault properties ($\mu_d = 0.46$), the moment magnitude of the endglacial earthquake becomes 0.4 units higher than that of the present-day earthquake. This corresponds to an increase in the seismic moment M_0 by a factor of approximately four (cf Equation (1-2)).

To illustrate the response of the model during rupture under endglacial conditions, results from the Gen27-21_SH145_UM-EG model are presented and discussed here. In this model the Base case assumptions were applied, i.e., the background σ_H orientation is set to N145°E, $\mu_d = 0.46$ and the rupture is initiated at HC1 (see Figure 6-1). It turns out that the response of this model is, in general, similar to the response of the other endglacial models with other input assumptions. Thus, the discussion in the following paragraphs is representative for the other models as well.

The evolution of rupture is illustrated by the slip velocity plots in Figure 6-10. The rupture is initiated according to the routine described in Section 4.3. First, the rupture front propagates radially. When it reaches the surface, it continues along the surface trace of ZFMA2 until it reaches the intersection with ZFMNW0017.

In Figure 6-11 the propagation directions of the rupture front at different parts of the fault plane are indicated by arrows. The arrows show how the rupture propagates systematically outward from the initiation point until it reaches the region close to the ground surface. In that region the zone is in low compression and thus has low shear resistance. There are also intersecting zone planes (primarily ZFMENE0060A, ZFMENE0062A) that form rock blocks that tend to reduce the shear resistance further. This, and possibly waves that are reflected in the nearby ground surface, gives a complex fault response with very high rupture speeds and back propagation in places. Over most of the ZFMA2 joint plane the propagation speed is in the range $0.8\,V_s$–$0.9\,V_s$, which is typically observed in real earthquakes (Scholz 2002). However, due to the low stability close to the ground surface, there are locations where the calculated propagation speed V_r exceeds V_s and even locally exceeds the rock mass compressional wave speed V_p, which here is approximately $1.7\,V_s$ (cf Table 4-2). An earthquake rupture cannot propagate faster than V_p. The unphysical speeds exceeding V_p is an artefact that appears when nearby joint sub-contacts in the low-stability region close to the surface rupture (almost) simultaneously and the rupture speed calculation breaks down (cf Figure 6-12). Note, however, that this calculation is done after completed rupture simulation and thus the artefact does not influence the numerical solution during rupture.

Another output parameter that is interesting is the slip velocity. It has importance for the strength of the stress waves that are generated during rupture and fault slip and hence has importance for the secondary effects. It is also a parameter that can be compared with observations made in real earthquakes to assess the relevance of the simulated earthquake source. The plots in Figure 6-10 indicate simulated slip velocities on the order of a few meters per second. In Figure 6-13, values of peak slip velocity at all positions are plotted. The peak velocities are in the range 0.5–1.5 m/s over most of the rupture area. The velocity exceeds 1 m/s over about 40 % of the area. Close to the surface at the intersection with ZFMNW0017 higher velocities are obtained locally. The magnitudes of the velocities seem to agree with observations. Data indicates that the fault slip velocities in real events are on the order of one or some metres per second. For instance, the inversion model by Wald et al. (1996) of the M_w 6.7 Northridge 1994 earthquake indicates velocities in the range 1–1.5 m/s. Similar velocities were determined by both Olsen et al. (1997) and Wald and Heaton (1994) for the 1992 Landers earthquake. For some events, higher velocities have been inferred. For the 1999 M_w 7.6 Chi-Chi Taiwan earthquake, for instance, the highest slip velocities were estimated to be in the order of 4 m/s (Ma et al. 2003).
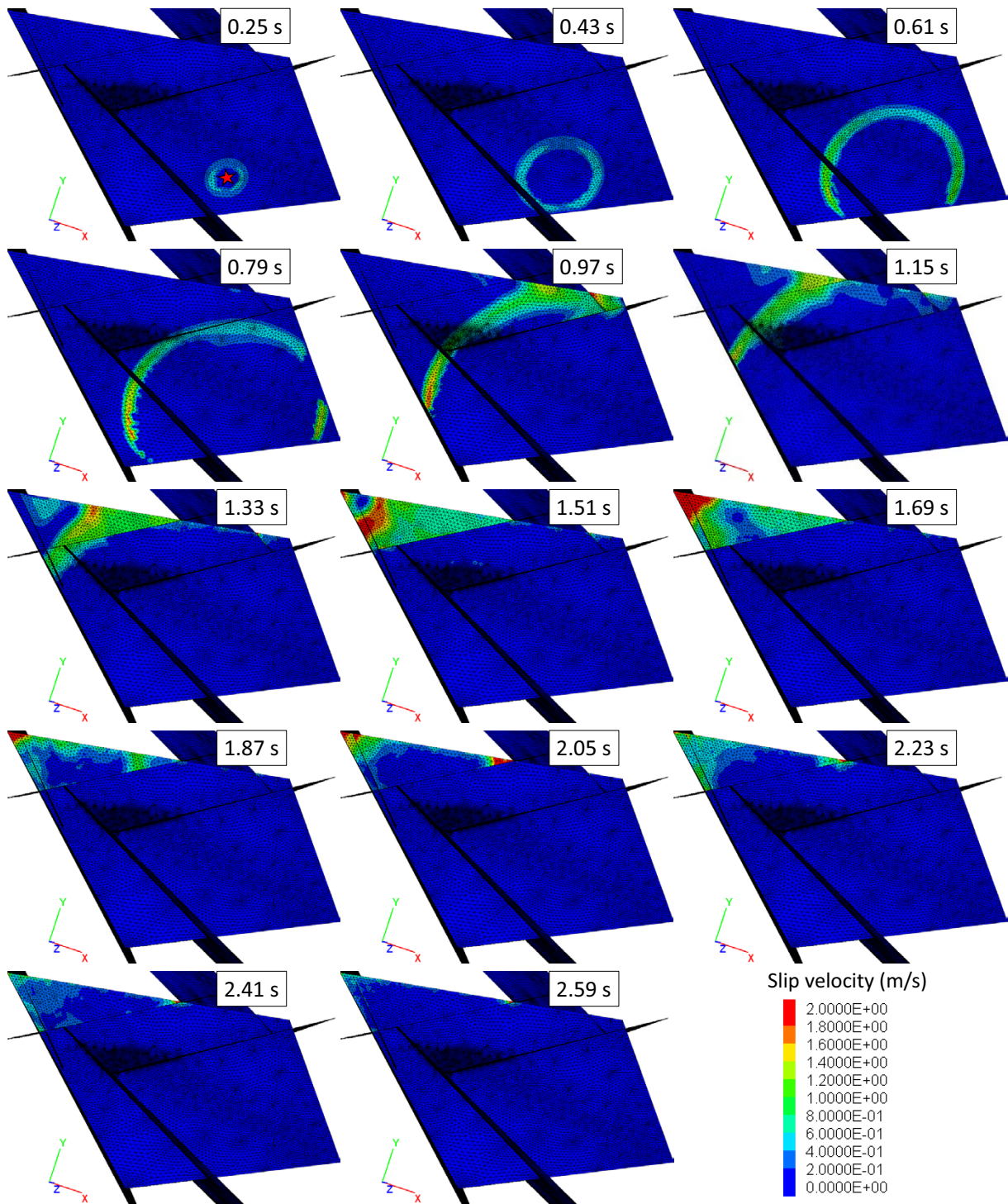
Figure 6-10. *The evolution of rupture illustrated by contours of slip velocity at different time instances. To make the plots clearer the colour scale is set to saturate at 2 m/s. The red star indicates the hypocentre. The results are obtained from the Gen27-21_SH145_UM-EG model.*
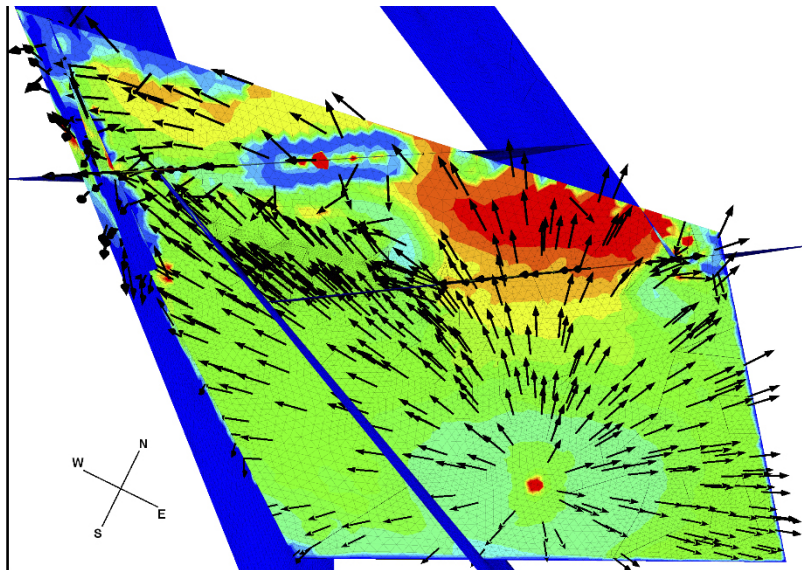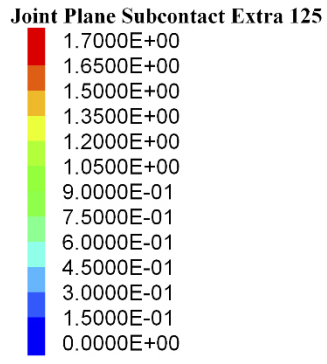
Figure 6-11. *Contours of rupture velocity normalised to the rock mass shear wave velocity V_s. The vectors show the propagation direction of the rupture front. The results are obtained from the Gen27-21_SH145_UM-EG model.*

$$V_r = \frac{x^{n+} - x^n}{t_i^{n+1} - t_i^n}$$
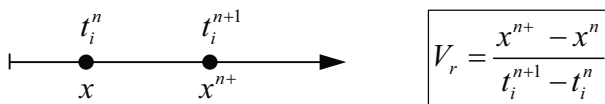
Figure 6-12. *Illustration of the principle for calculation of rupture propagation speed V_r in the one-dimensional case including two adjacent sub-contacts at positions x^n and x^{n+1} and which have rupture initiation times t_i^n and t_i^{n+1}.*
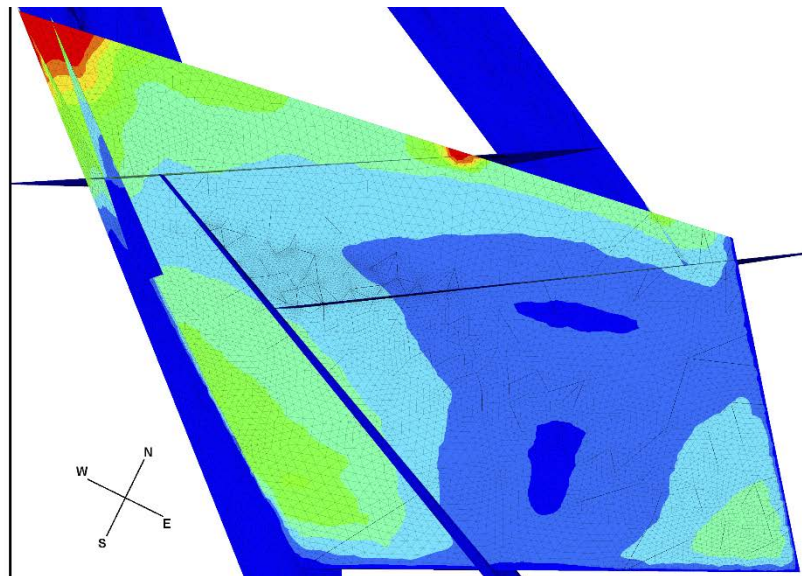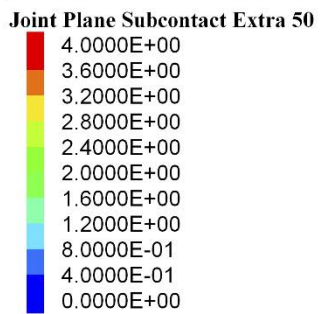
Figure 6-13. *Contours of peak slip velocity (m/s). The results are obtained from the Gen27-21_SH145_UM-EG model. For illustrative purposes, the plotted values are determined from the stored peaks values using a moving spatial averaging over a circular area with 80 m radius.*

The distribution of slip that is generated during rupture is shown in Figure 6-14. Notable is that the intersections of the other deformation zone planes have a clear impact on the displacement distribution close to the ground surface. Particularly the blocks that are formed north of ZFMENE0060A means that the displacements along the surface trace of ZFMA2 becomes increased. The impact of these fault intersections is possibly exaggerated due to the assumption of a linear elastic rock mass and due to the absence of damping in the model.

When comparing the source parameters in Table 6-2 for the endglacial earthquakes, it can be noted that the response of the fault is similar for cases where the same assumptions regarding stress field, fault properties and hypocentre have been made. This indicates that the rebuilding of the model geometry for different target fracture orientations does not influence the overall response of the model in any significant way. The exception from this is found in the models where short fracture-to-fault distances are considered. Including intersecting fractures and fault damage zone meant a more extensive rebuilding of the model geometry. In the case where no damage zone is considered, this model generates about 5 % larger seismic moment than the other models with the same input assumptions (cf e.g. Gen27-21_SH145_UM-EG and RUN1_SH145_UM_EG in Table 6-2). This slight change in model response can be attributed to the rebuilding of the model geometry. Then, the case with damage zone ($\mu = 0.78$) gives an increase of the seismic moment by about 20 % (cf e.g. Gen27-21_SH145_UM-EG and RUN1_SH145_UM_EG_mu078 in Table 6-2).
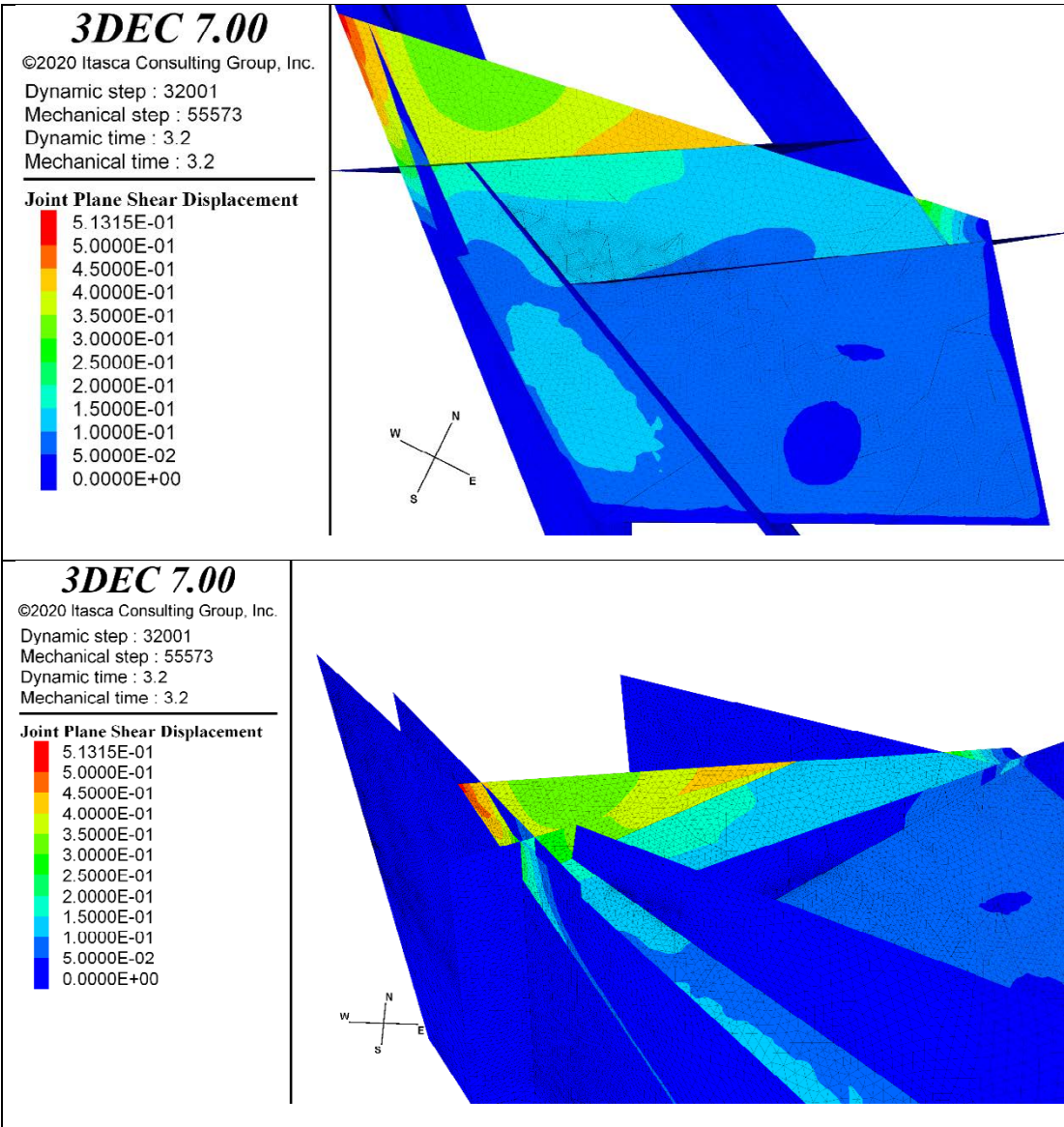

Figure 6-14. Contours of shear displacement (m) shown from two directions. The results are obtained from the Gen27-21_SH145_UM-EG model.

The sensitivity of the model response to other input parameters is commented in the following list (see Table 6-2):

- Dynamic friction coefficient μ_d: Reducing μ_d from the Base case value 0.46 to 0.44 gives about 25 % increase in the seismic moment. The relative sensitivity to the μ_d reduction is lower here than in the present-day case where the same reduction gives 80 % increase in seismic moment. One explanation to this difference can be that the entire ZFMA2 plane is ruptured in the endglacial case. This means that the μ_d reduction gives only a minor increase in rupture area. In the present-day case, however, the rupture area is smaller since it does not cover the entire ZFMA2. Hence, in the present-day case the area expands downwards along ZFMA2 as μ_d is reduced.

- Background σ_H trend: The alternative trend of the background σ_H tested here (N125°E) means that ZFMA2 becomes less optimally oriented for slip. This is reflected in the source parameters. The seismic moment is reduced by approximately 25 % and the average stress drop is reduced by a similar amount.

- Background σ_h magnitude: The 43 % reduction of the background minor horizontal stress σ_h gives about 10 % lower average stress drop and seismic moment compared to the corresponding case with the Base case stress field. The modest alteration of the earthquake source in response to this considerable reduction in stress can partly be explained by the fact that the ZFMA2 orientation relative to the stress field means that σ_h has a minor importance relative to that of the major horizontal stress σ_H. Another part of the explanation could be that close to the ground surface the endglacial stress additions are high relative to the background stresses (Fälth et al. 2015) and hence alterations in the background stresses may have limited impact.

- Hypocentre location: Relocation of the rupture initiation from HC1 to HC2 gives an increase in seismic moment and average stress drop of about 20 % and 10 %, respectively. As shown in Figure 6-1, HC2 is located closer to the western edge of ZFMA2 and hence farther away from the eastern edge. This means a longer rupture propagation distance to the eastern part of ZFMA2, with higher slip velocities and larger slip on this part of the fault plane as consequence (cf the discussion in Section 5.2.2).

- Discretisation: A comparison of the output from the models with different discretisation (Gen27-21_SH145_UM-EG_mud046, Gen27-21_SH145_UM-EG_mud046_f and Gen27-21_SH145_UM-EG_mud046_f2) indicates that the refinement of the discretisation tested here does not change the fault response more than marginally.

6.4.2 Secondary stress effects and target fracture shear displacements

In the following two subsections, secondary stress effects and target fracture displacements are presented. Of main interest are the target fracture displacements induced during the dynamic calculation step, but secondary stress effects generated during the quasi-static step are first presented. This could help to understand the distribution of the co-seismic target fracture displacements.

Quasi-static calculation step

The considerable shear displacements generated primarily on ZFMA2 during the quasi-static calculation step cause alterations of the stress field in the rock volume where the target fractures are located. This may influence the stability of the fractures and hence the amount of co-seismic fracture displacement that is induced during the following dynamic calculation step.

To examine how the stability of the fractures is influenced, *CFS* (Equation (1-1)) was calculated for virtual fracture planes (dip/dd = 27/141) within the target fracture region from continuum stresses at the end of the quasi-static calculation step. Given the endglacial stress field, fractures with this orientation would be optimally oriented for slip (cf Figure 4-6). The calculation was based on the stress output in the Gen27-141_SH145_UM-EG model. The results are shown in Figure 6-15. In Figure 6-16 the target fracture shear displacements generated in the same model are shown. The following can be observed:

- The gently dipping target fractures in the model are initially in a state of failure (positive *CFS*) (see Figure 4-6). Hence, they generate slip (Figure 6-16) and associated local stress relaxation during calculation. This is shown in Figure 6-15 as local reductions of *CFS* along the fracture planes. The increased *CFS* between the fractures along each row can be attributed to local stress alterations caused by the fracture displacements.

- At the farthest distance from ZFMA2, *CFS* between the target fracture rows is in the range 4-4.5 MPa. This corresponds approximately to the initial *CFS* for the fracture orientation assumed in the calculation before zone and fracture slip has taken place (cf Figure 4-6). This indicates that the stress redistribution caused by the quasi-static slip on the ZFMA2 zone has a modest impact at this distance.

- The displacements generated in the rock mass in response to the fault displacement give reduced vertical stresses in the central part of the target fracture region. This tends to destabilise gently dipping fractures. This is reflected by the increased *CFS* values (reaching about 5 MPa) (Figure 6-15) as well as larger target fracture displacements (Figure 6-16) in this part of the model.

- At the shortest distances from ZFMA2, *CFS* is reduced due to vertical stress increase and stress relaxations. The stabilisation is also reflected in the smaller fracture displacements (Figure 6-16).
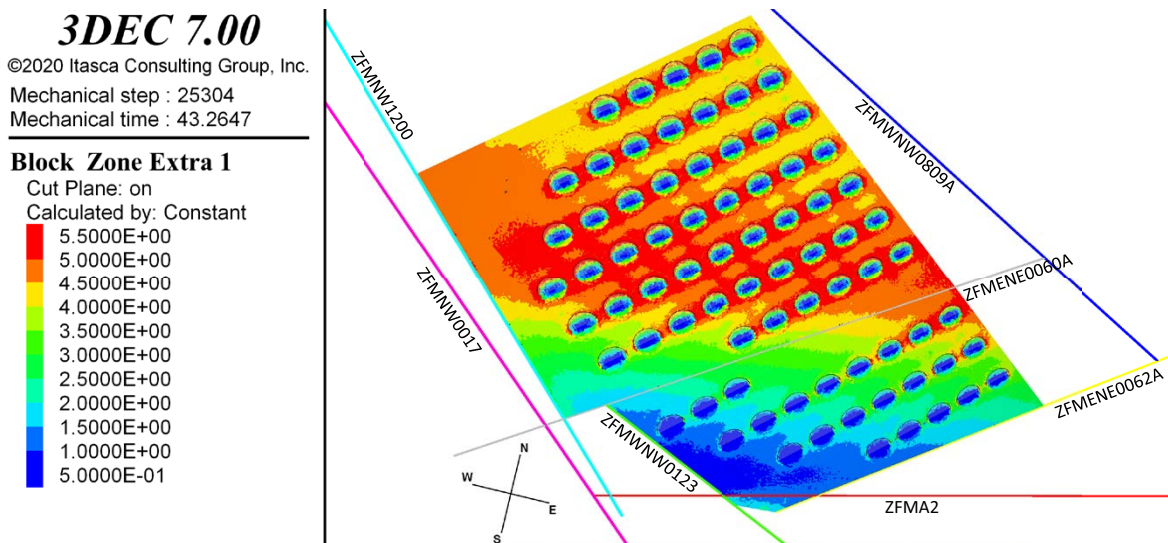
Figure 6-15. *Contours of CFS (MPa) (Equation (1)) calculated for virtual fracture planes from continuum stresses at the end of the quasi-static calculation step and shown on a horizontal projection plane at 470 m depth. The following was assumed in the CFS calculation: Hydrostatic pore pressure increased by 1 MPa, fracture (dip/dip direction) = (27/141) and µ = 0.7. Note how CFS has been reduced locally around the target fractures due to the slip that has been generated on those. The results were obtained from the Gen27-141_SH145_UM-EG model.*
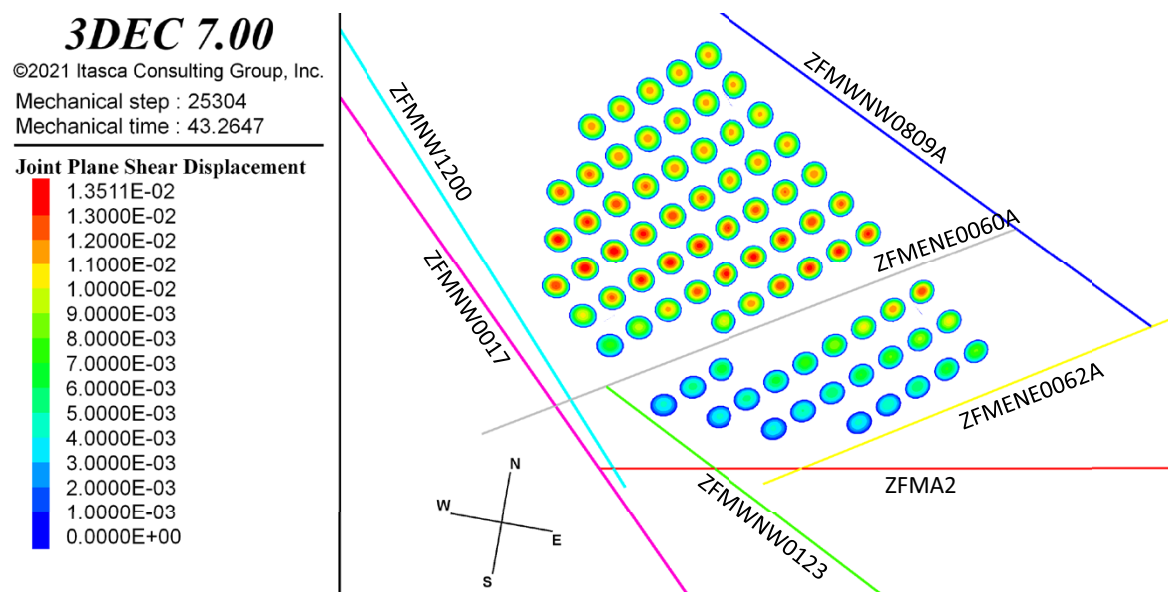

Figure 6-16. *Contours of target fracture shear displacements (m) generated during the quasi-static calculation step in the Gen27-141_SH145_UM-EG model.*

Dynamic calculation step

This section is divided into several subsections. To demonstrate how the stress transients that are generated by the primary fault rupture affect the target fractures, examples of stress evolutions and corresponding *CFS* evolutions are presented in the first subsection. In the next subsection, target fracture peak displacements for Base case assumptions are presented. In the subsections following that, the sensitivity of the induced fracture displacements to variations in model input is demonstrated. Recall that all displacements generated during the previous quasi-static calculation step are reset prior to rupture initiation. Hence, the displacements presented here are co-seismic only.

Stress effects

As seen in the results presented in the previous section, the stability of a target fracture at the time of earthquake rupture initiation, and hence its potential to generate slip, may depend on its position (recall that the stability is also a function of fracture orientation, cf Figure 4-6). For the fracture set considered in the previous section, there are slight differences in *CFS* on fractures at different positions after the quasi-static phase (Figure 6-15). When the rupture is initiated and propagates along the primary fault (here ZFMA2) stress waves are generated, primarily at the rupture front. Hence, the rupture front acts as a moving transmitter generating stress waves that will interact in a complicated way depending on e.g., the hypocentre location, the rupture front speed and on reflections at the ground surface. The timing and magnitude of the waves that hit a target fracture depend on the position of the fracture.

Figure 6-17 shows a map view of final target fracture displacements in the Gen27-141_SH145_ UM-EG model. To demonstrate how stress waves hit fractures at different positions and how these impact on the fractures, stresses were recorded in the model continuum at two positions between target fractures (Figure 6-17). Based on the temporal evolution of the stress tensor, shear- and normal stresses as well as the corresponding *CFS* was calculated for virtual fractures at these positions (cf Equation (1-1)). The *CFS* evolution could then be compared with the displacements that were generated on adjacent target fractures, i.e., fractures that are subjected to effectively the same stress histories as the virtual fractures. The *CFS* evolution based on continuum stresses can be seen as a measure of the potential for fracture slip at that position. Note that *CFS* values calculated based on the shear- and normal stresses on a slipping fracture would not exceed zero since all positive *CFS* would instead be "spent" on generating slip.

Figure 6-18 shows the stress-, *CFS*- and fracture displacement histories at the points and on the fractures indicated in Figure 6-17. The target fracture displacements were obtained from the Gen27-141_SH145_UM-EG model. In the *CFS* calculation it was assumed that the virtual fractures had dip and dip directions 27° and 141°, respectively, and that $\mu = 0.7$. First, it can be noted that the initial *CFS* values at both positions are positive (cf Figure 6-15). This indicates that fractures at these positions with the assumed orientation and friction coefficient would be unstable and slip. This is what has already happened on the nearby target fractures during the quasi-static calculation step (Figure 6-16). This means that the fractures are close to the stability limit and will slip if the initial load (*CFS*) is exceeded (As noted above, the quasi-static displacements are reset prior to the dynamic calculation step).

The stress waves generated by the earthquake rupture hit point #1 after about 0.7 s. There is a momentary drop in *CFS* after 0.8 s that is followed by a small peak (Figure 6-18a, cf Figure 6-19 and Figure 6-20). As *CFS* exceeds the initial (base line) value the nearby fracture slips. A similar process is found at point #2, but at a later time instance (Figure 6-18b). At point #2, the initial *CFS* is higher (cf Figure 6-15), but most important here is that the stress transients become stronger. The stronger transients appear to be caused by wave reflections at the ground surface (see Figure 6-18b, Figure 6-19 and Figure 6-20 at $t = 1.5$ s). The stronger transients lead to larger fracture displacement.

From the results presented here, it appears that, for an earthquake rupture occurring on ZFMA2, there will be a significant spatial variability of the stress waves within the projected repository volume. It also seems that this is the factor that mainly determines at which positions the potential for co-seismic secondary fracture displacements would be highest.
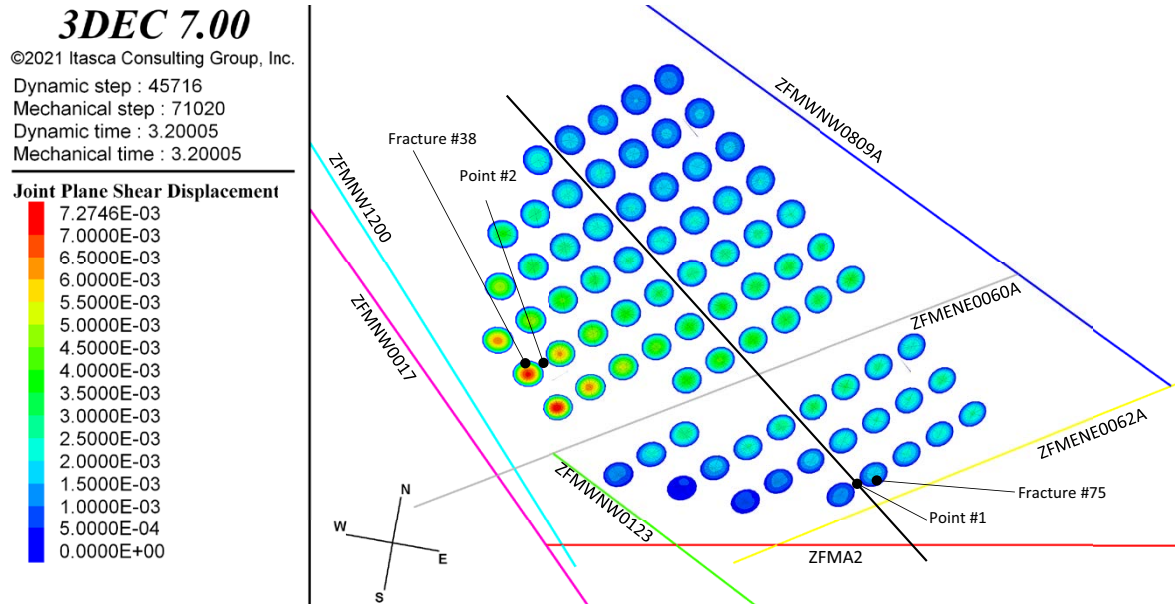

Figure 6-17. Map view showing target fracture displacements (m) at the end of earthquake rupture simulation in the Gen27-141_SH145_UM-EG model. Point #1 and point #2 indicate positions for stress monitoring. The fracture numbers are in accord with the numbering shown in Appendix B. The dashed line indicates the location of the vertical viewing plane for the CFS plots in Figure 6-19.
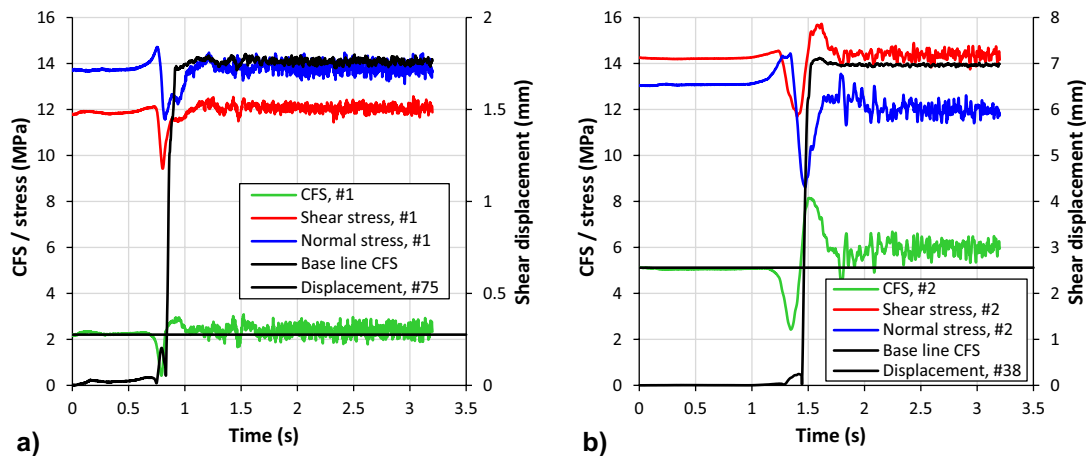
Figure 6-18. Temporal evolution of shear stress, normal stress and corresponding CFS on virtual fractures with dip/dd = 27/141 and μ = 0.7 plotted along with fracture displacements on nearby fractures in the Gen27-141_SH145_UM-EG model (cf Figure 6-17). a) Stress/CFS at point #1 and displacement on fracture #75. b) Stress/CFS at point #2 and displacement on fracture #38.
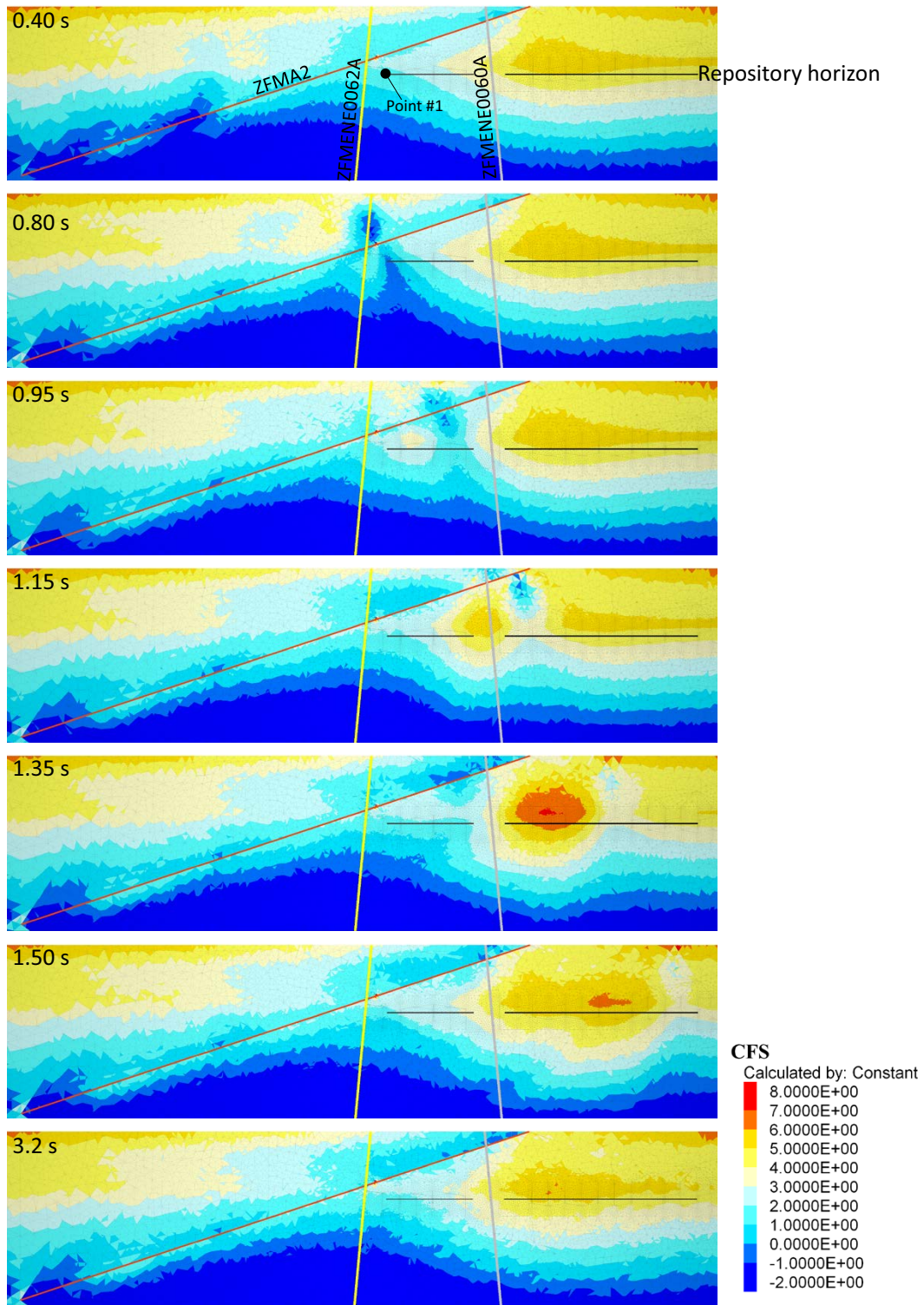
Figure 6-19. *CFS (MPa) on virtual fracture planes with dip/dd = 27/141 and μ = 0.7 at seven time instances. The last time instance is the final stage of the simulation. The CFS values are projected on the vertical viewing plane indicated in Figure 6-17 and Figure 6-20. The results were generated in an endglacial model with glued target fractures that generate no slip. Point #1 in the upper panel indicates position for stress monitoring (cf Figure 6-17).*
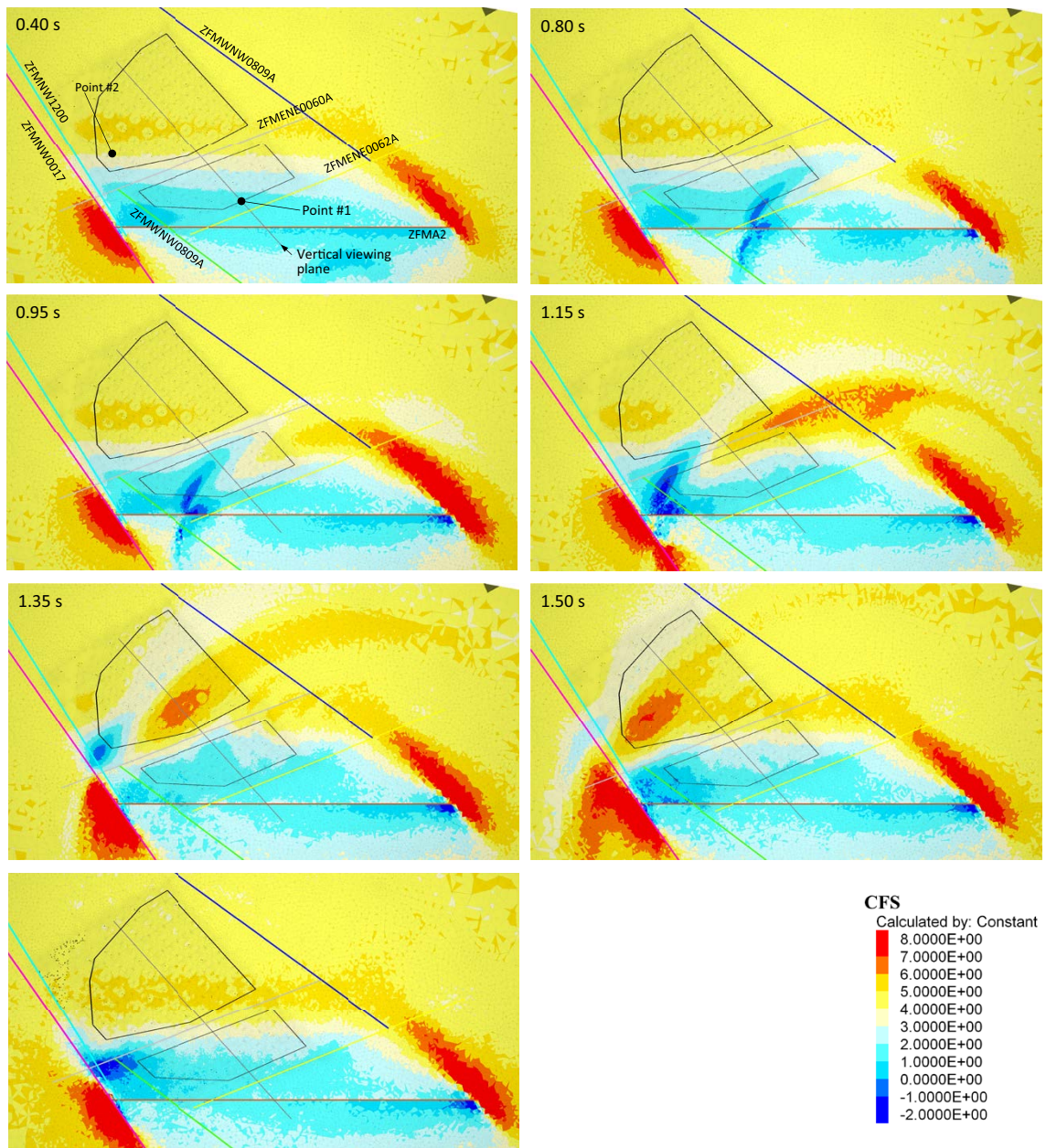
Figure 6-20. *CFS (MPa) on virtual fracture planes with dip/dd = 27/141 and μ = 0.7 at seven time instances. The last time instance is the final stage of the simulation. The CFS values are projected on a horizontal viewing plane at 470 m depth. The grey line indicates the location of the vertical viewing plane for the CFS plots in Figure 6-19. The results were generated in an endglacial model with glued target fractures that generate no slip.*

Fracture displacements – Base case assumptions

During the earthquake rupture simulation, the shear displacements at the target fracture centres are monitored and the peak displacements are stored. Peak target fracture displacements generated on a gently dipping fracture set at different distances from the ZFMA2 plane are shown in Figure 6-21 for present-day stress conditions. The largest displacements, which amount to about 5 mm, are generated at some 300–500 m distance where the initial stability tends to be lowest (cf Figure 6-15) and the co-seismic stress transients tend to be strongest (cf Figure 6-19, Figure 6-20).

The results shown in the following are obtained in the case with endglacial stress conditions. Peak target fracture displacements at different distances from the ZFMA2 plane are shown in Figure 6-22 for gently dipping and sub-horizontal sets (upper) as well as for steeply dipping sets (lower). The results are obtained for Base case assumptions. The distribution of displacements with distance follows the same trend as that shown in Figure 6-21, i.e., the largest displacements are found in the distance range 300 m to 500 m. The largest displacements amount to about 9 mm and are generated on the gently dipping sets with the lowest initial stability. Due to its high initial stability, the sub-horizontal set generates only negligible elastic displacements (Figure 6-22 upper, cf Figure 4-6). Among the steeply dipping sets there is one set on which the stability limit is exceeded, and actual slip is generated (Figure 6-22. lower). Besides this, the displacements are elastic and hence negligible. It is difficult to provide a detailed explanation to why these few steep fractures become unstable and slip. As indicated in Figure 6-19 and Figure 6-20, the stress wave pattern becomes complex, and the waves influence the stability of the target fractures differently depending on the fracture orientation and position. However, the tendency for larger displacements on fractures with lower initial stability is in accord with observations in previous similar studies (Fälth et al. 2016, Fälth et al. 2010).
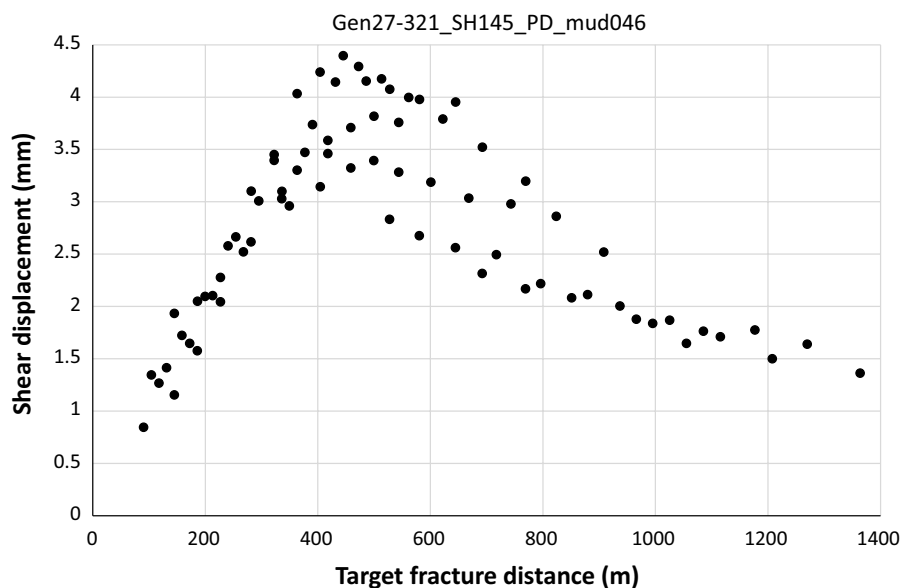

Figure 6-21. Target fracture peak displacements versus distance from ZFMA2 in the case with present-day stress conditions. The distances are measured from the centre of each fracture to the nearest point on the ZFMA2 plane (see also Appendix B).
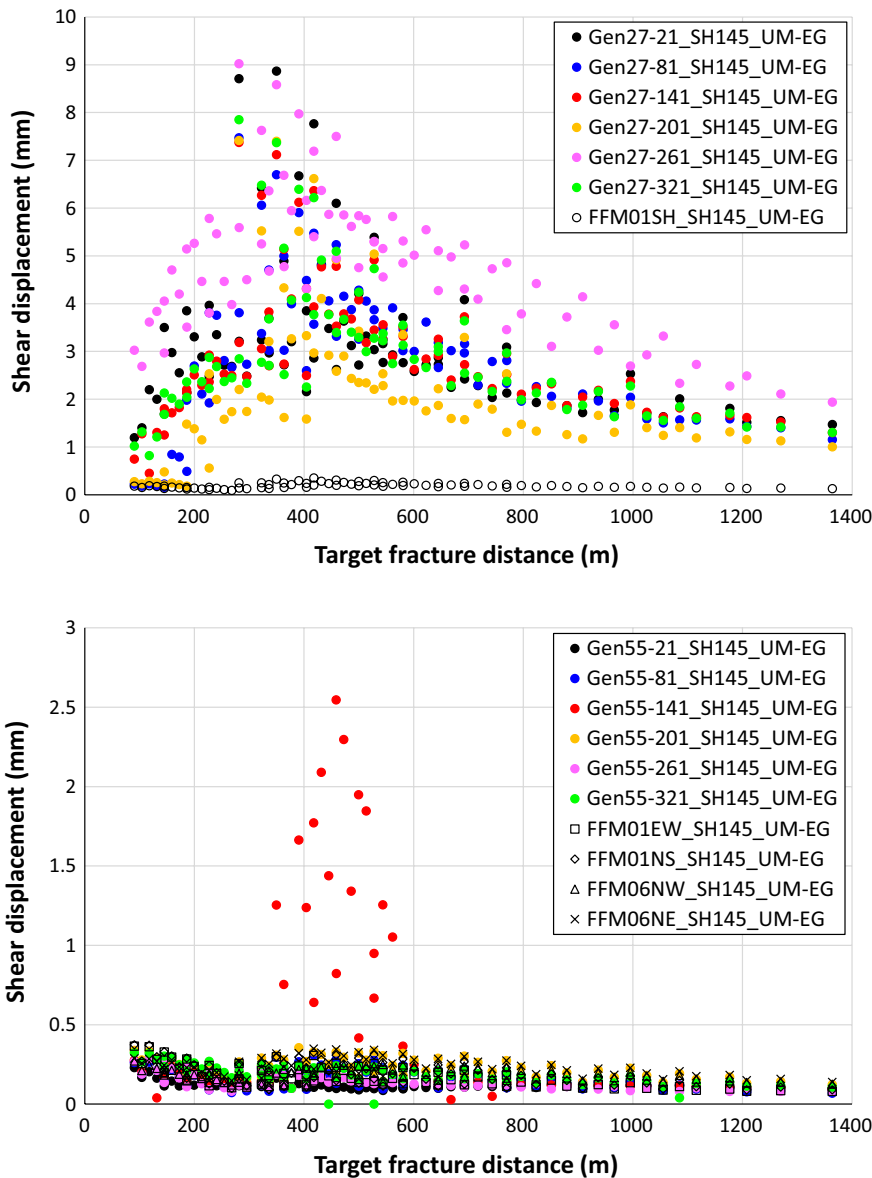
Figure 6-22. *Target fracture peak displacements versus distance from ZFMA2 in the endglacial case. Upper: Gently dipping and sub-horizontal sets. Lower: Steeply dipping sets. The distances are measured from the centre of each fracture to the nearest point on the ZFMA2 plane (see also Appendix B).*

The rheological properties of the bentonite buffer surrounding the canister are strain rate dependent (Börgesson et al. 2010). The resistance of the buffer against deformation is higher the higher the deformation rate. Hence, in the case of fracture shearing across a deposition hole, the forces generated in the buffer by the rock deformation will be higher and more effectively transferred to the canister in the case of a high fracture shear velocity. The risk for canister damage is higher if the displacement on the intersecting fracture takes place at a higher rate. The 50 mm canister damage criterion is based on results from simulations where it was assumed that the shear velocity on the intersecting fracture is 1 000 mm/s (Börgesson and Hernelind 2006, SKB 2011).

The upper diagram in Figure 6-23 shows target fracture peak shear velocities plotted versus distance from the ZFMA2 plane in six endglacial models. The target fracture shear velocities were derived from shear displacement histories using a sampling time interval of 0.01 s. Note that this interval is shorter than that used during the simulations when estimating shear velocities on the primary fault plane. A shorter time interval is used here to reduce the risk of underestimation of the velocities (cf the discussion in Section 6.4.1). The highest velocity amounts to some 200 mm/s, i.e., about 1/5 of the velocity assumed when the canister damage criterion was established. The distribution of velocity shows the same trend as that of the corresponding displacements (cf Figure 6-22, upper). This indicates that there is a correlation between displacement and velocity. The correlation is illustrated by the lower diagram in Figure 6-23.
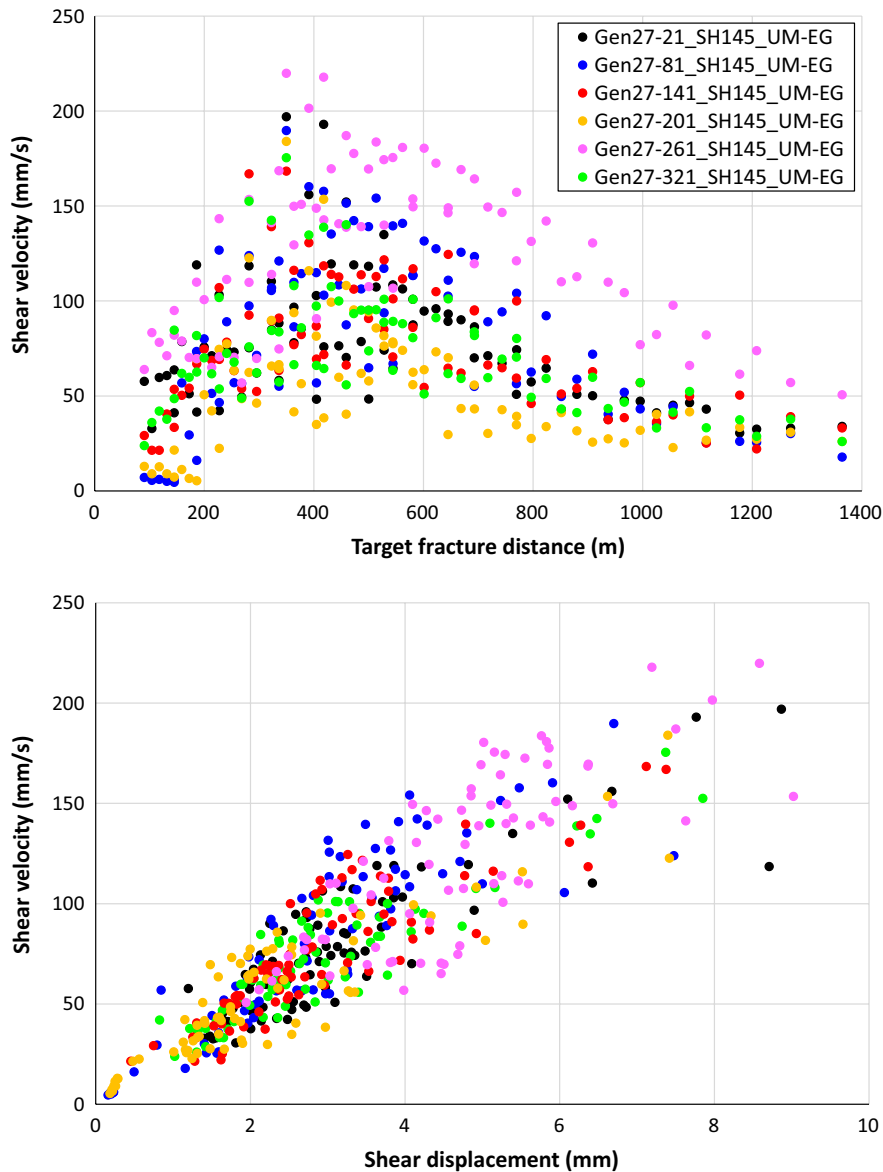

Figure 6-23. *Upper: Target fracture peak shear velocities versus distance from ZFMA2 in six endglacial simulation cases. The distances are measured from the centre of each fracture to the nearest point on the ZFMA2 plane (see also Appendix B). Lower: Target fracture peak shear velocity versus fracture peak shear displacement in the same six models.*

Fracture displacements at short distances

Figure 6-24 shows peak target fracture displacements generated in the models where fractures were located close to and even in contact with the slipping ZFMA2 zone. The upper row shows results from the model variant without any explicit representation of the deformation zone width, i.e., no damage zone surrounding the slip plane was included. This corresponds to the assumption made in all other models discussed above. The two lower rows in Figure 6-24 show results from the models where a 50 m wide damage zone was modelled using a Mohr-Coulomb material model. Two assumptions of the rock mass friction coefficient were tested, $\mu = 0.7$ and $\mu = 0.78$. The lower value corresponds to the value suggested in the Forsmark rock mechanics site report (Glamheden et al. 2007) while the higher value is the value assigned as static friction coefficient μ_s in the simulation of the dynamic earthquake rupture (cf Section 4.3). The following can be observed:

- In general, the displacements induced at 100 m and 150 m distance in the case without damage zone (Figure 6-24, upper) are similar to the displacements induced at the same distances in the Base case models (Figure 6-22). Gently dipping fractures move some 5 mm, at maximum, while more steeply dipping and horizontal fractures, which tend to be more stable, generate only insignificant displacements. Closer to the zone and inside the zone, the displacements increase. For gently dipping fractures the largest displacement becomes about three times the largest displacement generated at 100 m distance from the fault slip plane.

- The displacements generated at 100 m and 150 m distance in the case with the damage zone included agree well with the corresponding displacements generated in the case without damage zone (cf Figure 6-24 (upper) and Figure 6-24 (middle, lower)). This indicates that the way the deformation zone is modelled has minor importance for fracture displacements that are generated outside the zone. A similar observation can be made in the corresponding results by Fälth et al. (2019) who also examined simulation cases with an explicitly modelled damage zone.

- For fractures at 0 m and 50 m distance, including the damage zone may have a significant impact on the displacement. For instance, the displacement on the fracture at 0 m belonging to the GEN 27/141 set increases from 15 mm to 30 mm when the damage zone is included (cf Figure 6-24 (upper) and Figure 6-24 (lower)). Likewise, at 50 m distance the displacement on the GEN 55/81 fracture increases from about 3 mm to 16 mm. Note, however, that fractures that have no mechanical contact with the damage zone and/or the slip plane are nearly unaffected (GEN 27/141 and GEN 27/201 at 50 m distance).

- The tendency is that a lower friction coefficient of the damage zone gives larger secondary fracture displacements (cf Figure 6-24 (middle) and Figure 6-24 (lower)). However, the reduction of the friction coefficient from 0.78 to 0.7 has, in general, smaller impact than including the damage zone (i.e. changing from $\mu =$ infinite to $\mu = 0.78$).
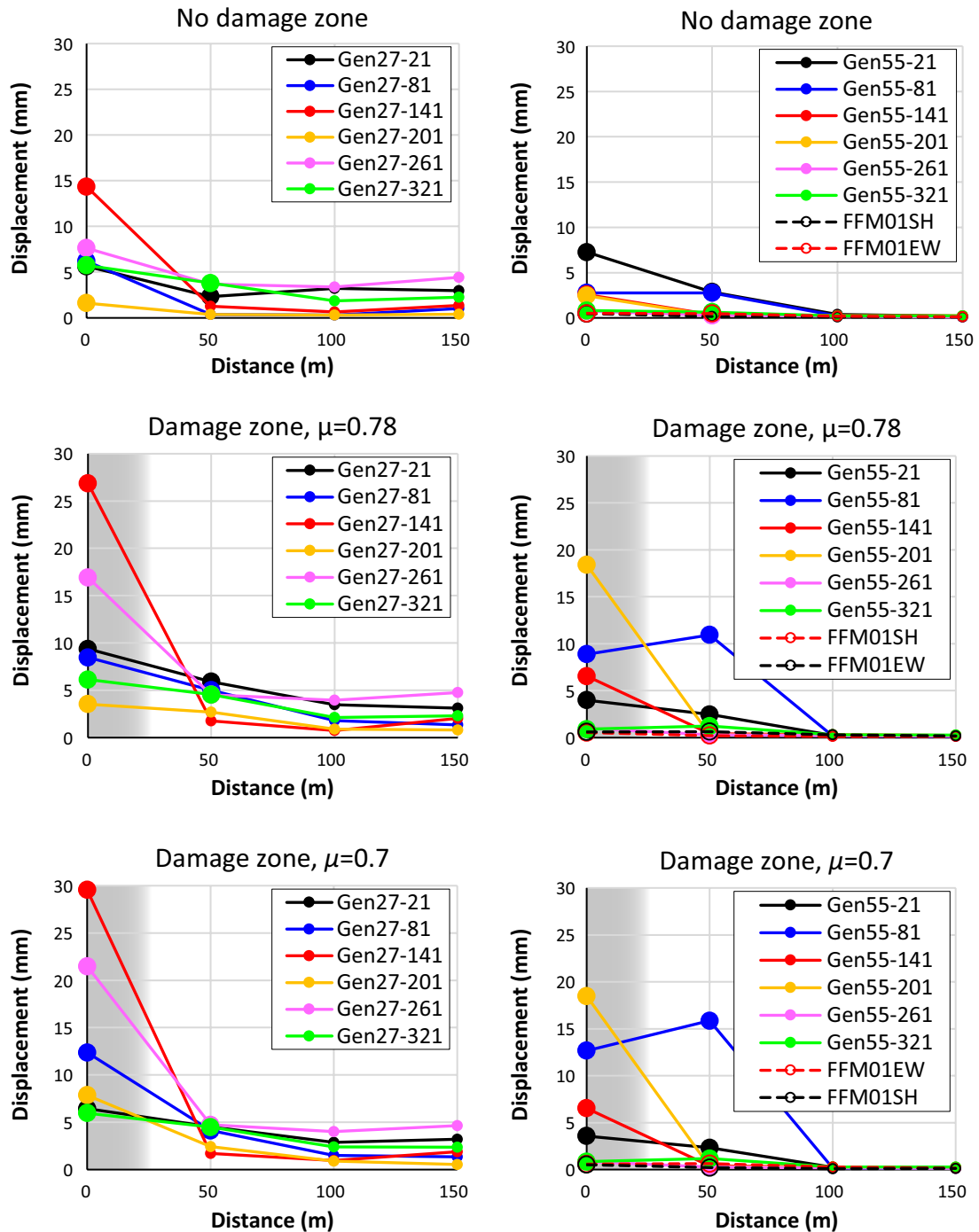
Figure 6-24. *Target fracture peak shear displacements versus distance from the ZFMA2 slip plane to target fracture centre. Note that the four distances correspond to the target fracture centre locations, but the peak displacement may take place at another location on the fracture. An enlarged plot symbol indicates that some part of the fracture is in contact with the damage zone and/or the slip plane (cf Figure 6-2). The shaded region indicates the extent of the damage zone. The left column shows results for gently dipping fractures and the right column shows results for steeply dipping and horizontal fractures. Upper: No damage zone included (elastic). Middle: Damage zone with μ = 0.78. Lower: Damage zone with μ = 0.7.*

Sensitivity to hypocentre location

As noted above, the mode and magnitude of the stress waves hitting the target fractures depend on the location of the rupture initiation point. Figure 6-25 shows induced target fracture displacements for the case with rupture initiation at HC1 (Base case) along with results from the case with initiation at HC2. The results for the three target fracture sets that have been examined here show that the induced displacements are reduced at some locations and for some fracture orientations whereas other combinations of location and orientation mean increased displacements. Under all circumstances, the results indicate that the effect of this movement of the hypocentre is significant in relative terms at some positions, but in absolute terms, the effect is modest and the differences in displacements amount to a few mm.
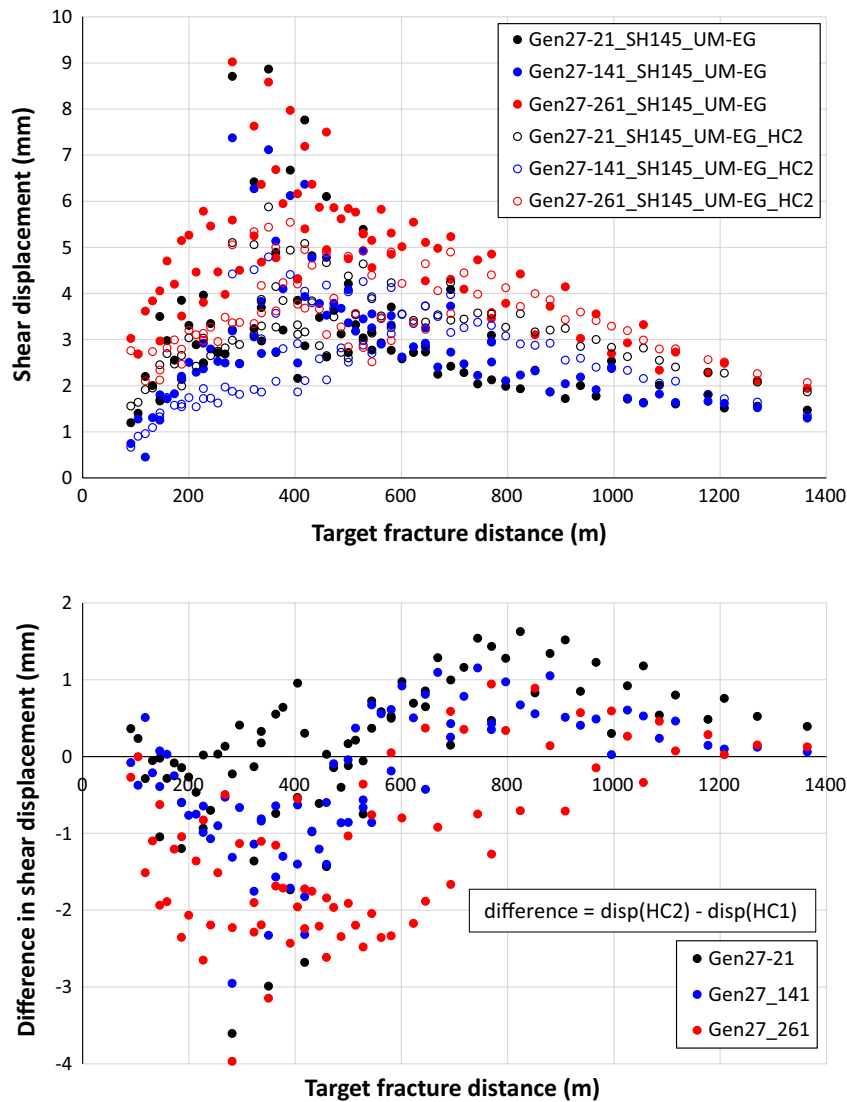

Figure 6-25. Upper: The effect on target fracture displacements of moving the earthquake rupture initiation from HC1 to HC2 (cf Figure 6-1). Lower: Same results as in the upper diagram but here the differences in displacements are shown. The distances are measured from the centre of each fracture to the nearest point on the ZFMA2 plane (see also Appendix B).

Sensitivity to a lower primary fault dynamic friction coefficient μ_d

As shown above, assigning a lower value of the dynamic friction coefficient μ_d to the rupturing primary fault means that a stronger seismic source with larger stress drop and larger slip is simulated. In the case where present-day stress conditions are assumed, the lowest μ_d value tested here ($\mu_d = 0.44$) gives an increase in seismic moment M_0 of about 80 % relative to that generated when applying the Base case value $\mu_d = 0.46$. In Figure 6-26 the target fracture peak displacements for the three present-day cases are shown. The cases with lower μ_d values generate (with a few exceptions) systematically larger secondary fracture displacements. However, the largest difference in fracture displacement between the $\mu_d = 0.44$ and $\mu_d = 0.46$ cases is modest and becomes about 4 mm. The largest displacement reaches about 7 mm.

The corresponding results for the endglacial case are shown in Figure 6-27. Here, the μ_d reduction from 0.46 to 0.44 gives about 25 % increase in M_0 and the reduction to 0.43 gives about 50 % M_0 increase (Table 6-2). These reductions have a minor impact on the secondary displacements, relative to their impact in the present-day case (cf Figure 6-26 and Figure 6-27). All changes in fracture displacement in response to the changes in μ_d tested here are very modest and less than 1 mm at most positions. At the shortest distances, the stronger seismic source tends to give slightly larger displacements, as could be expected, but at longer distances the displacements are reduced at most locations.
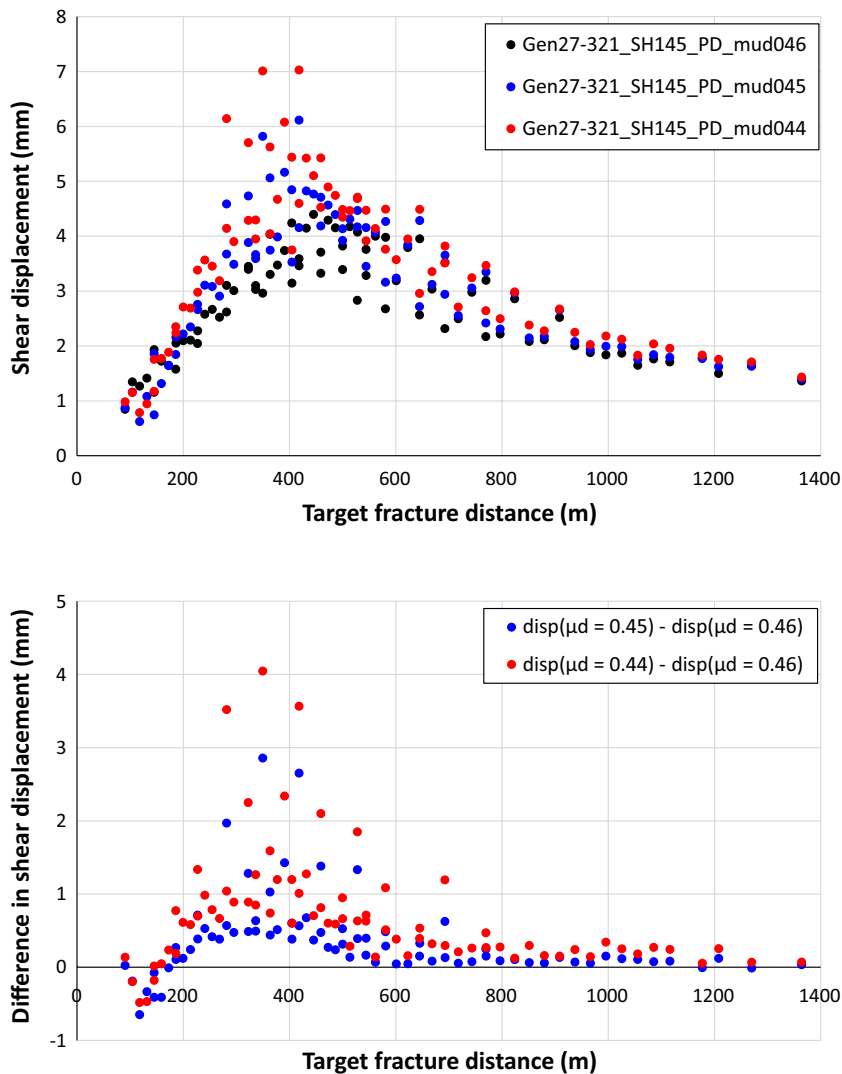

Figure 6-26. *Upper: Target fracture peak shear displacements for different values of primary fault dynamic friction coefficient μ_d in the case with present-day stress conditions. Note that $\mu_d = 0.46$ is the Base case value (cf Figure 6-21). Lower: Same results as in the upper diagram but here the differences in displacements are shown. The distances are measured from the centre of each fracture to the nearest point on the ZFMA2 plane (see also Appendix B).*

To summarise, in the present-day case there is a systematic increase in fracture displacements while the endglacial case gives more subtle changes and even displacement reductions in places. The difference in sensitivity to μ_d variations between the present-day and endglacial cases may be attributed, at least partly, to the larger difference in M_0 in the present-day case. In particular, as pointed out earlier, the μ_d reduction leads to a more pronounced increase in rupture area in the present-day case. This leads to a more significant alteration of the primary fault rupture dynamic evolution and hence more significant alterations of the secondary stress effects.
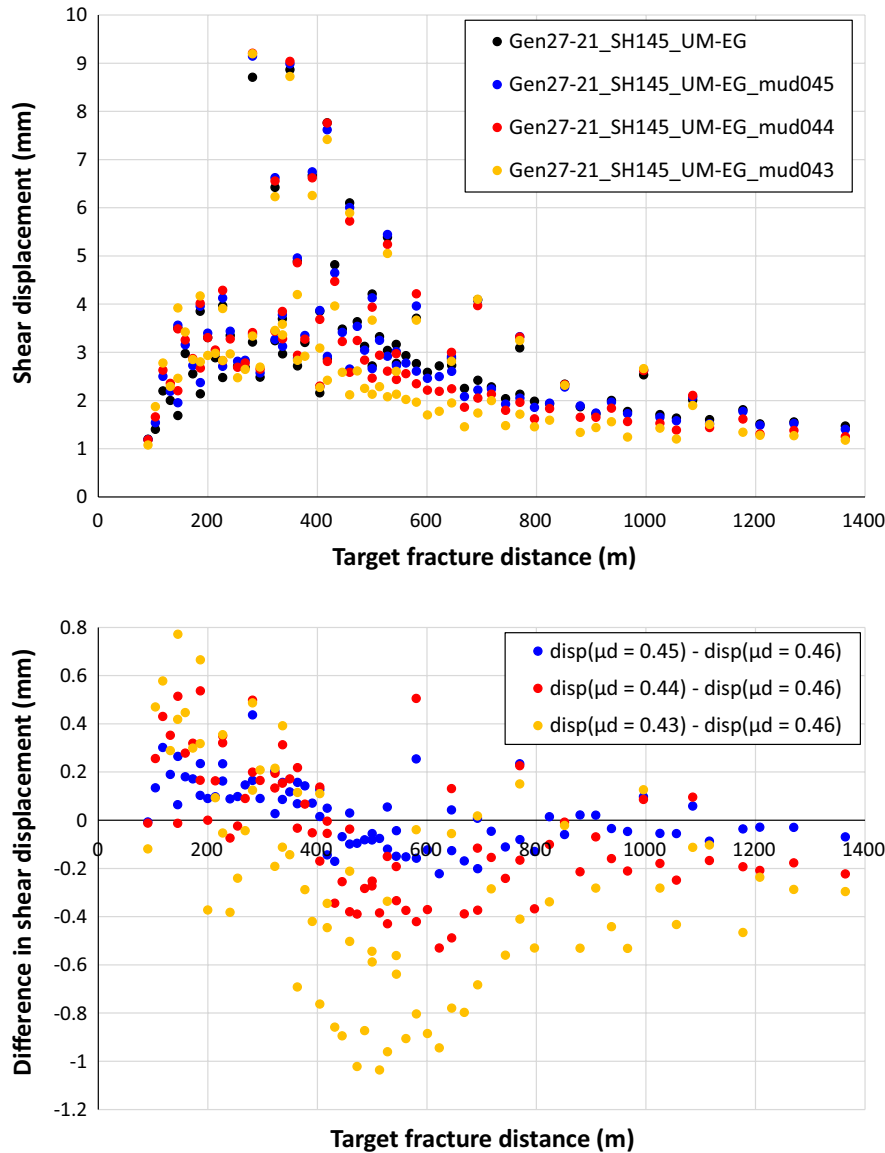

Figure 6-27. *Upper: Target fracture peak shear displacements for different values of primary fault dynamic friction coefficient μ_d in the case with endglacial stress conditions. Note that the Base case value $\mu_d = 0.46$ is applied in the Gen27-21_SH145_UM-EG model. Lower: Same results as in the upper diagram but here the differences in displacements are shown. The distances are measured from the centre of each fracture to the nearest point on the ZFMA2 plane (see also Appendix B).*

Sensitivity to the background *σH* stress trend

The sensitivity of the secondary displacements to a change in the background stress orientation is examined for the endglacial case. In addition to the Base case σ_H stress trend N145°E, an alternative trend of N125°E is tested for three fracture orientations. The results are shown in Figure 6-28. For most fracture orientations and locations, the displacements are reduced when applying the N125°E. This can be attributed to the change in fracture stability that comes from the change in stress field, but also to the reduction of the earthquake moment magnitude (see Table 5-2). In general, this change in stress field gives modest differences in the secondary displacements. In about 80 % of the cases, the differences are smaller than 1 mm and no difference exceeds 4 mm.
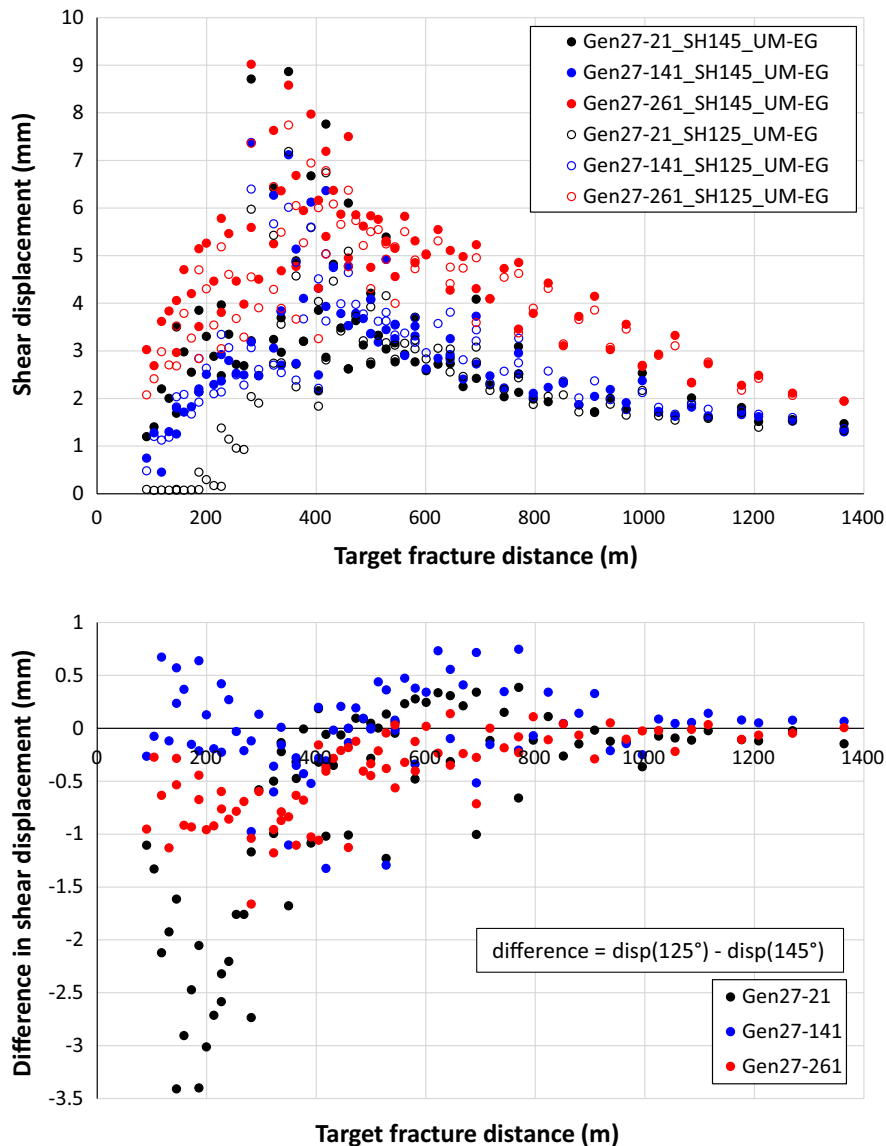

Figure 6-28. Upper: Target fracture peak shear displacements in the endglacial case for different trends of the background major horizontal stress σ_H. Lower: Same results as in the upper diagram but here the differences in displacements are shown. The distances are measured from the centre of each fracture to the nearest point on the ZFMA2 plane (see also Appendix B).

Sensitivity to the background σ_h stress magnitude

The potential effect of having a lower magnitude of the background minor horizontal stress σ_h is examined. A lower σ_h means a higher stress anisotropy in the horizontal plane and a lower normal stress on steep fractures with dip directions parallel or sub-parallel with the direction of σ_h. Here, to obtain a clear model response, a bounding case is tested. The background σ_h is reduced such that it becomes equal to σ_v at depths above 2 km (see Section 2.2.1). Hence, a strike-slip background stress field is applied in this depth range. This is done for three target fracture orientations that are considered particularly sensitive to this change in stress field.

The results are presented in Figure 6-29 along with the corresponding Base case results. For two out of the three fracture sets the σ_h reduction has a negligible effect. For the GEN 55/201 set, however, the effect is significant. The stress reduction means that the fractures in this set become unstable and slip. The largest displacement is still modest, about 5 mm, and the displacement-distance relation is qualitatively similar to that found for other slipping sets (see e.g. Figure 6-22).

Sensitivity to the rock mass Young's modulus

As noted in Section 1.6, given that elastic conditions can be assumed, the resulting shear displacement on a fracture scales inversely with the shear modulus of the surrounding rock mass (Eshelby 1957). This holds for quasi-static displacements. To examine if this scaling seems to be relevant also for the dynamic case simulated here and to see how local variations of the rock mass stiffness may affect induced secondary fracture displacements, a case with reduced Young's modulus E in volumes surrounding certain target fractures is simulated (Figure 6-30). Young's modulus is reduced by 30 % and since the shear- and bulk moduli are linearly dependent on Young's modulus, these are reduced correspondingly. Seismic velocities scale as $V \sim \sqrt{E}$. Hence, the reduction of E made here corresponds to a reduction of the seismic velocities by about 16 %.

The map view in Figure 6-30 shows the fracture displacements in the Gen27-21_SH145_UM-EG_ LowY model with reduced rock mass modulus normalised to the corresponding Base case displacements. Outside the low-modulus volumes the fracture displacements are in general unaffected, except for the displacements at a few locations near the low-modulus volumes. On these fractures the displacements are increased by a few percent (20 % on one fracture indicated by an arrow in Figure 6-30). The displacements on the 11 fractures inside the low-modulus regions are increased significantly. The largest increase is 43 %, but on average the displacements are increased by 30 %, i.e., in accordance with the assumed reduction in Young's modulus.

The results indicate that the modulus-displacement scaling seems to hold approximately for a case where a fracture is subjected to a dynamic load. Furthermore, the results suggest that the contribution from the uncertainty in the rock mass stiffness to the overall uncertainty in the simulation results should correspond to the reported uncertainty in the rock mass stiffness at Forsmark. In other words, the uncertainty in the rock mass stiffness reported for Forsmark amounts to a few percent (Glamheden et al. 2007), and hence this amount of uncertainty could possibly be added to the simulated fracture displacements. Note, however, that this should hold provided that the variations in modulus can be expected to be on such a length scale that large fractures are systematically surrounded by low-stiffness rock, as simulated here. If the variations are on a smaller scale, the impact on potential fracture displacements will be weaker. Calculations by Bürgmann et al. (1994) indicate that the size of a low-stiffness inclusion intersected by a fracture must be of the same order as the size of the fracture, and its stiffness must be tens of percent lower than the stiffness of the surrounding rock mass, for the displacement of that fracture to increase more than 20 %.
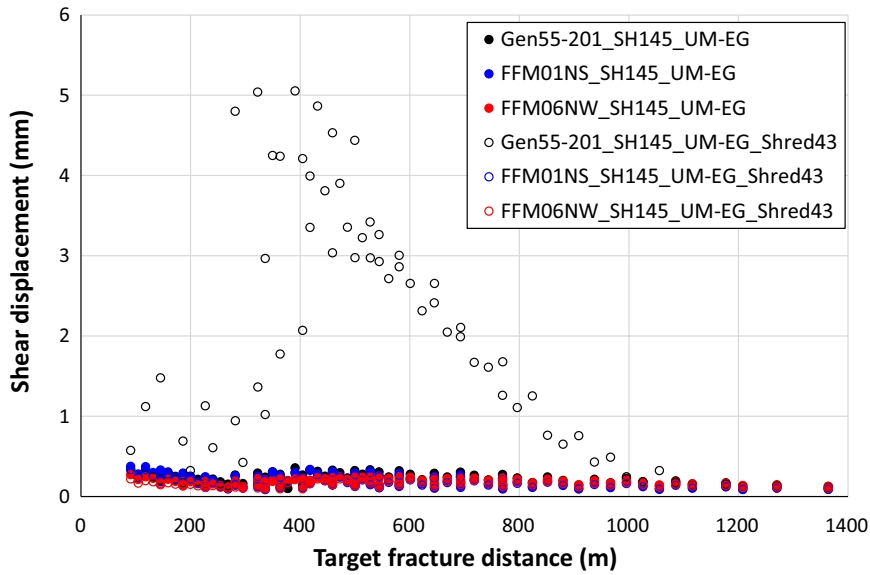
Figure 6-29. *Target fracture peak shear displacements in the endglacial case for different magnitudes of the background minor horizontal stress σ_h. The distances are measured from the centre of each fracture to the nearest point on the ZFMA2 plane (see also Appendix B).*
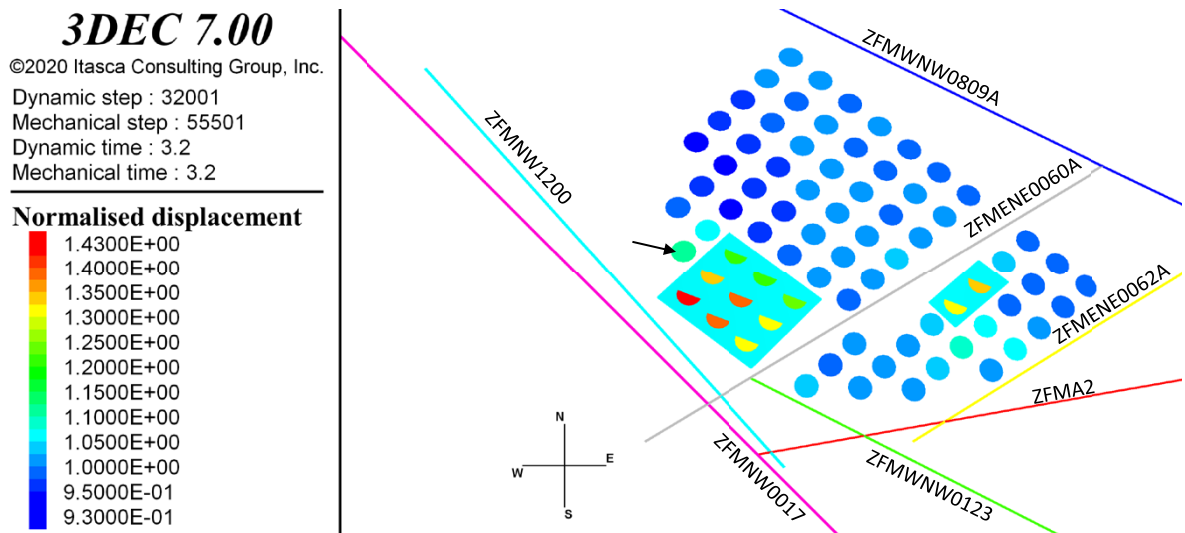

Figure 6-30. *Map view showing target fracture peak shear displacements in the case with reduced rock mass deformation modulus (Gen27-21_SH145_UM-EG_LowY model) normalised to the corresponding Base case displacements. The light blue areas indicate the two volumes where the deformation modulus is reduced. The arrow indicates a fracture outside the low-modulus volume on which the displacement increased about 20 %.*

Sensitivity to pore pressure coupling

The basic assumption in the simulations presented here is that no pore pressure coupling is considered. The impact on the simulated fracture displacements of a pore pressure coupling is examined. The effect of pore pressure variations on the fractures is modelled as described in Section 6.2 and the value of Skempton's coefficient is set to $B = 0.5$. This was done for two generic fracture orientations.

Figure 6-31 shows fracture displacements in the case with pore pressure coupling normalised to the corresponding Base case results. The results show that the pore pressure coupling leads to a small but systematic reduction in displacement on fractures that lose stability and slip. On most of the fractures in the Gen55_141 set, only insignificant elastic displacements are generated (cf Figure 6-22). On these fractures the pore pressure coupling is of no importance. For fractures that slip, the reduction can be understood from the following. According to the model for pore pressure coupling adopted here, the change in pore pressure scales linearly with the change in average stress, with Skempton's coefficient as proportionality constant (Equation (6-2)). Hence, an increase in average stress leads to an increase in pore pressure, and vice versa. When the average stress around a target fracture is reduced by an arriving wave, this is typically accompanied by a reduction of the normal stress on the fracture. The reduction of normal stress promotes instability and corresponding fracture slip. However, if pore pressure coupling is considered, the pore pressure on the fracture will also be reduced. This will dampen the reduction of the effective normal stress on the fracture and thus contribute to maintaining fracture compression and stability. In the Base case, where the pore pressure is assumed to be constant, this damping does not take place.

Given that the model for pore pressure coupling adopted here can be regarded as reasonably relevant, the results indicate that the Base case assumption of zero pore pressure coupling contributes to overestimated rather than underestimated secondary fracture displacements.

Sensitivity to target fracture friction coefficient

The sensitivity to variations in the target fracture frictional strength was tested for two generic (Gen27-261, Gen55-141) and two site-specific (FFM01NS, FFM06NE) target fracture sets. As indicated in Figure 4-6, the site-specific fractures, which are steeply dipping, have considerable initial stability margins, given the base case assumption of friction coefficient $\mu = 0.7$. The fractures with generic orientations are less steep and thus more prone to slip.

The difference in initial stability is reflected in the results. For the two site-specific fracture sets, the variation in friction coefficient evokes no difference in response. None of the fractures in these sets become unstable and slip for any of the friction coefficient values tested here.
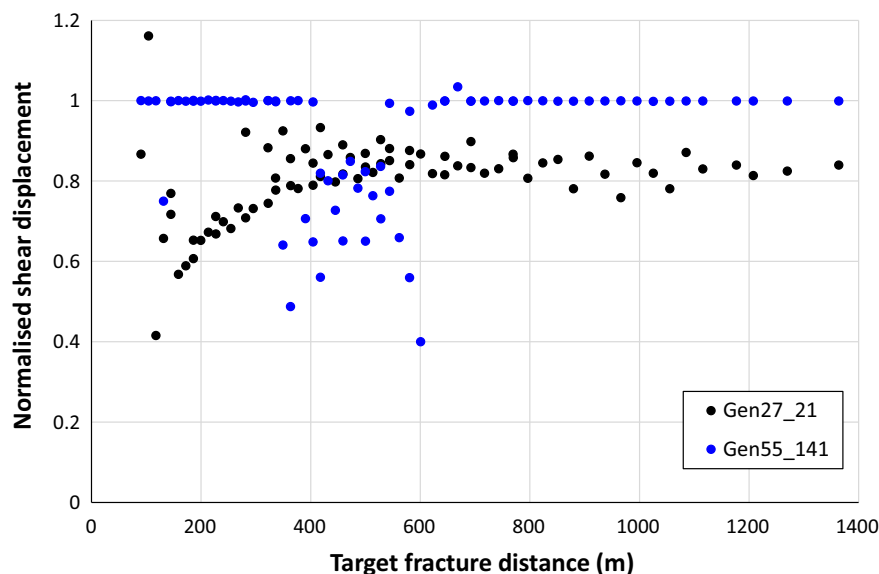

Figure 6-31. *Target fracture peak shear displacements in the case with pore pressure coupling normalised to the corresponding Base case results. The distances are measured from the centre of each fracture to the nearest point on the ZFMA2 plane (see also Appendix B).*

For the Gen55-141 set, where only a few fractures slip in the region with strongest secondary effects when applying base case friction (Figure 6-22, lower), the increase to $\mu = 0.8$ has a negligible effect (Figure 6-32, lower). The same fractures become unstable and slip, but by slightly smaller amounts. The reduction to $\mu = 0.6$, however, leads to a reduction of the initial stability, but most of the fractures remain stable during the quasi-static calculation step. During the following dynamic calculation step, the reduced stability and associated increase in sensitivity to load changes lead to the seismic waves inducing slip on almost all fractures, with a significant increase in the co-seismic displacements as consequence.

The gently dipping fractures in the Gen27-261 set are less sensitive to variations in friction coefficient than the more steeply dipping fractures are. The change in displacement in response to the variation in friction coefficient is modest and of no practical importance (Figure 6-32, upper). It can be noted, though, that for some fractures the strength variation tends to give counterintuitive results; a reduction in friction coefficient gives reduced displacement, and vice versa. This can be attributed to the fracture slip that takes place prior to the initiation of the earthquake rupture. With a lower friction coefficient, the pre-slip tends to be larger, and thus more stresses are relaxed around the fracture. The larger stress relaxation leaves less strain energy left to be released when the co-seismic stress waves arrive, and the co-seismic displacement may be reduced. Such a dependence on fracture friction coefficient was also observed in the simulations performed by Fälth and Hökmark (2012).
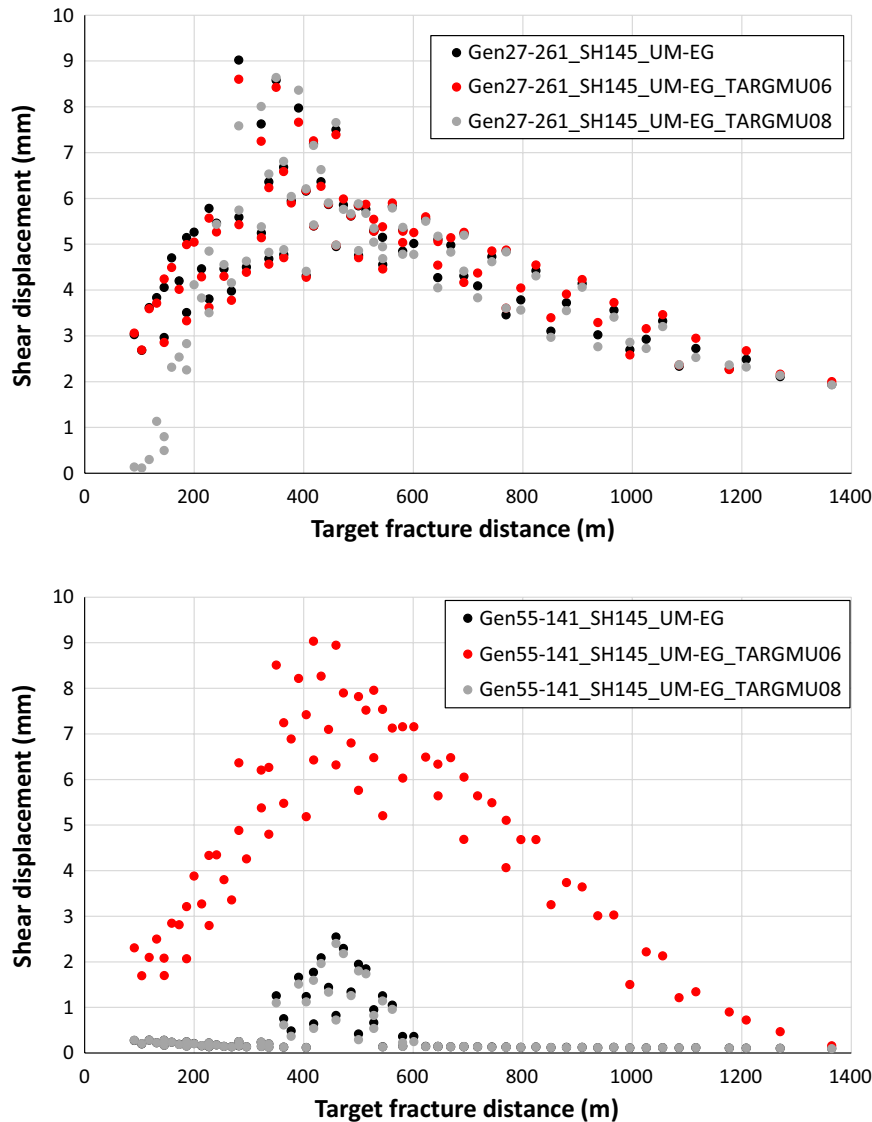

Figure 6-32. Target fracture peak shear displacements generated in cases with alternative values of fracture friction coefficient. The results are plotted along with the corresponding Base case results. The distances are measured from the centre of each fracture to the nearest point on the ZFMA2 plane (see also Appendix B).

Sensitivity to model discretisation

The influence of the numerical model discretisation, i.e., the edge lengths of the finite difference elements, is examined by running two simulations where the discretisation is refined. In these models the average edge length is set to be 80 % and 60 %, respectively, of that in the Base case model. This reduction is made in the central part of the model containing the deformation zone planes and the target fractures. In the Base case model, the edge length in the target fracture volume corresponds to 12 finite difference element edge lengths per target fracture diameter ($N = 12$). The corresponding values for the 80 % and 60 % cases are $N = 16$ and $N = 20$, respectively.

Figure 6-33 shows target fracture displacements in the 80 % and 60 % (Gen27-21_SH145_UM-EG_f and Gen27-21_SH145_UM-EG_f 2) models normalised to the corresponding Base case results (Gen27-21_SH145_UM-EG model). The reduction to 80 % edge length gives about 4 % increase in displacement, on average, while the reduction to 60 % length gives about 6 % average increase. This sensitivity to the model discretisation is in general agreement with the sensitivity observed by Fälth et al. (2019).

As can be noted in Figure 6-33 there are several fractures on which the increase becomes 10 % and more. It should be pointed out, however, that all displacements are small and so are the differences in absolute terms. All fracture displacements generated in the models reported in Figure 6-33 are less than 9.5 mm and no increase exceeds 0.5 mm.
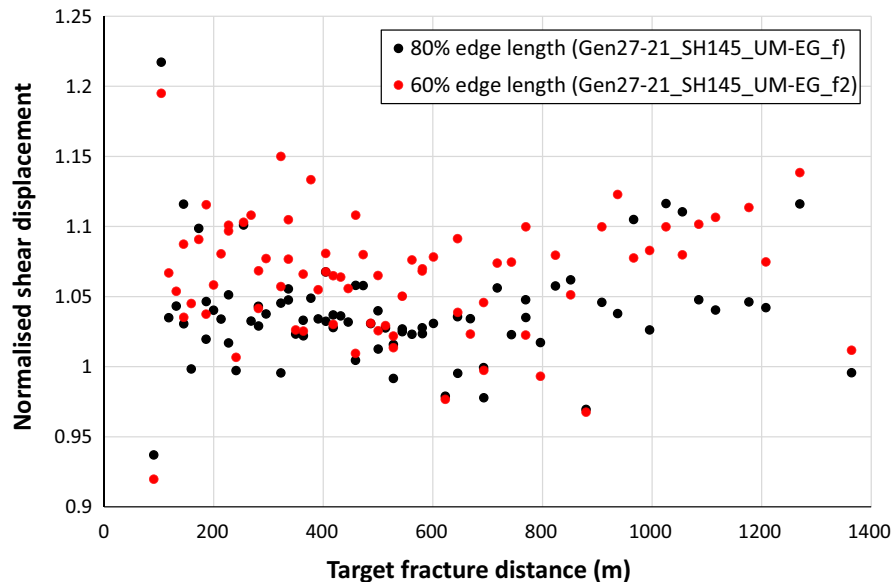

Figure 6-33. *Target fracture peak shear displacements in the two models with reduced finite difference element sizes normalised to the corresponding displacements in the Base case model. The distances are measured from the centre of each fracture to the nearest point on the ZFMA2 plane (see also Appendix B).*

7 Discussion

7.1 General

The issues addressed in this work, i.e., deformation zone stability and secondary fracture displacements, depend on complex processes that evolve during long periods of time and that may have considerable spatial variations. For instance, the temporal evolutions and the spatial extents of future ice loads as well as the associated pore pressure effects and glacially induced stresses are genuinely uncertain. There are also uncertainties associated with the site-specific input data, such as the geometries and mechanical properties of deformation zones and fractures, the properties of the rock mass, and the magnitudes and orientations of the background stresses. In addition, when setting up a model, the complexities of the real problem cannot be represented in detail. Simplifications almost always must be made, but in a way such that the essence of the problem is still captured.

A consequence of the uncertainties and of the model simplifications is that the simulated secondary fracture displacements reported here should be regarded to be approximate estimates rather than exact quantifications. The input parameter variations that are made in this work are intended to help when setting bounds to the uncertainties in the results.

The following subsections contain a discussion of the relevance and validity of the modelling assumptions that are made here. There is also a discussion about how the simulated earthquake source parameters relate to those estimated for real events, as well as a discussion about how the simulated endglacial target fracture displacements relate to those generated in the previous Forsmark study by Fälth et al. (2016).

7.2 Relevance and validity

7.2.1 Stress field and timing of earthquake rupture

The *CFS* calculations made here show that the stability of the steep deformation zones at Forsmark tends to be lowest close to the ground surface under forebulge stress conditions. The result confirms what can be observed in the stability estimates made by Hökmark et al. (2019) (Figure 1-5). The results in Figure 1-5 show that having the lowest stability close to the surface is a general trend that holds also for present-day and endglacial conditions. In addition, close to the surface, where the background stresses are lowest, the relative importance of the glacial stress changes is the highest. The average of the horizontal glacial stress changes during the forebulge is 8 % of the Base case average horizontal background stress magnitude at 500 m depth, while at 1 500 m and 2 500 m depths, the corresponding numbers are 4 % and 3 %, respectively. For the glacial stress additions applied in the endglacial phase, the corresponding numbers are 29 %, 15 % and 11 %, respectively.

Since the stability tends to be lowest at shallow depths, the stress conditions at these depths are of particular importance for the analyses made here. From the results of the calculations and simulations made here, it appears that it is the stress field above about 1 km depth which is the most critical for the stability of the steep zones. It can also be noted that the ZFMA2 zone, which is the least stable of all Forsmark zones, extends to some 1.5 km depth. Hence, the stress field close to the surface is most critical also for this zone. Altering the magnitudes of the components in the background stress field at these depths clearly changes the estimated potential for faulting.

Out of the three background stress fields tested here (Figure 2-1), the Base case stress field is regarded to be the most relevant since it is in general accordance with the most likely stress field reported for Forsmark down to about 1 km depth (Glamheden et al. 2007, Martin 2007). The case with 11 % σ_h reduction yields a σ_H-to-σ_h ratio at repository depth that is in the upper end of the range reported for Forsmark (Glamheden et al. 2007). Hence, given the present understanding of the stress conditions at Forsmark, it seems unlikely that higher σ_H-to-σ_h ratios than those generated by the 11 % reduction stress model are found at Forsmark. The case with 43 % σ_h reduction, resulting in strike-slip stress conditions above 2 km depth, should be regarded as a hypothetical bounding case.

At larger depths, the data about the stress field is more limited and the uncertainties are larger. However, as implied in the discussion above, the details of the assumed stress field are less critical at depths below some 2 km. The background stress field at these depths is here assumed to be of strike-slip type, in agreement with observations. The stress anisotropy in the depth range 4 to 6 km is in general agreement with anisotropy values observed at similar depths in the Siljan region (Lund and Zoback 1999).

The glacial stress additions applied here are based on the UMISM reconstruction (Näslund 2006) of the Weichselian glaciation. Hence, it was schematically assumed that a future glaciation will have an evolution that is similar to that of the last one. The properties of future ice covers (e.g. timing, spatial extents, height) are uncertain, and it cannot be excluded that the crustal stress additions generated by next glaciation will differ significantly from those estimated for the Weichselian glaciation. Given that this would be the case, it is also uncertain which implications this could have for deformation zone stability and for the potential for co-seismic secondary displacements. The way the simulations are carried out here, i.e., with an adjustment of the fault and fracture system (i.e. quasi-static slip) to the endglacial stress field prior to rupture initiation, applying higher glacial stress additions may not necessarily mean that a larger earthquake and larger co-seismic secondary displacements would be simulated. However, this should possibly be examined in further work.

The glacial stress additions were picked at the time instances with maximum fault- and fracture instability (cf Figure 2-4). However, the unstable conditions develop gradually, and instead of being generated during one large slip event as is assumed in the simulations here, fault movement may as well develop at an earlier stage as several smaller (or a few larger) slip events. The events may generate fault slip at seismic velocities or take place slowly. In the latter case, negligible dynamic secondary effects would be generated. The assumption made here, with one large earthquake occurring at the time of maximum instability, was considered to provide the most pessimistic results.

7.2.2 Pre-slip on target fractures

It is recalled that the target fracture displacements that are reported here are co-seismic displacements, i.e., those generated during earthquake rupture. As shown in the results section, suitably oriented and located fractures may slip some 15 mm during the quasi-static calculation step when the endglacial initial loads are applied. These displacements are not included in the reported co-seismic fracture shear displacement results. The forebulge and endglacial stress conditions considered here, and the associated fracture instability, may take some hundreds of years to develop (Figure 2-4), and it is assumed that such pre-slip would be generated mainly aseismically in response to the slow change of the stress field. Since the stiffness of the bentonite buffer surrounding the canister is rate dependent (Börgesson et al. 2010), it is assumed that the displacements take place slow enough such that the bentonite buffer in an intersected deposition hole will have time to accommodate the movements without transferring any significant loads to the canister. It is further assumed that density inhomogeneities that may arise in the buffer due to the deformation have time to be levelled out and that the buffer is in its initial, undisturbed state at the time of earthquake rupture initiation. It was beyond the scope of this study to speculate whether the canister failure criterion should be modified to account for accumulated deformations.

It should also be pointed out that some of the target fracture pre-slip simulated here takes place in response to the excess in stress and associated instability caused by the background (present-day) stress field. This is seen as a positive *CFS* at time 0 in Figure 2-4, i.e., when the glacial stress additions are zero. Hence, this part of the pre-slip would have taken place prior to the construction of the repository and deposition of the canisters. Given that the pre-slip can be assumed to scale approximately with the positive *CFS* values, the present-day pre-slip can, depending on the assumed fracture orientation, be estimated to be some 30 % of the total simulated endglacial pre-slip (compare *CFS* at time = 0 and *CFS* at time = 58 ka (500 m depth) in Figure 2-4).

7.2.3 Representation of the rock mass

The rock mass between faults and target fractures was modelled as an isotropic continuum. With exception for the models where the presence of a damage zone was considered, the continuum was also assumed to be homogeneous and linear elastic. Given that the rock mass at Forsmark is of high quality (Glamheden et al. 2007), with fractures in high compression, the linear elastic assumption should serve as a good approximation for the purpose of this study (Scholz 2002).

The assumption of an elastic continuum, which was made in most of the cases here, means that potential effects of fracture propagation are omitted. The size of the target fractures remains constant. For a real fracture slipping by a large amount, the stresses generated at its tips may cause inelastic deformation of the rock and growth of the fracture. In a study by La Pointe et al. (2000) it was concluded that fracture propagation will consume energy and thereby contribute to reduce fracture slip. That would mean that the assumption of elasticity is conservative. However, the fracture propagation criterion applied by La Pointe et al. (2000) was schematic and generic, and the impact on the fracture displacement is uncertain. Under all circumstances, the potential effect of propagation should be modest. According to results presented by Cowie and Scholz (1992), a fault that is ruptured along its entire length during a single slip event may grow in size by 2–3 %, at most.

Since the rock mass was assumed to behave elastically (with the exception for the cases where the damage zone was represented), attenuation was not accounted for explicitly in the models whereas seismic waves attenuate in real rock masses because of inelastic deformations. The attenuation effects caused by target fracture slip in the models is judged to be of marginal importance. The total fracture surface area is small relative to the rock volumes involved. In addition, the way the target fractures are located, i.e., all at the same depth, means that most of the stress waves do not pass any fractures, or only pass a few of them, on their way to more distant positions. For the short distances and the competent rock mass considered for the present purpose, attenuation effects are judged to be small. Ignoring these effects is nevertheless conservative.

7.2.4   Properties of faults and fractures

The rupturing faults as well as the target fractures were modelled as planar discontinuities and were given homogeneous properties. This assumption contrasts with the well-known fact that faults and fractures are undulated at different length scales (Candela et al. 2012, Power and Tullis 1991), but was made for practical reasons; modelling undulations on faults and fractures would add considerable complexity to the models.

The assumption of planarity and homogeneity may have implications for the validity of the simulated secondary fracture displacements. Results of earlier studies (Fälth 2018, Johri et al. 2014) indicate that the potential for secondary fracture displacement close to a slipping fault may increase locally by some tens of percent due to stress concentrations generated around asperities on the fault. On the other hand, the results by Fälth (2018), as well as results by others (Fang and Dunham 2013), show that surface roughness can add significantly to the shear resistance of a fault or fracture. The roughness of natural rock surfaces can be described as a self-similar fractal in the sense that the root-mean-square height fluctuations are proportional to profile length. The amplitude-to-wavelength ratio is typically in the range $10^{-4} – 10^{-2}$ (Power and Tullis 1991). Assuming an amplitude-to-wavelength ratio of 5×10^{-3}, Fälth (2018) obtained about 35 % slip reduction when applying roughness to a fault surface. This indicates that the assumption of planar target fractures may contribute to an overestimation of the secondary displacements. However, due to the limited amount of data on properties of large fractures at Forsmark, the potential overestimation is difficult to quantify.

It was assumed here that the target fractures respond to loads according to an idealised elasto-plastic material model with constant stiffness and shear failure according to a Coulomb criterion (Figure 4-8). The response of this model resembles, in a general way, the response of a fracture loaded in shear. However, there are other models that simulate the response of a loaded fracture in less schematic ways. For instance, the continuously yielding joint model is intended to simulate the internal mechanism of progressive damage of joints under shear (Cundall and Lemos 1990, Itasca 2020), cf e.g. Jacobsson and Flansbjer (2006). There are also models that consider the slip history as well as the slip velocity of the joint, i.e. rate-and-state models (Ruina 1983). It is difficult, however, to say if these alternative material models, in general, would lead to any significant differences in the simulated fracture displacements compared to those simulated here.

When estimating the stability of deformation zones, the friction coefficient was assumed to be constant over time and hence unaffected by, e.g., the heating of the repository rock mass. The same assumption was made for the friction coefficient of the target fractures. This approach is the same as that taken in the latest safety assessment SR-Site (SKB 2010b) and hence considered to be relevant here.

The fault rupture propagation is a complex process that may involve, e.g., heating and pore pressure transients, which can have a significant impact on the shear resistance during slip (Rice 2006, Yao et al. 2018). Hence, it is difficult to assess the relevance of different models used for simulation of the rupture. However, the results in Appendix C suggest that the velocity-weakening model (see Section 4.3) applied here to simulate the dynamic earthquake rupture generates co-seismic secondary stress effects and associated secondary fracture displacements that are overestimates rather than underestimates. In the comparison made in Appendix C, the secondary fracture displacements generated when applying the velocity-weakening model were on average 5 times larger than those generated when applying the widely used slip-weakening model. From this observation, it appears that the uncertainty in the results related to the choice of fault constitutive model is at least on par with the uncertainties related to the parameters variations that were made here (see Section 6.4.2). It is noted here though, that adopting other combinations of input parameter values to the velocity-weakening model (i.e. combinations of μ_s, μ_d and v^*) than that adopted here may result in alterations of the simulated secondary fracture displacements. For instance, results from a previous study (Fälth and Hökmark 2015) indicate that a higher value of μ_s may lead to stronger secondary effects (see also Section 4.3). However, considering the considerable impact of using another constitutive model (as indicated in Appendix C), the choice of parameter setting to a given model could possibly be regarded to be less important than the choice of model. This should hold as long as variations of the input parameter setting give only modest alterations of the earthquake source parameters.

7.2.5 Model discretisation

The numerical discretisation (here, the edge lengths of the finite difference elements) has importance for how stresses and strains are calculated. In dynamic simulations it has an impact on how well stress waves are propagated in the model volume. According to Kuhlemeyer and Lysmer (1973), the longest element edge length should not exceed 1/10–1/8 of the shortest wavelength in the wave spectrum that is considered in the model. According to Itasca (2020), this criterion is valid for 3DEC models, and has been confirmed by Fälth et al. (2015).

In general, a finer discretisation (shorter edge lengths of the finite difference elements) means that a more accurate numerical solution is achieved. From the simulations made here, it appears that a finer discretisation tends to give larger calculated fracture displacements. This is in accord with the results in Fälth et al. (2019). Hence, it is desirable to make the discretisation as fine as possible to obtain a satisfactory solution and to reduce the risk of underestimating the secondary displacements. However, when determining the level of discretization, one must find a balance between computer run time and accuracy. Refinement of the discretization may give a considerable increase of computer memory consumption, shorter time steps, and hence longer run times.

The continuously increasing performance of computer hardware and software allows for increasingly extensive and refined numerical models to be built and analysed. The discretisation of the models used in the present work means a considerable refinement compared to the discretisation of the models used by Fälth et al. (2016, 2015). For instance, in those studies the volume containing the target fractures was discretised using finite difference edge lengths of 50 m. For the target fracture diameter used in those models (300 m) this corresponds to $N = 6$ edge lengths per fracture diameter. In the models used in the present work, the edge length in the target fracture volume was about 12 m, i.e., about ¼ of the edge length used in the studies by Fälth et al. (2016, 2015). With the target fracture diameter used in the present models (150 m), this corresponds to $N = 12$ edge lengths per fracture diameter.

As shown earlier in this report, a reduction of the edge length to 80 % ($N = 16$) of the Base case edge length gives about 4 % increase in target fracture displacement, on average, while the reduction to 60 % edge length ($N = 20$) gives about 6 % increase. It was concluded that this sensitivity to the discretisation is in general agreement with the sensitivity observed by Fälth et al. (2019). Given that the trend observed by Fälth et al. (2019) holds also when the discretisation is refined further such that very small finite different elements are used, the uncertainty in the present results related to numerical discretisation is estimated to be about 15 %.

7.2.6 Comparison of simulated results with data from real events and with data from previous simulation

The simulation work presented here aimed at generating estimates of secondary fracture displacements that are based on less pessimistic assumptions than those applied by e.g. Fälth et al. (2016). The effect of this is illustrated by the results shown in Figure 7-1 and Figure 7-2. The moment magnitudes and average fault displacements of the synthetic earthquakes simulated here are reduced considerably compared to the corresponding output from the models of Fälth et al. (2016). As shown in Figure 7-1, the moment magnitudes of the present models lay in the lower end of the catalogue data range. Considering the shallow depths of the synthetic events, this appears to be relevant; only one of the catalogue events has a focal depth less than 5 km (Figure 7-2). Also note the depths of the intraplate events listed in Section 1.3. Recall that larger depths mean higher stresses and, in general, higher stress drops with corresponding larger displacements.

Note the low magnitude of the forebulge earthquake with 11 % σ_h reduction (ZFMNW0017_ FFM01NW_Shred11 model) (Figure 7-1). As for the reverse synthetic earthquakes, this can partly be attributed to the shallow location of the rupture. For this model, (and for the ZFMNW0017_ FFM01NW_Shred43 model) which simulates a strike-slip event occurring under forebulge stress conditions, the relatively low stress anisotropy in the horizontal plane (cf σ_H-σ_h and σ_H-σ_v-differences at shallow depth in Figure 2-1) also means lower driving stresses for this type of event. Recall that, due to the shallow location and the low stress anisotropy, the rupture in this model is limited to the rupture nucleation region (Section 5.2.2). The ZFMNW0017_FFM01NW_Shred43 model, where the background σ_h is set equal to σ_v, generates a considerably higher moment magnitude. However, as noted in Section 7.2.1 this can be regarded a hypothetical bounding case.
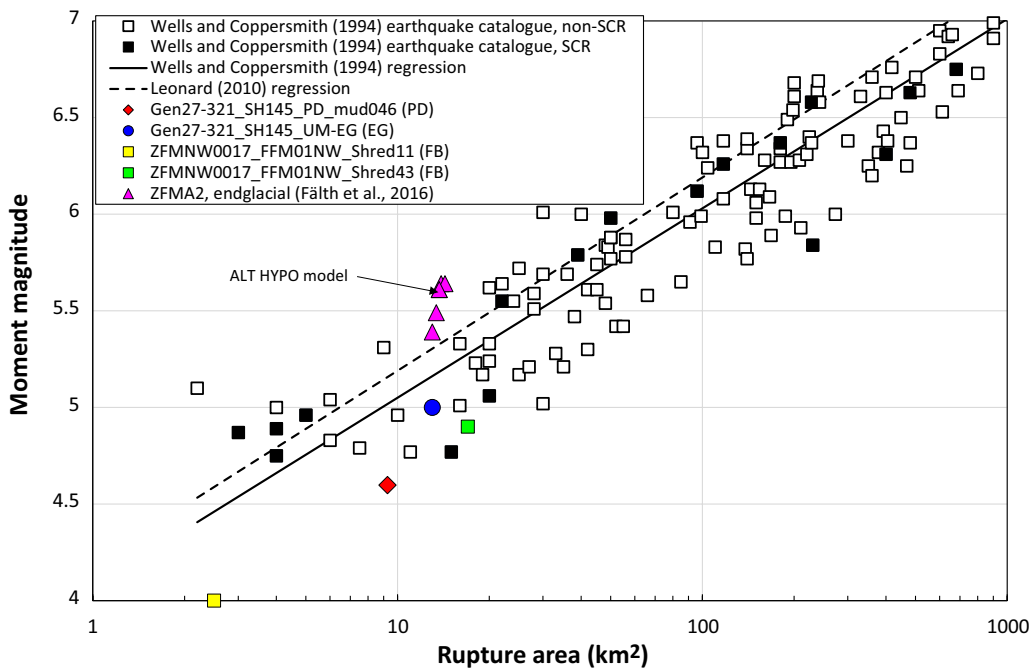

Figure 7-1. *Moment magnitude M_w versus rupture area RA for simulations by Fälth et al. (2016) and for simulations made here (FB = forebulge, PD = present-day, EG = endglacial). The simulated data is plotted along with corresponding data for earthquakes in the Wells and Coppersmith (1994) catalogue. "SCR" means Stable Continental Region.*
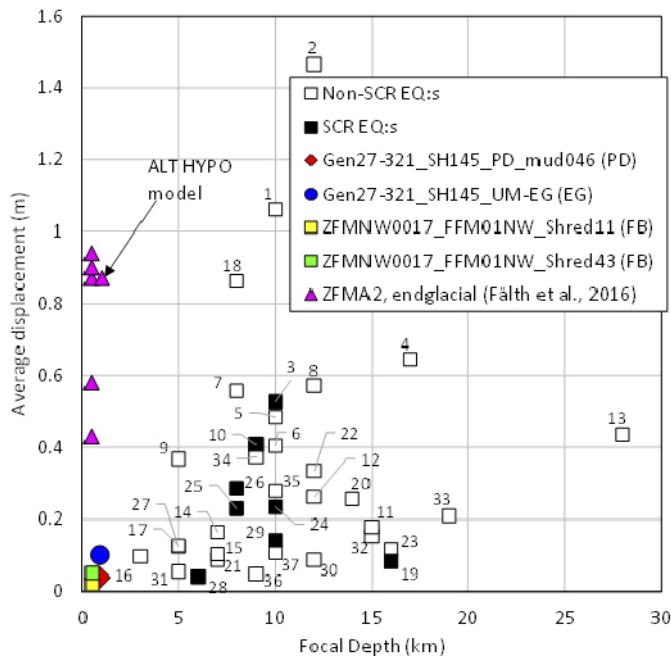
Figure 7-2. *Average displacement versus focal depth for simulated earthquakes (FB = forebulge, PD = present-day, EG = endglacial) plotted along with corresponding data for events in the Wells and Coppersmith (1994) catalogue. "SCR" means Stable Continental Region. The catalogue set is limited to earthquakes with rupture areas up to 40 km². The data labels refer to the references in Table 1-1 supporting the given focal depths. The average displacements were calculated as described in Section 1.5.2.*

Figure 7-3a shows a map view of target fracture peak displacements at all fracture positions. The results were compiled from all Base case endglacial models, i.e., for all target fracture orientations considered here. Figure 7-3b shows the corresponding results reported by Fälth et al. (2016) for their ALT HYPO model (Figure 7-1) (for 300 m diameter fractures). In that model Fälth et al. (2016) assumed the hypocentre to be located close to the lower end of the ZFMA2 plane. It was in that model case they obtained the largest secondary displacements. This was the rationale for using a similar hypocentre location in the models used in the present study.

It is recalled here that the fault displacements generated in the present simulation were considerably smaller than those in the ALT HYPO model by Fälth et al. (2016). The seismic moment of the synthetic earthquake here was about 1/8 (or 12 %) of that generated in the ALT HYPO model (see Figure 7-1 and Figure 7-2).

Stress concentrations generated around fault edges may significantly increase the secondary displacements in those regions (Fälth et al. (2016). In the present models, only target fractures in the footwall of ZFMA2 and at positions away from the ZFMA2 edges were included. This is because fractures were included only within the planned repository areas. Thus, only footwall results away from the ZFMA2 edges in the Fälth et al. (2016) model should be considered in the comparison. The following can be observed in Figure 7-3:

- At 200 m perpendicular fault-fracture distance, the present model generates displacements that are about 50 % of those generated in the Fälth et al. (2016) model. Hence, the displacements appear to scale with the difference in target fracture size; the fracture diameter in the present model is 50 % of the diameter in the Fälth et al. (2016) model.

- In the present model the largest displacements are generated in the 300 m to 400 m distance range while in the Fälth et al. (2016) model these are found in the 400 m to 600 m range. The cause of this slight change in distance is difficult to determine in detail but could be due to the difference in the hypocentre location and due to differences in how the rupture process is simulated. However, notable is that the largest displacement in the present model is about 25 % of the largest displacement in the Fälth et al. (2016) model while one would expect it to be 50 % given the difference in fracture size. The larger reduction in displacement can be attributed to the lower seismic moment generated in the present model and to the associated reduction of the secondary stress effects.

- At 800 m distance the displacements in the Fälth et al. (2016) model are 6–8 times larger than in the present model.

To summarise, the spatial distribution of secondary displacements in the footwall of ZFMA2 is similar in the models; the largest displacements tend to be in a region in the 300 m to 600 m distance range from ZFMA2. The largest displacement generated in the present model are considerably smaller than that generated in the model by Fälth et al. (2016). In the present model, the largest displacement normalised to the target fracture diameter is $9/150 = 0.06$ mm/m while the corresponding displacement in the Fälth et al. (2016) model is $37/300 = 0.12$ mm/m. Considering the considerable difference in seismic moment between these cases, one would possibly expect a larger difference in secondary displacement. However, as noted in Section 7.2.5, the numerical discretisation of the present model was much finer, and this tends to give larger simulated displacements. Then, there are also differences in the details of how the fault rupture was simulated. This may also have importance for the simulated secondary displacements (see Appendix C).
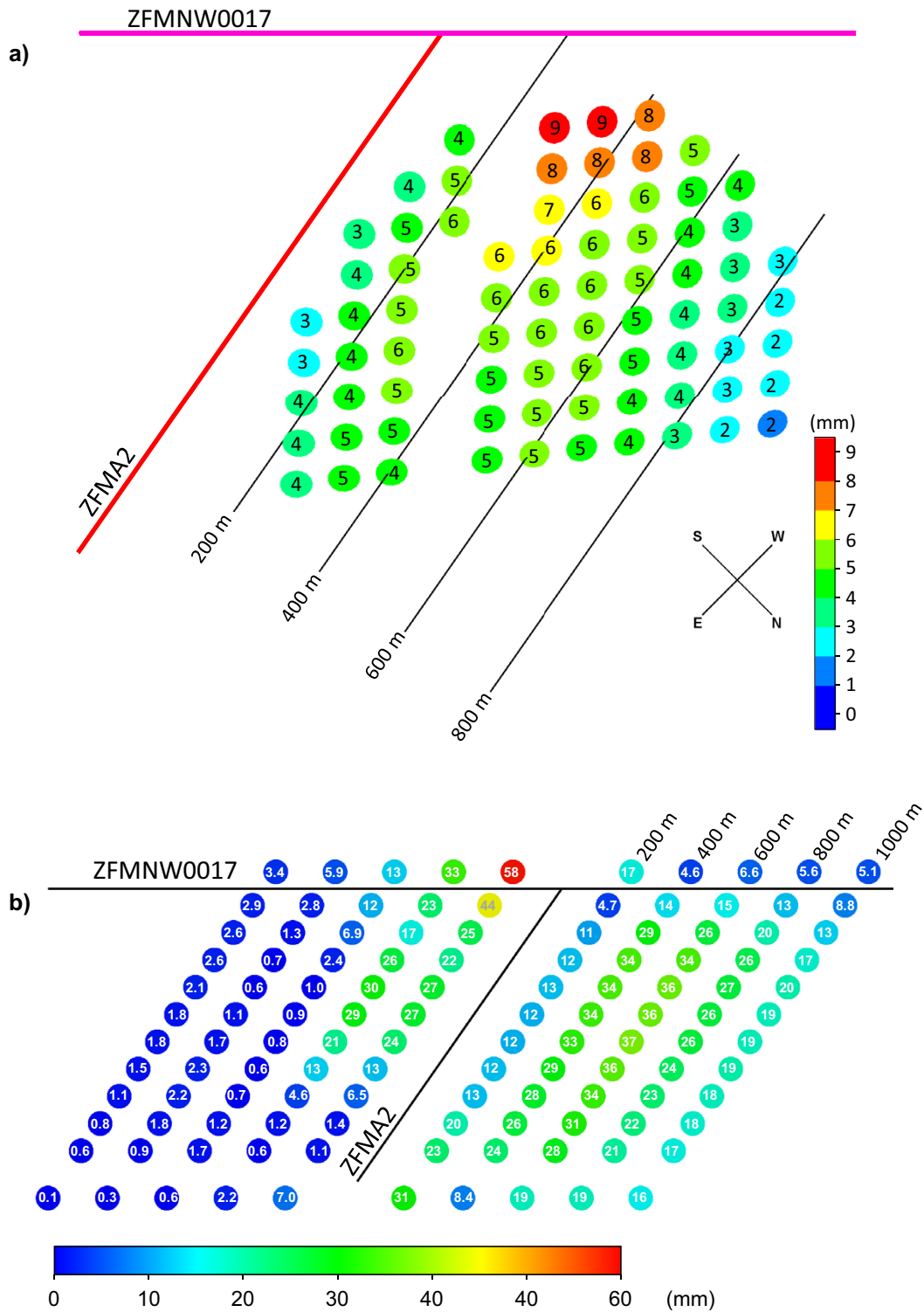
Figure 7-3. *a) Map view of target fracture peak displacements at all positions (fracture diameter 150 m). The results were compiled from all Base case assumption endglacial models. The black lines indicate perpendicular distances to the ZFMA2 plane. b) The corresponding result redrawn from Figure 11 (lower) in Fälth et al. (2016) (fracture diameter 300 m).*

8 Summary and conclusions

The work presented in this report had two main objectives:

*   To make estimates of the long-term stability of the six steeply dipping deformation zones at Forsmark, ZFMNW0017, ZFMNW1200, ZFMWNW0123, ZFMWNW0809A, ZFMENE0060A and ZFMENE0062A. The focus was on the stability under forebulge conditions, when the stability of steep zones tends to be lowest, but the impact on the zone stability of the heat generated by the decaying spent fuel was also examined.

*   To make estimates of co-seismic secondary fracture displacements at the Forsmark site. The intention was to generate estimates of secondary fracture displacements that are based on less pessimistic assumptions than those applied by e.g. Fälth et al. (2016). In addition, it was examined how sensitive the results may be to variations in model input. Several of the model cases and the variations in model input tested here address items that were identified by Hökmark et al. (2019) to be important for further examination.

The stress field used in both the stability calculations and in the earthquake simulations was the sum of a background stress field and glacially induced stresses obtained from a GIA simulation. As indicated by the results presented here, the stress field close to the surface, above some 2 km depth, is most critical for zone stability and for the potential of faulting. In this depth range, the Base case background stress field was in accord with the most likely stress model developed for the Forsmark site.

8.1 Deformation zone stability

The deformation zone stability was evaluated in terms of Coulomb Failure Stress (*CFS*) using analytical calculations. Based on the calculations, the following could be concluded regarding the stability under forebulge conditions:

*   Given the Base case background stress field, no zone becomes unstable during forebulge for any assumption of the stress trend or for any of the zone strike and dip values considered here. Given their nominal average orientations, all zones have stability margins exceeding 5 MPa (i.e. *CFS* < −5 MPa) over more than 85 % of the zone depth extensions assumed here.

*   The sensitivity of the stability to the variations in zone strike and dip is modest. At the depth with the lowest stability, *CFS* varies by about 1 MPa, at most, for strike and dip angles deviating from the nominal values.

*   Reducing the background minor horizontal stress σ_h gives a stability reduction due to the increased stress anisotropy in the horizontal plane. With 11 % reduction, the ZFMNW0017, ZFMNW1200, ZFMWNW0123 and ZFMWNW0809A obtain modest instability close to the surface (*CFS* reaching 2 to 3 MPa). With 43 % reduction, all zones except ZFMENE0060A and ZFMENE0062A obtain considerable positive *CFS* values that reach between 5 and 10 MPa at the surface.

*   ZFMENE0060A and ZFMENE0062A have considerable stability margins at all depths and for all assumptions made here.

The *CFS* calculation for the heated phase shows that, given the Base case background stress field or the 11 % σ_h reduction background stress field, the stability changes induced by the heating will have too low magnitudes for any of the steep zones to become unstable.

8.2 Secondary displacements

The secondary fracture displacements were estimated using numerical simulations of what-if earthquake rupture scenarios. Earthquakes were simulated for forebulge conditions, present-day conditions, and for endglacial conditions. The focus was on the endglacial scenario when fault stability is estimated to be particularly low at Forsmark. All 76 target fractures, on which the secondary displacements were simulated, had a diameter of 150 m, and were located within the projected repository volume. The fracture diameter was half of the diameter used in the previous Forsmark study (Fälth et al. 2016) since this gave room for a larger number of fractures to be included in the model volume. Both fractures with orientations in accordance with Forsmark site data and fractures with generic orientations were considered.

8.2.1 Forebulge conditions

For those cases were the analytic *CFS* calculation predicted instability on a zone, dynamic earthquake rupture initiation was simulated to evaluate the potential for extensive earthquake ruptures and for co-seismic secondary fracture shear displacements. For each rupture scenario, three fracture orientations were considered. Based on the simulations, the following can be concluded:

- For the stress assumption that is regarded to be the most relevant one out of those considered in the simulations, i.e., background stress field with 11 % σ_h reduction, the rupture is effectively restricted to the earthquake initiation region where a forced rupture is imposed. This indicates that the conditions for having an extensive earthquake rupture are not fulfilled. The largest simulated moment magnitude is 4.0 with average fault slip of 20 mm.

- Applying the hypothetical background stress field with 43 % σ_h reduction gives a considerable increase of the simulated earthquake magnitudes and rupture areas. Ruptures that propagate along the entire fault traces are obtained. The largest simulated moment magnitude becomes 4.9 with a corresponding average fault slip of 51 mm.

- The secondary fracture shear displacements are very modest in all cases. In the 11 % background σ_h reduction case, no fracture moves more than 0.1 mm. When applying the 43 % reduction stress model the largest secondary displacement becomes about 4 mm.

8.2.2 Present-day and endglacial conditions

In total 51 simulations of present-day and endglacial earthquakes were performed. In all simulations the ruptures were assumed to initiate on the shallow and gently dipping ZFMA2 zone. Secondary displacements were simulated on target fractures located at distances in the range 0 to 1 400 m from ZFMA2, and 17 target fracture orientations were considered. The impact of variations in the following input parameters was examined:

- Hypocentre location.
- Fault dynamic friction coefficient (moment magnitude).
- Background (present-day) σ_H stress trend.
- Background σ_h stress magnitude.
- Rock mass deformation modulus in repository volume.
- Coupling between stress transients and pore pressure.
- Target fracture friction coefficient.
- Model discretisation.

Based on the simulation results it can be concluded that the glacial stress additions have a significant impact on the earthquake magnitude. When assuming Base case fault properties the present-day synthetic earthquake generated a moment magnitude of M_w 4.6. Given the same properties, the endglacial model generated a moment magnitude of M_w 5.0. This corresponds to an increase in seismic moment relative to the present-day case by a factor of four.

The seismic moment generated in the present endglacial model is about 1/8 of the seismic moment generated in the endglacial model by Fälth et al. (2016). Hence, the present simulation can be regarded to represent a considerably less pessimistic case than that simulated by Fälth et al. (2016). Yet, the moment magnitudes and average fault displacements simulated in both the present-day and endglacial models here, appear to be on par with those generated by earthquakes that nucleate at considerable larger depths where the stress levels and the expected earthquake stress drops are higher. Hence, the synthetic earthquakes simulated here should represent realistic-pessimistic cases.

When considering the simulated secondary displacements on target fractures at distances larger than 100 m from the ZFMA2 slip plane, the following can be observed:

- For the gently dipping low-stability target fracture orientation considered in the present-day model, the largest displacement reaches some 5 mm when assuming Base case fault properties. For the same fracture orientation, the maximum displacement in the endglacial case was about 8 mm.

- The largest displacement generated in the endglacial case was 9 mm (Base case assumptions). This was obtained on a gently dipping generic low-stability fracture set. No displacement generated on the site-specific fracture sets exceeded 1 mm.

- A general observation is that the largest displacements tend to be generated on gently dipping low-stability fractures. This is in accordance with results in previous studies (Fälth et al. 2016, Fälth et al. 2010).

- The fracture shear velocity tends to be proportional to the shear displacement. The highest shear velocity observed here was about 200 mm/s.

The simulations of secondary displacements at distances shorter than 100 m from the ZFMA2 slip plane indicate that the induced displacement on a fracture in mechanical contact with the slip plane and/or the damage zone can be highly sensitive to the mechanical properties of the damage zone. Here, the displacements on some fractures in mechanical contact with the slip plane and/or the damage zone increased several times when the damage zone was included in the model. However, the impact on fractures outside the damage zone was modest and of no practical importance. No simulated displacement on fractures in contact with the damage zone and/or the slip plane of ZFMA2 exceeded 30 mm.

Out of the model input parameter variations that were made here, the variation in target fracture friction coefficient appears to have the largest potential to influence the results. For the sub-vertical site-specific fracture sets as well as for the gently dipping set, the change in results in response to the variation in friction coefficient was modest and of no practical importance. However, for the steeper generic fracture set (dip 55°), the reduction of friction coefficient and the associated reduction in initial stability margin led to a considerable increase in co-seismic displacements. The largest displacement reached about 9 mm, i.e., on par with the largest displacement obtained on the gently dipping sets.

For the other parameter variations made here, it can be concluded that the sensitivity in the results is modest. The change in secondary displacements in response to these parameter variations amounts to a few mm, at most. The largest secondary displacement simulated here on fractures at distances ≥ 100 m from the ZFMA2 slip plane reached about 12 mm. This result was obtained in a simulation where the rock mass Young's modulus had been reduced 30 % around selected fractures. The results from that simulation indicate that the increase in secondary displacement due to a reduction of the rock mass deformation modulus appear to scale approximately with the modulus reduction, in accord with results from corresponding quasi-static calculations (Eshelby 1957).

Assuming Base case rock mass and target fractures properties, no simulated secondary displacement exceeded 10 mm. Furthermore, it is also indicated by the results presented here that including the effect of pore pressure transients in the simulation appears to give slightly reduced secondary displacements as compared to a simulation without pressure variations. Hence, the Base case assumption with no pore pressure coupling should promote pessimistic results.

The comparison of simulation results from the present study with previous results shows that the largest displacement normalised to the target fracture diameter became about 50 % of the largest normalised displacement generated in the corresponding model by Fälth et al. (2016).

8.3 Final remarks

It appears that the forebulge earthquake ruptures simulated here represent hypothetical scenarios. Given the most likely present-day Forsmark stress field, glacial stress additions based on the UMISM glacial reconstruction and properties in accordance with Forsmark site data, the results indicate that the steeply dipping Forsmark zones will be stable under forebulge stress conditions. For the case with the background σ_h stress component reduced 11 %, i.e., assuming the maximum reported σ_H-to-σ_h-ratio at repository depth, the numerical simulations indicate that conditions for the initiation of an earthquake rupture on the steep Forsmark deformation zones do not exist.

The largest co-seismic secondary fracture displacements simulated here outside the damage zone are on the order of 10 mm on 150 diameter fractures. This was obtained on low-stability generic fracture sets. Given that background stresses according to Forsmark data are assumed, only insignificant displacements (~1 mm) were obtained on the site-specific sets.

The secondary displacements were simulated when adopting a fault rupture model that appears to give significantly stronger secondary stress effects compared to other rupture models. Even though the present secondary displacements are considerably smaller than those reported in the previous Forsmark study, this suggests that they still are overestimates rather than underestimates.

References

SKB's (Svensk Kärnbränslehantering AB) publications can be found at www.skb.com/publications.

Andrews, D J, 2005. Rupture dynamics with energy loss outside the slip zone. Journal of Geophysical Research-Solid Earth, vol. 110 (B1). https://doi.org/10.1029/2004jb003191

Arvidsson, R, Wahlström, R, Kulhánek, O, 1992. Deep-crustal earthquakes in the southern Baltic Shield. Geophysical Journal International, vol. 108(3), 767–777.

Beeler, N M, Tullis, T E, Goldsby, D L, 2008. Constitutive relationships and physical basis of fault strength due to flash heating. Journal of Geophysical Research, vol. 113. https://doi.org/10.1029/2007JB004988

Bizzarri, A, 2010. How to Promote Earthquake Ruptures: Different Nucleation Strategies in a Dynamic Model with Slip-Weakening Friction. Bulletin of the Seismological Society of America, vol. 100(3), 923–940. https://doi.org/10.1785/0120090179

Bizzarri, A, 2011. On the deterministic description of earthquakes. Reviews of Geophysics, 49 (3). https://doi.org/10.1029/2011rg000356

Bürgmann, R, Pollard, D D, Martel, S J, 1994. Slip distributions on faults – effects of stress gradients, inelastic deformation, heterogeneous host-rock stiffness, and fault interaction. Journal of Structural Geology vol.16 (12), 1675–1690. https://doi.org/10.1016/0191-8141(94)90134-1

Bödvarsson, R, Lund, B, Roberts, R, Slunga, R, 2006. Earthquake activity in Sweden. Study in connection with a proposed nuclear waste repository in Forsmark or Oskarshamn SKB R-06-67, Svensk Kärnbränslehantering AB.

Börgesson, L, Dueck, A, Johannesson, L E, 2010. Material model for shear of the buffer – evaluation of laboratory test results. SKB TR-10-31, Svensk Kärnbränslehantering AB.

Börgesson, L, Hernelind, J, 2006. Earthquake induced rock shear through a deposition hole. Influence of shear plane inclination and location as well as buffer properties on the damage caused to the canister. SKB TR-06-43, Svensk Kärnbränslehantering AB.

Candela, T, Renard, F, Klinger, Y, Mair, K, Schmittbuhl, J, Brodsky, E E, 2012. Roughness of fault surfaces over nine decades of length scales. Journal of Geophysical Research-Solid Earth vol. 117. https://doi.org/10.1029/2011jb009041

Chan, T, Christiansson, R, Boulton, G S, Eriksson, L O, Hartikainen, J, Jensen, M R, Wallroth, T, 2005. DECOVALEX III/BENCHPAR projects. The thermal-hydro-mechanical responses to a glacial cycle and their potential implications for deep geological disposal of nuclear fuel waste in a fractured crystalline rock mass. SKI 2005:28, Strålsäkerhetsmyndigheten (Swedish Radiation Safety Authority), Sweden.

Choy, G L, Boatwright, J, Dewey, J W, Sipkin, S A, 1983. A teleseismic analysis of the New Brunswick earthquake of January 9, 1982. Journal of Geophysical Research, vol. 88 (NB3), 2199–2212. https://doi.org/10.1029/JB088iB03p02199

Courjault-Radé, P, Darrozes, J, Gaillot, P, 2009. The M = 5.1 1980 Arudy earthquake sequence (western Pyrenees, France): a revisited multi-scale integrated seismologic, geomorphologic and tectonic investigation. International Journal of Earth Sciences, vol. 98(7), 1705–1719. https://doi.org/10.1007/s00531-008-0320-5

Cowie, P A, Scholz, C H, 1992. Growth of faults by accumulation of seismic slip. Journal of Geophysical Research-Solid Earth, vol. 97(B7), 11085–11095. https://doi.org/10.1029/92jb00586

Cundall, P A, 1971. A computer model for simulating progressive large scale movements in blocky rock systems. In Rock Fractures: Proceedings of the International Symposium on Rock Mechanics, Nancy, France, 4–6 October 1971, Vol. 1, paper II-8.

Cundall, P A, Lemos, J V, 1990. Numerical simulation of fault instabilities with a continuously-yielding joint model. In: Fairhurst, C (ed). Rockbursts and Seismicity in Mines. Rotterdam: Balkema 147–152.

Dreger, D, Helmberger, D, 1991. Source parameters of the Sierra Madre earthquake from regional and local body waves. Geophysical Research Letters, vol. 18(11), 2015–2018. https://doi.org/10.1029/91gl02366

Ellsworth, W L, 1975. Bear Valley, California, earthquake sequence of February–March 1972. Bulletin of the Seismological Society of America, vol. 65(2), 483–506.

Ellsworth, W L, Campbell, R H, Hill, D P, Page, R A, Alewine, R W, Hanks, T C, Whitcomb, J H, 1973. Point Mugu, California, Earthquake of 21 February 1973 and its aftershocks. Science, vol. 182(4117), 1127–1129. https://doi.org/10.1126/science.182.4117.1127

Eshelby, J D, 1957. The determination of the elastic field of an ellipsoidal inclusion, and related problems. Proceedings of the Royal Society of London. Series A, Mathematical and Physical Sciences, vol. 241(1226), 376–396. https://doi.org/10.1098/rspa.1957.0133

Evans, D G, McEvilly, T V, 1982. A note on relocating the 1963 Watsonville earthquakes. Bulletin of the Seismological Society of America, 72(4), 1309–1316.

Fang, Z, Dunham, E M, 2013. Additional shear resistance from fault roughness and stress levels on geometrically complex faults. Journal of Geophysical Research-Solid Earth, 118(7), 3642–3654. https://doi.org/10.1002/jgrb.50262

Fox, A, La Pointe, P, Hermanson, J, Öhman, J, 2007. Statistical geological discrete fracture network model. Forsmark modelling stage 2.2. SKB R-07-46, Svensk Kärnbränslehantering AB.

Frankel, A, 1984. Source parameters of two ML ~5 earthquakes near Anza, California, and a comparison with an Imperial-Valley aftershock. Bulletin of the Seismological Society of America, vol. 74(5), 1509–1527.

Fälth, B, 2018. Simulating earthquake rupture and near-fault fracture response. Doctoral thesis. Uppsala University, Sweden.

Fälth, B, Hökmark, H, 2012. Modelling End-Glacial Earthquakes at Olkiluoto. Expansion of the 2010 Study. Posiva Working Report 2012-08, Posiva Oy, Finland.

Fälth, B, Hökmark, H, 2015. Effects of Hypothetical Large Earthquakes on Repository Host Rock Fractures. Posiva Working Report 2015-18, Posiva Oy, Finland.

Fälth, B, Hökmark, H, Lund, B, 2016. Simulation of co-seismic secondary fracture displacements for different earthquake rupture scenarios at the proposed nuclear waste repository site in Forsmark. International Journal of Rock Mechanics and Mining Sciences vol. (84C), 142–158. https://doi.org/10.1016/j.ijrmms.2016.02.009

Fälth, B, Hökmark, H, Lund, B, Mai, P M, Roberts, R, Munier, R, 2015. Simulating earthquake rupture and off-fault fracture response: Application to the safety assessment of the Swedish nuclear waste repository. Bulletin of the Seismological Society of America, vol. 105(1). https://doi.org/10.1785/0120140090

Fälth, B, Hökmark, H, Munier, R, 2010. Effects of large earthquakes on a KBS-3 repository. Evaluation of modelling results and their implications for layout and design. SKB TR-08-11, Svensk Kärnbränslehantering AB.

Fälth, B, Lönnqvist, M, Hökmark, H, 2019. Co-seismic secondary fracture displacements under different stress conditions. Posiva Working Report 2019-10, Posiva Oy, Finland.

Glamheden, R, Fredriksson, A, Röshoff, K, Karlsson, J, Hakami, H, Christiansson, R, 2007. Rock Mechanics Forsmark. Site descriptive modelling Forsmark stage 2.2. SKB R-07-31, Svensk Kärnbränslehantering AB.

Haessler, H, Hoangtrong, P, Schick, R, Schneider, G, Strobach, K, 1980. The September 3, 1978, Swabian Jura earthquake. Tectonophysics, vol. 68(1-2), 1–14. https://doi.org/10.1016/0040-1951(80)90005-0

Hanks, T C, Kanamori, H, 1979. A moment magnitude scale. Journal of Geophysical Research, vol. 84(NB5), 2348–2350. https://doi.org/10.1029/JB084iB05p02348

Hardebeck, J L, 2010. Seismotectonics and Fault Structure of the California Central Coast. Bulletin of the Seismological Society of America, vol. 100(3), 1031–1050. https://doi.org/10.1785/0120090307

Harris, R A, 1998. Introduction to special section: Stress triggers, stress shadows, and implications for seismic hazard. Journal of Geophysical Research, vol. 103(B10), 24347–24358. https://doi.org/10.1029/98jb01576

Hartzell, S, Brune, J N, 1979. Horse Canyon earthquake of August 2, 1975 – two-stage stress-release process in a strike-slip earthquake. Bulletin of the Seismological Society of America, vol. 69(4), 1161–1173.

Hasegawa, H, S, Wetmiller, R, J, 1980. The Charlevoix Earthquake of 19 August 1979 and its Seismo-Tectonic Environment. Seismological Research Letters, vol. 51(4), 23–38.

Hauksson, E, Jones, L M, 1991. The 1988 and 1990 Upland earthquakes: Left-lateral faulting adjacent to the central transverse ranges. Journal of Geophysical Research-Solid Earth and Planets, vol. 96(B5), 8143–8165. https://doi.org/10.1029/91jb00481

Hauksson, E, Jones, L M, Davis, T L, Hutton, L K, Brady, A G, Reasenberg, P A, Cranswick, E, 1988. The Whitter Narrows earthquake in the Los-Angeles metropolitan area, California. Science, vol. 239(4846), 1409–1412. https://doi.org/10.1126/science.239.4846.1409

Horton, S P, dePolo, D M, Walter, W R, 1997. Source parameters and tectonic setting of the 1990 Lee Vining, California, earthquake sequence. Bulletin of the Seismological Society of America, vol. 87(4), 1035–1045.

Hökmark, H, Fälth, B, 2014. Approach to Assessing the Stability of Olkiluoto Deformation Zones During a Glacial Cycle. Posiva Working Report 2013-37, Posiva Oy, Finland.

Hökmark, H, Fälth, B, Lönnqvist, M, Munier, R, 2019. Earthquake simulations performed to assess the long-term safety of a KBS-3 repository. Overview and evaluation of results produced after SR-Site. SKB TR-19-19, Svensk Kärnbränslehantering AB.

Hökmark, H, Lönnqvist, M, Fälth, B, 2010. THM-issues in repository rock. Thermal, mechanical, thermo-mechanical and hydro-mechanical evolution of the rock at the Forsmark and Laxemar sites. SKB TR-10-23. Svensk Kärnbränslehantering AB.

Ida, Y, 1972. Cohesive force across the tip of a longitudinal-shear crack and Griffith's specific surface energy. Journal of Geophysical Research, vol. 77(20), 3796–3805. https://doi.org/10.1029/JB077i020p03796

Itasca, 2020. 3DEC – 3-Dimensional Distinct Element Code, Version 7, User's Guide. In (vol. 2020). Minneapolis: Itasca Consulting Group Inc.

Jacobsson, L, Flansbjer, M, 2006. Borehole KFM09A Normal loading and shear tests on joints. Forsmark site investigation. SKB P-06-29, Svensk Kärnbränslehantering AB.

Jaeger, J C, Cook, N G W, 1979. Fundamentals of rock mechanics. Third ed. London: Science Paperbacks/Chapman and Hall.

Johnson, L R, McEvilly, T V 1974. Near-field observations and source parameters of central California earthquakes. Bulletin of the Seismological Society of America, vol. 64(6), 1855–1886.

Johri, M, Dunham, E M, Zoback, M D, Fang, Z, 2014. Predicting fault damage zones by modeling dynamic rupture propagation and comparison with field observations. Journal of Geophysical Research-Solid Earth, 119(2), 1251–1272. https://doi.org/10.1002/2013jb010335

Kanamori, H, Anderson, D L, 1975. Theoretical basis of some empirical relations in seismology. Bulletin of the Seismological Society of America, 65(5), 1073–1095.

Kuhlemeyer, R L, Lysmer, J 1973. Finite Element Method accuracy for wave propagation problems. Journal of the Soil Mechanics and Foundations Division, vol. 99(SM5), 421–427.

La Pointe, P R, Cladouhos, T T, Outters, N, Follin, S, 2000. Evaluation of the conservativeness of the methodology for estimating earthquake-induced movements of fractures intersecting canisters. SKB TR-00-08, Svensk Kärnbränslehantering AB.

Lagerbäck, R, Sundh, M, 2008. Early Holocene faulting and paleoseismicity in northern Sweden. Research Paper C, vol. 836.

Langer, C J, Bollinger, G A, 1991. The southeastern Illinois earthquake of 10 June 1987: the later aftershocks. Bulletin of the Seismological Society of America, vol. 81(2), 423–445.

Lund, B, Roberts, R, Smith, C A, 2017. Review of paleo-, historical and current seismicity in Sweden and surrounding areas with implications for the seismic analysis underlying SKI report 92:3. SSM 2017:35, Strålsäkerhetsmyndigheten (Swedish Radiation Safety Authority). (In Swedish.).

Lund, B, Schmidt, P, Hieronymus, C, 2009. Stress evolution and fault stability during the Weichselian glacial cycle. SKB TR-09-15, Svensk Kärnbränslehantering AB.

Lund, B, Schmidt, P, Hossein Shomali, Z, Roth, M, 2021. The Modern Swedish National Seismic Network: Two Decades of Intraplate Microseismic Observation. Seismological Research Letters. https://doi.org/10.1785/0220200435

Lund, B, Shomali, H, Buhcheva, D, Högdahl, K, Tryggvason, A, Jørgensen, P, 2014. The 2014 magnitude 4.1 Sveg earthquake. Proceedings from the 45th Nordic Seismology Seminar, Visby, Sweden, 8–10 October 2014.

Lund, B, Uski, M, Shomali, H, Buhcheva, D, Amini, S, Kortström, J, 2016. The recent Bothnian Bay M4.1 earthquake: where, how and why? The 47th Nordic Seismology Seminar, Reykjavik, Iceland, 11–13 October 2016.

Lund, B, Zoback, M D, 1999. Orientation and magnitude of in situ stress to 6.5 km depth in the Baltic Shield. International Journal of Rock Mechanics and Mining Sciences, vol. 36, 169–190. https://doi.org/10.1016/S0148-9062(98)00183-1

Lönnqvist, M, Hökmark, H, 2013. Approach to estimating the maximum depth for glacially induced hydraulic jacking in fractured crystalline rock at Forsmark, Sweden. Journal of Geophysical Research, vol. 118(3), 1777–1791. https://doi.org/10.1002/jgrf.20106

Ma, K F, Brodsky, E E, Mori, J, Chen, J, Song, T R A, Kanamori, H, 2003. Evidence for fault lubrication during the 1999 Chi-Chi, Taiwan, earthquake (Mw7.6). Geophysical Research Letters, vol. 30(5). https://doi.org/10.1029/2002gl015380

Ma, K F, Kanamori, H, 1991. Aftershock sequence of the 3 December 1988 Pasadena earthquake. Bulletin of the Seismological Society of America, vol. 81(6), 2310–2319.

Makhnenko, R Y, Labuz, J F, 2016. Elastic and inelastic deformation of fluid-saturated rock. Philosophical Transactions of the Royal Society a-Mathematical Physical and Engineering Sciences, vol. 374(2078). https://doi.org/10.1098/rsta.2015.0422

Martin, C D, 2007. Quantifying in situ stress magnitudes and orientations for Forsmark. Forsmark stage 2.2. SKB R-07-26, Svensk Kärnbränslehantering AB.

Mauk, F J, Christensen, D, Henry, S, 1982. The Sharpsburg, Kentucky, earthquake 27 July 1980: mainshock parameters and isoseismal maps. Bulletin of the Seismological Society of America, vol. 72(1), 221–236.

Mesri, G, Adachi, K, Ullrich, C R, 1976. Pore pressure response in rock to undrained change in all-round stress. Geotechnique, vol. 26(2), 317–330. https://doi.org/10.1680/geot.1976.26.2.317

Moreno, D G, Camelbeeck, T, 2013. Comparison of ground motions estimated from prediction equations and from observed damage during the M = 4.6 1983 Liege earthquake (Belgium). Natural Hazards and Earth System Sciences, vol. 13(8), 1983–1997. https://doi.org/10.5194/nhess-13-1983-2013

Munier, R, Adams, J, Brandes, C, Brooks, G, Dehls, J, Einarsson, P, Tassis, G, 2020. International database of Glacially Induced Faults PANGAEA. https://doi.org/10.1594/PANGAEA.922705

Nabelek, J, Suarez, G, 1989. The 1983 Goodnow earthquake in the central Adirondacks, New York: rupture of a simple, circular crack. Bulletin of the Seismological Society of America, vol. 79(6), 1762–1777.

Näslund, J O, 2006. Ice sheet dynamics, in Climate and climate related issues for the safety assessment SR-Can. SKB TR-06-23, Svensk Kärnbränslehantering AB.

Olofsson, I, Simeonov, A, Stephens, M, Follin, S, Nilsson, A C, Röshoff, K, Persson, L, 2007. Site descriptive modelling Forsmark, stage 2.2. A fracture domain concept as a basis for the statistical modelling of fractures and minor deformation zones, and interdisciplinary coordination. SKB R-07-15, Svensk Kärnbränslehantering AB.

Olsen, K B, Madariaga, R, Archuleta, R J, 1997. Three-dimensional dynamic simulation of the 1992 Landers earthquake. Science, vol. 278(5339), 834–838. https://doi.org/10.1126/science.278.5339.834

Peppin, W A, Honjas, W, Somerville, M R, Vetter, U R, 1989. Precise master-event locations of aftershocks of the 4 October 1978 Wheeler Crest earthquake sequence near Long Valley, California. Bulletin of the Seismological Society of America, vol. 79(1), 67–76.

Pisarska-Jamroży, M, Belzyt, S, Börner, A, Hoffmann, G, Hüneke, H, Kenzler, M, van Loon, A J, 2018. Evidence from seismites for glacio-isostatically induced crustal faulting in front of an advancing land-ice mass (Rügen Island, SW Baltic Sea). Tectonophysics, vol. 745, 338–348. https://doi.org/https://doi.org/10.1016/j.tecto.2018.08.004

Power, W L, Tullis, T E, 1991. Euclidean and fractal models for the description of rock surface roughness. Journal of Geophysical Research-Solid Earth and Planets, vol. 96(B1), 415–424. https://doi.org/10.1029/90jb02107

Rice, J R, 2006. Heating and weakening of faults during earthquake slip. Journal of Geophysical Research-Solid Earth, vol. 111(B5). https://doi.org/10.1029/2005jb004006

Rice, J R, Cleary, M P, 1976. Some basic stress diffusion solutions for fluid-saturated elastic porous media with compressible constituents. Reviews of Geophysics, vol. 14(2), 227–241. https://doi.org/10.1029/RG014i002p00227

Ruina, A, 1983. Slip instability and state variable friction laws. Journal of Geophysical Research, vol. 88(NB12), 359–370. https://doi.org/10.1029/JB088iB12p10359

Scholz, C H, 2002. The Mechanics of Earthquakes and Faulting, 2nd edition. Cambridge, Cambridge University Press.

Simpson, G, 2001. Influence of compression-induced fluid pressures on rock strength in the brittle crust. Journal of Geophysical Research-Solid Earth, vol.106(B9), 19465–19478. https://doi.org/10.1029/2001jb000314

SKB, 2008. Site description of Forsmark at completion of the site investigation phase. SDM-Site Forsmark. SKB TR-08-05, Svensk Kärnbränslehantering AB.

SKB, 2010a. Buffer, backfill and closure process report for the safety assessment SR-Site. SKB TR-10-47, Svensk Kärnbränslehantering AB.

SKB, 2010b. Geosphere process report for the safety assessment SR-Site. SKB TR-10-48, Svensk Kärnbränslehantering AB.

SKB, 2011. Long-term safety for the final repository for spent nuclear fuel at Forsmark. Main report of the SR-Site project, SKB TR-11-01, Svensk Kärnbränslehantering AB.

Slunga, R S, 1991. The Baltic Shield earthquakes. Tectonophysics, vol. 189, 323–331.

Spence, W, Langer, C J, Choy, G L, 1996. Rare, large earthquakes at the Laramide deformation front – Colorado (1882) and Wyoming (1984). Bulletin of the Seismological Society of America, vol. 86(6), 1804–1819.

Steffen, R, Steffen, H, 2021. Reactivation of Non-Optimally Orientated Faults Due to Glacially Induced Stresses. Tectonics, vol. 40(11), e2021TC006853. https://doi.org/https://doi.org/10.1029/2021TC006853

Stephansson, O, Ljunggren, C, Jing, L, 1991. Stress measurements and tectonic implications for Fennoscandia. In: Tectonophysics, vol. 189, 317–322.

Stephens, M, B, Simeonov, A, 2015. Description of deformation zone model version 2.3, Forsmark, SKB R-14-28. Svensk Kärnbränslehantering AB.

Stephens, M B, Fox, A, La Pointe, P, Simeonov, A, Isaksson, H, Hermanson, J, Öhman, J, 2009. Geology Forsmark. Site descriptive modelling Forsmark stage 2.2. SKB R-07-45, Svensk Kärnbränslehantering AB.

Thatcher, W, Hamilton, R M, 1973. Aftershocks and source characteristics of 1969 Coyote-Mountain Earthquake San-Jacinto Fault zone, California. Bulletin of the Seismological Society of America, vol. 63(2), 647–661.

USGS, 2020. U.S. Geological Survey WebSite. Available at: https://earthquake.usgs.gov/earthquakes/sarch/. USGS.

Wald, D J, Heaton, T H, 1994. Spatial and temporal distribution of slip for the 1992 Landers, California, earthquake. Bulletin of the Seismological Society of America, vol. 84(3), 668–691.

Wald, D J, Heaton, T H, Hudnut, K W, 1996. The slip history of the 1994 Northridge, California, earthquake determined from strong-motion, teleseismic, GPS, and leveling data. Bulletin of the Seismological Society of America, vol. 86(1), S49–S70.

Walter, W R, 1993. Source parameters of the June 29, 1992 Little Skull Mountain Earthquake from complete regional wave-forms at a single station. Geophysical Research Letters, vol. 20(5), 403–406. https://doi.org/10.1029/92gl03031

Wei, B Z, Chung, W Y, 1993. Regional waveform constraints on the source parameters of the Xunwu, China, earthquake of 2 August 1987, with implications for mid-plate seismotectonics. Physics of the Earth and Planetary Interiors, vol. 78(1-2), 57–68. https://doi.org/10.1016/0031-9201(93)90084-m

Wells, D L, Coppersmith, K J, 1994. New empirical relationships among magnitude, rupture length, rupture width, rupture area and surface displacement. Bulletin of the Seismological Society of America, vol. 84(4), 974–1002.

Wesson, R L, Nicholson, C, 1986. Studies of the January 31, 1986 northeastern Ohio earthquake. A report to the U.S. Nuclear Regulatory Commission. USGS-Open-File report 86-331. US Geological Survey, Reston, Virginia. https://doi.org/10.3133/ofr86331

Westaway, R, Gawthorpe, R, Tozzi, M, 1989. Seismological and fieldobservations of the 1984 Lazio-Abruzzo Earthquakes – Implications for the active tectonics of Italy. Geophysical Journal International, vol. 98(3), 489–514. https://doi.org/10.1111/j.1365-246X.1989.tb02285.x

Xu, S, Ben-Zion, Y, Ampuero, J P, 2012. Properties of inelastic yielding zones generated by in-plane dynamic ruptures-I. Model description and basic results. Geophysical Journal International, vol. 191(3), 1325–1342. https://doi.org/10.1111/j.1365-246X.2012.05679.x

Yao, L, Ma, S L, Chen, J Y, Shimamoto, T, He, H L, 2018. Flash Heating and Local Fluid Pressurization Lead to Rapid Weakening in Water-Saturated Fault Gouges. Journal of Geophysical Research-Solid Earth, vol. 123(10), 9084–9100. https://doi.org/10.1029/2018jb016132

Zhou, Y, McNally, K C, Lay, T, 1993. Analysis of the 1986 Mt. Lewis, California, earthquake: preshock sequence-mainshock-aftershock sequence. Physics of the Earth and Planetary Interiors, vol. 75(4), 267–288. https://doi.org/10.1016/0031-9201(93)90005-t

Zoback, M D, Townend, J, 2001. Implications of hydrostatic pore pressures and high crustal strength for the deformation of intraplate lithosphere. Tectonophysics, vol. 336(1-4), 19–30. https://doi.org/10.1016/S0040-1951(01)00091-9

The sensitivity of zone stability to zone orientation and background stress trend

CFS of the six steep Forsmark deformation zones is calculated at different depths under forebulge stress conditions for different zone orientations (strikes and dips) and different background stress field orientations. The two longest zones (ZFMNW0017 and ZFMWNW0123) are assumed to reach 5 km depth while the maximum depth extension for the other zones is assumed to be 3 km. The friction coefficient of the zones is assumed to be $\mu = 0.7$. The following parameter values are considered:

- Three values of the σ_H trend of the background stress field: N125°E, N145°E and N165°E.

- The strikes of the zones are varied according to the uncertainty ranges given in Table 2-1.

- The dip angles of the zones are varied according to the uncertainty ranges given in Table 2-1. Note that for all zones, the upper end of the range means a dip angle > 90°. Here, the maximum dip is set to 90°.

Each of Figure A-1 to Figure A-6 shows contour plots of *CFS* for one zone. In these plots the Base case σ_h stress magnitude is applied (Equation 2-1). Each column shows results for one σ_H stress trend. In the upper row, *CFS* values for different strikes are presented (keeping the dip angle at the nominal value) while *CFS* variations with respect to dip are shown in the bottom row (keeping the strike at the nominal value).
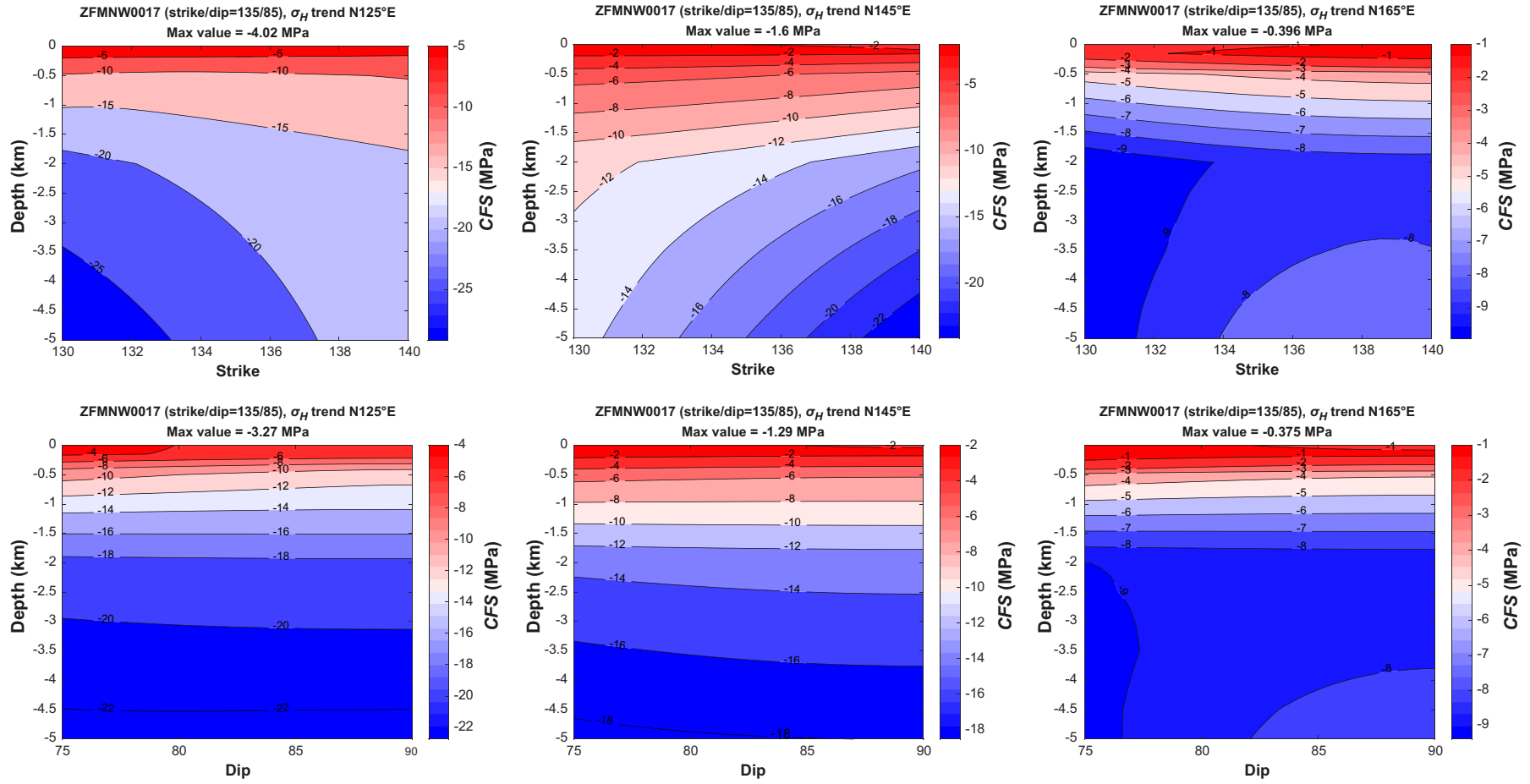
Figure A-1. *CFS on ZFMNW0017 for different input assumptions.*
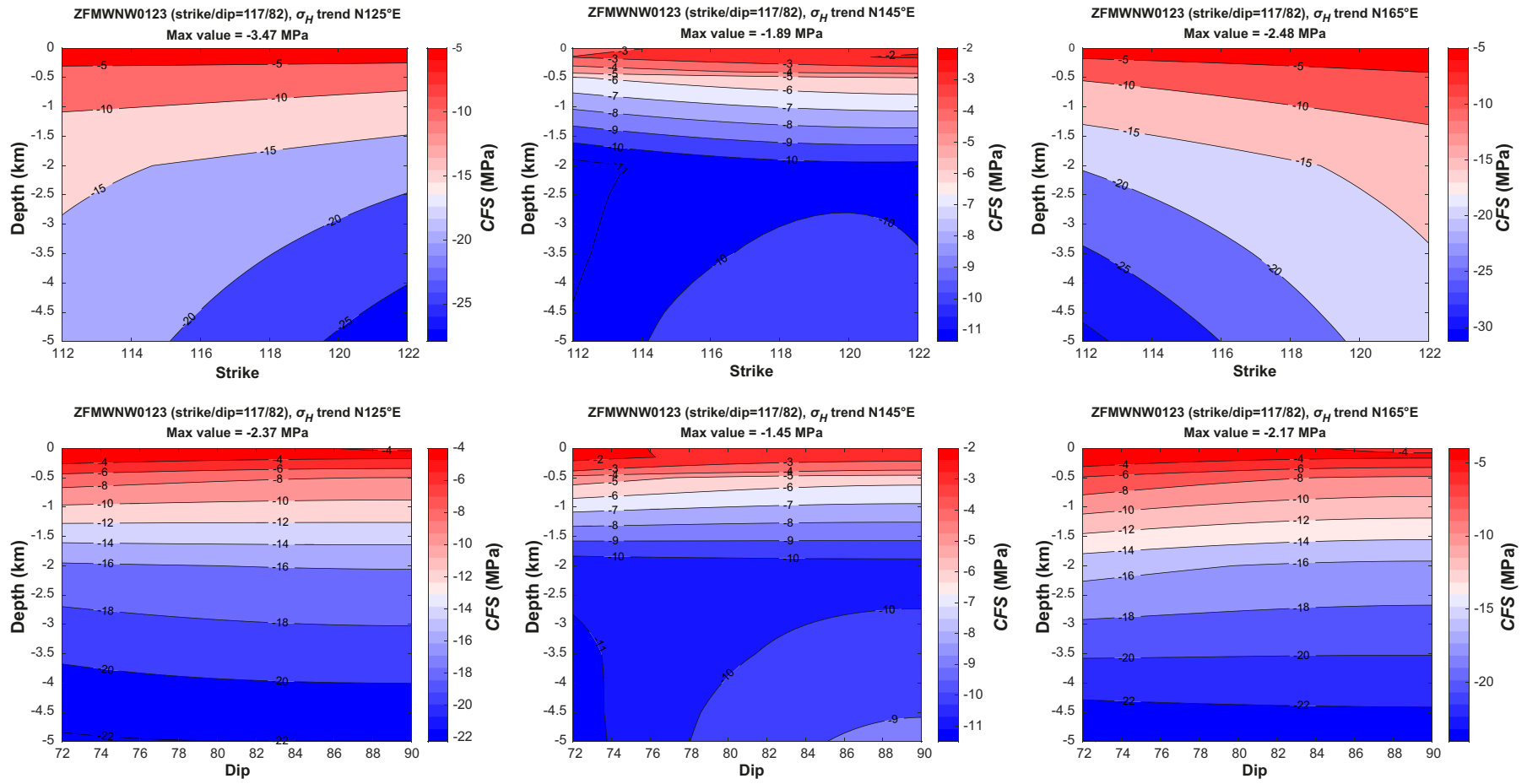
Figure A-2. *CFS on ZFMWNW0123 for different input assumptions.*
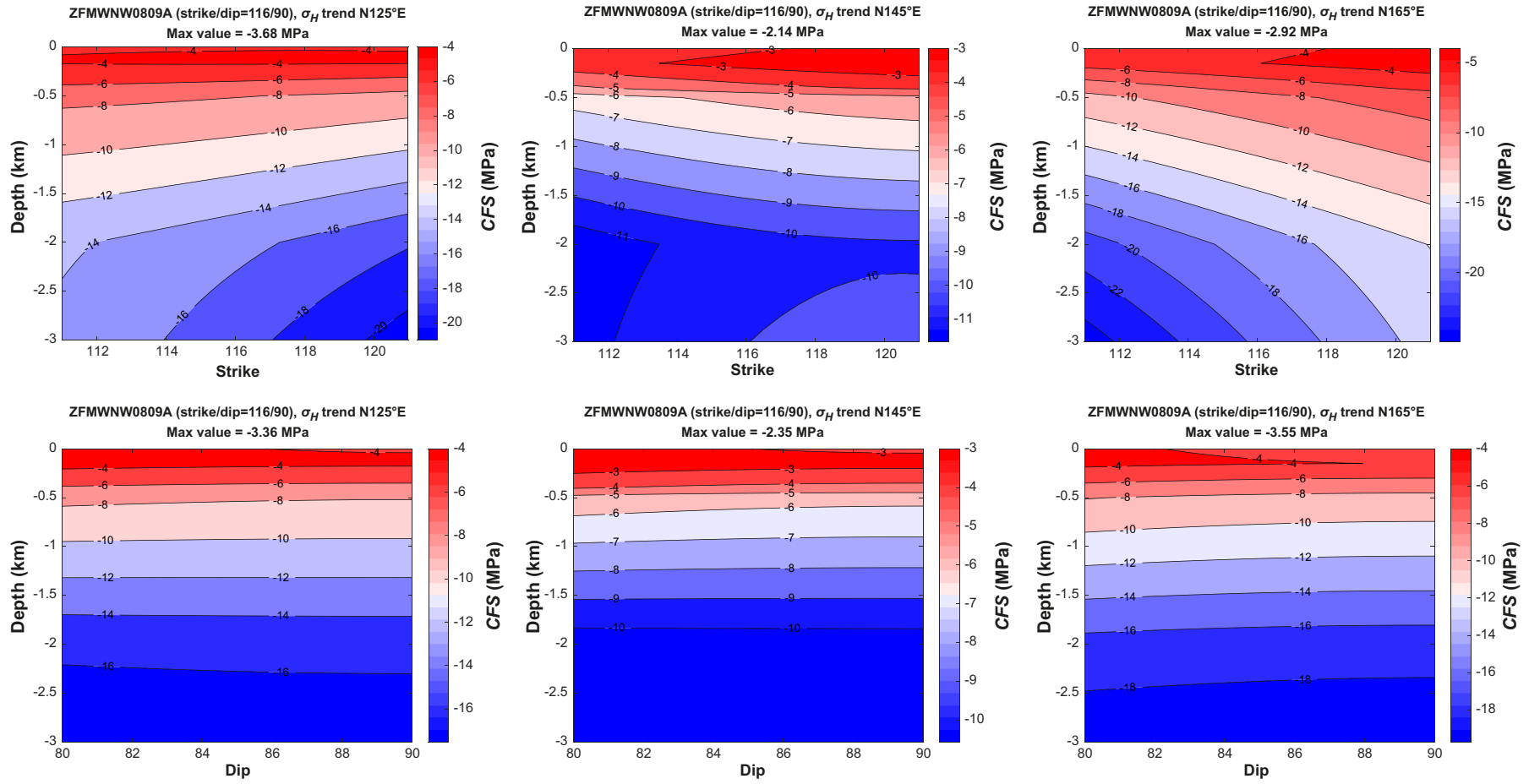
Figure A-3. *CFS on ZFMWNW0809A for different input assumptions.*
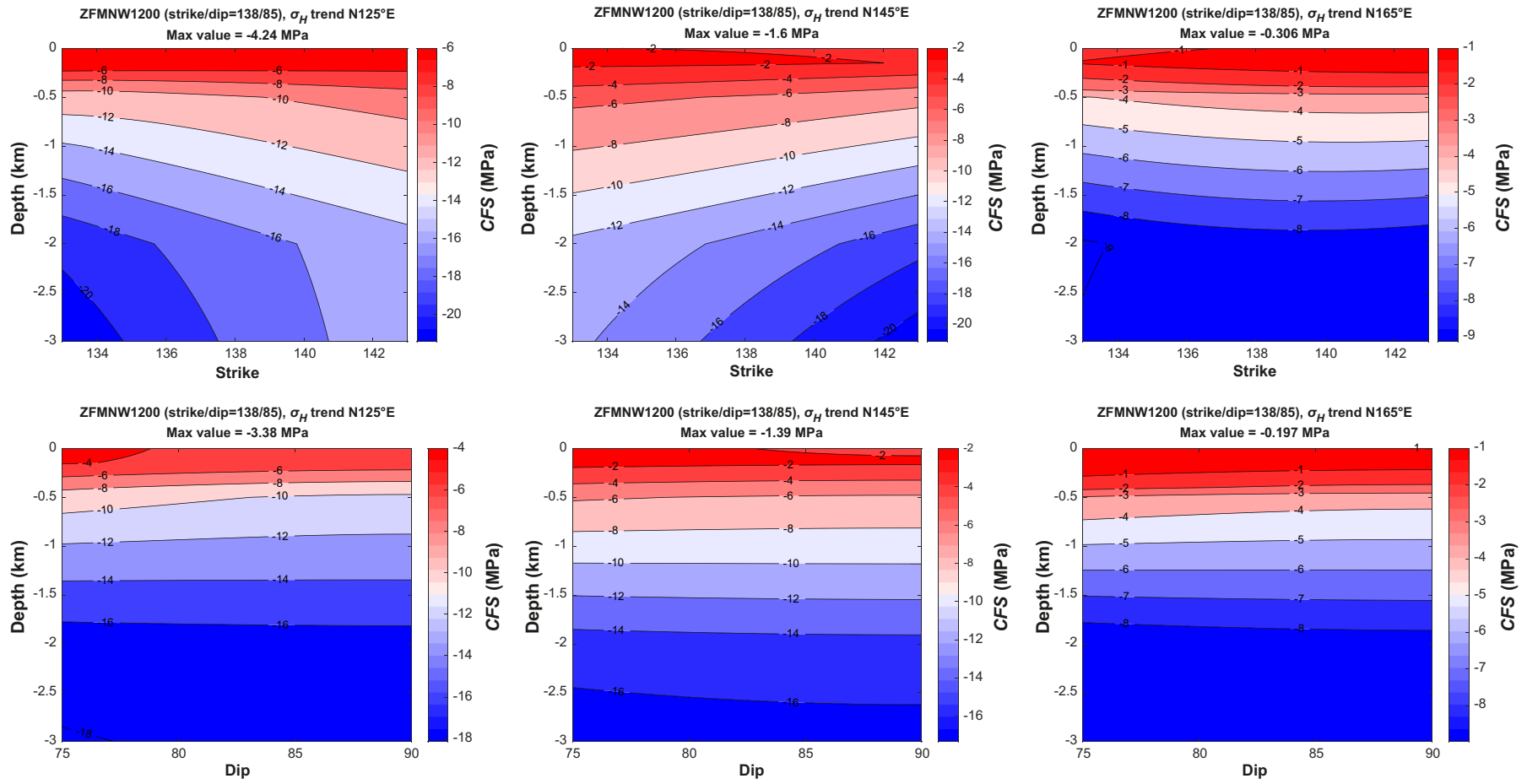
Figure A-4. *CFS on ZFMNW1200 for different input assumptions.*
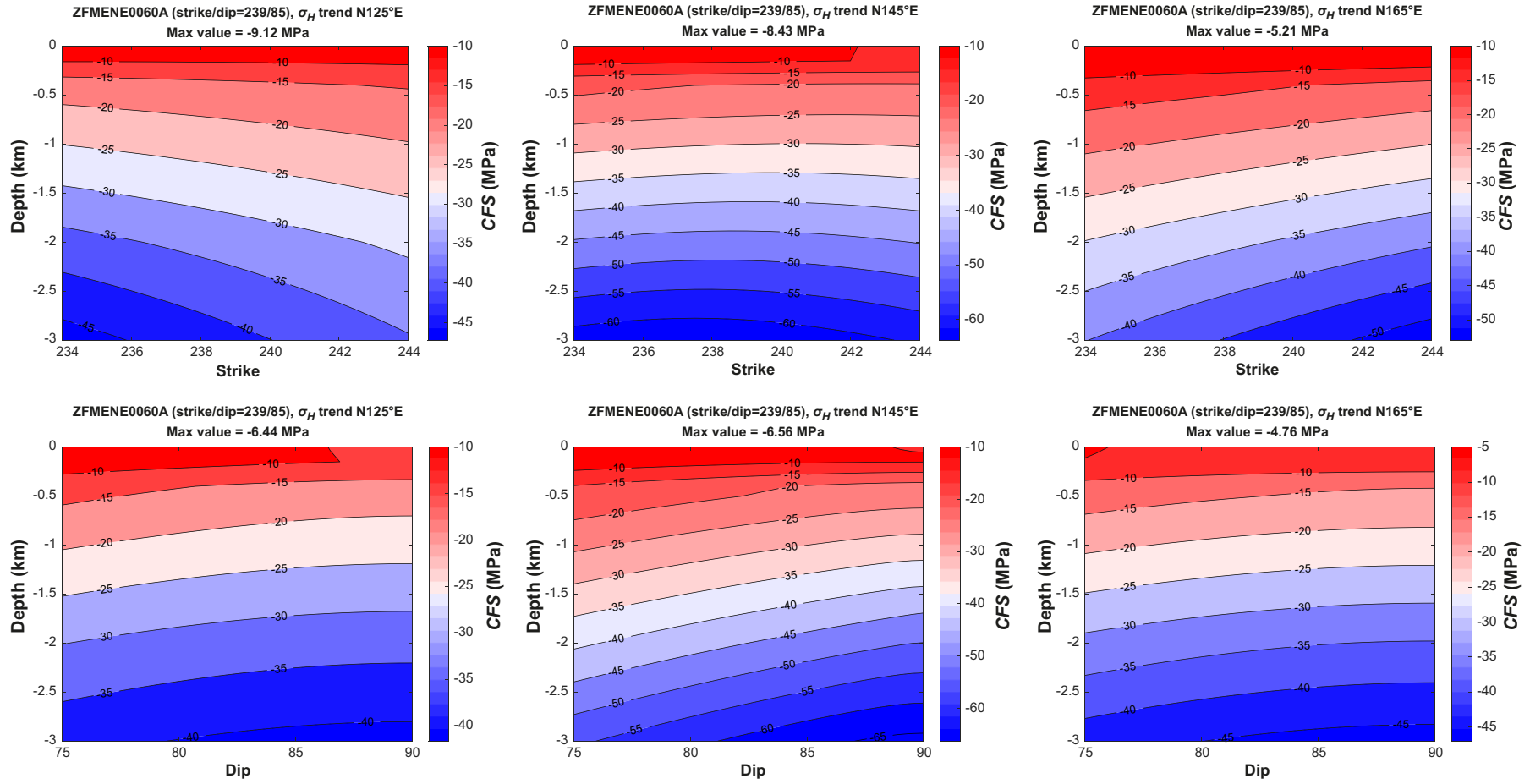
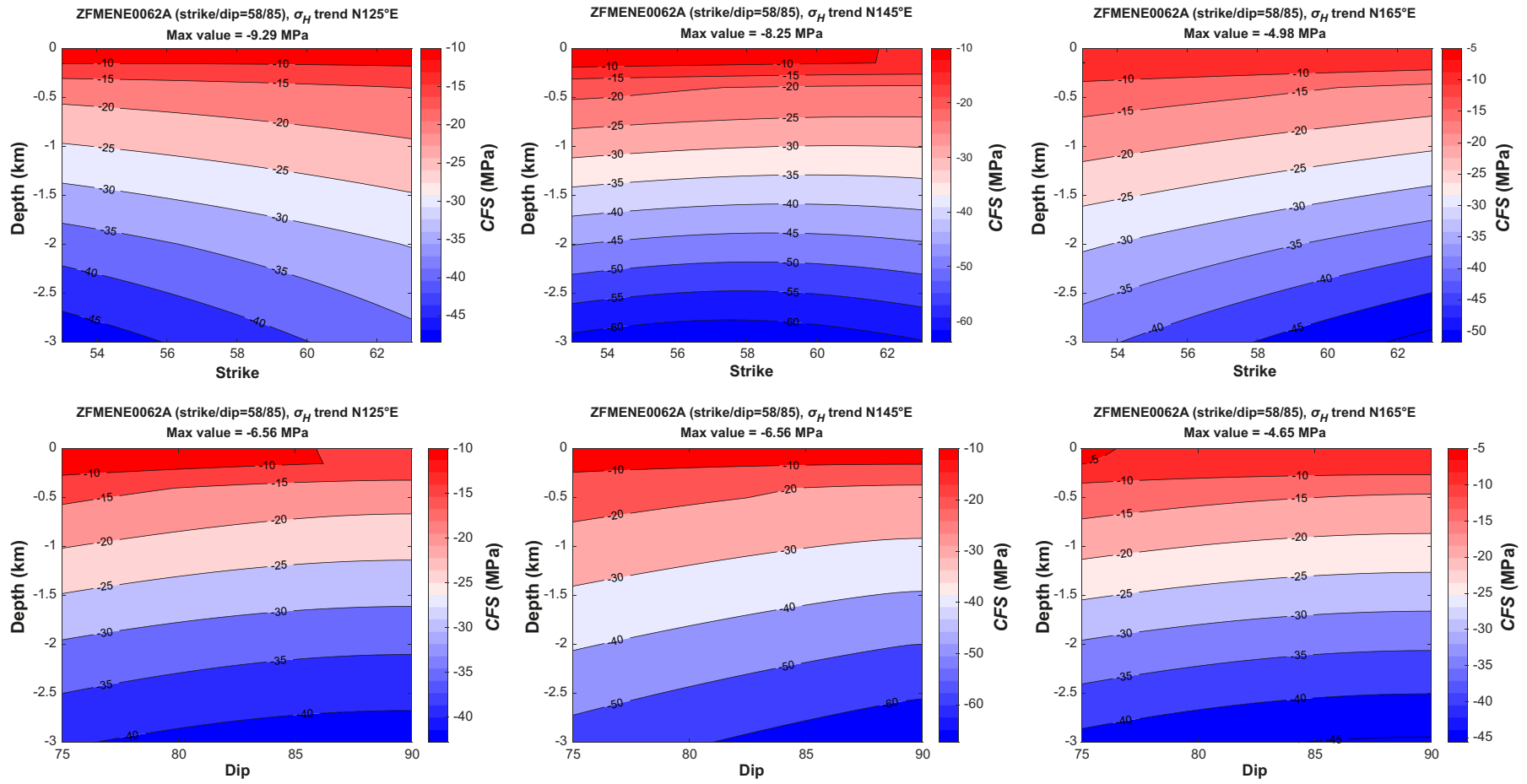**Figure A-5.** *CFS on ZFMENE0060A for different input assumptions.*

Figure A-6. *CFS on ZFMENE0062A for different input assumptions.*

Target fracture locations

Figure B-1 shows an overview of the target fracture locations. The fracture numbers refer to the numbers given in Table B-1 where the distances between target fractures and deformation zones are presented. The distances are measured from the target fracture centre to the closest point on respective zone plane.
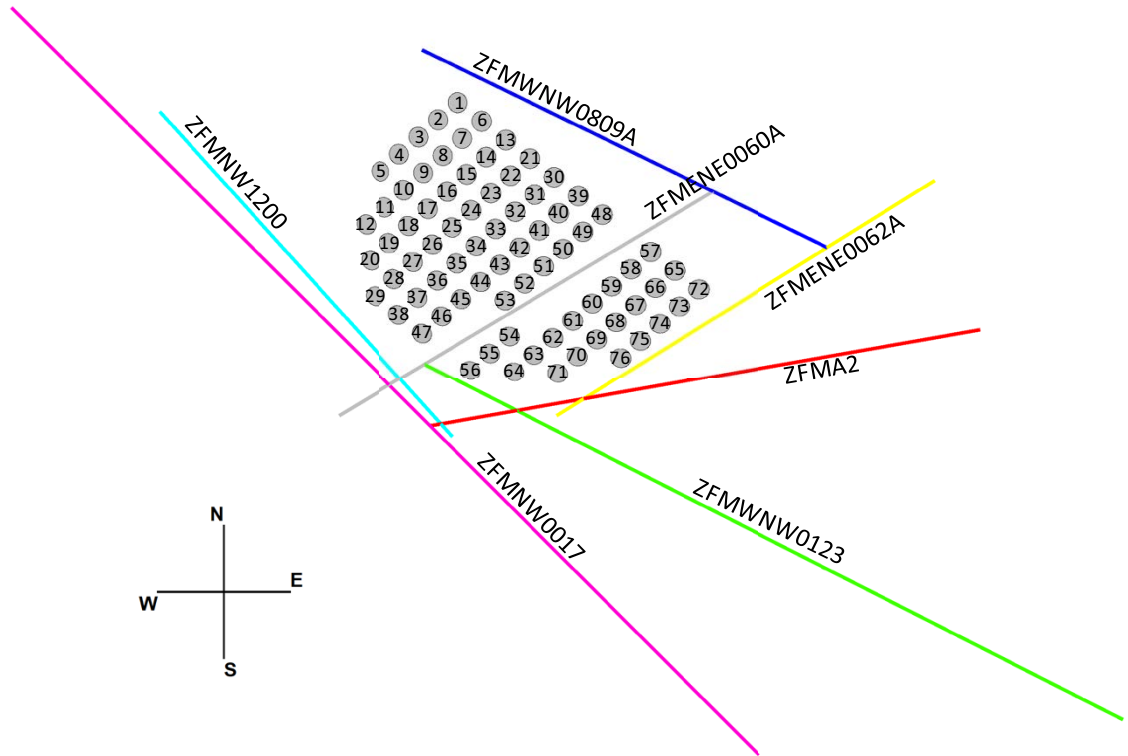
Figure B-1. *Map view at repository depth (470 m) showing target fracture locations.*

Table B-1. Target fracture-to-zone plane distances.

| Fracture | Shortest distance from given deformation zone plane (m) | | | | | | |
	ZFMA2	ZFMNW 0017	ZFMWNW 0123	ZFMNW 1200	ZFMWNW 0809A	ZFMENE 0060A	ZFMENE 0062A
1	1364	1839	1957	1687	237	1535	2359
2	1270	1647	1818	1495	416	1500	2327
3	1177	1455	1689	1303	594	1465	2296
4	1085	1263	1573	1110	772	1430	2264
5	995	1071	1472	918	951	1395	2236
6	1208	1868	1849	1727	283	1324	2147
7	1116	1676	1697	1535	462	1290	2116
8	1025	1484	1554	1343	640	1255	2084
9	937	1292	1422	1150	818	1220	2052
10	851	1100	1304	958	997	1185	2021
11	769	908	1205	766	1175	1150	2003
12	692	716	1129	573	1353	1115	2003
13	1055	1896	1763	1767	330	1114	1935
14	966	1704	1599	1575	508	1079	1904
15	880	1512	1442	1383	686	1044	1872
16	796	1320	1293	1190	865	1010	1841
17	717	1128	1156	998	1043	975	1809
18	645	936	1036	806	1221	940	1785
19	580	744	939	613	1400	905	1781
20	528	552	873	421	1578	870	1797
21	908	1924	1702	1807	376	904	1724
22	824	1732	1527	1615	554	869	1692
23	743	1540	1357	1423	733	834	1661
24	668	1348	1192	1230	911	799	1629
25	601	1156	1035	1038	1089	765	1598
26	544	964	891	846	1268	730	1568
27	500	772	767	653	1446	695	1559
28	459	580	674	461	1624	660	1573
29	418	388	627	269	1803	625	1610
30	770	1953	1659	1848	422	694	1512
31	693	1761	1482	1655	600	659	1480
32	622	1569	1304	1463	779	624	1449
33	562	1377	1126	1270	957	589	1417
34	513	1185	952	1078	1135	554	1386
35	472	993	784	886	1314	519	1354
36	432	801	629	693	1492	485	1338
37	391	609	498	501	1670	450	1349
38	350	417	416	309	1849	415	1386
39	645	1981	1618	1888	468	483	1300
40	581	1789	1440	1695	647	448	1269
41	528	1597	1262	1503	825	414	1237
42	486	1405	1084	1310	1003	379	1206
43	445	1213	906	1118	1182	344	1174
44	404	1021	728	926	1360	309	1143
45	363	829	550	733	1538	274	1118
46	322	637	377	541	1717	239	1124
47	281	445	230	349	1895	205	1163
48	544	2010	1576	1928	515	273	1089
49	500	1818	1398	1735	693	238	1057
50	459	1626	1220	1543	871	203	1026
51	418	1434	1042	1350	1050	168	994
52	377	1242	864	1158	1228	134	962
53	336	1050	686	966	1406	99	931
54	227	886	467	813	1631	146	688

Table B-1. Continued.

Fracture	Shortest distance from given deformation zone plane (m)						
	ZFMA2	ZFMNW 0017	ZFMWNW 0123	ZFMNW 1200	ZFMWNW 0809A	ZFMENE 0060A	ZFMENE 0062A
55	186	694	289	621	1809	181	676
56	145	502	111	429	1987	216	718
57	404	2066	1492	2008	607	148	665
58	363	1874	1314	1815	785	182	634
59	323	1682	1136	1623	964	217	602
60	282	1490	958	1431	1142	252	571
61	241	1298	780	1238	1320	287	539
62	200	1106	603	1046	1499	322	508
63	159	914	425	853	1677	357	476
64	118	722	247	661	1855	391	453
65	336	2095	1450	2055	653	358	454
66	295	1903	1272	1863	832	393	422
67	254	1711	1094	1671	1010	428	390
68	213	1519	916	1480	1188	462	359
69	172	1327	738	1289	1367	497	327
70	131	1135	561	1098	1545	532	296
71	90	943	383	909	1723	567	264
72	268	2123	1408	2124	699	568	242
73	227	1931	1230	1935	878	603	210
74	186	1739	1052	1747	1056	638	179
75	145	1547	874	1560	1234	673	147
76	104	1355	696	1374	1413	708	116

Comparison of rupture models

Model description

To examine how the model for rupture propagation could impact on the near-fault secondary stress effects, a quasi-2D model was set up in 3DEC. The model was used to simulate an earthquake rupture along a 6 km long fault (Figure C-1).

The model comprised a thin slice of linear elastic, homogeneous and isotropic continuum with the dimensions 14 000 m, 12 m, and 6 000 m in the x-, y- and z-directions, respectively. A 6 km long discontinuity was included centrally in the model (at $z = 0$) (Figure C-1). As in the other models described in this report, the discontinuity responded to loads according to an idealized elasto-plastic material model with constant stiffnesses in both the normal and shear directions, and failure was modelled according to a Coulomb criterion (Itasca 2020). Both shear- and normal stiffness were set to 10 GPa/m and the cohesion was set to zero. An initial stress field according to Table C-1 was applied. The continuum properties are given in Section 4.3 in the main text.

Table C-1. Initial stresses.

σ_{xx}	σ_{yy}	σ_{zz}	σ_{xy}	σ_{xz}	σ_{yz}
24.76	20.00	17.24	0	−10.34	0

Three models for rupture propagation were tested:

- Velocity-weakening (VW) (Beeler et al. 2008) (applied in this study, see Section 4.3 in the main text).

- Slip-weakening (SW) (e.g. Ida 1972).

- Time-weakening (TW) (cf e.g. Fälth et al. 2016).
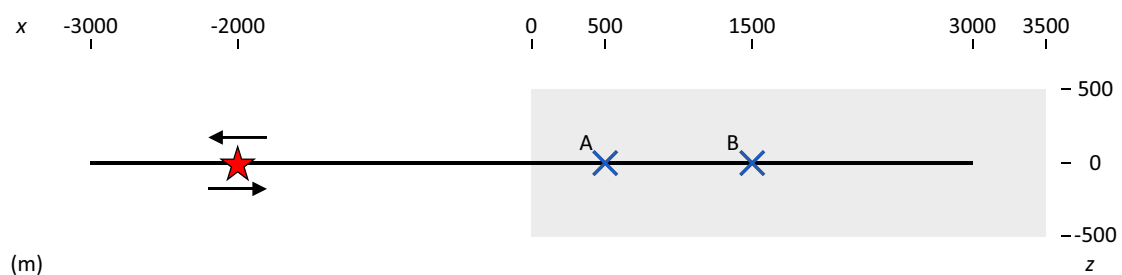
Figure C-1. *Outline of fault plane and monitoring points. The rupture initiation point is indicated by the red star. The blue crosses indicate positions for monitoring of fault slip and strength evolution. During simulation, CFS on optimally oriented virtual planes was calculated from continuum stresses within the shaded area.*

In the SW model, the friction coefficient of the fault plane is ramped down linearly as a function of slip from the static friction coefficient μ_s to the dynamic friction coefficient μ_d. For slip values exceeding the critical slip distance d_c, the dynamic friction coefficient μ_d is set (Figure C-2, left). As in the case with the VW model, the rupture propagates spontaneously, governed by the stress conditions at the rupture front.

In the TW case, a constant and forced rupture speed V_r is adopted, and at rupture front arrival the friction coefficient is ramped down to μ_d over a specified time t_{red}. (Figure C-2, right). Here, the fault strength is assumed to be infinite. Prior to the programmed rupture front arrival, slip is suppressed by assignment of the friction coefficient such that it matches the shear-to-normal stress ratio on the fault.

First, a VW simulation was performed. In that simulation the input parameters were set such that the rupture velocity was kept below the shear wave velocity of the continuum, i.e., $V_r/V_s < 1$. Then, by running several test simulations, the input parameters to the SW model were calibrated such that the seismic moment M_0 (cf Equation 1-2 in the main text) matched approximately that generated in the VW simulation. Of particular importance in this respect is the value of μ_d, which is the parameter of primary importance for stress drop and slip. To reduce influence of the rupture initiation routine, the seismic moment was evaluated for $x \geq 0$, cf Figure C-1. Finally, the TW simulation was performed. Here, t_{red} was set such that it matched approximately the corresponding value obtained in the VW case. Two cases of rupture speed V_r were tested, $V_r/V_s = 0.85$ and $V_r/V_s = 0.63$. These V_r values were chosen such that the rupture front arrival times at monitoring points A and B matched approximately the times obtained in the VW and SW cases, respectively. The value of μ_d was set equal to that in the SW simulation, meaning that approximately the same seismic moment M_0 was generated. The input parameter values set in the different rupture models are summarised in Table C-2. Note that the value of μ_s had to be reduced in the SW case to make a spontaneous rupture possible. Note also that the VW parameters differ from those applied in the Forsmark model presented in the main report. The parameters here were set to give a stable rupture at subshear speed, i.e., $V_r/V_s < 1$, and strong secondary stress effects. Recall that the purpose here was not to mimic reality but to compare the impact of different rupture models.

The rupture was initiated at the initiation point shown in Figure C-1. In the VW and SW cases, where the rupture propagates spontaneously, it was initiated using the methodology described in Section 4.3 in the main text.

Table C-2. Model input parameter values.

Model	μ_s	μ_d	v^* (m/s)	d_c (m)	t_{red} (s)	V_r/V_s
VW	0.74	0.28	0.75	-	-	-
SW	0.70	0.577	-	0.007	-	-
TW, Vr0.85	Inf.	0.577	-	-	0.025	0.85
TW, Vr0.63	Inf.	0.577	-	-	0.025	0.63
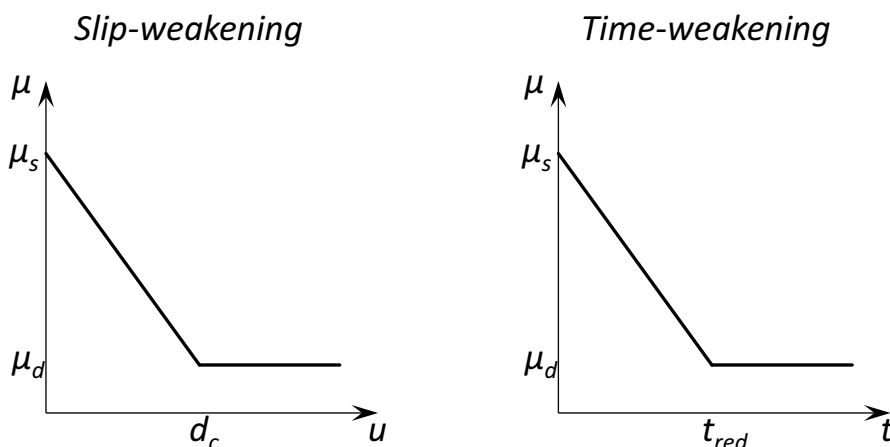
Figure C-2. *Left: Linear slip-weakening model. Right: Time-weakening model.*

Results

The source parameters for all simulation cases are summarised in Table C-3. The source parameters were evaluated at positions where $x \geq 0$. The seismic moment and average slip differ some 3–4 % between the highest and lowest values. Despite the similarity in seismic moment, slip and stress drop, there are significant differences in peak slip velocity. The difference is most pronounced when comparing the value of the VW model with the values of the other models. Since the friction coefficient is modelled as a function of slip velocity in the VW model, the fault strength is fully recovered when the velocity goes back to zero after a slip episode. Hence, there is just a short pulse of slip during which the velocity must be high to generate the same amount of slip as in the SW and TW cases. In those latter cases the strength degradation is assumed to be permanent and hence a much higher μ_d value must be set to obtain the same amount of slip as that generated in the VW case.

The differences in fault strength and slip evolution are illustrated in Figure C-3 and Figure C-4, where those quantities as monitored at point A and B, respectively, are shown. First, one can note that the arrival of the rupture in the SW case is somewhat later than in the VW case. This indicates that the rupture velocity in the SW tends to be lower. Most notable is the short slip period in the VW case, with large drop in friction coefficient and associated high slip velocity. This response differs significantly from what is obtained in the other cases where the strength degradation is permanent. Note also the increase of μ in the TW model as the rupture front approaches the monitoring point. This is due to the increase in shear stress. This effect is more pronounced at longer propagation distances and hence the stress peak is higher at monitoring point B than at A (cf Figure C-3 and Figure C-4). This effect is also reflected in the higher slip velocities obtained at point B.

Table C-3. Source parameters.

Model	M_0 (-10^{13} Nm)	$\Delta\tau_{avg}$ (MPa)	u_{avg} (m)	Peak slip vel. (m/s)
VW	6.40	0.49	0.063	2.9
SW	6.50	0.39	0.064	0.42
TW, Vr0.85	6.64	0.39	0.065	0.39
TW, Vr0.63	6.47	0.39	0.064	0.35
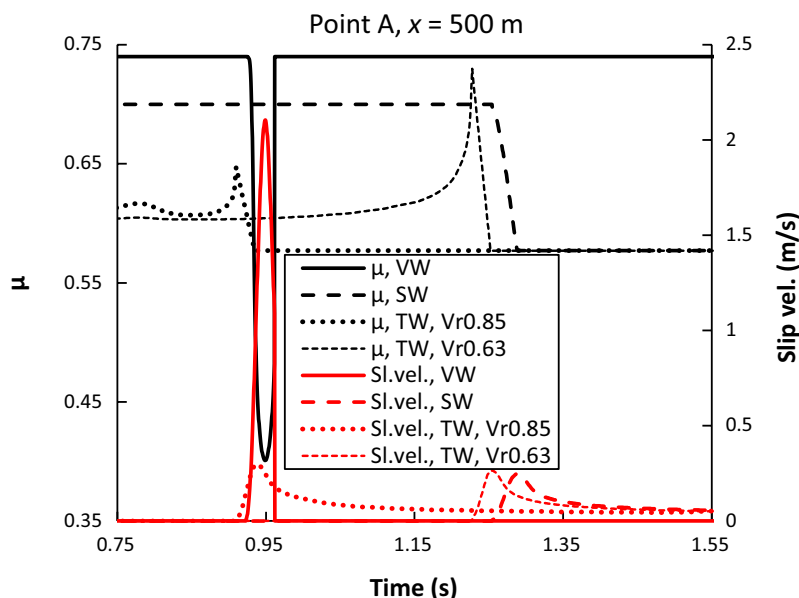
Figure C-3. Temporal evolution of friction coefficient and slip velocity at monitoring point A (x = 500 m, cf Figure C-1) in all four simulated cases.
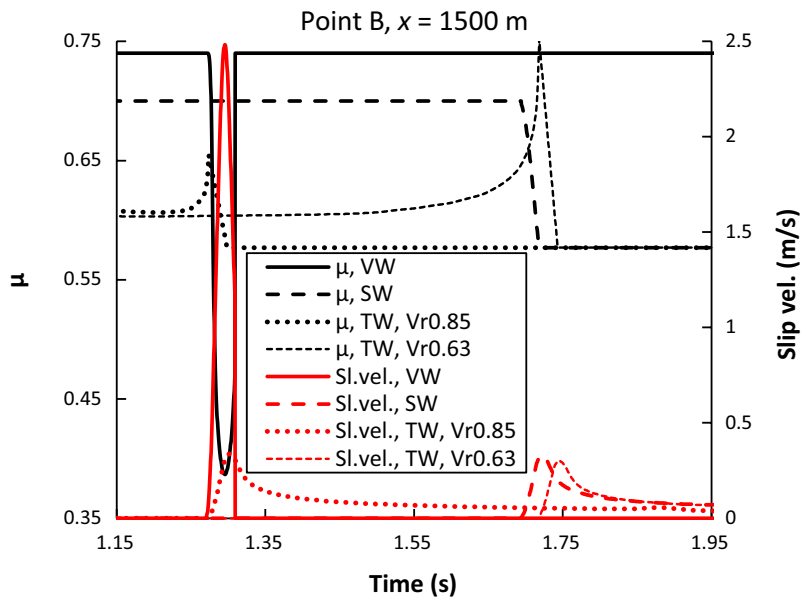
Figure C-4. *Temporal evolution of friction coefficient and slip velocity at monitoring point B (x = 1 500 m, cf Figure C-1) in all four simulated cases.*

During calculation, based on continuum stresses around the fault plane (cf Figure C-1), *CFS* (Equation 1-1 in the main text) was calculated on optimally oriented virtual fracture planes and the peak values were stored. Contours of peak *CFS* values generated in the VW and SW cases are shown in Figure C-5. Corresponding results along a scan-line 200 m (at *z* = 200 m) from the fault plane are shown in Figure C-6. The results show that the short high velocity slip periods in the VW case generate near-fault stress transients that are significantly stronger than those generated in the other cases.
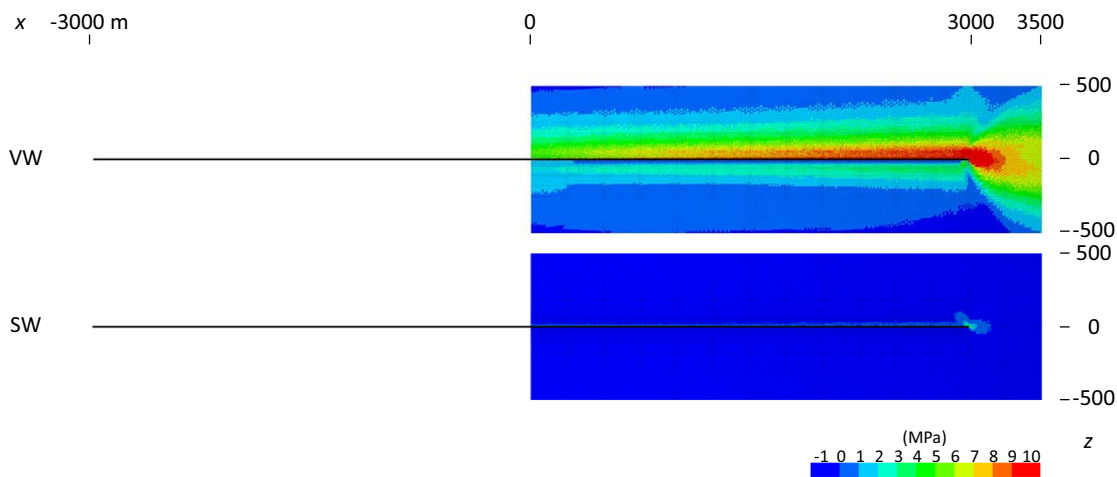
Figure C-5. *Contours of peak CFS values on optimally oriented virtual planes in the VW and SW cases. The black lines indicate the fault plane (cf Figure C-1).*
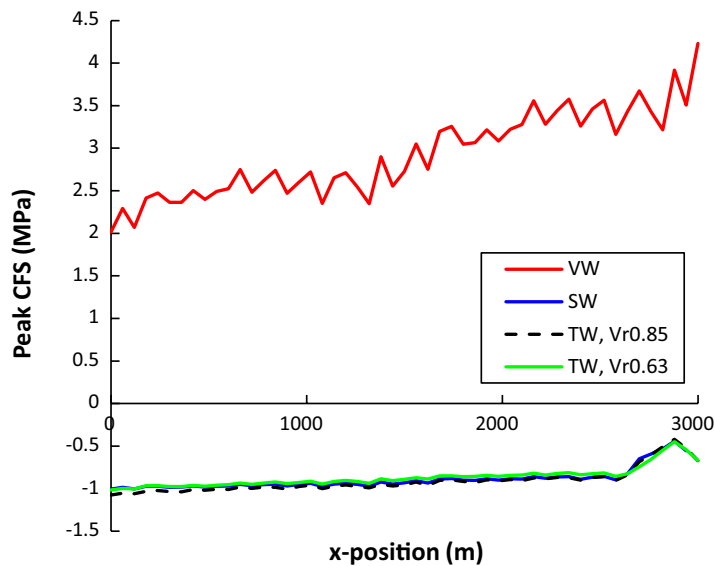
Figure C-6. *Peak CFS values on optimally oriented virtual planes at 200 m distance (z = 200 m) from the fault plane. The values were calculated from continuum stresses.*

The results presented above indicate that co-seismic secondary fracture displacements generated in a simulation where the VW model is used to simulate the primary fault rupture will tend to be larger than those obtained in a corresponding SW rupture simulation. To examine this further, an endglacial Forsmark simulation similar to the Gen27-21_SH145_UM-EG model was run, but with the SW model applied instead of the VW model. The model input parameters were set such that the model generated a seismic moment like that in the Gen27-21_SH145_UM-EG model (see Table 6-2 in the main text). The input parameters and source parameters in the SW model are summarised in Table C-4. The seismic moment differs about 5 % from that of the Gen27-21_SH145_UM-EG model.

Table C-4. Input parameters and source parameters in the Forsmark SW model.

Model	μ_s	μ_d	d_c (m)	M_0 (-10^{16} Nm)	u_{avg} (m)
Gen27-21_SH145_UM-EG-SW	0.78	0.645	0.015	4.1	0.063

Figure C-7 shows peak target fracture displacements in the Gen27-21_SH145_UM-EG model (cf Figure 6-22 in main text) along with the corresponding fracture displacements generated when applying the SW model for rupture propagation. The results in Figure C-7 are in accord with the results from the test models presented above; the VW model tends to give stronger secondary stress effects and larger secondary fracture displacements. The secondary fracture displacements generated when applying the VW model are on average 5 times larger than those generated when applying the SW model.
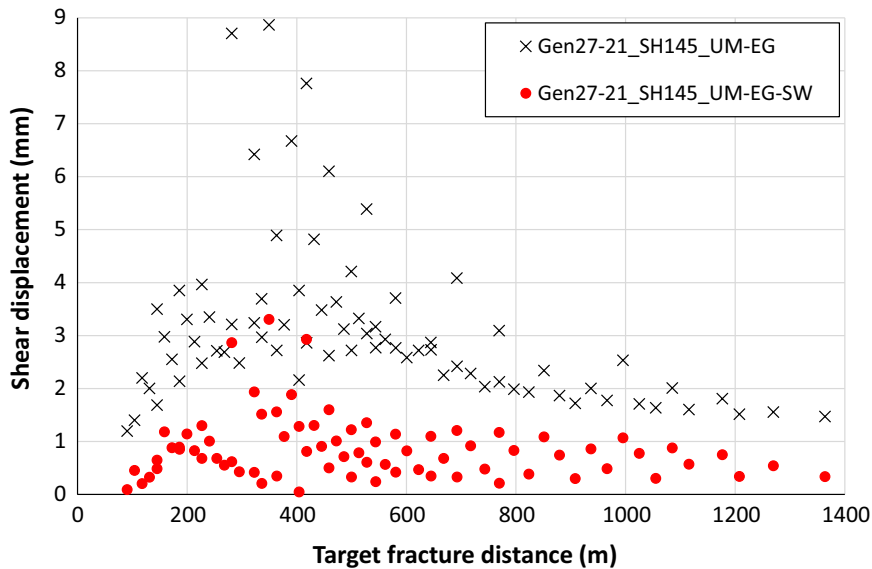
Figure C-7. *Target fracture peak shear displacements in the Gen27-21_SH145_UM-EG model (cf Figure 6-22 in main text) along with corresponding results generated in the Forsmark SW model. The distances are measured from the centre of each fracture to the nearest point on the ZFMA2 plane (see also Appendix B).*

Fault response in forebulge models

Here, plots of the fault response in all simulated forebulge rupture scenarios are presented. For each scenario, plots of normalised rupture velocity (V_r/V_s), peak slip velocity and slip are shown (Table D-1).

Table D-1. List of figures.

Figure number	Initiation on zone	σ_h reduction (%)	Plotted parameter
Figure D-1	ZFMNW0017	11	V_r/V_s
Figure D-2	ZFMNW0017	11	Peak slip velocity (m/s)
Figure D-3	ZFMNW0017	11	Slip (m)
Figure D-4	ZFMNW0017	43	V_r/V_s
Figure D-5	ZFMNW0017	43	Peak slip velocity (m/s)
Figure D-6	ZFMNW0017	43	Slip (m)
Figure D-7	ZFMNW1200	11	V_r/V_s
Figure D-8	ZFMNW1200	11	Peak slip velocity (m/s)
Figure D-9	ZFMNW1200	11	Slip (m)
Figure D-10	ZFMNW1200	43	V_r/V_s
Figure D-11	ZFMNW1200	43	Peak slip velocity (m/s)
Figure D-12	ZFMNW1200	43	Slip (m)
Figure D-13	ZFMWNW0123	11	V_r/V_s
Figure D-14	ZFMWNW0123	11	Peak slip velocity (m/s)
Figure D-15	ZFMWNW0123	11	Slip (m)
Figure D-16	ZFMWNW0123	43	V_r/V_s
Figure D-17	ZFMWNW0123	43	Peak slip velocity (m/s)
Figure D-18	ZFMWNW0123	43	Slip (m)
Figure D-19	ZFMWNW0809A	11	V_r/V_s
Figure D-20	ZFMWNW0809A	11	Peak slip velocity (m/s)
Figure D-21	ZFMWNW0809A	11	Slip (m)
Figure D-22	ZFMWNW0809A	43	V_r/V_s
Figure D-23	ZFMWNW0809A	43	Peak slip velocity (m/s)
Figure D-24	ZFMWNW0809A	43	Slip (m)
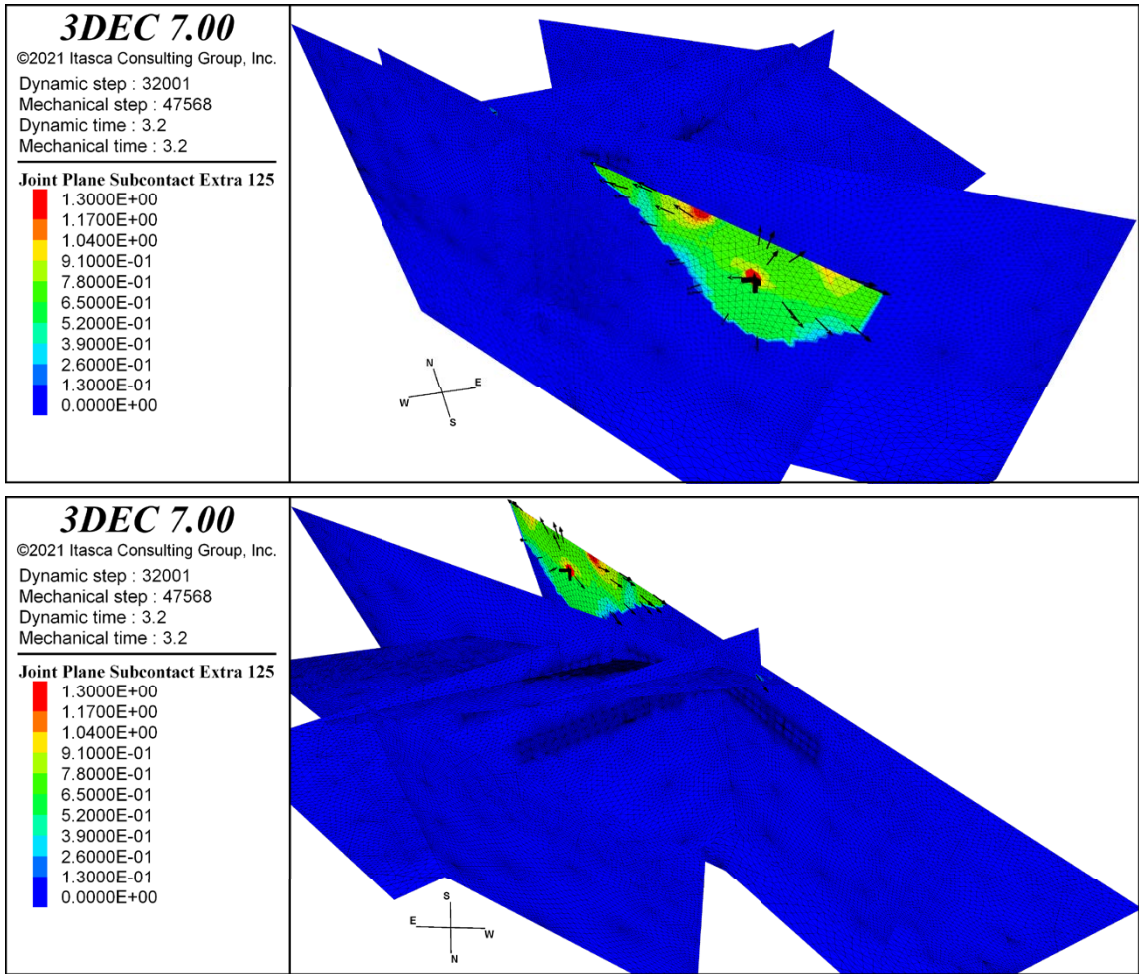
Figure D-1. *Two views showing normalised rupture velocity V_r/V_s along with rupture direction vectors in the case with 11 % σ_h reduction and rupture initiation on ZFMNW0017. The black cross indicates the hypocentre.*
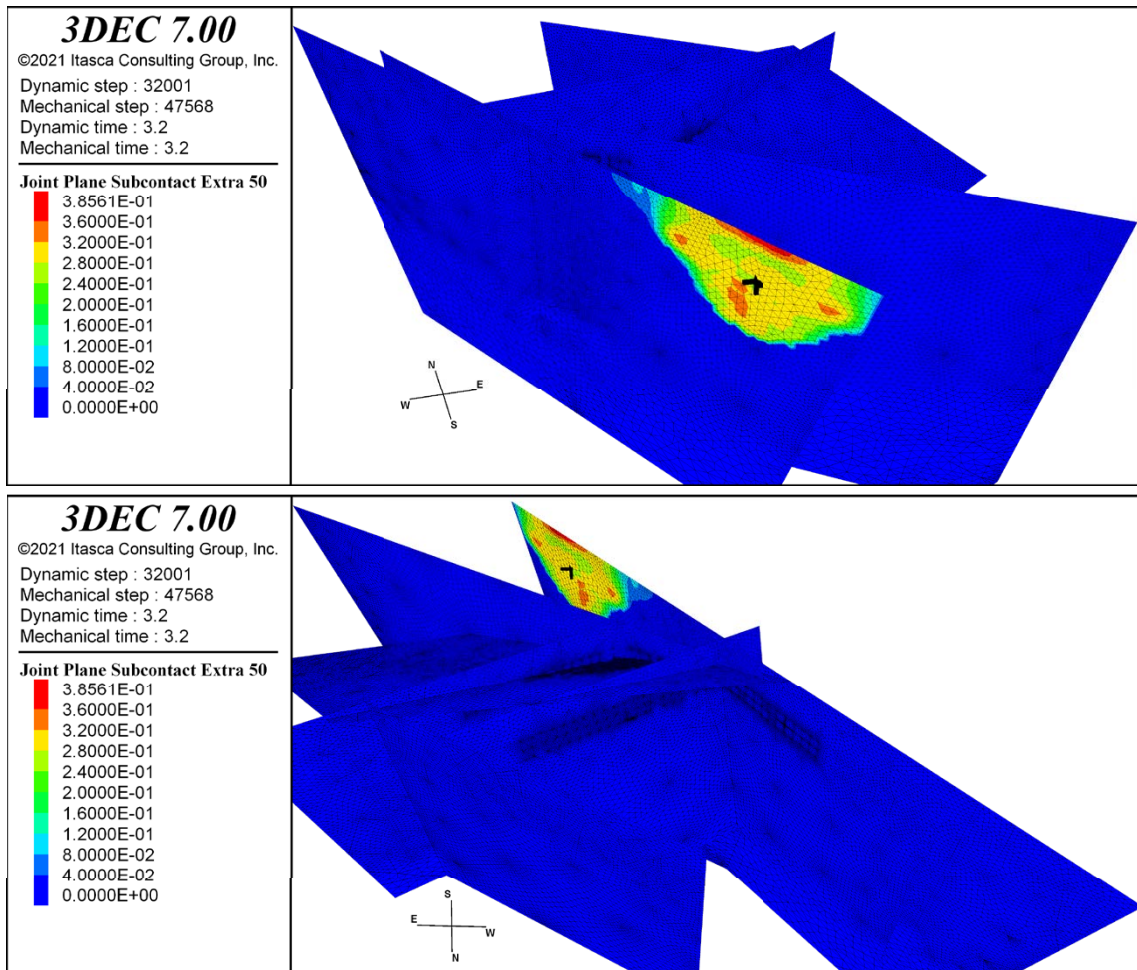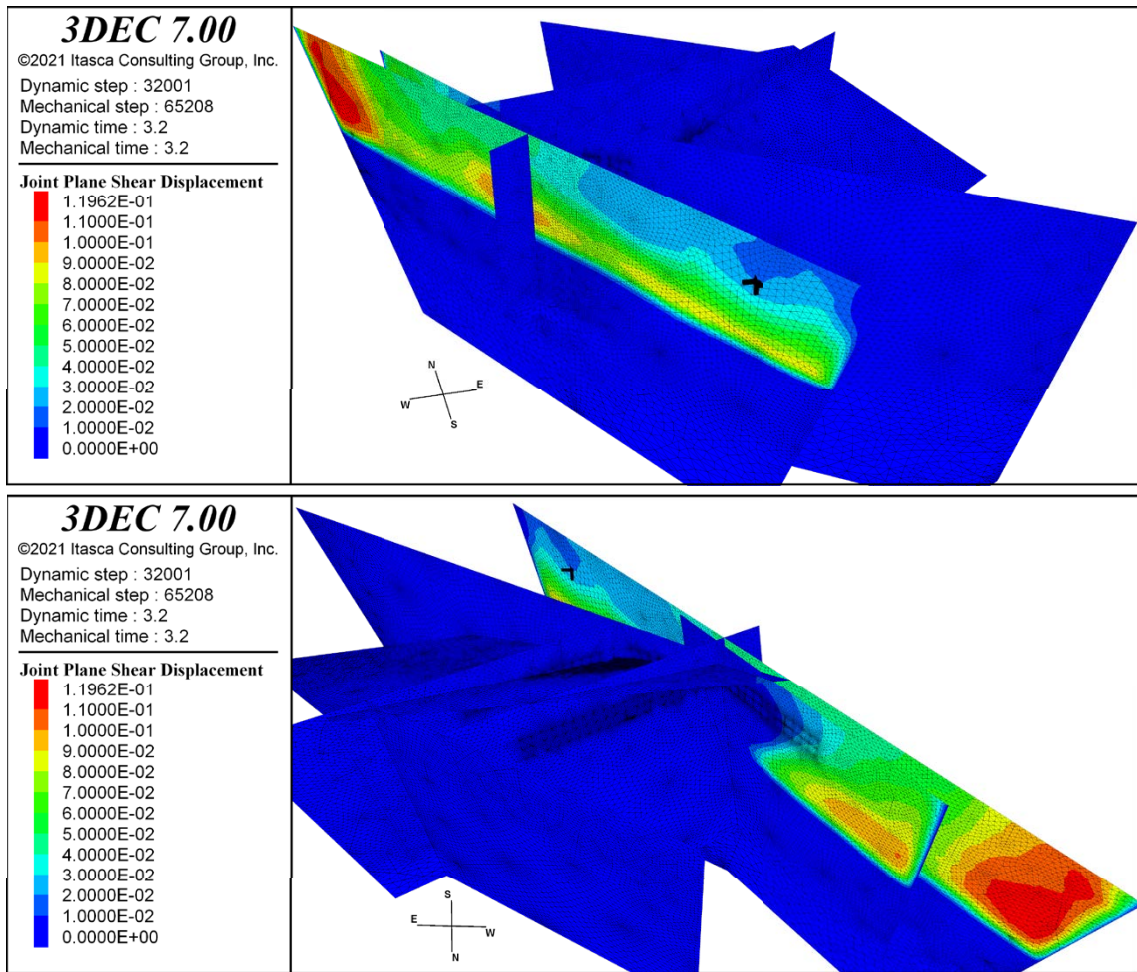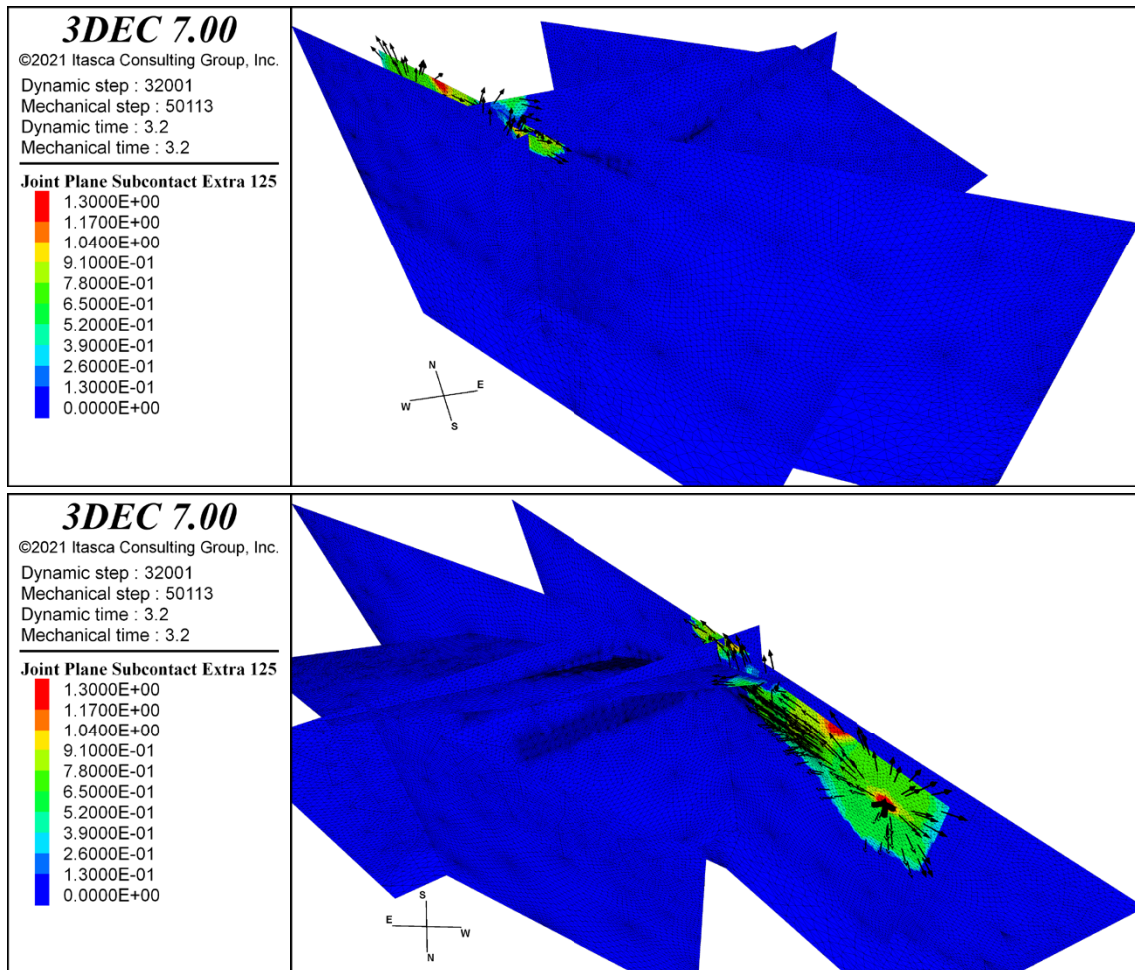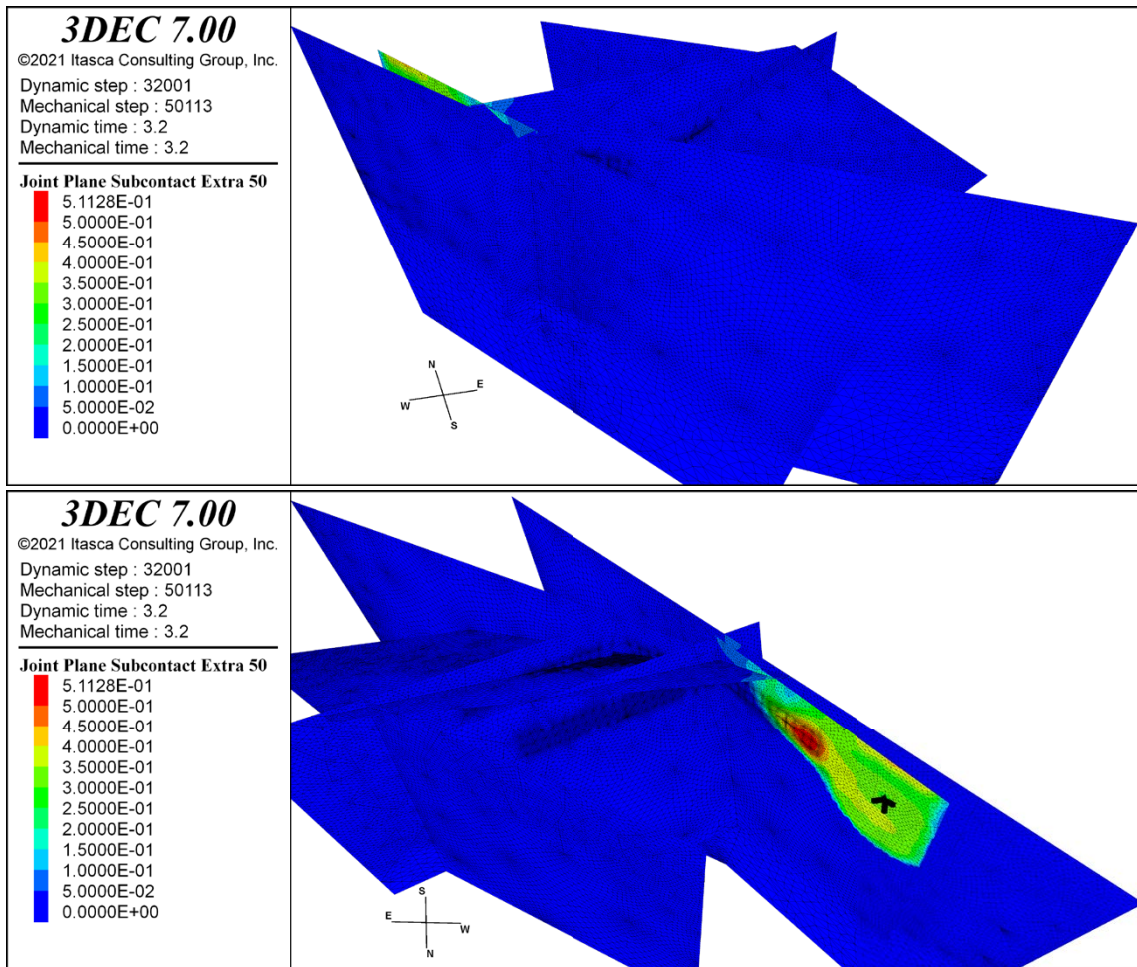
Figure D-2. *Two views showing peak slip velocity (m/s) in the case with 11 % σ$_h$ reduction and rupture initiation on ZFMNW0017. The black cross indicates the hypocentre. For illustrative purposes, the plotted values are determined from the stored peaks values using a moving spatial averaging over a circular area with 80 m radius.*
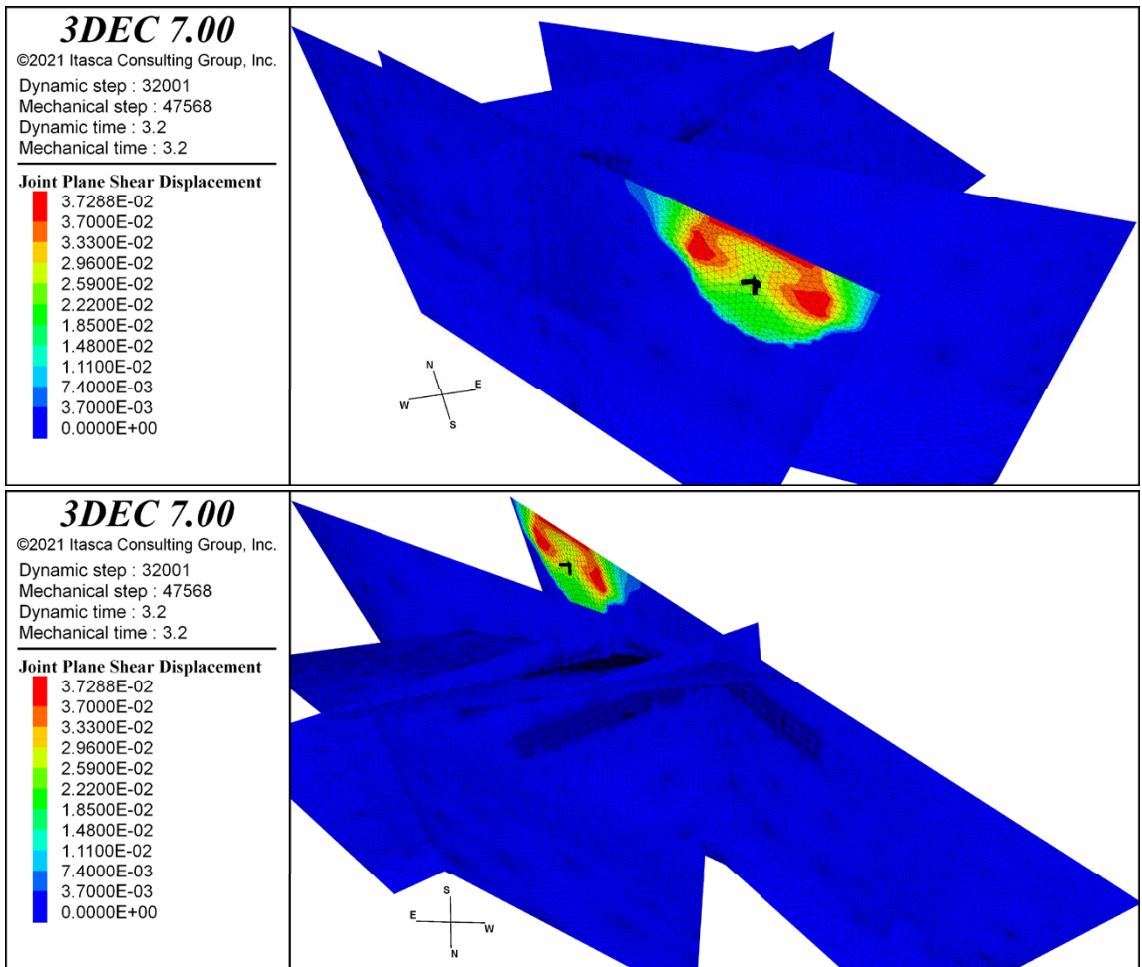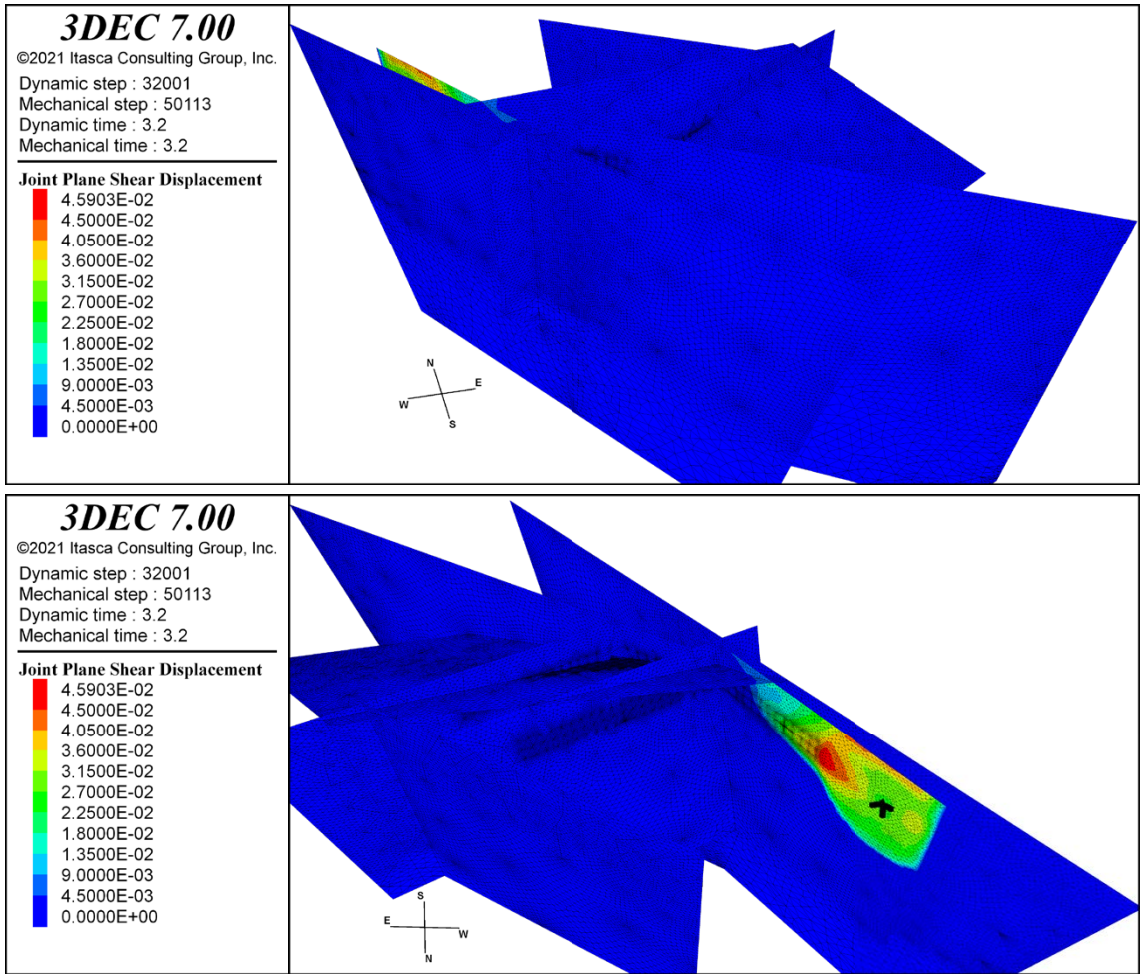
Figure D-3. *Two views showing fault slip (m) in the case with 11 % σ_h reduction and rupture initiation on ZFMNW0017. The black cross indicates the hypocentre.*
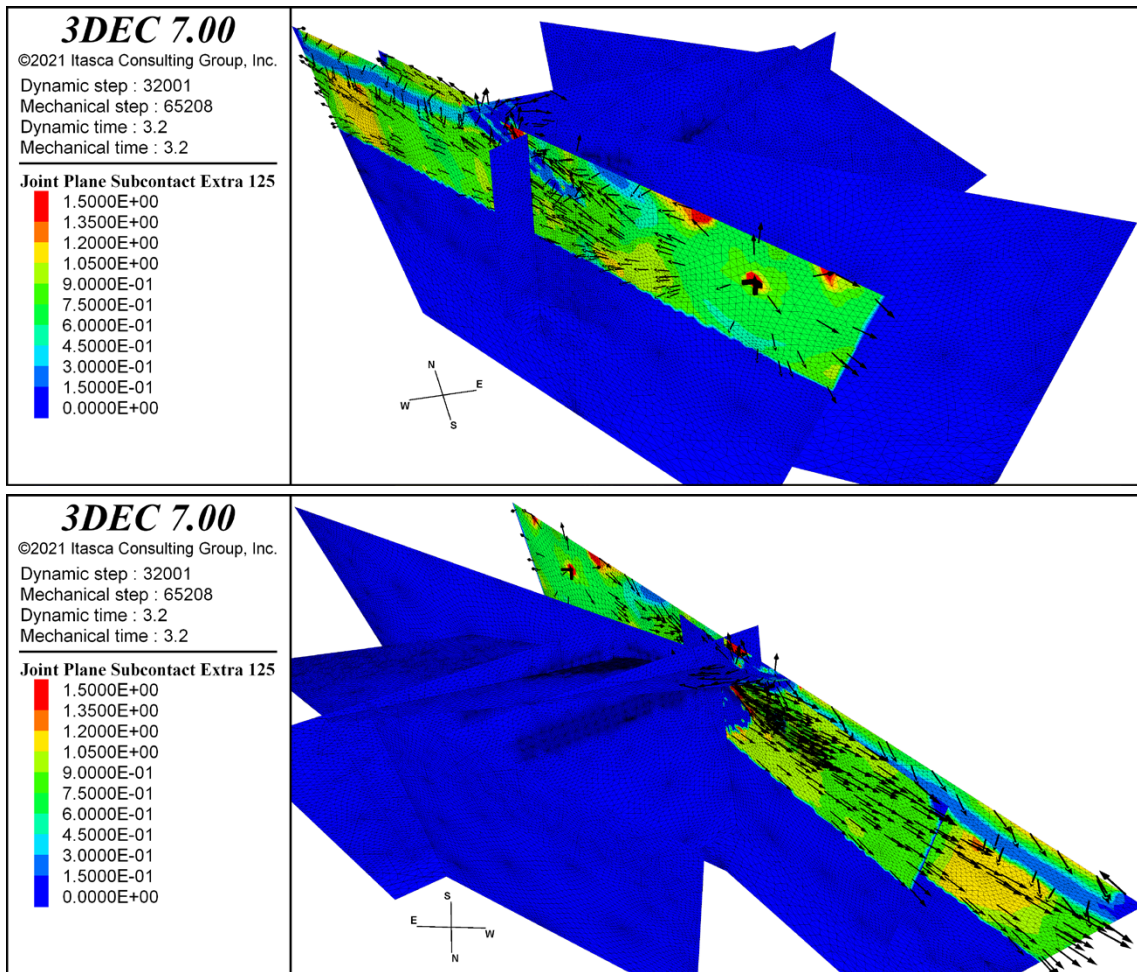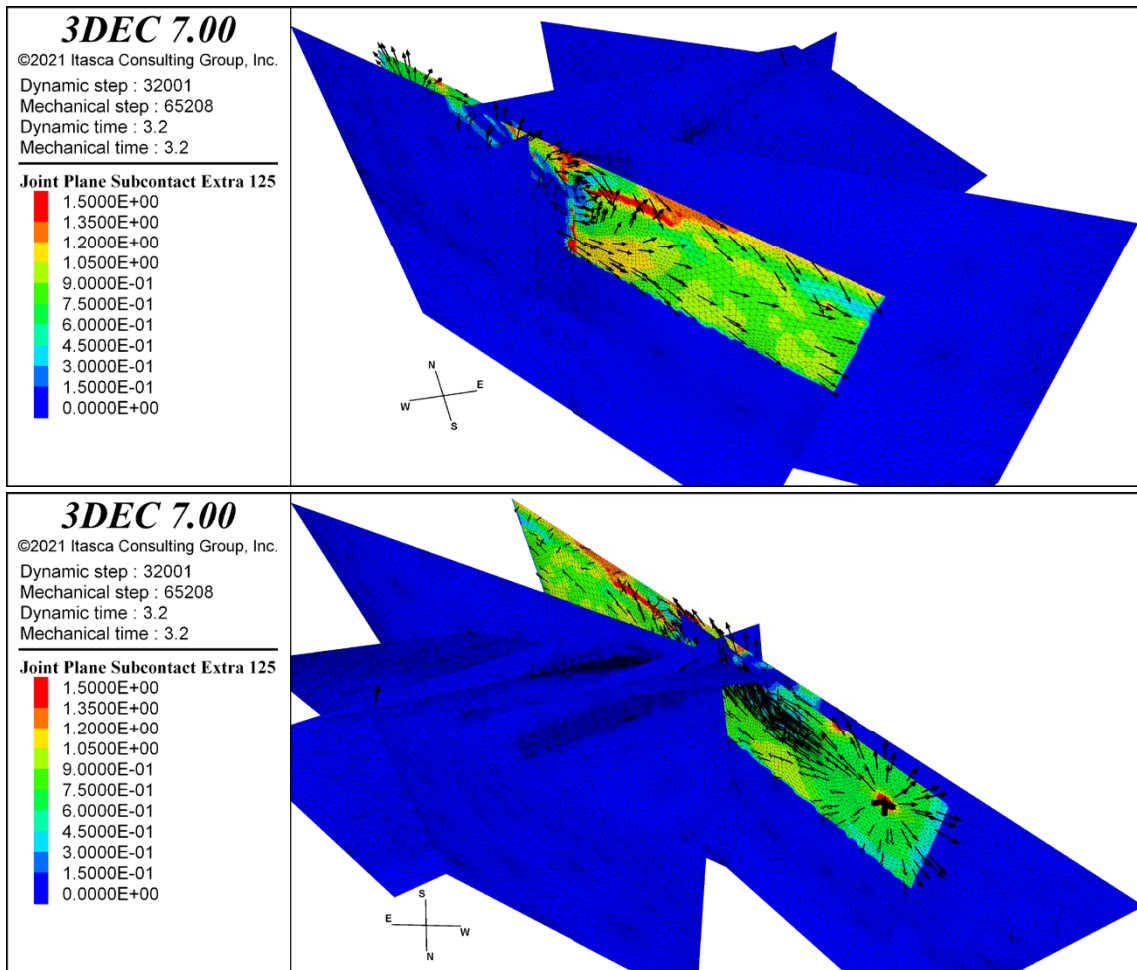
Figure D-4. *Two views showing normalised rupture velocity V_r/V_s along with rupture direction vectors in the case with 43 % σ_h reduction and rupture initiation on ZFMNW0017. The black cross indicates the hypocentre.*
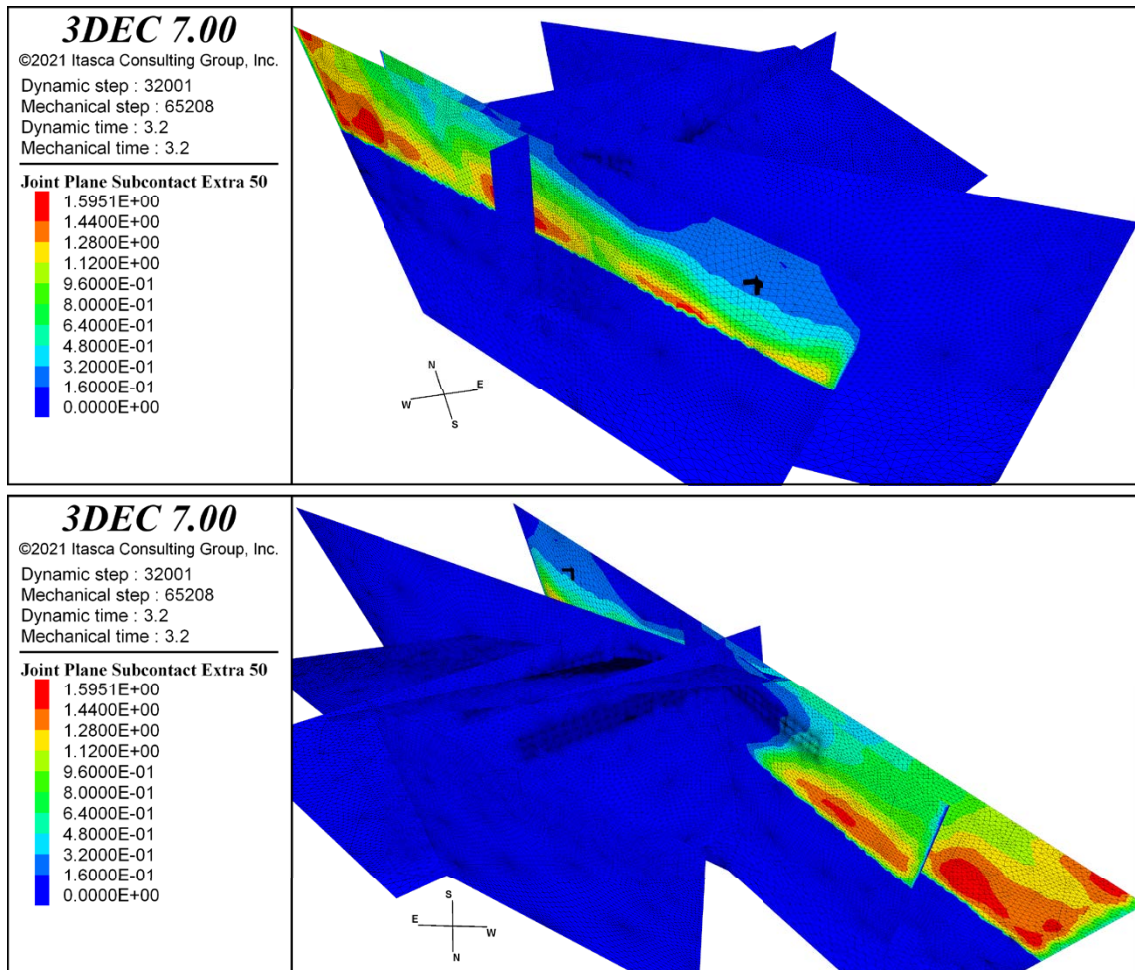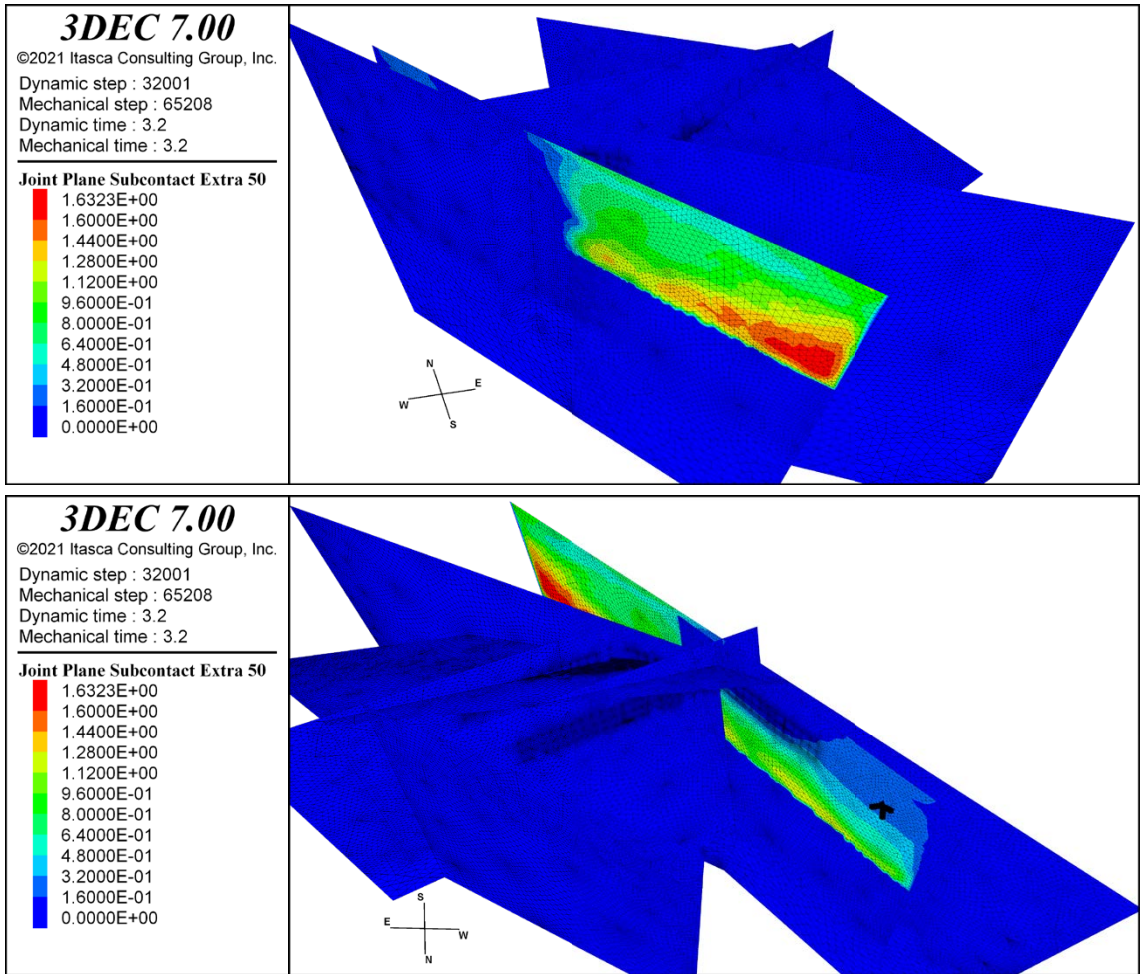
Figure D-5. *Two views showing peak slip velocity (m/s) in the case with 43 % σ_h reduction and rupture initiation on ZFMNW0017. The black cross indicates the hypocentre. For illustrative purposes, the plotted values are determined from the stored peaks values using a moving spatial averaging over a circular area with 80 m radius.*
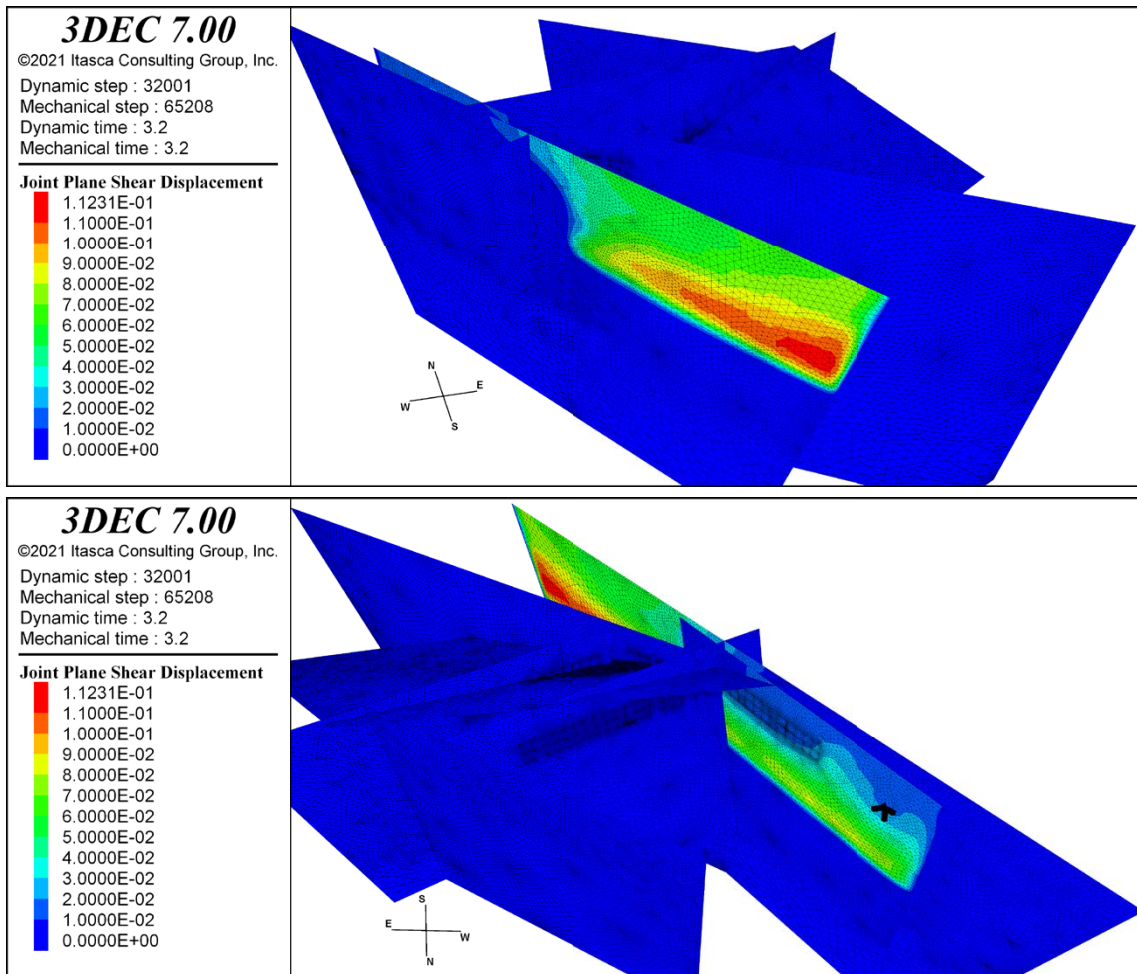
Figure D-6. *Two views showing fault slip (m) in the case with 43 % σ_h reduction and rupture initiation on ZFMNW0017. The black cross indicates the hypocentre.*
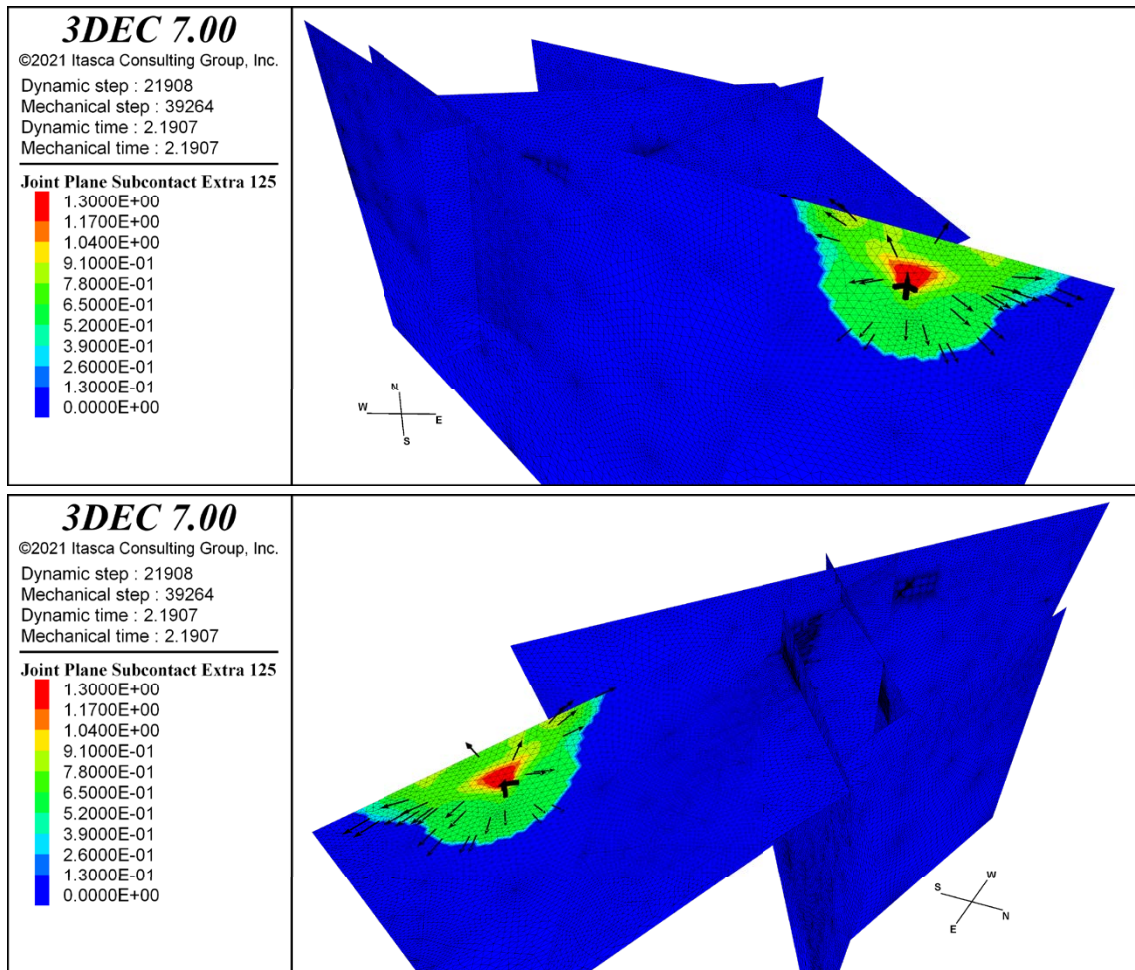
Figure D-7. *Two views showing normalised rupture velocity V_r/V_s along with rupture direction vectors in the case with 11 % σ_h reduction and rupture initiation on ZFMNW1200. The black cross indicates the hypocentre.*
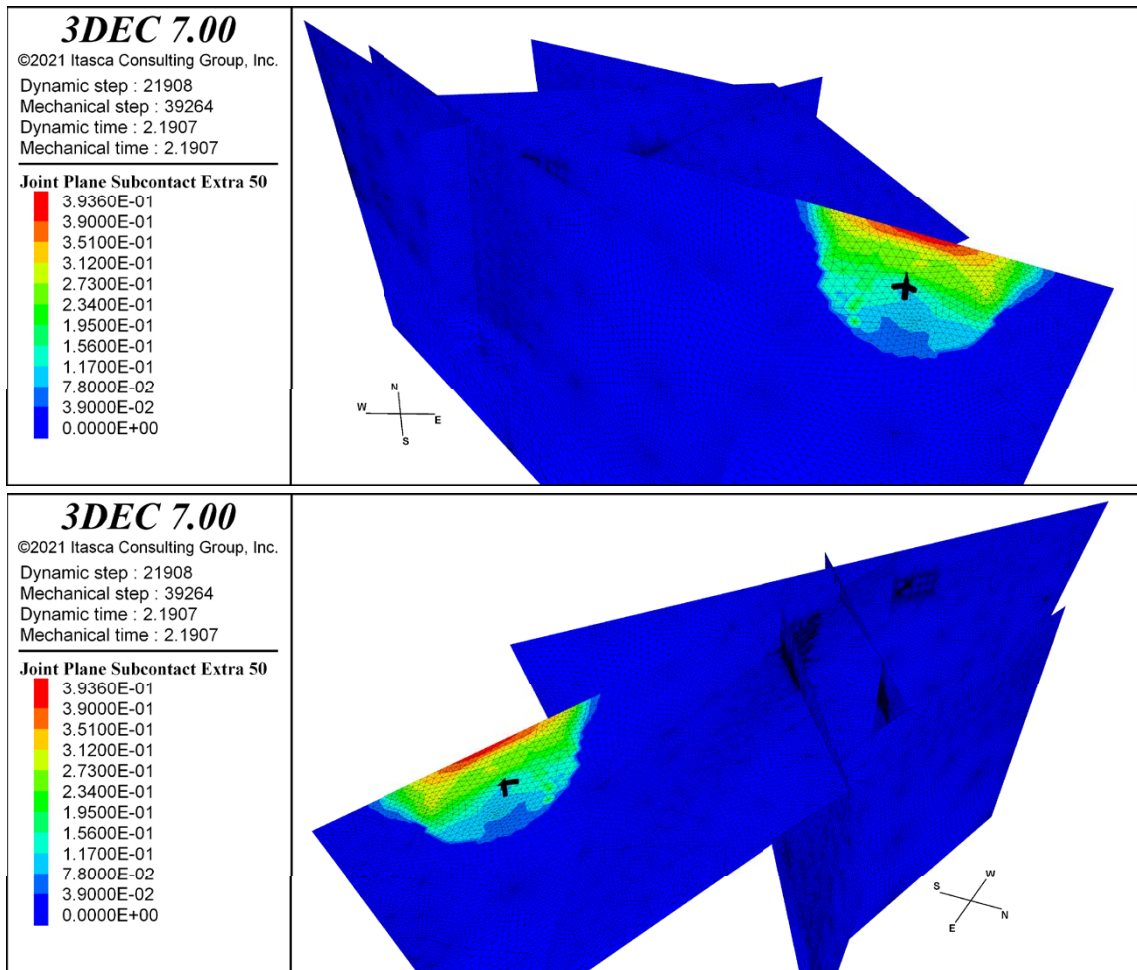
Figure D-8. *Two views showing peak slip velocity (m/s) in the case with 11 % σ_h reduction and rupture initiation on ZFMNW1200. The black cross indicates the hypocentre. For illustrative purposes, the plotted values are determined from the stored peaks values using a moving spatial averaging over a circular area with 80 m radius.*

Figure D-9. *Two views showing fault slip (m) in the case with 11 % σ_h reduction and rupture initiation on ZFMNW1200. The black cross indicates the hypocentre.*

Figure D-10. *Two views showing normalised rupture velocity V_r/V_s along with rupture direction vectors in the case with 43 % σ_h reduction and rupture initiation on ZFMNW1200. The black cross indicates the hypocentre.*

Figure D-11. *Two views showing peak slip velocity (m/s) in the case with 43 % σ_h reduction and rupture initiation on ZFMNW1200. The black cross indicates the hypocentre. For illustrative purposes, the plotted values are determined from the stored peaks values using a moving spatial averaging over a circular area with 80 m radius.*
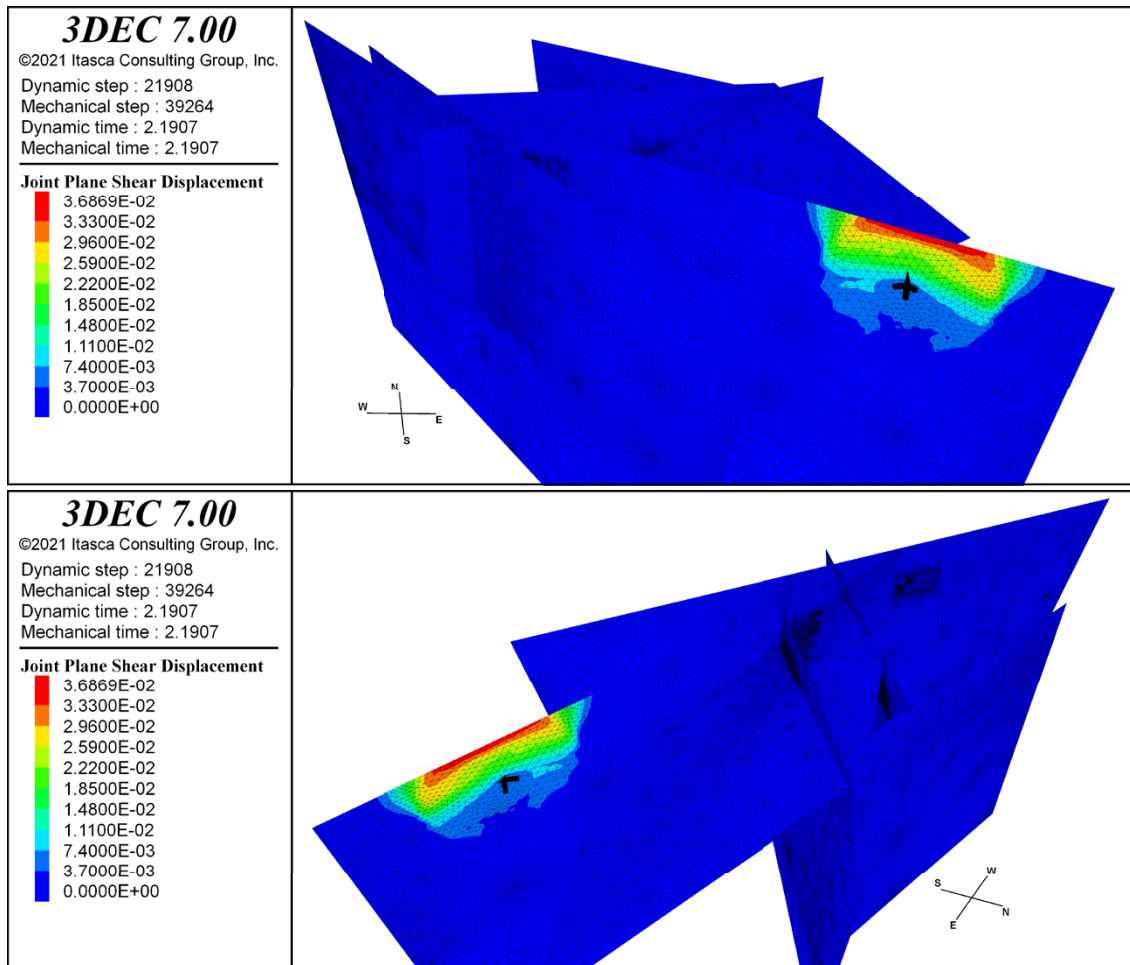
Figure D-12. *Two views showing fault slip (m) in the case with 43 % σ_h reduction and rupture initiation on ZFMNW1200. The black cross indicates the hypocentre.*
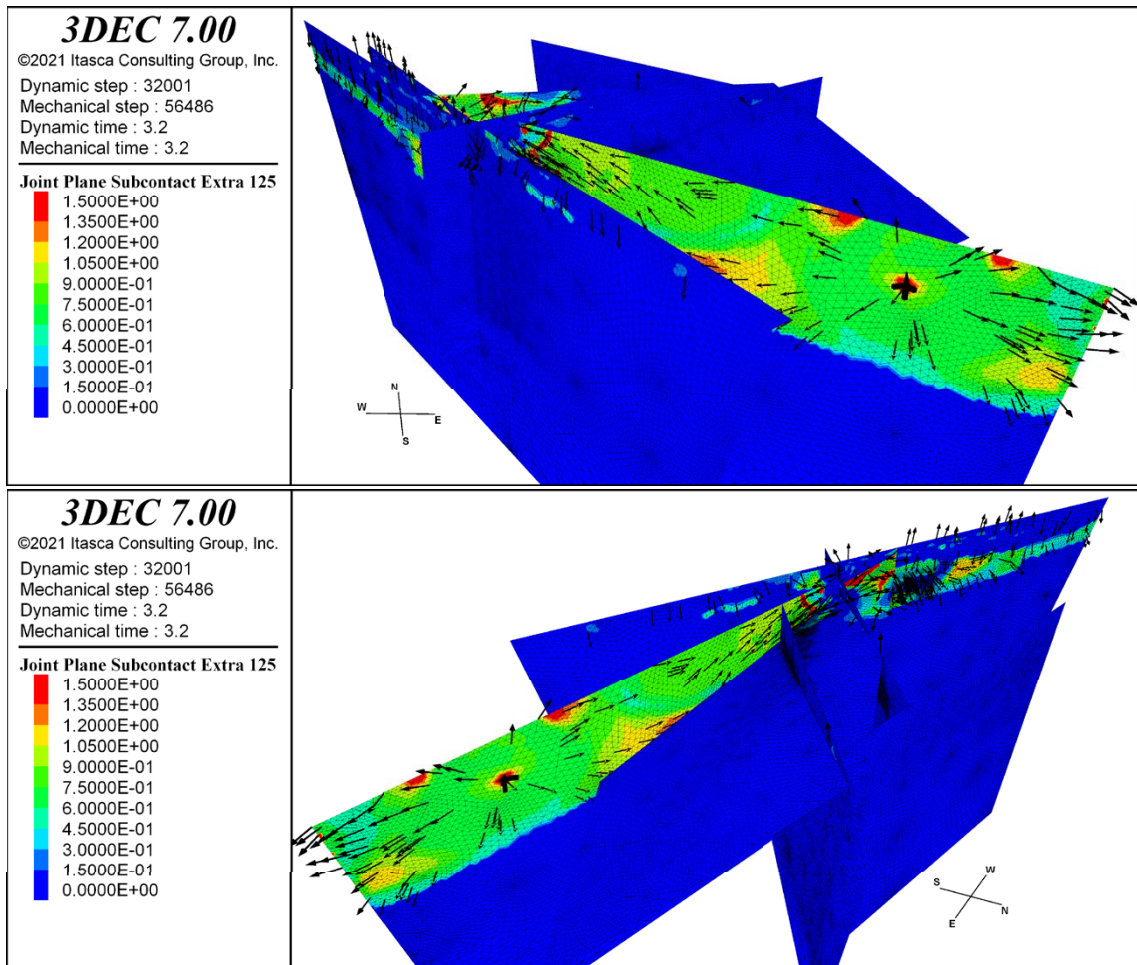
Figure D-13. *Two views showing normalised rupture velocity V_r/V_s along with rupture direction vectors in the case with 11 % σ_h reduction and rupture initiation on ZFMWNW0123. The black cross indicates the hypocentre.*
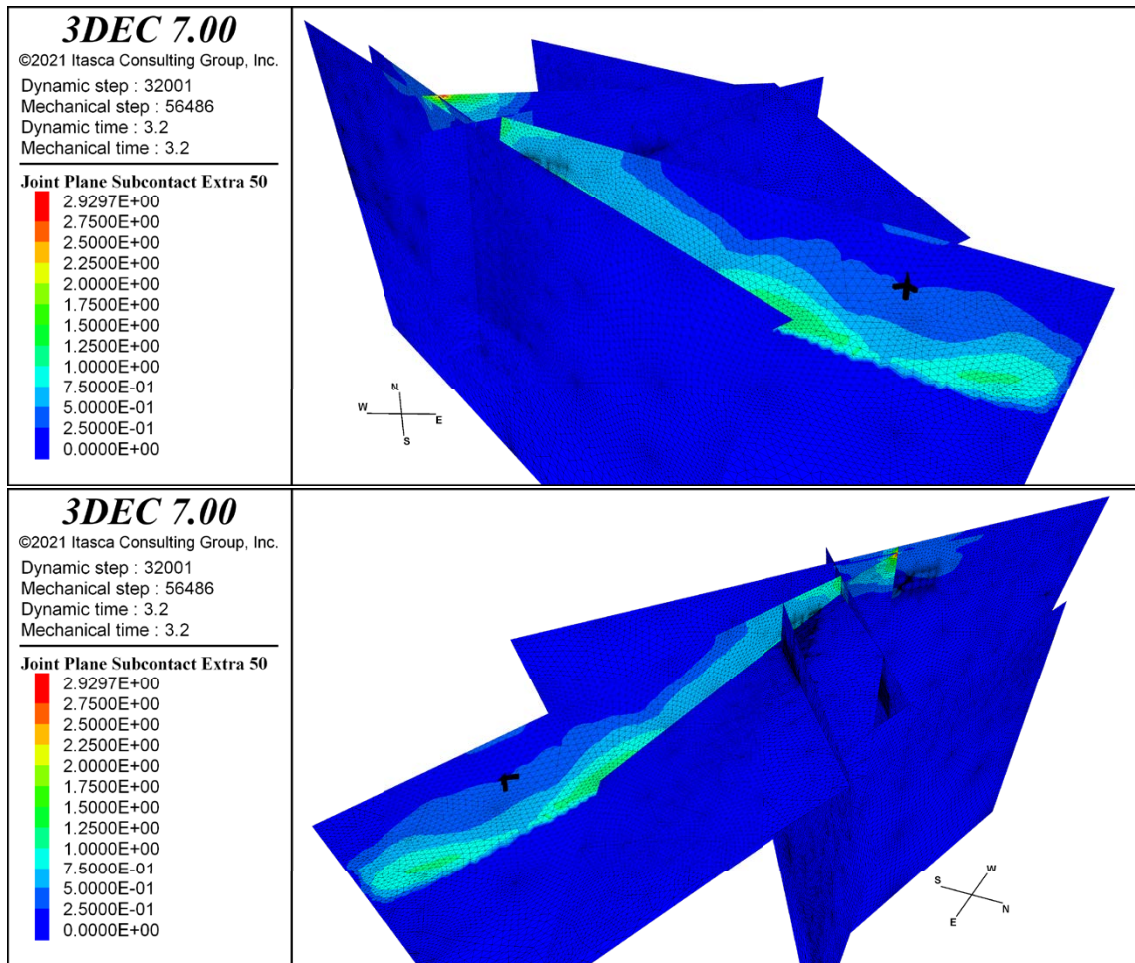
Figure D-14. *Two views showing peak slip velocity (m/s) in the case with 11 % σ$_h$ reduction and rupture initiation on ZFMWNW0123. The black cross indicates the hypocentre. For illustrative purposes, the plotted values are determined from the stored peaks values using a moving spatial averaging over a circular area with 80 m radius.*
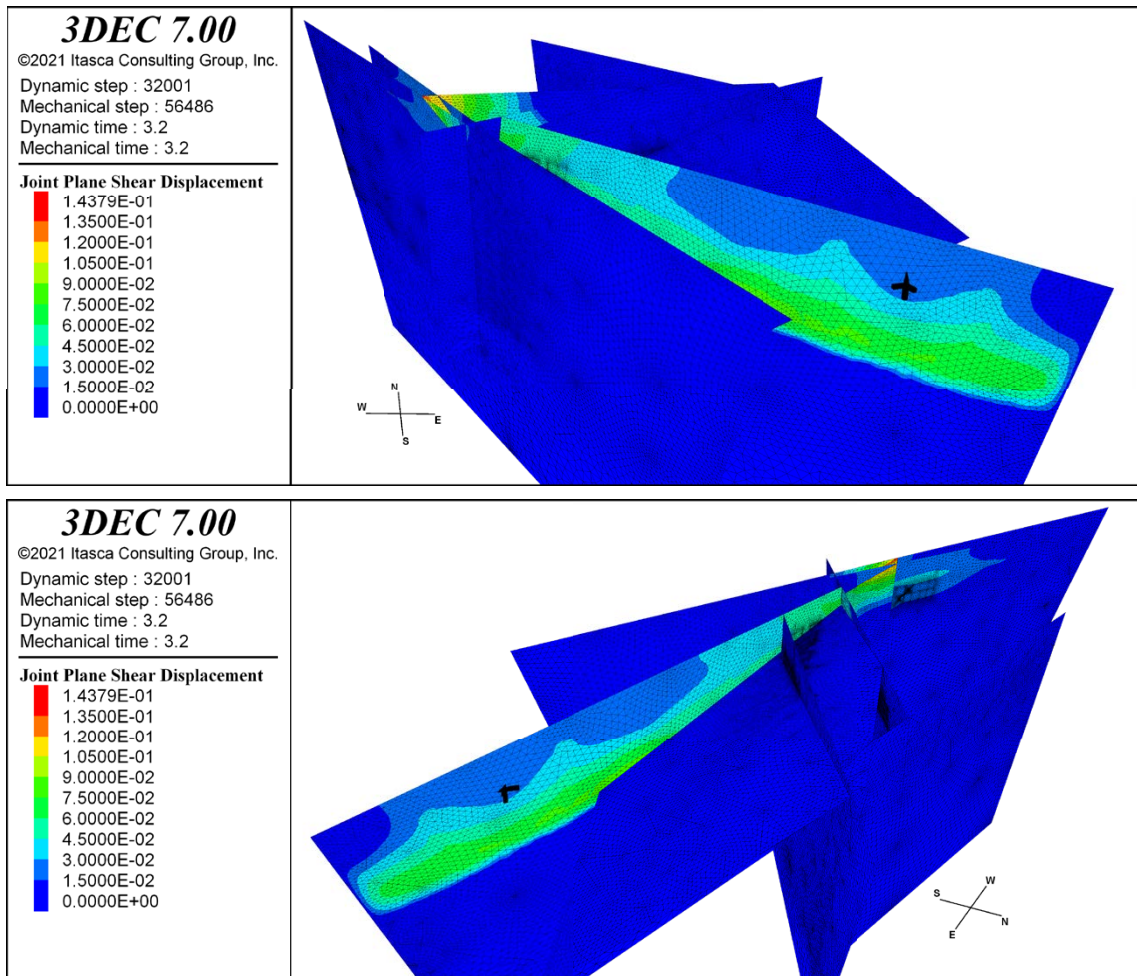
Figure D-15. *Two views showing fault slip (m) in the case with 11 % σ_h reduction and rupture initiation on ZFMWNW0123. The black cross indicates the hypocentre.*
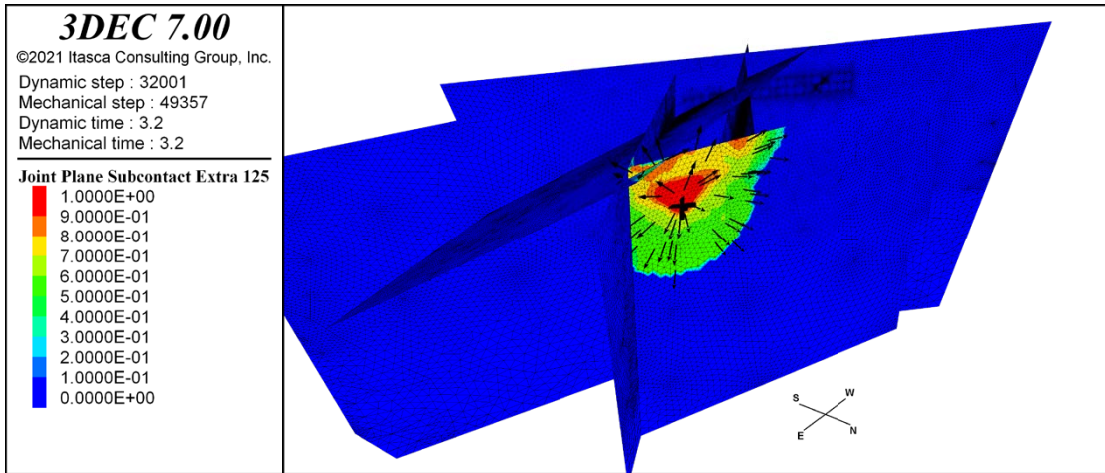
Figure D-16. *Two views showing normalised rupture velocity V_r/V_s along with rupture direction vectors in the case with 43 % σ_h reduction and rupture initiation on ZFMWNW0123. The black cross indicates the hypocentre.*

Figure D-17. *Two views showing peak slip velocity (m/s) in the case with 43 % σ_h reduction and rupture initiation on ZFMWNW0123. The black cross indicates the hypocentre. For illustrative purposes, the plotted values are determined from the stored peaks values using a moving spatial averaging over a circular area with 80 m radius.*

Figure D-18. *Two views showing fault slip (m) in the case with 43 % σ$_h$ reduction and rupture initiation on ZFMWNW0123. The black cross indicates the hypocentre.*

Figure D-19. *Normalised rupture velocity V_r/V_s along with rupture direction vectors in the case with 11 % σ_h reduction and rupture initiation on ZFMWNW0809A. The black cross indicates the hypocentre.*
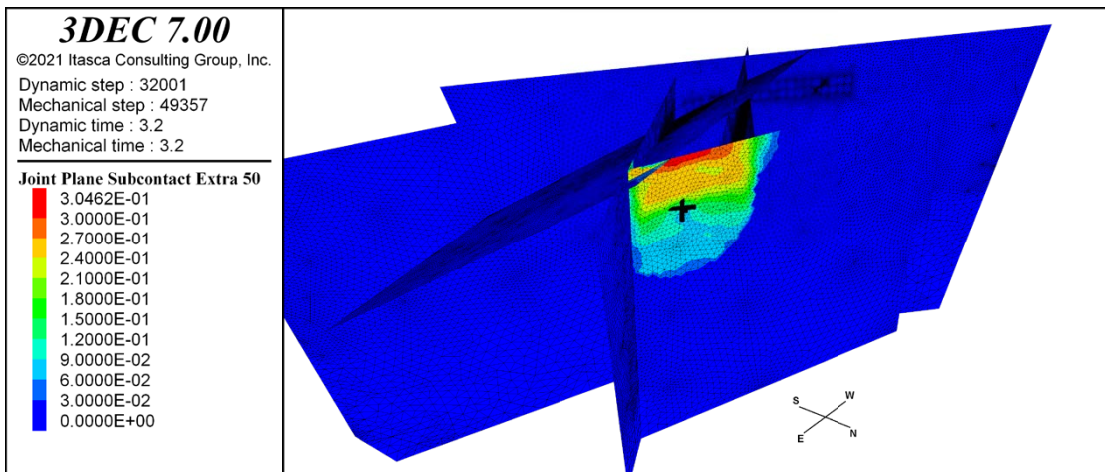

Figure D-20. *Peak slip velocity (m/s) in the case with 11 % σ_h reduction and rupture initiation on ZFMWNW0809A. The black cross indicates the hypocentre. For illustrative purposes, the plotted values are determined from the stored peaks values using a moving spatial averaging over a circular area with 80 m radius.*
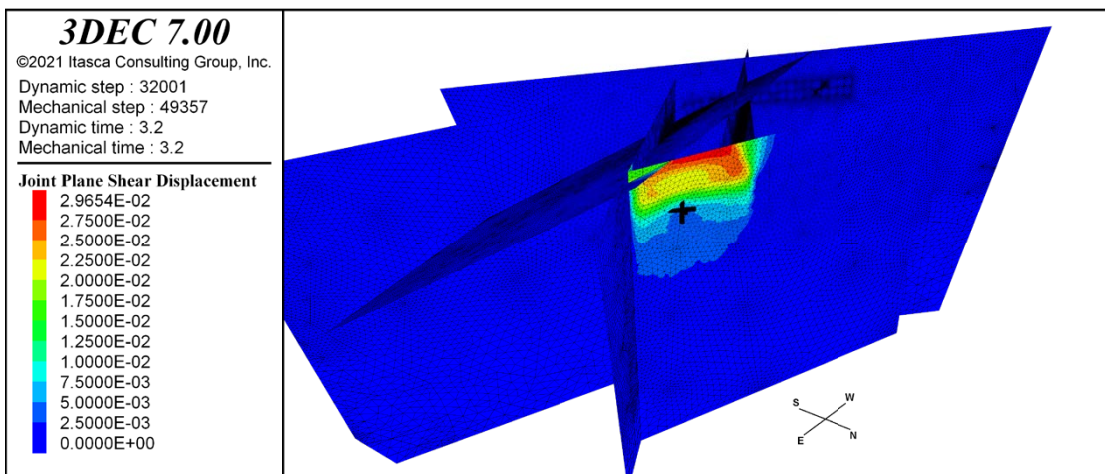

Figure D-21. *Fault slip (m) in the case with 11 % σ_h reduction and rupture initiation on ZFMWNW0809A. The black cross indicates the hypocentre.*
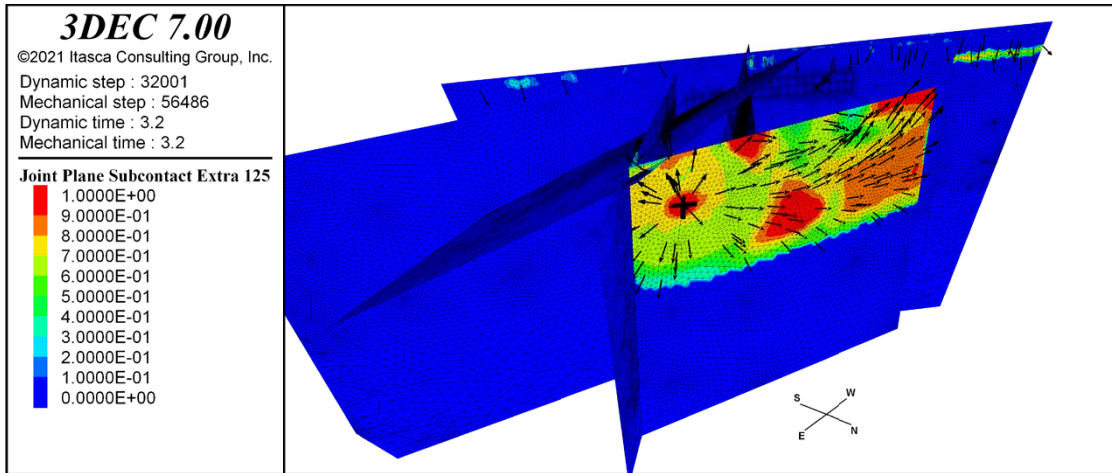
Figure D-22. *Normalised rupture velocity V_r/V_s along with rupture direction vectors in the case with 43 % σ_h reduction and rupture initiation on ZFMWNW0809A. The black cross indicates the hypocentre.*
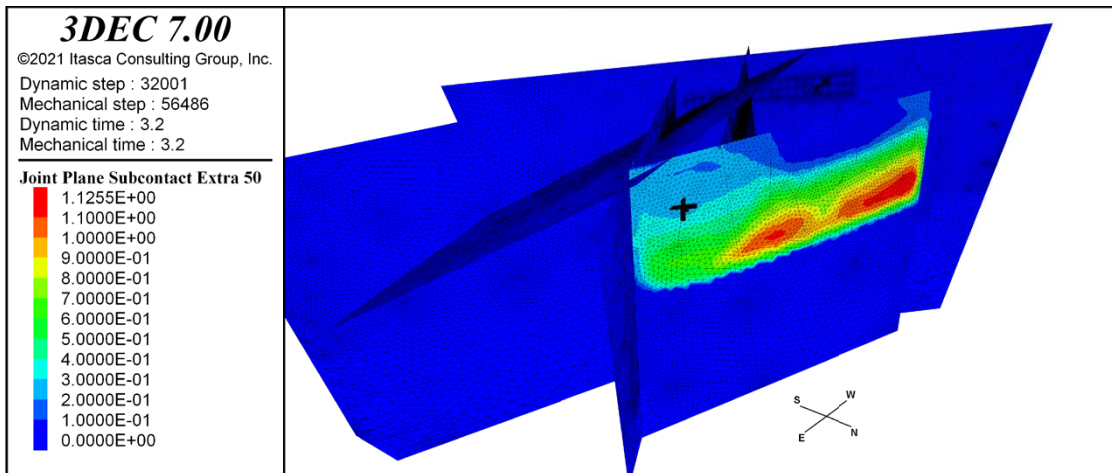

Figure D-23. *Peak slip velocity (m/s) in the case with 43 % σ_h reduction and rupture initiation on ZFMWNW0809A. The black cross indicates the hypocentre. For illustrative purposes, the plotted values are determined from the stored peaks values using a moving spatial averaging over a circular area with 80 m radius.*
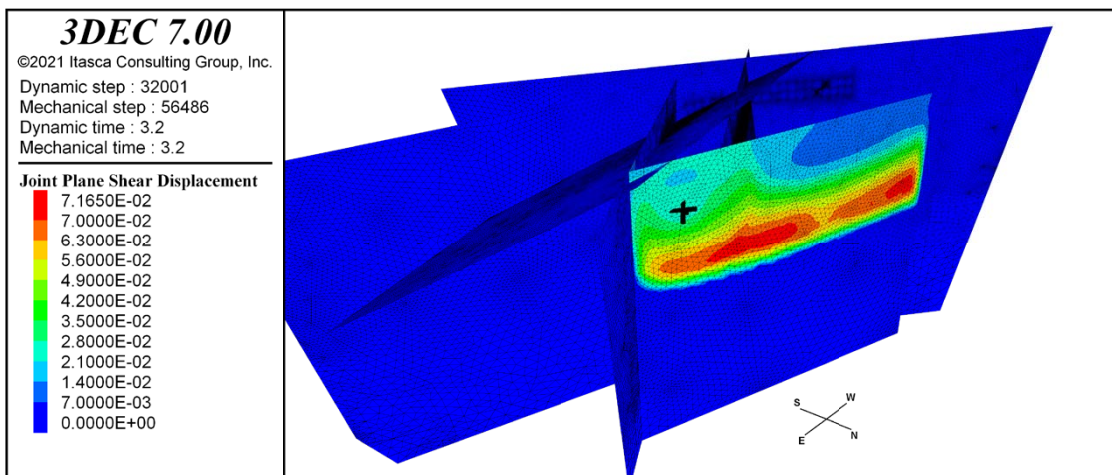

Figure D-24. *Fault slip (m) in the case with 43 % σ_h reduction and rupture initiation on ZFMWNW0809A. The black cross indicates the hypocentre.*

SKB is responsible for managing spent nuclear fuel and radioactive waste produced by the Swedish nuclear power plants such that man and the environment are protected in the near and distant future.

skb.se